WIRELESS ANTENNA SENSORS FOR STRAIN AND CRACK MONITORING

A Dissertation
Presented to
The Academic Faculty

by

Xiaohua Yi

In Partial Fulfillment
of the Requirements for the Degree
Doctor of Philosophy in the
School of Civil and Environmental Engineering

Georgia Institute of Technology

August 2014

WIRELESS ANTENNA SENSORS FOR STRAIN AND CRACK MONITORING

Approved by:

Dr. Yang Wang, Advisor
School of Civil and Environmental Engineering
Georgia Institute of Technology

Dr. Roberto T. Leon, Co-advisor
Department of Civil and Environmental Engineering
Virginia Polytechnic Institute and State University

Dr. Barry Goodno
School of Civil and Environmental Engineering
Georgia Institute of Technology

Dr. Manos M. Tentzeris
School of Electrical and Computer Engineering
Georgia Institute of Technology

Dr. Kenneth M. Will
School of Civil and Environmental Engineering
Georgia Institute of Technology

Date Approved: June 27, 2014

ACKNOWLEDGEMENTS

I would like to express my deepest gratitude to my advisor, Dr. Yang Wang for his continuous support and guidance throughout my Ph.D. life at Georgia Tech. I truly appreciate his patience and encouragement and am fortunate to have the opportunity to work with such a great advisor and mentor. I would also like to thank Dr. Roberto T. Leon for his guidance and insightful comments throughout my graduate studies at Georgia Tech. I want to thank Dr. Manos M. Tentzeris for his guidance through my study in the field of computational electromagnetics and radiofrequency engineering. I would also like to thank Dr. Kenneth M. Will, Dr. Barry Goodno for being part of my thesis committee and for their time and support for my research.

I would like to acknowledge Federal Highway Administration for funding the research project under Grant No. DTFH61-10-H-00004.

I want to thank Chunhee Cho for being an integral part of the research project. I am grateful for the assistance provided by Jiawei Lin, Xinjun Dong, Dapeng Zhu, Shuo Chen, Hongchuang Liu, Lei Feng, Chia-Hung Fong, Xi Liu, and Gabriel Lantz with the sensor validation experiments, Terence Wu, Amin Rida, Rushi J. Vyas, Vesileios Lakafosis, Cecilia Occhiuzzi, Hoseon Lee, James Cooper, Benjamin S. Cook, and Taoran Le for sharing their expertise and providing assistance during my graduate study. I would also like to thank Andy Udell for his help with fabrication of experimental setups.

Most importantly, I would like to express my heartfelt gratitude to my parents and my wife. I will always be indebted to you for your love, encouragement and unconditional support.

TABLE OF CONTENTS

Page

LIST OF TABLES

LIST OF FIGURES

LIST OF SYMBOLS AND ABBREVIATIONS

Δf_N	Normalized resonance frequency change
[C]	Inductance matrix
$[C^e]$	Elementary inductance matrix
[R]	Damping matrix
$[R^e]$	Elementary damping matrix
[T]	Capacitance matrix
$[T^e]$	Elementary capacitance matrix
$[\Delta A_j]$	Difference between [A] matrices at two adjacent strain steps ε_j and ε_{j+1}
$[\Delta B_j]$	Difference between [R] matrices at two adjacent strain steps ε_j and ε_{j+1}
$\{\Phi\}$	Right eigenvector
$[\Phi_{j+1}]$	Right eigenvector matrix at strain step j+1
$[\Phi_j]$	Right eigenvector matrix at strain step j
$\{\Psi\}$	Left eigenvector
$[\Psi_{j+1}]$	Left eigenvector matrix at strain step j+1
$[\Psi_j]$	Left eigenvector matrix at strain step j
C_{ij}^e	(i, j) entry of elementary inductance matrix for element e
R_{ij}^e	(i, j) entry of elementary damping matrix for element e
T_{ij}^e	(i, j) entry of elementary capacitance matrix for element e
E	Electric field

EPC	Electronic product code
E_{x}	*x* component of global electric field
E_{y}	*y* component of global electric field
E_{z}	*z* component of global electric field
E_i^e	Tangential electric field along the *i*-th edge of element *e*
f	Interrogation frequency of the reader
F	Functional
f_{R}	Resonance frequency of the sensor
f_{R0}	Resonance frequency of the sensor at zero strain level
$\mathbf{H}$	Magnetic field
HPBW	Half-power beam-width
H_x	*x* component of the magnetic field
H_y	*y* component of the magnetic field
H_z	*z* component of the magnetic field
[I]	Identity matrix
IC	Integrated circuit
j	Imaginary unit
k_0	wave number
L	Length of the top copper cladding of the sensor
L'	Additional length due to fringe effect
L_{R}	Loading ratio
$\mathbf{N}_i^e$	shape function of *i*-th edge of element *e*
P	Interrogation power level; Power transmitted back to the

	reader from the frequency doubling sensor
P_0	Incident power received at the frequency doubling sensor
P_1	Power transmitted from 2.9GHz antenna to the matching network
P_2	Power transmitted from the matching network to the 5.8GHz antenna
PEC	Perfect electrical conductor
PML	Perfectly matched layer
PTFE	Poly-tetra-fluoro-ethylene
Q	Quality factor of the sensor
R^2	Coefficient of determination
RFID	Radiofrequency identification
R_K	Surface impedance on the impedance sheet
s	Matrix scaling factor
S_{11}	Reflection coefficient
S_{11}^R	Reflection coefficient of the 2.9GHz receiving antenna
S_{11}^T	Reflection coefficient of the 5.8GHz transmitting antenna
S_{21}^M	Transmission coefficient between two ports of the matching network
SHM	Structural health monitoring
S_N	Normalized strain sensitivity
S_T	Resonance frequency change of the sensor due to temperature change
STD	Standard deviation
UHF	Ultra high frequency
V^i	Incident voltage

V^r	Reflected voltage
W	Sensor width
WISP	Wireless identification sensing platform
β	Material permittivity
β_0	Air permittivity
β_r	Material relative permittivity (dielectric constant)
β_{reff}	Material effective dielectric constant
Δf_{3dB}	3dB bandwidth around the resonance frequency
ΔT	Temperature difference
$\Delta\varepsilon_i$	Difference between measured strain and strain estimated using the linear relationship at the *i*-th strain level
ε	Strain
β_r^T	Substrate dielectric constant at temperature *T*
$[\Lambda_{j+1}]$	Diagonal eigenvalue matrix at strain step *j*+1
$[\Lambda_j]$	Diagonal eigenvalue matrix at strain step *j*
μ	Permeability
μ_0	Air permeability
μ_r	Relative permeability
$\tilde{\omega}$	Angular frequency

SUMMARY

This research explores a series of wireless antenna sensors that are developed for convenient and low-cost monitoring of structures. The electromagnetic resonance frequency of an antenna changes when the antenna undergoes deformation, which is how strain or stress concentration is sensed. Building upon latest wireless technology, two antenna sensing mechanisms, radiofrequency identification (RFID) and frequency doubling, are adopted for antenna sensor designs. A multi-physics coupled simulation framework is proposed to improve the simulation accuracy. In order to improve the simulation efficiency, eigenvalue perturbation techniques are investigated for solving the eigenvalue problems formulated in electromagnetic domain.

This thesis first describes the RFID and frequency doubling mechanisms for strain/crack sensing. Based on the two mechanisms, a series of RFID antenna sensors and frequency doubling antenna sensors are designed. To improve the strain sensing simulation accuracy of the antenna sensors, mechanics-electromagnetics coupled simulation is proposed to use one finite element model that incorporated both mechanic and electromagnetic behaviors. To further improve the simulation accuracy, the dielectric constant change of the sensor substrate is quantified at different strain levels through experimental testing. The relationship between the dielectric constant and strain is incorporated into the mechanics-electromagnetics coupled simulation.

The mechanics-electromagnetics coupled simulation is usually time consuming, especially with large amount of frequency steps and complex sensor features. The antenna resonance frequency at each strain level can be solved as an eigenvalue problem in electromagnetic domain. To improve the simulation efficiency, two eigenvalue perturbation methods, first order eigenvalue perturbation method and the inverse Rayleigh quotient iteration method, are investigated and integrated with the coupled simulation process. Instead of solving the electromagnetic eigenvalue problem at every

strain step, the eigenvalue at a new strain step is directly updated according to eigenvalue results in the previous strain step. The simulation efficiency can be greatly improved by the proposed eigenvalue perturbation approaches.

In terms of implementation, a passive RFID folded patch antenna sensor is first developed. Experimental test results show that the sensor can measure strain as small as 20 με and as high as 10,000 με. Using a Yagi reader antenna, the antenna sensor can achieve consistent strain sensing results when the interrogation distance is increased up to 84 in. An array of sensors in close proximity is also demonstrated for effective strain measurement. Furthermore, the experimental results demonstrate that the sensor is capable of measuring small cracks and tracking crack propagation area. To reduce the sensor footprint, two RFID slotted patch antenna sensors are developed. Planar of sensor is only about half of the folded patch antenna sensor. With an active slotted patch antenna sensor that can receive power from a small solar cell, the interrogation distance can be further increased to 156 in. The slotted patch antenna sensors are also demonstrated for tension and compression strain sensing, emulated crack sensing, and fatigue crack sensing of both aluminum and steel specimens.

To further improve the strain sensitivity, multiple frequency doubling antenna sensors are designed and fabricated to operate at higher GHz frequencies. A Schottky diode is integrated in the sensor design for generating output signal at twice frequency of the input signal, which allows the wireless reader to easily distinguish backscattered sensor signal from unwanted environmental reflections. The frequency doubling antenna sensor includes two patch antennas, serving as 2.9GHz receiving antenna and 5.8GHz transmitting antenna, and a Schottky diode integrated matching network. The experimental results demonstrate that the strain sensitivity can be improved as five times higher than the RFID antenna sensors.

CHAPTER 1 INTRODUCTION

In this chapter, Section 1.1 first briefly introduces the background and motivation of this research. Section 1.2 discusses research purpose and objective. Finally, Section 1.3 presents the organization of this dissertation.

1.1 Background and Motivation

In order to accurately assess deterioration of civil, mechanical, and aerospace structures, a large volume of research in structural health monitoring (SHM) has been inspired over the past few decades [1]. SHM systems can advance time-based maintenance into more cost effective condition-based maintenance. Sensors have been developed to measure various structural responses and operating conditions, including strain, displacement, acceleration, humidity, temperature, *etc*. Among the measurements, strain can be an important indicator for stress concentration and crack development. Metal foil strain gages are currently among the most common solutions for strain measurement, owing to their low-cost, simple circuitry, and acceptable reliability in many applications. However, when applied to large structures, traditional metal foil strain gages require lengthy cable connections for power supply and data acquisition, which can significantly increase installation time and system cost [2]. One objective of this research is to develop low-cost wireless antenna sensors for monitoring stress concentration and crack propagation in structures. Since the electromagnetic resonance frequency of an antenna is related to the antenna's physical dimension, the resonance frequency changes when the antenna experiences strain. After bonding or embedding the antenna to a structure, this relationship between resonance frequency and strain can be used for stress/strain measurement. In order to efficiently design antenna sensors, multi-physics coupled simulation, as well as eigenvalue perturbation techniques, is also discussed. Literature review of relevant research topics is provided in the following three subsections. Section 1.1.1 first reviews conventional wireless SHM technologies. Section

1.1.2 introduces the state of the art of wireless antenna sensors. Section 1.1.3 discusses multi-physics coupled simulation techniques for antenna sensor designs. Eigenvalue perturbation algorithms are also briefly reviewed.

1.1.1 Conventional Wireless Structural Health Monitoring (SHM) Technologies

Among many new SHM technologies, wireless sensing can help to significantly reduce instrumentation time and system cost [3-6]. An exhaustive review on wireless sensing for SHM can be found in Lynch and Loh [7], which summarizes development of various academic and industrial wireless sensing devices. A wireless sensing device usually has three functional modules: sensing interface (converting analog sensor signal to digital data), computing core (data storage and processing), and wireless transceiver (digital communication with peers or a wireless gateway server). To obtain different types of measurements, various sensors can be connected with the sensing interface of a wireless sensing device. For example, strain measurement is obtained by interfacing the device with a metal foil strain gage. In addition, current wireless sensing devices usually operate on external power source, such as batteries.

To avoid periodic battery replacement in the field, rechargeable batteries are usually deployed. These batteries are charged by an integrated energy harvester. Typical sources for energy harvesting include solar energy, mechanical vibration, and thermal gradients, *etc* [8]. However, even with a reliable source for energy harvesting, rechargeable batteries usually have a limited life span. Alternatively, passive wireless sensors can eliminate the dependency on battery power [9]. One of the approaches is to adopt radiofrequency identification (RFID) technology passive sensing [10]. An RFID-based wireless sensor can capture operation power from wireless interrogation signal emitted by a reader. For example, a WISP (wireless interrogation and sensing platform) unit receives operation power from an ultra-high frequency (UHF) RFID reader, and

communicates with the reader through RFID interface [11]. Nevertheless, a WISP unit still contains a programmable microcontroller and an analog-to-digital converter, which makes its basic architecture belong to conventional wireless sensing devices as summarized by Lynch and Loh [7].

In summary, while wireless SHM systems improve installation convenience and economic efficiency, long term field application is limited due to its requirement of extra power supply. To alleviate the problem, passive wireless antenna sensors are developed. The next section briefly introduces the research status of wireless antenna sensors.

1.1.2 Wireless Antenna Sensors

Other researchers have proposed wireless passive strain sensors based on inductive coupling that involves two adjacent inductors [12-14]. The interrogation distance achieved by inductive coupling is usually limited to several inches, which is inconvenient for practical applications. Similarly, Matsuzaki *et al* [15] proposed a half wave-length dipole antenna to detect damage in CFRP structures. The damage introduced antenna property changes, including power spectrum and return loss, are measured and used as the damage indicator. A circular patch antenna sensor has been proposed for omnidirectional strain sensing by wirelessly measuring scattering parameter [16]. Another passive on-chip RF-MEMS strain sensor is developed for bio-medical application [17]. Without proper signal modulation, the sensor operates in the near field of a reader antenna. As a result, the wirelessly received sensor signal is mixed with background reflection; only limited interrogation distance is achieved.

In order to increase interrogation distance, electromagnetic backscattering techniques have been exploited for wireless strain sensing. For example, a patch antenna has been designed for wireless strain sensing [18, 19], where a phototransistor is adopted for modulating the RF signal backscattered from the antenna sensor. As a result of the

modulation, backscattered sensor signal can be distinguished from environmental reflections. However, besides requiring line of sight, the light-switching mechanism is not practical for outdoor application, where light intensity is usually so strong that the phototransistor is constantly activated and thus, loses ability of switching. As another example, Thomson *et al*. [20] developed an RF cavity sensor for wireless strain sensing. An external antenna needs to be connected with the cavity sensor for interrogation. Due to the cavity configuration, the sensor is more suitable for embedment inside concrete, instead of installation on a metallic surface. To distinguish sensor signal from environmental noise, signal modulation mechanism is important to ensure reliable signal-to-noise ratio, and thus the sensor performance. Occhiuzzi *et al* [21] proposed a meander-line RFID antenna sensor for wireless strain sensing. The shift in the power level is correlated with applied strain to determine structural deformation. Since the power level is susceptible to environmental noise, the measurement accuracy is limited.

The current commercial off-the-shelf RFID chips have limited operating frequency range [22]. In order to design sensors operating at higher frequency range for improved strain sensitivity, an alternative way of signal differentiation mechanism is frequency doubling. The frequency doubling operation is implemented through a Schottky diode, which is a nonlinear circuit device and can generate output signal with frequencies at harmonics (multiples) of input frequency. For example, with an input signal at frequency f, the output signals are located at $2f$, $3f$, and other multiples of its input frequency. Diode frequency multipliers have been adopted for energy harvesting [23], insect tracking [24], among others. In [25], a high efficiency frequency doubling device is designed using a GaAs Schottky diode that provides 1% conversion efficiency at -30 dBm input power. Nevertheless, to the author's best knowledge, no other literature uses Schottky diode to enable frequency doubling for wireless passive strain sensing.

Based on the strain/crack sensing mechanism of RFID antenna sensors and frequency doubling antenna sensors, the sensor design processes are usually realized in

commercial software packages specialized on electromagnetic structures, such as HFSS (High Frequency Structural Simulator), CST (Computer Simulation technology), ADS (Advanced Design System), Sonnet Suites, *etc*. The adopted simulation techniques are briefly reviewed in the following section.

1.1.3 Multi-physics Coupled Simulation

Since traditional antenna designs are all related with computational electromagnetics, special techniques can be applied to improve the simulation efficiency and accuracy. A large amount of studies have been conducted to develop various simulation methods in computational electromagnetics, such as finite difference time domain (FDTD) method [26, 27], multiresolution time-domain method (MRTD) [28], finite element method (FEM) [29, 30], finite integration technique (FIT) [31], method of moment (MOM) [32, 33], transmission-line-matrix method [34, 35], method of lines (MOL) [36], *etc*. While the specialized techniques provide accurate and efficient solvers in electromagnetics, they may have difficulties when integrated with modeling in other physical domains, such as mechanics. In order to accurately simulate strain sensing performance of antenna sensors, it is necessary to use coupled simulation to model different boundary conditions in different domains. There are also some commercial multi-physics coupled simulation software packages available, such as COMSOL Multiphysics [37], ANSYS [38], CST [39], *etc*. More accurate simulation results are expected with coupled simulation implementation.

The coupled simulation discussed in this research is mainly mechanics and electromagnetics coupling, i.e. mechanical deformation induced electromagnetic performance change of antenna sensors. In this application, the coupled simulation needs to identify the relationship between the resonance frequency shift and strain. The resonance frequency can be determined by antenna reflection coefficient (S_{11}) plot from

frequency domain solver [40]. In the S_{11} plot between simulated frequency (x-axis) and S_{11} results (y-axis), the minimum point of the S_{11} curve is defined as the resonance frequency of antenna sensors. In order to identify the resonance frequency at each strain step, the S_{11} parameter needs to be simulated for many frequency points in a relatively large frequency range. The process is even more time-consuming when the simulation needs to be performed for tens or hundreds of strain steps. To significantly increase simulation accuracy, eigenvalue solver can be adopted to effectively determine the resonance frequency through a formulation of eigenvalue problem. Compare with frequency domain solver, eigenvalue solver can improve simulation efficiency, but requires large computer memory. Furthermore, for a complex 3D model, the dimensions of large matrices involved with the eigenvalue problem usually have the order of magnitude around 10,000 or 100,000. As a result, the eigenvalue solution can be computationally expensive.

To further improve the coupled simulation efficiency for multiple strain steps, this dissertation proposes to apply eigenvalue perturbation technique for determining eigenvalues. Instead of solving the eigenvalue problem from scratch at each and every strain step, an eigenvalue perturbation technique utilizes eigenvalue and eigenvector results from previous strain step to improve solution efficiency. Many eigenvalue perturbation techniques have been developed in the last several decades, such as the first-order eigenvalue perturbation method [41, 42], the Rayleigh quotient iteration [43], and the homotopy method [44]. The eigenvalue perturbation methods have been applied to many different problems with small matrix variations, such as structural damage detection [41, 45], modal reanalysis [46, 47], adaptive finite element analysis [48], *etc*. The perturbation theory also finds good application in electromagnetics, such as Slater's cavity perturbation theorem to determine perturbed electromagnetic field [49-51], eigenvalue perturbation for shifted material boundaries [52, 53], *etc*. By utilizing eigenvalue perturbation techniques, the simulation efficiency is expected to be improved.

The simulation performance of these perturbation methods need to be investigated for the mechanics-electromagnetics coupled simulation.

1.2 Purpose and Objective

The main research objective of this dissertation is to develop a multi-physics modeling and simulation framework for designing wireless strain/crack antenna sensors. For efficient and accurate sensor design, a series of key issues, including multi-physics coupled simulation, electrical property characterization of substrate materials under mechanical deformation, and eigenvalue perturbation algorithms, are investigated. The objectives are elaborated in the following list:

1. To improve the simulation accuracy of the antenna sensor design through multi-physics coupled simulation. Previously, antenna sensor design is analyzed in the electromagnetic domain only, using inaccurate deformed antenna shape. To evaluate strain effect to the sensor behavior, simple scaling according to applied strain and Poisson's ratio is usually adopted. To improve the simulation accuracy, mechanics-electromagnetics coupled simulation will be investigated. The multi-physics coupled simulation renders accurate deformed antenna shapes available for characterizing antenna behavior under strain. In addition, this research will quantify dielectric property change of the substrate material under mechanical deformation. The variation of the substrate dielectric constant will be investigated when the material is subjected to mechanical deformation. The relationship between dielectric constant change and applied strain will be further integrated with multi-physics coupled simulation.

2. To improve the simulation efficiency by investigating eigenvalue perturbation techniques in the coupled simulation. The determination of antenna sensor resonance frequency will be formulated as an eigenvalue problem first. Several eigenvalue perturbation algorithms, including the first-order eigenvalue perturbation method (FOP),

the inverse Rayleigh quotient iteration method (RQI), and Arnoldi solvers with different starting vectors, will be studied and applied to the formulated eigenvalue problem. A 2D dipole antenna and a 3D slotted patch antenna sensor will be adopted as validation examples to investigate the algorithm performance on different problems. To achieve a detailed comparison, both the perturbation efficiency and accuracy will be discussed with different perturbed strain sizes.

3. To design and validate a series of antenna sensors for strain and crack sensing. Two different types of antenna sensors are validated, including RFID antenna sensors and frequency doubling antenna sensors. Specifically, four RFID antenna sensors are developed, including folded patch antenna sensor, passive slotted patch antenna sensor, active slotted patch antenna sensor, and silver-nanoparticle antenna sensor. The folded patch antenna sensor is first designed to validate the strain sensing concept. The passive slotted patch antenna sensor is then designed to reduce the sensor footprint, while maintaining same operating frequencies. The active slotted patch antenna sensor is then designed to improve the interrogation distance by integrating an off-the-shelf solar cell. The silver-nanoparticle antenna sensor is further designed to reduce the fabrication cost. Another four frequency doubling antenna sensors are designed to operate in a higher frequency band. Targeting with field application requirements, the antenna sensors are investigated for their sensing capabilities on interrogation distance, resolution, range, consistency, sensor array capability. The sensors will also be verified for their crack sensing capability by simulated crack test and fatigue test. All antenna sensors will also be compared for their performance.

1.3 Organization of Dissertation

The rest of this dissertation is organized as follows.

CHAPTER 2 introduces strain/crack sensing mechanisms of two types of antenna sensors, RFID antenna sensor and frequency doubling antenna sensor. Section 2.1 presents strain and crack sensing mechanisms of RFID antenna sensors in Section 2.2 presents strain sensing mechanism of frequency doubling antenna sensors. The relationship between applied strain and resonance frequency shift is discussed and analyzed.

CHAPTER 3 proposes multi-physics coupled simulation framework of antenna sensors. Specifically, mechanics-electromagnetics coupled simulation is proposed for RFID antenna sensors, while mechanics-AC/DC-electromagnetics coupled simulation is proposed for frequency doubling antenna sensors. To further improve the coupled simulation, the substrate dielectric constant is characterized under strain and further applied to the coupled simulation. Several coupled simulation examples are presented to validate the simulation framework. Section 3.1 first presents the coupled simulation framework. Section 3.2 presents dielectric constant characterization of the substrate material under strain. Based on the coupled simulation framework, the modeling results of some representative antenna sensors in this research are presented in Section 3.3, including folded patch antenna sensor, slotted patch antenna sensors, and frequency doubling antenna sensors.

CHAPTER 4 proposes eigenvalue perturbation framework to determine resonance frequency changes of antenna sensors at multiple strain steps. The antenna sensor simulation is formulated as an eigenvalue problem. Several eigenvalue perturbation methods are then applied to the formulated eigenvalue problem. Further examples are presented to validate the perturbation efficiency and accuracy. Section 4.1 first describes

the finite element formulation of the antenna sensor design in. Based on the formulation, first-order eigenvalue perturbation method and inverse Rayleigh quotient iteration method are introduced to improve the simulation efficiency in Section 4.2. Section 4.3 presents 2D dipole antenna and slotted patch antenna as examples to validate the perturbation accuracy and efficiency. The perturbation results are also compared between different perturbation algorithms.

CHAPTER 5 presents strain and crack sensing results of antenna sensors. Section 5.1 presents the sensing results of folded patch antenna sensor, including strain sensing resolution, range, interrogation distance, consistency, sensor array, emulated crack, and fatigue crack sensing. To improve the temperature stability of the antenna sensor, a folded patch antenna sensor based on temperature insensitive substrate is designed and tested (Section 5.1.8). Section 5.2 describes the sensing results of passive slotted patch antenna sensor and compared with previous folded patch antenna sensor results. Section 5.3 presents test results of the active slotted patch antenna sensor, which is designed to improve the interrogation distance of antenna sensors by integrating an off-the-shelf solar cell. To reduce the fabrication cost, a silver-nanoparticle antenna sensor is designed based on inkjet printing technology. Section 5.4 presents the strain sensing results of the silver-nanoparticle printed antenna sensor. Section 5.5 presents the test results of four prototypes of frequency doubling antenna sensors. The results are also compared among the four prototypes.

CHAPTER 6 presents a summary of the research and the primary conclusions. Further research topics are recommended based on the results from this research.

CHAPTER 2 ANTENNA SENSOR DESIGN MECHANISMS

As introduced in the previous chapter, two major categories of antenna sensors are explored in this research, RFID (radiofrequency identification) antenna sensor and frequency doubling antenna sensor. In general, an antenna is used for radiating or receiving wireless radio waves [54]. When the antenna is also used to detect certain physical parameter, the antenna works as a wireless sensor. For example, antenna sensors have been developed for measuring displacement [55], strain [56], crack [57], corrosion [58], *etc*. An RFID sensor-reader system includes a reader and an antenna sensor. The system operation relies on electromagnetic backscattering. However, the antenna itself cannot distinguish the sensor signal from environmental noise. In order to differentiate the antenna reflection (backscattering), RFID signal modulation is a widely implemented technique [10]. With signal modulation, the return signal from the antenna sensor is modulated with unique pattern to differentiate environmental noise and interrogation signal. An RFID antenna sensor contains an integrated RFID chip for signal modulation. In [59], an RFID antenna sensor is developed for strain sensing, where magnitude of the strain sensitivity is approximately the same as the initial designed resonance frequency of the antenna. In order to further increase the strain sensitivity, it is needed to significantly increase the initial designed resonance frequency of antenna. There are some active RFID systems and sensors available around the 2.45 GHz frequency band for vibration sensing [60], temperature sensing [61], *etc*. However, they require extra on-board battery, which is not suitable for the long-term structural health monitoring. In order to design sensors working at higher resonance frequency (e.g. S band (2~4 GHz) or C band (4~8 GHz)), some other signal differentiation technique (instead of RFID) is needed. One option is the frequency doubling mechanism [25]. A frequency doubling sensor contains two antennas, a receiving one and a transmitting one. The receiving antenna receives the interrogation signal from a reader. Then the transmitting antenna emits signal at the doubled frequency

back to the reader. In this research, The frequency doubling performance is achieved by using the second harmonic generation of a Schottky diode integration [62]. Because the backscattered signal from sensor is different from the original interrogation signal frequency of reader, the backscattered signal is easily distinguished from environmental noise at the original interrogation frequency.

This chapter introduces strain and crack sensing mechanisms of both types of antenna sensors. Section 2.1 describes the strain/crack sensing mechanism of the RFID antenna sensor. Section 2.2 presents the strain/crack sensing mechanism of frequency doubling antenna sensors.

2.1 RFID Antenna Sensor

The RFID technology has become a pervasive in everyday life [10, 63, 64]. The technique has been greatly adopted in logistics [65], inventory management, homeland and personal security, and mobile health care [66]. Fig. 2.1 shows a passive wireless antenna sensing system, which consists of an RFID reader and an RFID antenna sensor. Functioning as a wireless strain/crack sensor, the RFID antenna sensor includes an antenna for data transmission and an integrated RFID chip for signal modulation. The modulation function of the RFID chip helps the antenna sensor to differentiate sensor signal from environmental noise. The RFID chip adopted in this research is SL3ICS1002 from NXP Semiconductors [67]. The chip conforms with EPC Class-1 Generation-2 UHF RFID Protocol and operates in a frequency range between 860 MHz and 960 MHz [22]. Operation of the RFID system relies on the backscattering mechanism, which refers to the reflection of electromagnetic wave from an illuminated object back to a source. The reader emits interrogation electromagnetic wave to the antenna sensor. If the power received by the antenna sensor is higher than the activation power threshold of the RFID chip, the sensor is activated and reflects electromagnetic wave back to the reader.

Because the RFID antenna sensor receives all operating power wirelessly from the reader, the operation is passive (battery-free).

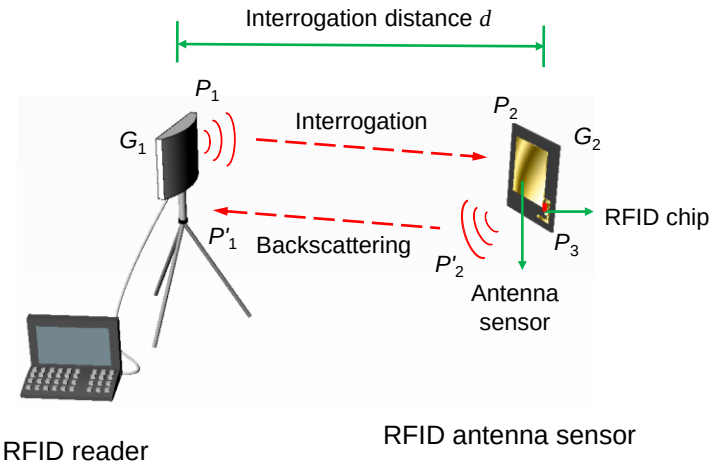

Fig. 2.1. Power transmission and backscattering in a passive RFID system with wireless antenna sensors

As shown in Fig. 2.1, upon the interrogation from the RFID reader, the power received at the sensor-side antenna is denoted as P_2. Assuming there is no obstacle between the reader and the sensor, the relationship between P_1 and P_2 can be approximated by the Friis free-space formula [68]:

$$P_2 = P_1 G_1 G_2 \left(\frac{\lambda}{4\pi d} \right)^2 \tag{2.1}$$

where G_1 and G_2 are the gain of the reader antenna and sensor-side antenna, respectively, d is the distance between the reader and the antenna sensor, and λ is the wavelength of the interrogation electromagnetic signal. The antenna gain is determined by the shape and dimension of each antenna.

Inside the RFID antenna sensor, the power is then transferred from the sensor-side antenna to the RFID chip. This power transfer process is similar to the scenario of a battery (with its own internal resistance) powering an outside resistor. The power transfer is maximized only when the electrical impedance of the power source (i.e. the

sensor-side antenna in this application) matches the impedance of the load (i.e. the RFID chip). When impedance mismatch occurs between the sensor-side antenna and the chip, a portion of the power is reflected back from the chip to the sensor-side antenna. The power reflection coefficient of the sensor-side antenna, η, can be calculated as a measure of the reflected signal strength [69]:

$$\eta(f) = \left| \frac{Z_{\text{ANT}}^{*} - Z_{\text{Load}}}{Z_{\text{ANT}} + Z_{\text{Load}}} \right|^2 = |S_{11}|^2 \tag{2.2}$$

where Z_{Load} and Z_{ANT} represent the impedance of the chip and the sensor-side antenna, respectively; S_{11} is the reflection coefficient of the antenna. Both impedance parameters are functions of the interrogation frequency *f*. The superscript "*" represents the conjugate of a complex number. In general, the analytical form of η as a function of the interrogation frequency *f* is difficult to obtain.

The relationship between the power interrogated by the sensor-side antenna, P_2, and the power received at the chip, P_3, is determined by the power reflection coefficient $\eta(f)$:

$$P_3 = P_2\left(1-\eta(f)\right) \tag{2.3}$$

The antenna sensor is classified as passive because the sensor does not require its own power supply, i.e. the sensor receives its operation power entirely through the electromagnetic emission/illumination from the reader. The minimum operating power for the adopted chip (SL3ICS1002 from NXP Semiconductors) is 0.03mW (milliwatt, P_{IC}), which is a constant irrelevant to the interrogation frequency in the UHF frequency range. For a certain interrogation frequency *f*, the power threshold of an RFID antenna sensor is defined as the minimum interrogation power P_1 required to activate the RFID chip, so that the chip responds to the reader. At each reading frequency, a reader operating in power threshold mode can automatically adjust the interrogation power P_1 so that P_3 is just enough to activate the RFID chip:

$$P_3 = P_{IC} \tag{2.4}$$

Substitute Eq. (2.4) into Eq. (2.3) and Eq. (2.1), the interrogation power threshold can be obtained:

$$P_1(f) = \frac{(4\pi df)^2 P_{IC}}{c^2 G_1 G_2 (1-\eta(f))} \tag{2.5}$$

The RFID antenna sensor has been designed in a way that when the interrogation frequency f is equal to the resonance frequency of the RFID antenna sensor, best impedance matching between the sensor-side antenna and the RFID chip occurs. Therefore, the least amount of power needs to be transmitted by the reader for activating the RFID antenna sensor, which means the interrogation power threshold plot $P_1(f)$ (measured by the reader) achieves minimum value at the resonance frequency.

Once an antenna sensor is bonded on a structural surface for strain/crack measurement, the sensor deforms together with the structure. As a result, the antenna length changes with structural deformation. Eq. (2.6) shows that resonance frequency of a regular patch antenna (without folding), f_{R0}^{Patch}, is related to antenna length [70]:

$$f_{R0}^{Patch} = \frac{c}{2(L+L')\sqrt{\beta_{reff}}} . \tag{2.6}$$

where c is the speed of the light, L is the physical length of the copper cladding on the antenna, β_{reff} is the effective dielectric constant of the antenna substrate, and L' is the additional electrical length corresponding to β_{reff}. Because the width-to-thickness ratio is much smaller than one, the effective dielectric constant β_{reff} has approximately the same value as the dielectric constant β_{r0}, according to following Equation [70] :

$$\beta_{\text{reff}} = \frac{\beta_{\text{r0}}+1}{2} + \frac{\beta_{\text{r0}}-1}{2}\left[1+12\frac{h}{W}\right]^{-1/2} \approx \beta_{\text{r0}} \tag{2.7}$$

where h and W are thickness and width in the substrate, respectively, β_{r0} is the relative dielectric constant of the substrate at room temperature without any deformation. The wavelength of the patch antenna is determined as:

$$\lambda_0^{\text{Patch}} = \frac{c}{f_{\text{R}0}^{\text{Patch}}\sqrt{\beta_{\text{r0}}}} = 2\left(L+L'\right) \tag{2.8}$$

When strain ε occurs in the longitudinal direction, the resonance frequency is shifted to:

$$f_{\text{R}}^{\text{Patch}} = \frac{c}{2(1+\varepsilon)(L+L')\sqrt{\beta_{\text{r0}}}} = \frac{f_{\text{R}0}^{\text{Patch}}}{1+\varepsilon} \tag{2.9}$$

When strain ε is small, the resonance frequency changes approximately linearly with respect to strain:

$$f_{\text{R}}^{\text{Patch}} = f_{\text{R0}}^{\text{Patch}}(1-\varepsilon+\varepsilon^2-\varepsilon^3+\cdots) \approx f_{\text{R0}}^{\text{Patch}}(1-\varepsilon) \tag{2.10}$$

The equation shows that if strain ε is small, the resonance frequency shifting is approximately linear to strain. This linear relationship indicates that strain can be derived by measuring shift in the antenna resonance frequency. This serves as the fundamental strain sensing mechanism of the wireless antenna sensor. Although the width of the antenna also changes according to Poisson's ratio, the effect of width change to the resonance frequency is relatively small and can be neglected. Fig. 2.2(a) and (b) illustrate relationship between sensor deformation and antenna resonance frequency. The top copper cladding is the antenna pattern for receiving and transmitting signals. The bottom layer is also a copper cladding served as the ground plane. Sandwiched between them is the dielectric polymer substrate to separate top copper cladding from ground plane. When

strain ε is positive, the resonance frequency f decreases. On the other hand, if strain ε is negative, the resonance frequency f increases.

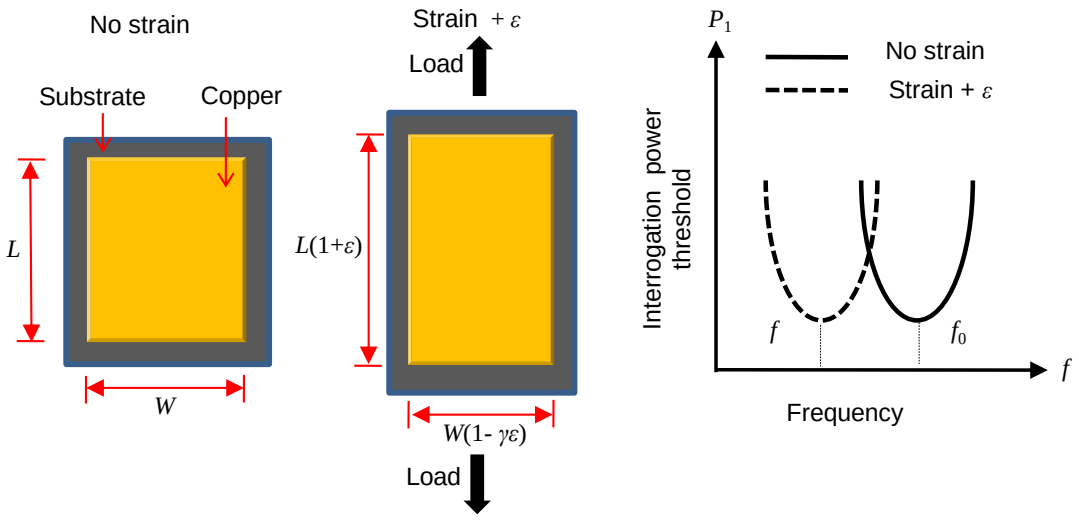

(a) Positive strain ε in the longitudinal direction

(b) Illustration of interrogation power threshold measurement

Fig. 2.2. Conceptual illustration of relationship between sensor deformation and resonance frequency change

Although the RFID protocol allows for a broad frequency range (840~960MHz) in America, Europe, and Asia, 824~896 MHz is within the cellular frequency band in the U.S. Therefore, for practical implementation, the resonance frequency of the folded patch antenna is shifted outside the cell phone frequency band (e.g. around 915 MHz), so that issues with environmental noise are avoided. In the microstrip patch antenna design, the effective electrical length of a patch antenna is around half wavelength. Resonance frequency of the patch antenna is dependent on the surface current path, as shown in Fig. 2.3. According to Eq. (2.8), the half wavelength on Rogers 5880 substrate is 110 mm at 915MHz resonance frequency. In other words, to maintain a resonance frequency at 915MHz, length of the entire current path needs to keep at 110mm. As a result, the antenna sensor should be around 110 mm long, which can be too large for concentrated

strain measurement. To reduce sensor size while maintaining the RFID operation frequency at 915MHz , current detouring on the RFID antenna sensor is needed.

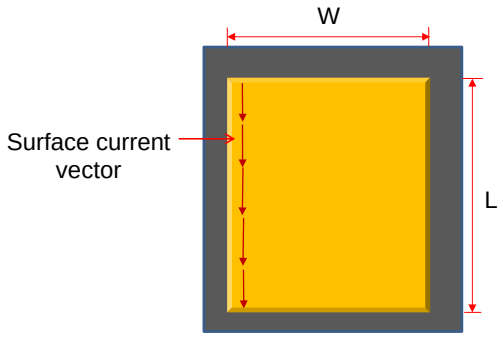

Fig. 2.3. Illustration of the surface current vector in the patch antenna sensor

To achieve current detouring, a folded patch antenna is first designed as a passive antenna sensor [56, 59]. Fig. 2.4 shows the design of the antenna sensor. The form of patch antenna is adopted to provide good radiation performance on metallic structural surfaces. The top cladding is the antenna pattern for signal receiving and transmitting. The bottom copper cladding serves as ground plane. Sandwiched between them is the dielectric polymer substrate. Vias through the substrate are used for connecting the top copper cladding with the ground plane on the back, forming a folded patch antenna. Fig. 2.5 shows the surface current paths of the folded patch antenna sensor. The dashed arrow line indicates the current patch on the bottom ground plane, while the solid arrow line indicates the current path on the top copper cladding. As shown in the figure, the surface current is detoured along the vias. The detoured surface current pattern reduces the sensor size by half, which makes the sensor to have a quarter wavelength design. The adopted substrate material is Rogers RT/duroid®5880 with a thickness of 31 mils (0.79mm). The material is a glass microfiber reinforced poly-tetra-fluoro-ethylene (PTFE) composite with a dielectric constant β_{r0} of 2.2.

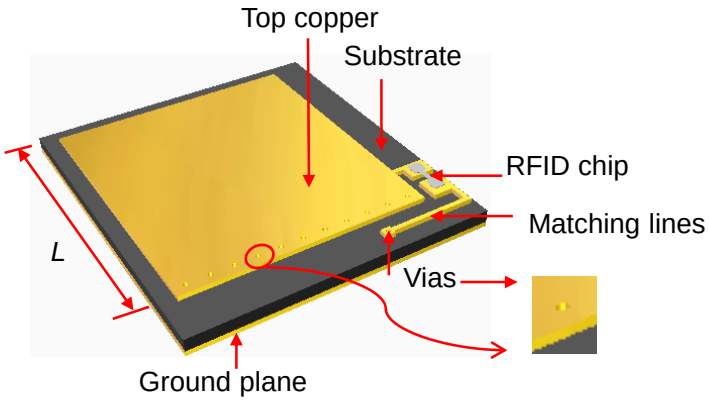

Fig. 2.4. RFID antenna as wireless antenna sensor for strain and crack sensing

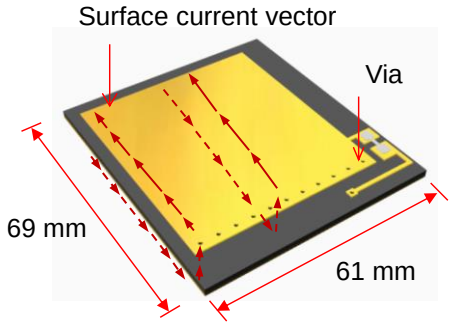

Fig. 2.5. Surface current paths of the folded patch antenna sensor

Due to current detouring, the antenna resonance frequency of the folded antenna at zero strain level, f_{R0}, can be estimated as:

$$f_{R0}^{\text{Folded}} = \frac{c}{4(L+L')\sqrt{\beta_{r0}}} \tag{2.11}$$

When the antenna experiences strain deformation of ε in the longitudinal direction, the resonance frequency shifts to:

$$f_{R}^{\text{Folded}} = \frac{c}{4(1+\varepsilon)(L+L')\sqrt{\beta_{r0}}} = \frac{f_{R0}^{\text{Folded}}}{1+\varepsilon} \approx f_{R0}^{\text{Folded}}(1-\varepsilon) \tag{2.12}$$

This approximately linear relationship indicates that the applied strain can be derived by measuring the antenna resonance frequency shift.

Due to sensor fabrication and installation tolerances in practice, zero-strain resonance frequencies of different pieces of installed antenna sensors can slightly differ. To alleviate the influence on strain measurement, a concept of normalized resonance frequency change is defined. The resonance frequency change is normalized by initial resonance frequency (i.e. f_{R0} at zero strain level) of each sensor according to following equation:

$$\Delta f_N = \frac{f_R - f_{R0}}{f_{R0}} \approx -\varepsilon \tag{2.13}$$

where Δf_N represents normalized frequency change, and f_R is the resonance frequency when antenna is under strain ε. Although Eq. (2.13) shows magnitude of Δf_N approximately equals magnitude of strain ε, in practice, Δf_N usually has a smaller magnitude. The primary reason is that only a percentage of the strain on structural surface is transferred through antenna substrate to the top copper layer of the sensor. This strain transfer effect reduces the achieved strain sensitivity, as described by following equation.

$$\Delta f_N = -S_N \varepsilon \tag{2.14}$$

Here S_N is the normalized strain sensitivity with a value close to and less than 1 ppm/με (ppm - parts per million).

The approximately linear relationship between resonance frequency shift and applied strain serves as sensing mechanism of the RFID antenna sensor. As explained in Eq. (2.12) and (2.13), the strain sensitivity is directly correlated with initial resonance frequency of the RFID antenna sensor. To further increase the strain sensitivity, it is essential to increase the antenna resonance frequency (e.g. up to a few GHz). However, the EPC Class-1 Generation-2 UHF RFID Protocol only operates from 860 MHz to 960 MHz [22]. There is no standard RFID protocol defined for GHz frequency range. Commercial passive RFID chips and readers are not available at desired GHz frequency

range for high-resolution strain sensing. Therefore, alternative approaches need to be exploited in order to operate at higher frequencies.

2.2 Frequency Doubling Antenna Sensor

Frequency doubling technique is one promising method to differentiate sensor signal from environmental noise without signal modulation through an RFID chip. A frequency doubling device consists of three main components, i.e., a receiving antenna (with resonance frequency f_{R0}), a transmitting antenna (with resonance frequency $2f_{R0}$), and a diode-integrated matching network between receiving and transmitting antennas. Fig. 2.6 illustrates the operation mechanism of a frequency doubling device. During operation, a wireless interrogation signal is emitted from the reader side by a function generator and through a transmitting reader antenna. If interrogation frequency f is in the neighborhood of f_{R0}, (resonance frequency of the receiving patch antenna at device side), interrogation power is captured by the sensor-side receiving patch antenna and transferred to the matching network. Due to nonlinear behavior of the diode, the output signal from diode has larger amplitude at harmonics (multiples) of the incident frequency. In this application, the second harmonic ($2f$) of the incident frequency is investigated and measured by the reader. The output signal at $2f$ is backscattered to reader through sensor-side transmitting patch antenna (resonance frequency at $2f_{R0}$). A spectrum analyzer finally measures the backscattered signal at reader side. Frequency of backscattered sensor signal is at $2f$, and the unwanted environmental reflections to original reader interrogation signal remains at f. Therefore, it is easy for the spectrum analyzer to distinguish backscattered sensor signal from unwanted environmental reflections.

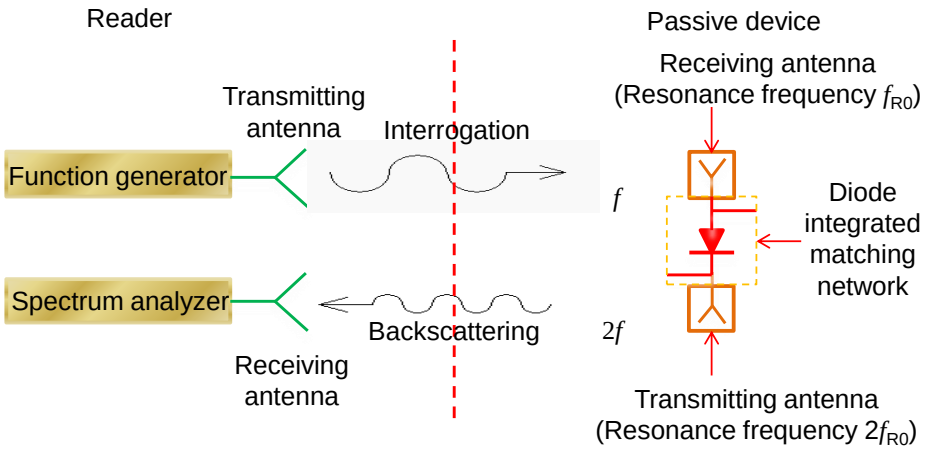

Fig. 2.6 Operation mechanism of a passive frequency doubling device

When a patch antenna is used as the receiving antenna at the sensor side, the antenna resonance frequency f_{R0} follows the same formulation as Eq. (2.6). The equation is repeated here:

$$f_{R0}^{Patch} = \frac{c}{2(L+L')\sqrt{\beta_{reff}}} \tag{2.15}$$

If only the receiving antenna part of the sensor is bonded on a structural surface, while other sensor components (i.e. matching network and transmitting antenna) remain floating, the resonance frequency of the device-side receiving antenna changes with strain (according to Eq. (2.10)). The shifted resonance frequency response then flows through the matching network and transmitting antenna, and finally backscatters to the reader-side spectrum analyzer. By quantifying resonance frequency change of the backscattered signal, structural strain can be derived.

As an example, Fig. 2.7 shows design drawing and photo of the frequency doubling sensor prototype A. In this sensor prototype, a 2.9 GHz patch works as the receiving antenna and a 5.8 GHz patch works as the transmitting antenna. In the matching network, a Schottky diode SMS7621-079LF from Skyworks Solutions, Inc. is installed to achieve frequency doubling. In addition, a 33 nH (nanohenries) inductor from Panasonic

Electronic Components (PCD1864CT) is connected in parallel with the diode to improve its power transmission efficiency [71].

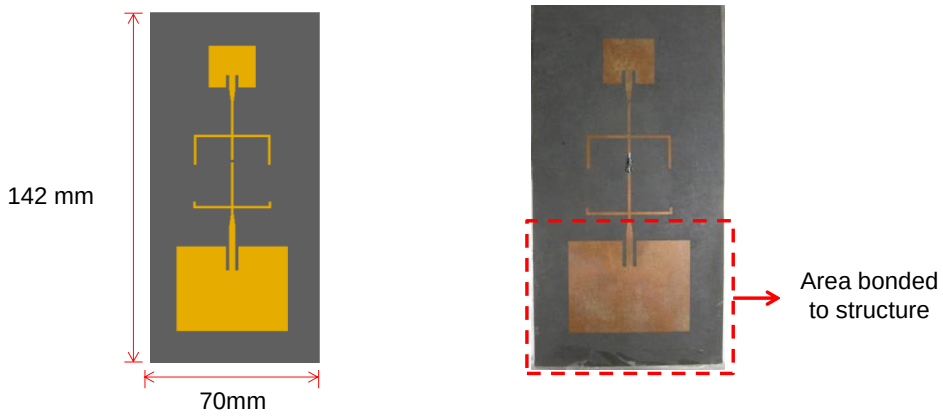

(a) Design drawing (b) Photo of fabricated sensor

Fig. 2.7. Frequency doubling sensor prototype A.

The frequency doubling sensor has a power flow mechanism as illustrated in Fig. 2.8. P_0 represents the received power at the 2.9 GHz receiving antenna. P_1 and P_2 denote the power before and after the matching network, respectively. Finally, P represents the power being backscattered to the reader. S_{11}^R and S_{11}^T are scattering-parameters of the receiving and transmitting antennas, respectively. If the 2.9 GHz patch antenna is deformed due to strain, the resonance frequency of the antenna shifts away from 2.9 GHz. From Port 1 to Port 2, frequency is doubled to 5.8 GHz by the diode in the matching network. The 5.8 GHz patch antenna receives the signal from Port 2, and finally, wirelessly backscatters to the 5.8 GHz reader antenna. Thus, the shift around doubled resonance frequency (due to strain) can be measured by the spectrum analyzer at the reader side. When the sensor is under strain, change in the backscattering performance can be interrogated by a wireless reader and used for detecting strain.

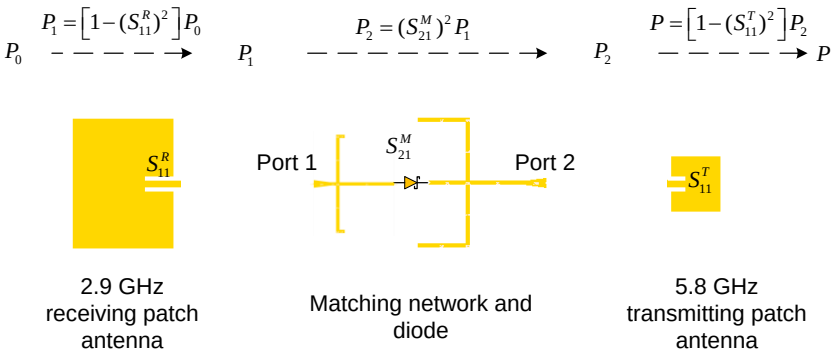

Fig. 2.8. Power flow of frequency doubling antenna sensor.

2.3 Summary

This chapter presents strain and cracking sensing mechanisms of RFID antenna sensor and frequency doubling antenna sensor. As the sensor-side antenna deforms along with the monitored structures, the electromagnetic resonance frequency changes accordingly. The resonance frequency shift is then correlated with applied strain. The relationship between resonance frequency change and strain is the sensing mechanism of the RFID antenna sensor and the frequency doubling antenna sensor. All RFID antenna sensors and frequency doubling antenna sensors presented in this research, including folded patch antenna sensor, slotted patch antenna sensors, and four prototypes of frequency doubling antenna sensors, are all designed to follow the presented strain and crack sensing mechanisms. The multi-physics coupled simulation results of these antenna sensors are presented in CHAPTER 3.

CHAPTER 3 MULTI-PHYSICS MODELING

As described in CHAPTER 1, several commercial software packages are available for multi-physics coupled simulation, such as COMSOL Multiphysics™, CST (Computer Simulation Technology), and ANSYS-HFSS (High Frequency Structural Simulator). Accurate simulation of the first type of antenna sensors described in Section 2.1, the RFID antenna sensors, involves mechanics-electromagnetics coupling. All three packages support the coupled multi-physics simulation, but CST has the limitation that the port location needs to be fixed during mechanical simulation. In addition, because the eigenvalue solver in both CST and ANSYS-HFSS do not support PML (perfectly matched layer), COMSOL is used for mechanics-electromagnetics coupled simulation of RFID antenna sensors.

Section 3.1 introduces framework of the multi-physics coupled simulation. Section 3.2 presents characterization of substrate dielectric constant change under strain. Both strain transfer test and resonator frequency change test are conducted to ensure the accuracy of the material property characterization. Section 3.3 first presents mechanics-electromagnetics coupled simulation of folded patch antenna sensor and slotted patch antenna sensor, followed by mechanics-AC/DC-electromagnetics coupled simulation of the frequency doubling antenna sensor.

3.1 Modeling Framework

Behavior of the RFID antenna sensors involves both mechanics and electromagnetics. Accurate simulation of the antenna behavior requires a multi-physics modeling framework. To obtain general ideas of how the antenna sensor behaves under mechanical deformation, a first attempt is to simply scale the antenna sensor dimensions according to the applied strain and Poisson's ratio. The simple scaling thus estimates sensor deformation with limited accuracy. Nevertheless, early literatures in antenna strain

sensors adopted this approach and performed electromagnetic simulation of deformed antenna using simply scaled shapes [56, 72]. Fig. 3.1 shows the strain distribution comparison between simple scaling and mechanical simulation of a folded patch antenna sensor when 2,000 με along *y*-direction is applied to the back/bottom of the antenna. With simple scaling, the strain generated on the top copper cladding is assumed to be uniformly 2,000 με along *y*-direction (Fig. 3.1(a)). For the mechanical simulation, the folded patch antenna is bonded to a long aluminum plate. Longitudinal displacement is applied to one end of the plate, so that 2,000 με along y-direction is generated in the aluminum plate. Fig. 3.1(b) shows that the strain distribution on the top copper cladding is not uniform and only strain at the center area is close to 2,000 με. The strain at the edges and around the vias is quite different. Fig. 3.1(c) shows that the A-A view of the deformed shape through simple scaling remains a regular rectangle shape. However, as shown in the Fig. 3.1(d) an accurate mechanical simulation demonstrates the warped deformed shape and the shear lag effect through the thickness of the antenna. Because even small shape differences affect electromagnetic simulation results of the antenna, instead of simple scaling, it is important to adopt mechanics-electromagnetics coupled simulation.

When modeling the RFID antenna sensors, the main goal is to simulate the electromagnetic resonance frequency change of the antenna under mechanical deformation. To simulate antenna performance under strain, the mechanics module is coupled with electromagnetics module to compute the new resonance frequency under strain. Since the electromagnetic fields have little effect on the mechanical behavior of the sensor, the mechanical simulation is first conducted at prescribed strain levels. After the mechanical simulation at certain strain level, the deformed meshing of the antenna structure is directly used for electromagnetic simulation. The convenience is achieved through the moving meshes, which indicates that accurate deformed shape is used for the electromagnetic simulation.

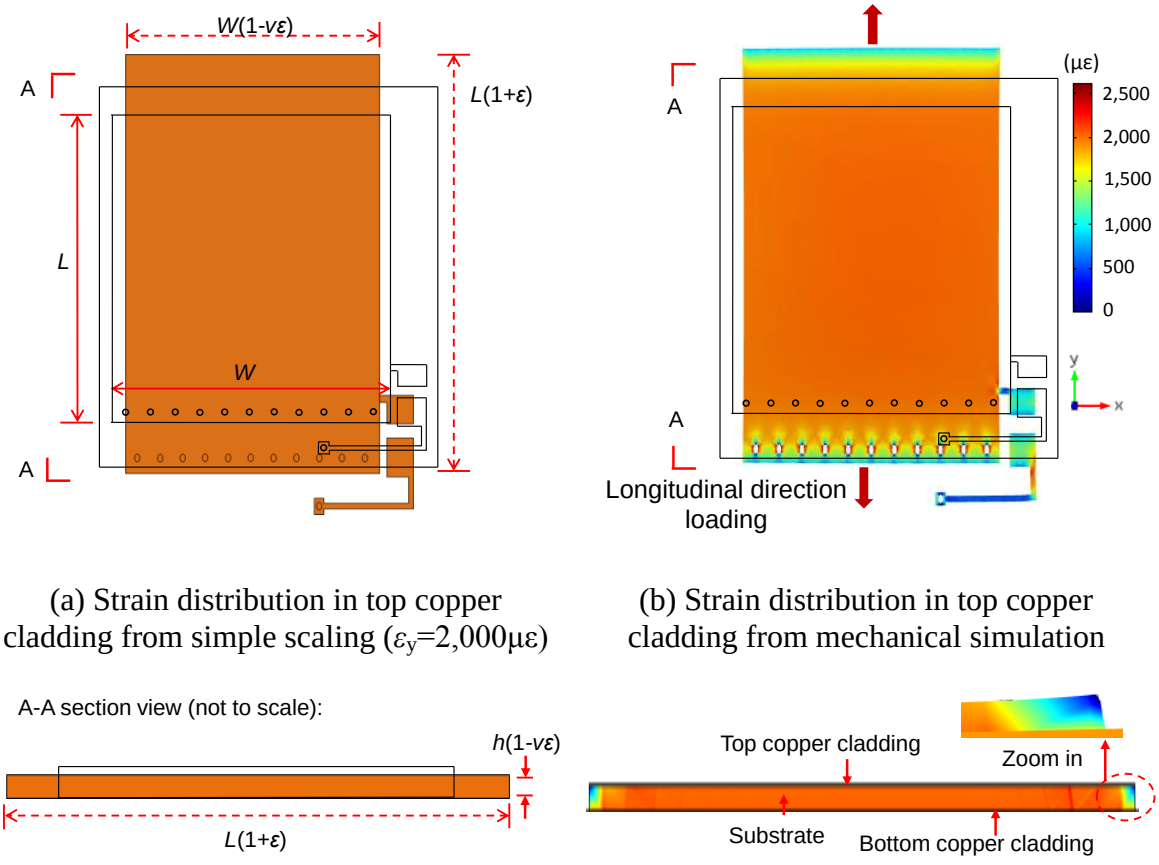

(a) Strain distribution in top copper cladding from simple scaling (ε_y=2,000με)

(b) Strain distribution in top copper cladding from mechanical simulation

(c) A-A section view of strain distribution from simple scaling

(d) A-A section view of strain distribution from mechanical simulation

Fig. 3.1. Strain distribution comparison between simple scaling and mechanical simulation

The second type of antenna sensors described in Section 2.2 is frequency doubling antenna sensor. As described in Section 2.2, a frequency doubling antenna sensor includes a receiving antenna (with resonance frequency f_{R0}), a transmitting antenna (with resonance frequency $2f_{R0}$), and a diode-integrated matching network between receiving and transmitting antennas. To simulate the nonlinear behavior of the diode needed for frequency doubling, the simulation software package needs to have an AC/DC module. Furthermore, harmonic balance simulation is needed to characterize the second harmonic performance of the diode output, i.e. at a frequency twice the diode's incident frequency [73]. Harmonic balance method is a frequency domain method for

calculating distortions in nonlinear devices or circuits. With incident frequency at f before entering the diode, the second harmonic (at frequency $2f$) of the output signal is computed by harmonic balance simulation in the ADS (Advanced Design System from Agilent Technology) software package. Because currently COMSOL does not support harmonic balance simulation, ADS is adopted for simulating the matching network (containing the diode) of frequency doubling sensors. Meanwhile, the rest of the frequency doubling antenna sensors, including the receiving and transmitting antennas, are simulated in COMSOL due to the need of coupling mechanics and electromagnetics.

Fig. 3.2 shows the flow chart of the multi-physics coupled simulation of the frequency doubling antenna sensor. To simulate strain sensing performance of the frequency doubling antenna sensor, the mechanical behavior of the 2.9 GHz sensor-side receiving antenna is first simulated in COMSOL. The displacement field and deformed antenna structure is then coupled to electromagnetic simulation of the same antenna. Within the electromagnetic simulation, the antenna impedance (Z_a) at each simulated frequency point is recorded, which is used as input port impedance of the harmonic balance simulation of the matching network in ADS. In this case, the matching network simulation has frequency dependent impedances to coordinate the sensor-side receiving antenna behavior. The harmonic balance simulation in ADS then generates and records the output power (P_{out} in Fig. 3.2) at twice the simulated frequency. The output power from ADS can be transformed as output port voltages (V_{out} in Fig. 3.2), which are further used as input port voltages of the sensor-side transmitting antenna simulation in COMSOL. In the end, the overall frequency doubling sensor performance is achieved by combining COMSOL and ADS results.

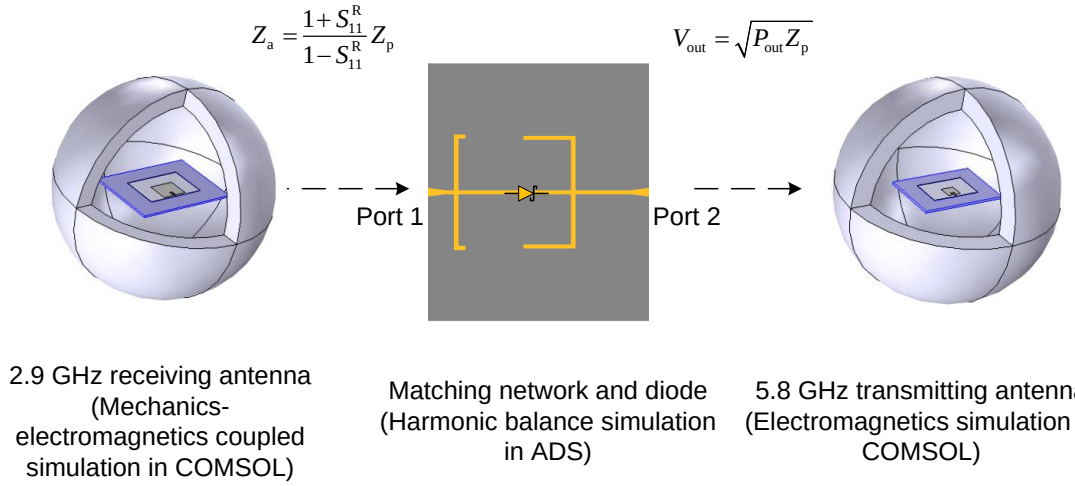

Fig. 3.2. Flow chart of the multi-physics coupled simulation of frequency doubling antenna sensor

3.2 Characterization of Substrate Dielectric Constant Change under Strain

Most radiofrequency (RF) applications using the adopted substrate material (Rogers RT/duroid® 5880) do not require the material to be under strain. As a result, the material manufacturer does not provide detailed electrical behaviors of the material under strain. However, different from ideal solid, small voids always exist in the material. When the material is under strain, distortion of the voids can affect the dielectric constant and thus, affect the antenna resonance frequency. In order to accurately model and simulate the antenna behavior under strain, the substrate dielectric constant change needs to be characterized under strain.

Many techniques have been developed to measure substrate dielectric constant in the past several decades [74-76]. The ASTM standard D3380-10 uses stripline techniques to measure the dielectric constant of substrates. The substrate material manufacturer Rogers Corporation also uses long stripline, which is fully embedded inside the substrate, to measure the dielectric constant of Rogers substrate from below 1 GHz to about 14 GHz [77]. Stripline test is also used to determine the substrate dielectric constant in X-band (8~12 GHz) frequency range [78]. The stripline is designed to be a resonator within

certain frequency range. The dielectric constant is determined by measuring resonance frequency and resonator dimensions. To have reproducibility of measurement results, both sides of the stripline is usually covered by fixtures in order to have stable and accurate measurement results. In other methods [79, 80], the substrate, with copper on both sides, is designed to be a cavity and the dielectric constant is also determined by measuring different resonance frequencies and substrate dimensions. In addition, microstrip line, which consists of conductive traces (e.g. copper) and separated from the ground plane with the substrate, can also be used to determine the substrate dielectric constant by reflection cancellation method and line balancing method [81]. In our research, the substrate dielectric constant is quantified at different deformation statuses. The fixture covered stripline is not applicable to this research, while the cavity design in [79, 80] does not fit with this research due to its double copper ground plane configuration. Instead, a microstrip line resonator is designed to determine the substrate dielectric constant.

3.2.1 Theoretical Analysis

Fig. 3.3 shows the design of a half-wavelength microstrip line resonator, which has a resonance frequency of 950 MHz. The resonator consists of top copper microstrip lines, which is separated from the bottom copper ground plane by the 31-mil Rogers 5880 substrate material. The resonance frequency is determined by the length of center microstrip line. Forward transmission coefficient (S_{21}) is used to quantify the power transmitted from Port 1 to Port 2 at certain electromagnetic frequency. S_{21} can be calculated according to the following equation:

$$S_{21} = \frac{V_2^o}{V_1^i} \tag{3.1}$$

where V_1^i is the incident voltage at Port 1 and V_2^o is the output voltage at Port 2 with same electromagnetic frequency as the input. While S_{21} can be quantified at different electromagnetic frequencies, maximum power can be transferred from Port 1 to Port 2 at resonance frequency. The peak of the S_{21} curve of a resonator corresponds to the resonance frequency of the resonator.

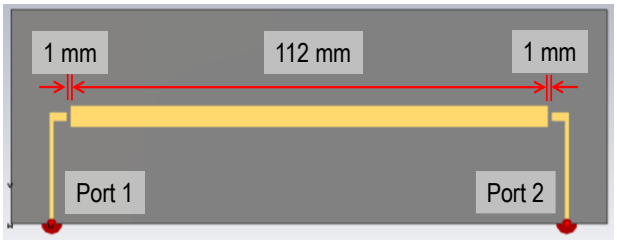

Fig. 3.3. Resonator design for characterizing of dielectric constant versus strain.

The resonance frequency of a resonator can be calculated as follows:

$$f_{R0} \approx \frac{c}{2L\sqrt{\beta_{r0}}} \tag{3.2}$$

where f_{R0} is the estimated resonance frequency of the resonator, c is the speed of light, L is the length of center transmission line, β_{r0} is the dielectric constant of the substrate at zero strain. During the measurement, the resonator is bonded to the structural surface by superglue. The bonding between the structural surface and the resonator is assumed to be perfect, as well as the bonding between the substrate and the top copper microstrip lines and bottom copper ground plane. However, the strain experienced by the top microstrip line is usually smaller than the strain on the bottom copper ground plane and the structural surface, due to shear lag effect through the 31-mil Rogers material. Note that Eq. (3.2) has similar form as Eq. (2.11). Nevertheless, previous formulation does not consider possible dielectric constant (β_{r0}) change due to strain, as well as strain transfer

ratio between bottom copper ground plane and top copper microstrip lines. Assuming the strain transfer ratio between the two copper claddings is η_m, which is defined as:

$$\eta_m = \frac{\varepsilon_t}{\varepsilon} \tag{3.3}$$

where ε_t is the strain experienced on the top copper cladding, and ε is the actual strain on the base structural surface (i.e. strain at the bottom copper cladding of the resonator). Considering dielectric constant variation over strain, when strain is applied to the bonded structural surface, the resonance frequency at strain ε_t can be estimated as:

$$f_{R\varepsilon_t} \approx \frac{c}{2(L+\Delta L)\sqrt{(\beta_{r0}+\Delta\beta_r)}} \tag{3.4}$$

where ΔL is the center transmission line length change due to strain ε_t; $\Delta\beta_r$ is the dielectric constant change with strain ε_t. Comparing Eq. (3.4) and (3.2), the resonance frequency change can be derived as:

$$\begin{aligned}\Delta f = f_{R\varepsilon_t} - f_{R0} &= \frac{c}{2}\left(\frac{1}{(L+\Delta L)\sqrt{(\beta_{r0}+\Delta\beta_r)}} - \frac{1}{L\sqrt{\beta_{r0}}}\right) \\ &= \frac{c\left(1-\sqrt{(1+\Delta\beta_r/\beta_{r0})}\right)}{2(L+\Delta L)\sqrt{(\beta_{r0}+\Delta\beta_r)}} - f_{R0}\frac{\Delta L}{(L+\Delta L)}\end{aligned} \tag{3.5}$$

According to Taylor expansion:

$$\sqrt{1+\frac{\Delta\beta_r}{\beta_{r0}}} \approx 1+\frac{1}{2}\frac{\Delta\beta_r}{\beta_{r0}} - \frac{1}{8}\left(\frac{\Delta\beta_r}{\beta_{r0}}\right)^2 + \cdots \tag{3.6}$$

Since $\Delta\beta_r << \beta_{r0}$, higher order terms of $\Delta\beta_r/\beta_{r0}$ in Eq. (3.6) is neglected, Eq. (3.5) is further simplified as:

$$\begin{aligned}\Delta f &\approx -\frac{c\Delta\beta_{\mathrm{r}}}{4\beta_{\mathrm{r0}}(L+\Delta L)\sqrt{(\beta_{\mathrm{r0}}+\Delta\beta_{\mathrm{r}})}} - f_{R0}\varepsilon_{\mathrm{t}} \\ &= -f_{\mathrm{R}\varepsilon}\frac{\Delta\beta_{\mathrm{r}}}{2\beta_{\mathrm{r0}}} - f_{\mathrm{R}0}\varepsilon_{\mathrm{t}}\end{aligned} \tag{3.7}$$

The resonance frequency change due to dielectric constant change and applied strain can be de-coupled according to Eq.(3.5). The relative dielectric constant change, when base structure is under strain ε, is thus derived:

$$\Delta\beta_{\mathrm{r}} = -\frac{2\beta_{\mathrm{r0}}}{f_{\mathrm{R}\varepsilon_{\mathrm{t}}}}\left(\Delta f + f_{\mathrm{R}0}\eta_{\mathrm{m}}\varepsilon\right) \tag{3.8}$$

According to Eq. (3.8), the dielectric constant can be updated at each strain level. The relationship in Eq. (3.8) needs to be implemented for accurate simulation of antenna behavior under strain. To quantify the actual dielectric constant change, the resonator design is fabricated for tensile testing, and the results are presented in the following section.

3.2.2 Dielectric Constant Characterization through Resonator Measurement

This section presents experimental results of the dielectric constant change under strain. In order to improve the characterization results, a strain transfer test is first conducted and presented in Section 3.2.2.1. The resonator test is further used to characterize the dielectric constant change under strain after the strain transfer calibration. The characterization results are presented in Section 3.2.2.2.

3.2.2.1 Strain transfer test

To achieve an accurate material characterization, the strain transfer ratio is first calibrated between the aluminum specimen and top copper cladding of the substrate material Rogers 5880. Fig. 3.4 shows the experimental setup of the strain transfer

calibration test. The resonator shown in Fig. 3.3 is bonded at the side of an aluminum specimen. Five metal foil strain gages are also installed in the center area of the aluminum specimen. To check the strain transfer ratio, another three metal foil strain gages are installed on the top copper cladding of the resonator. A National Instruments strain gage module (NI 9235), with a CompactDAQ Chassis (NI cDAQ-9172), is used for collecting data from metal foil strain gages. The axial force applied by the 100-kN Instron 8802 machine is configured so that approximately a 500 με strain increment is achieved at each loading step till 2,000 με.

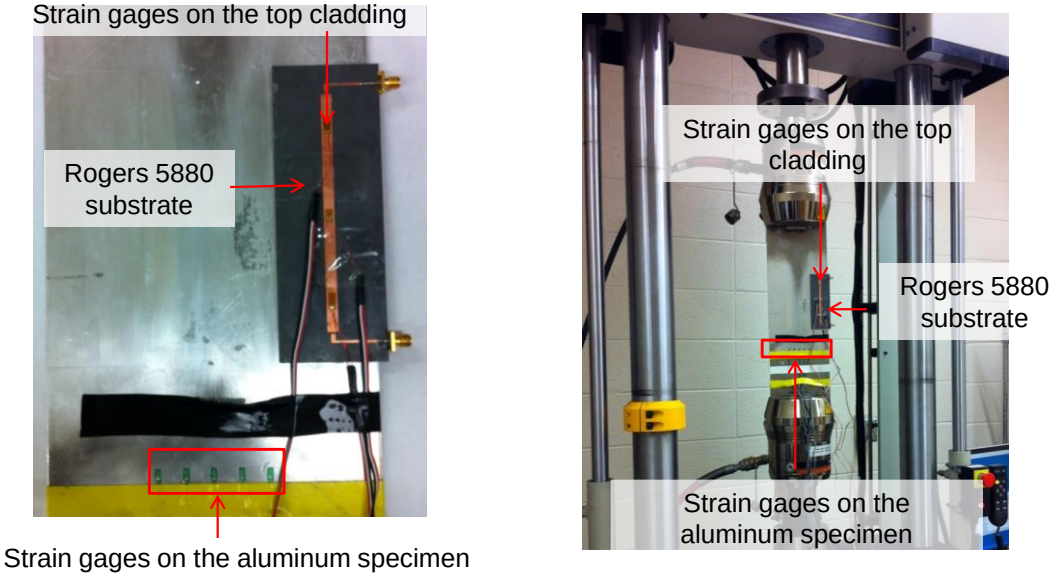

(a) Specimen configuration (b) Experimental setup

Fig. 3.4 Experimental setup for strain transfer calibration

Fig. 3.5 summarizes the experimental results of the strain transfer test. Fig. 3.5(a) shows the strain differences between strain of the aluminum specimen and the top copper cladding of the substrate material. As the applied strain increases, the strain difference also increases gradually. Fig. 3.5(b) shows the strain transfer ratio between the two

layers. The strain transfer results will be further used to calibrate the following electromagnetic measurement results.

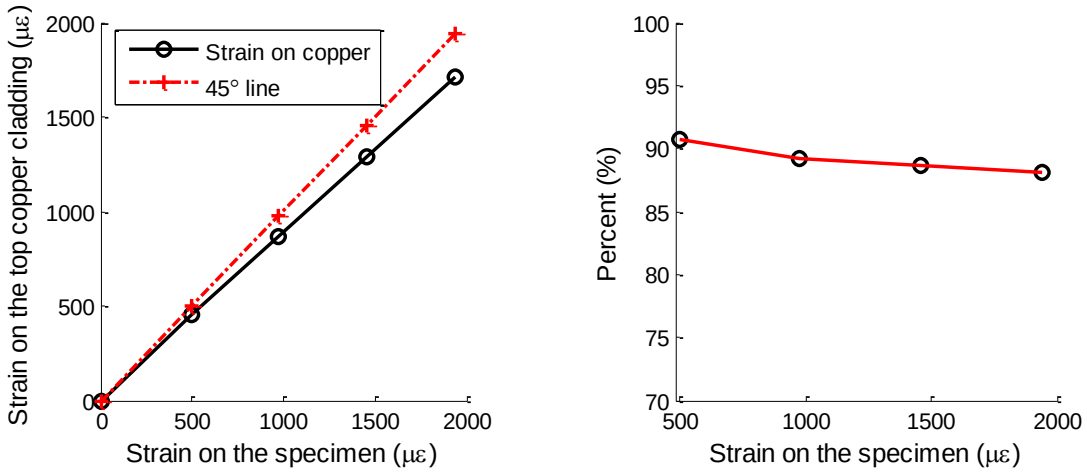

(a) Strain differences (b) Strain transfer ratio η_m

Fig. 3.5 Experimental results for strain transfer calibration

3.2.2.2 Tensile testing of the resonator

To calculate $\Delta\beta_r$ according to Eq.(3.8), the resonator in Fig. 3.3 is fabricated and tested under strain. Fig. 3.6 shows experimental setup for the tensile test. The resonator is installed along the side of an aluminum specimen, together with five metal foil strain gages in the center area of the specimen. The S_{21} coefficient of the resonator is measured by a vector network analyzer (VNA). A National Instruments strain gage module, with a CompactDAQ Chassis, is used for collecting data from metal foil strain gages. The axial force applied by the MTS-810 machine is configured so that approximately a 500 με strain increment is achieved at each loading step. The test starts with zero strain, and ends at around 2,000 με.

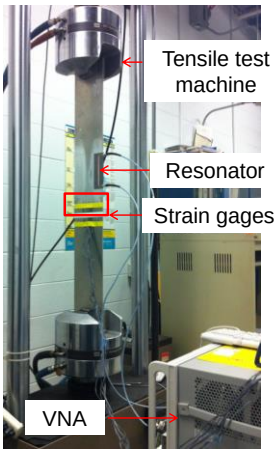

Fig. 3.6 Experimental setup for dielectric constant characterization

Fig. 3.7(a) plots measured S_{21} of the resonator at five different strain levels. The strain levels in Fig. 3.7(a) are the average value among the five metal foil strain gages, after strain transfer calibration [59]. Value of S_{21} reaches its maximum value at resonance frequency of the resonator. The resonance frequency of the resonator at zero strain level is f_{R0} =948.705 MHz. Fig. 3.7(a) shows a clear resonance frequency decrease during strain increment. For accuracy, a 4th order polynomial curve fitting is performed to the peak area of each plot [59]. The fitted 4th order polynomial is used for identifying the resonance frequency that corresponds to the maximum S_{21}. For example, the measured S_{21} at zero strain level is plotted as the solid line in Fig. 3.8. The received power reaches its maximum value at the resonance frequency. Since the peak area of the plot is relatively flat, the precise resonance frequency is not obvious. To resolve this difficulty, a 4th order polynomial curve fitting is performed to the peak area, which is shown as the dashed line in Fig. 3.8. The value of the fitted 4th order polynomial is evaluated at a frequency step of 0.001MHz, and the resonance frequency (for zero strain level) is identified as 948.705 MHz using the fitted polynomial.

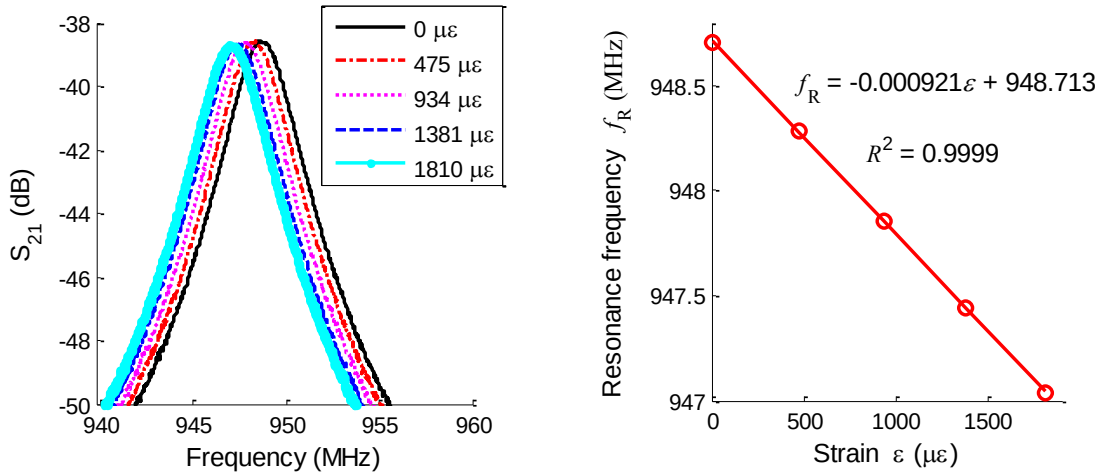

(a) Measured S_{21} plots at different strain levels

(b) Resonance frequency change under strain ε_t

Fig. 3.7 Experimental results of the tensile test for resonator

Fig. 3.7(b) shows the relationship between resonance frequency change and applied strain. The resonance frequency at strain ε_t =1,810 με is about 947.04 MHz. According to Eq.(3.8), the corresponding dielectric constant changes at different strain levels can be calculated and the results are shown in Fig. 3.9. As shown in this figure, the dielectric constant of the substrate decreases gradually as the applied strain increases. The dielectric constant decreases from 2.2 to 2.1998, when strain increases from 0 to 1,810 με. The relationship between the dielectric constant change and the strain is not linear, which indicates the necessity of dielectric constant calibration under strain in order to improve the simulation accuracy. The relationship between dielectric constant variation and applied strain calculated from Eq. (3.8) is to be used in mechanics-electromagnetics coupled simulation to further improve the simulation accuracy.

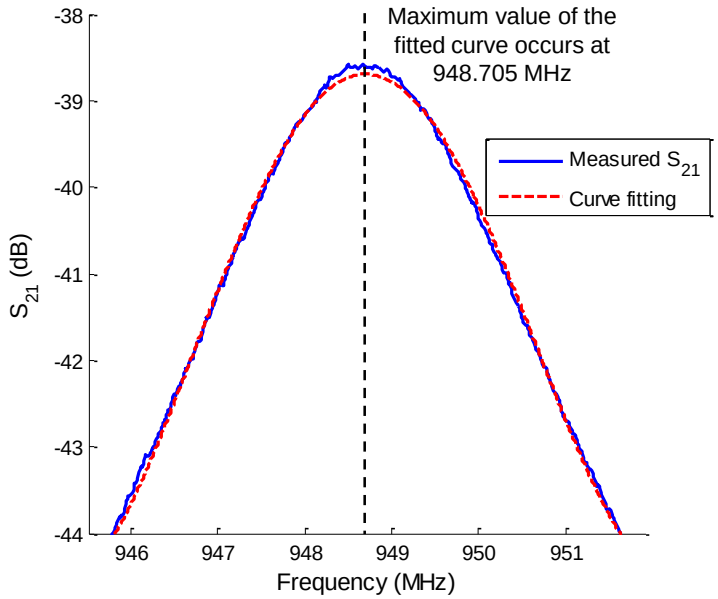

Fig. 3.8. Curve fitting to the S_{21} plot at zero strain level

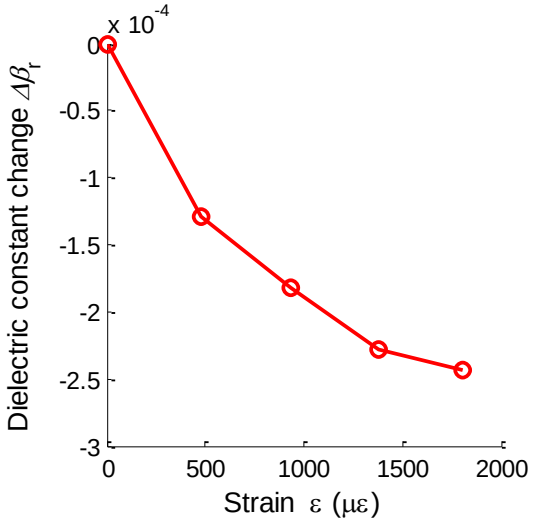

Fig. 3.9. Dielectric constant change under strain

3.3 Multi-Physics Modeling Examples

For illustration, multi-physics coupled simulation models of two RFID antenna sensors and one frequency doubling antenna sensor are presented in this section. Section 3.3.1 describes mechanics-electromagnetics coupled simulation of the folded patch antenna sensor in COMSOL. Section 3.3.2 describes the RFID slotted patch antenna

sensor simulation. Section 3.3.3 presents the multi-physics simulation of a frequency doubling antenna sensor modeled in ADS and COMSOL.

3.3.1 Folded Patch Antenna Sensor

Fig. 3.10 shows the simulation model for an RFID folded patch antenna sensor in COMSOL [37]. The sensor is bonded at the center of an aluminum plate. The RFID chip is simulated as a lumped port with the same electrical impedance (Z_c = 13.3-122 j Ω) as the chip. The bonding between the bottom copper cladding of the antenna sensor and the aluminum plate is assumed to be ideal, i.e. no relative displacement occurred at the interface. Similarly, bonding between the top/bottom copper cladding and the substrate material is assumed to be ideal. The antenna sensor and the aluminum plate are placed at the center of an air sphere. At the outer surface of the air sphere, boundary condition is set as a perfectly matched layer (PML). The PML boundary condition allows electromagnetic wave emitted by the antenna sensor to pass through with minimal reflections, which mimics the dissipation of electromagnetic wave into infinite free space. The two copper cladding layers, i.e. top and bottom, are meshed using shell elements with a thickness of 0.017mm. Key mechanical and electromagnetic properties of the materials are summarized in Table 3.1. Copper and aluminum materials are modelled as perfect electric conductor (PEC) in the electromagnetic simulation. In the mechanical simulation, tetrahedral and prism elements are adopted to model solid structures such as the aluminum specimen, substrate, and PML layer, and to efficiently resolve boundary layers. For modeling shell structures, such as top and bottom copper cladding, triangular elements are used to reduce discretization error and quadrilateral elements are adopted to achieve better numerical accuracy. In the electromagnetic simulation, the air sphere and the PML layer are similarly modelled as tetrahedral and prism elements. Table 3.2 lists the number of each type of element, and the number of DOFs in COMSOL model.

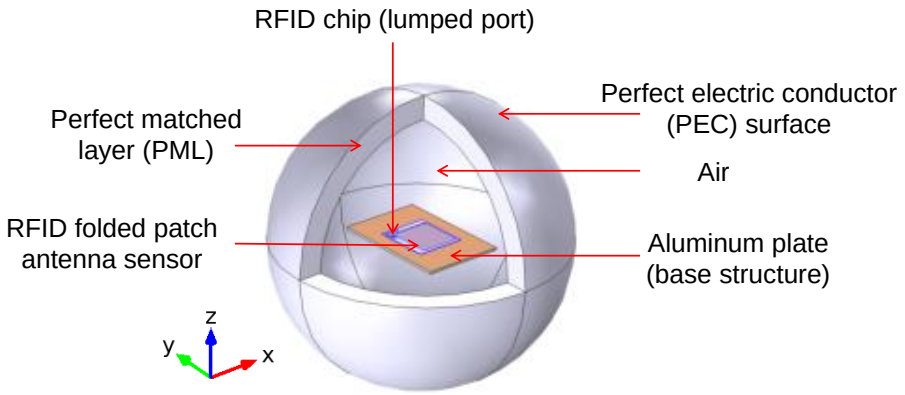

Fig. 3.10. Multi-physics simulation model of the folded patch antenna sensor using COMSOL

Table 3.1. Key properties of the materials using COMSOL simulation model

	Substrate	**Copper cladding**	**Aluminum**
Material type	Glass microfiber reinforced PTFE	Copper	6061 Aluminum alloy
Relative permittivity (β_{r0})	2.2	1	1
Conductivity (S/m)	0.5×10^{-9}	PEC	PEC
Poisson's ratio	0.4	0.35	0.33
Young's modulus (GPa)	1.07	110	69
Dimensions (mm^3)	$61\times69\times0.79$	$50\times56.5\times0.017$ (Top) $61\times69\times0.017$ (Bottom)	$150\times100\times3.175$

Table 3.2. Number of elements and degrees of freedom in the folded patch antenna sensor model

Number of Elements		**Number of DOFs**	
Tetrahedron	70,957	Mechanics	129,102
Prism	2,556		
Triangle	11,132	Electromagnetics	716,317
Quadrilateral	288		

In the mechanical simulation, only the aluminum plate and the antenna sensor (including the substrate and two copper layers) are involved, while the air sphere is neglected. Prescribed displacements are applied at two ends of the aluminum plate, so that five different strain levels (from 0 to 2,000με at an increment step of 500με) are generated in the aluminum plate. After the mechanical simulation at each strain level, the

deformed meshing is directly used for electromagnetic simulation to determine the resonance frequency of the antenna sensor under strain. During the electromagnetic simulation, a frequency domain solver is used to calculate reflection coefficient S_{11}. S_{11} quantifies impedance matching between the lumped port (RFID chip) and the antenna. Smaller S_{11} value means the RFID chip can emit more electromagnetic energy through the antenna into the air, indicating better matching and higher antenna efficiency. The simulated frequency range is 907.5~916.5 MHz with a frequency step of 0.05 MHz. The average computation time for one frequency point is about 503 seconds. The total computation time is roughly proportional to number of strain steps and number of frequency points per strain step. In this study with five strain steps and 181 frequency points per strain step, the total computing time on an 8GB Intel Core 2 Duo CPU machine is 455,216 seconds. The required memory for the computation in frequency domain solver is around 3 GB.

Fig. 3.11 (a) presents simulated strain distribution in the longitudinal direction on the aluminum plate and the antenna sensor, when the applied strain in the plate is 2,000 με (along y-direction). Approximately uniform strain distribution is achieved around the center of the aluminum plate. On the other hand, the strain distribution on top copper cladding is not uniform, especially close to vias. Fig. 3.11 (b) shows the surface current density distribution in y-direction on the top copper cladding. The figure clearly shows the surface current flows along top cladding and detours along the vias, which is the reason of adopting the folding pattern for sensor size reduction (Section 2.1).

Fig. 3.12 (a) and Fig. 3.12 (b) plot the normalized electric fields when the sensor is at zero strain, for two different interrogation frequencies (911.6 MHz and 909.95 MHz), respectively. Fig. 3.12 reveals that the electric field is stronger when the sensor operates at 911.6 MHz. In other words, at zero strain, a 911.6 MHz interrogation signal results in stronger antenna sensor radiation than a 909.95 MHz interrogation signal (with the same power level). As a matter of fact, resonance frequency of the antenna sensor at

zero strain is 911.6 MHz. Fig. 3.13 shows simulated normalized electric fields at the same two interrogation frequencies, when the antenna is at 2,000 με strain level. Opposite to Fig. 3.12, the electric field at 911.6 MHz is weaker than the electric filed at 909.95 MHz. In other words, at 2,000 με, a 909.95 MHz interrogation signal results in stronger antenna sensor radiation than a 911.6 MHz interrogation signal with the same power level. Likewise, the resonance frequency at 2,000 με is 909.95 MHz.

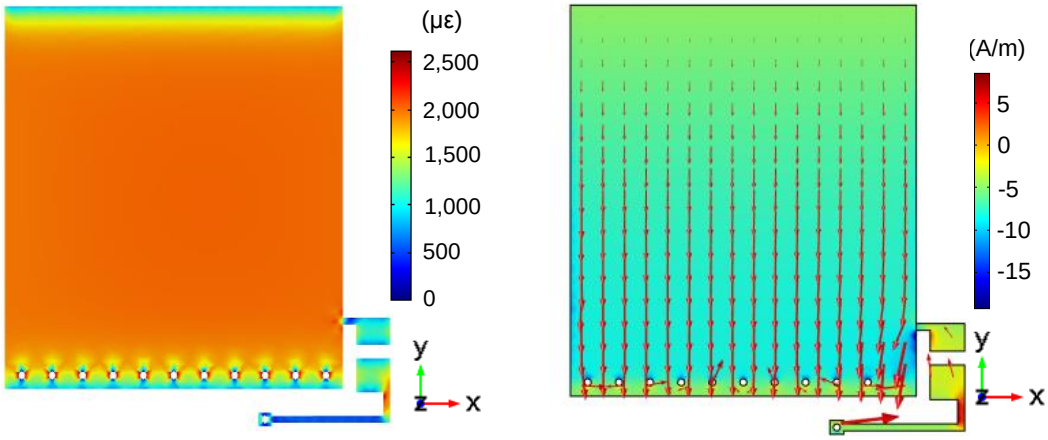

(a) Strain distribution in y-direction

(b) Surface current density in y-direction

Fig. 3.11. Field distributions from mechanics-electromagnetics coupled simulation of folded patch antenna sensor at 2,000 με.

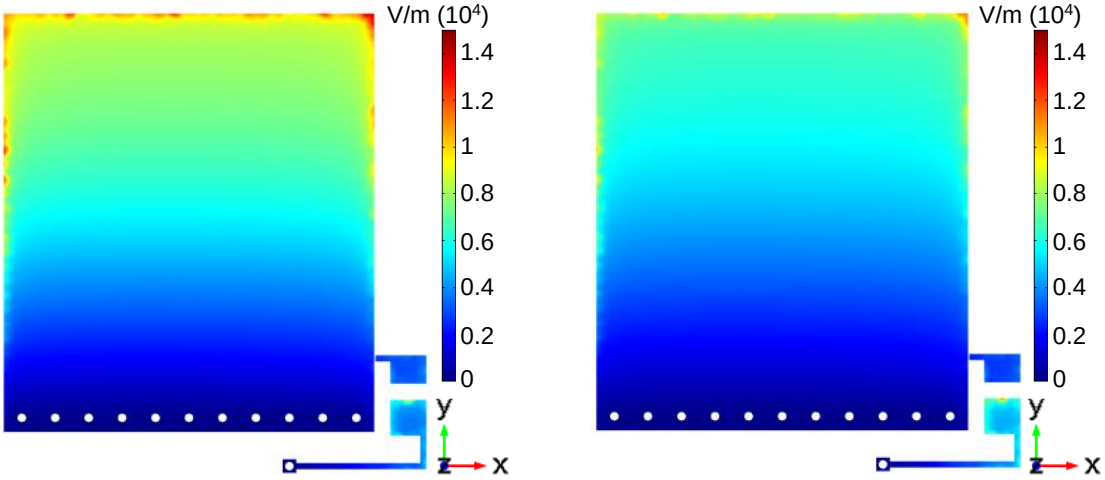

(a) Normalized electric field at 911.6 MHz (f_{R0} at 0 με)

(b) Normalized electric field at 909.95 MHz

Fig. 3.12. Normalized electric field at two different operating frequencies of the folded patch antenna sensor (0 με)

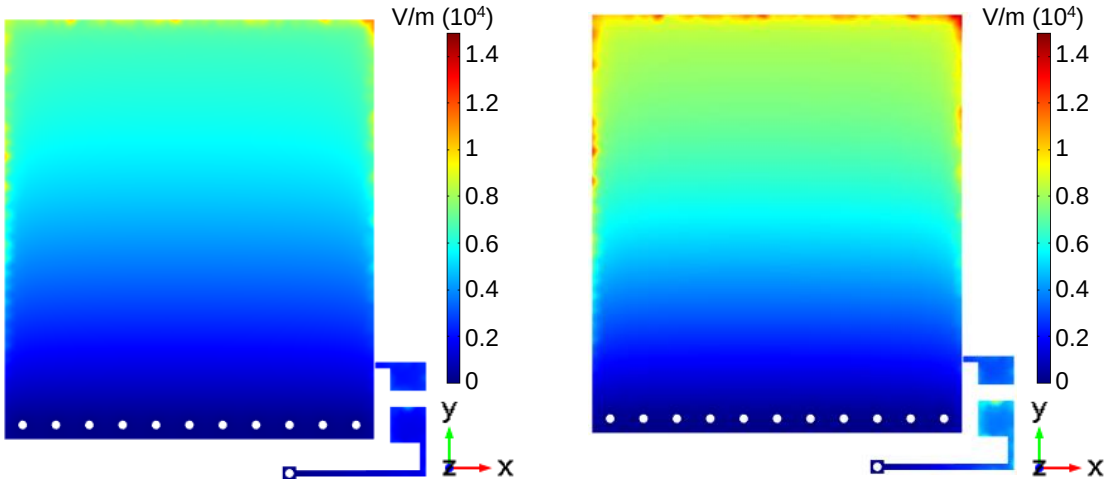

(a) Normalized electric field at 911.6 MHz

(b) Normalized electric field at 909.95 MHz (f_R at 2,000 με)

Fig. 3.13. Normalized electric field at two different operating frequencies of the folded patch antenna sensor (2,000 με)

Fig. 3.14(a) shows simulated S_{11} plot of the folded patch antenna sensor at five different strain levels. At each strain level, the antenna resonance frequency can be extracted by peak picking. Clear frequency decrease is observed when strain increases. As previously mentioned, at zero strain level, the antenna resonance frequency is found to be 911.6 MHz. At 2,000 με, the resonance frequency decreases to 909.95 MHz.

The resonance frequency at each strain level is extracted from Fig. 3.14(a) and the resonance frequency change versus strain relationship is plotted in Fig. 3.14(b). The strain sensitivity is –824 Hz/με, which means 1 με strain experience by the folded patch antenna sensor introduces 824 Hz sensor resonance frequency decrement. The corresponding normalized resonance frequency change is calculated according to Eq. (2.13). Fig. 3.14(c) plots the relationship between normalized resonance frequency change and strain. The normalized strain sensitivity is –0.8982 ppm/με, which means 1 με strain experienced by the folded patch antenna causes 0.8982 ppm decrease in resonance frequency. The normalized strain sensitivity is lower than –1 ppm/με, mainly due to shear lag effect described by Eq. (2.14) and dielectric constant change under mechanical strain explored in Section 3.2. The coefficient of determination (R^2) is

0.9996, which indicates a good linearity between normalized frequency change and simulated strain.

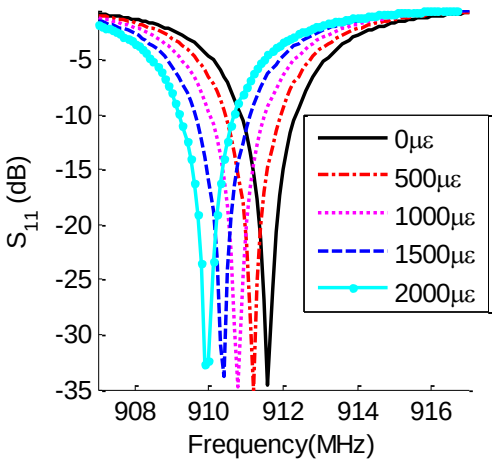

(a) Simulated S_{11} plots at different strain levels

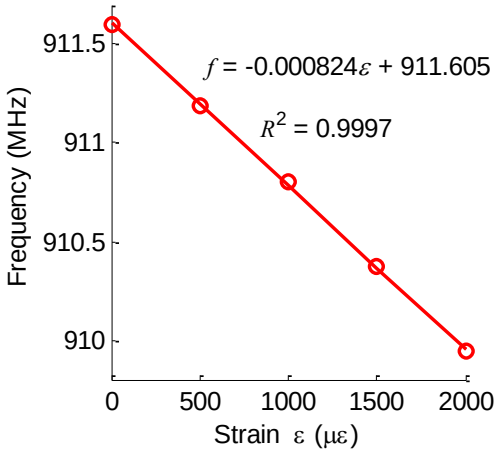

(b) Resonance frequency change versus strain ε

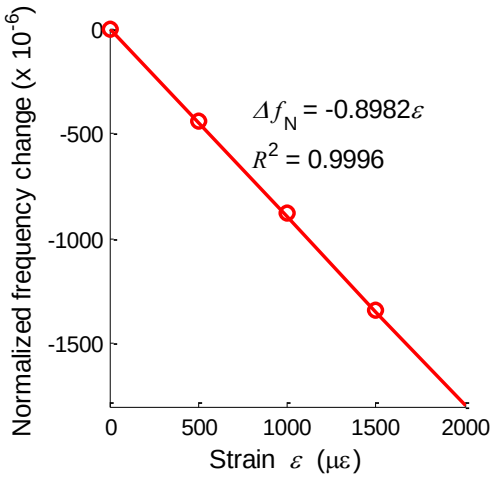

(c) Normalized resonance frequency change Δf_N versus strain ε (f_{R0} = 911.6 MHz)

Fig. 3.14. Simulation results for the folded patch antenna

To further improve the mechanics-electromagnetics coupled simulation accuracy, the dielectric constant change presented in Section 3.2 is integrated in the simulation. The dielectric constant changes in Fig. 3.7 are used to tune the dielectric constant at each simulated strain level. All other simulation setup is the same as presented early in this section. The simulation results are shown in Fig. 3.18. The strain sensitivity in Fig.

3.18(a) is –799 Hz/με, which is about 25 Hz/με smaller than the simulation results without considering dielectric constant change (Fig. 3.14(b)). The corresponding normalized strain sensitivity is –0.8752 ppm/με as presented in Fig. 3.18(b). These results will be compared with experimental results to verify the simulation accuracy.

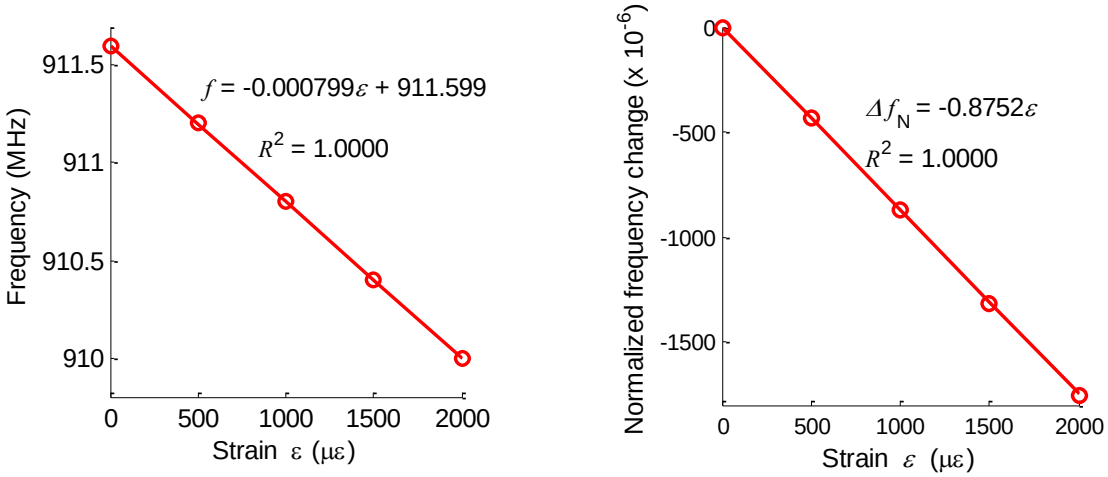

(a) Resonance frequency change versus strain ε

(b) Normalized resonance frequency change Δf_N versus strain ε

Fig. 3.15. Simulation results for the folded patch antenna after implementing dielectric constant changes

Similar as metal foil strain gages, the transverse (cross) sensitivity needs to be studied to investigate the effect of antenna width variation on strain sensitivity. The transverse sensitivity of the antenna sensor is the sensor behavior in response to strain perpendicular to the antenna length direction (i.e. strain along the direction of antenna width). In order to simulate the transverse sensitivity, prescribed displacements along x-direction are applied to two ends of the aluminum plate in Fig. 3.16, so that required strain levels are generated. At the same time, the other two ends of aluminum plate are fixed to prevent displacement in y-direction. These mechanical boundary conditions are aimed to generate strain primarily in sensor width direction, while keeping deformation in sensor length direction to be negligible.

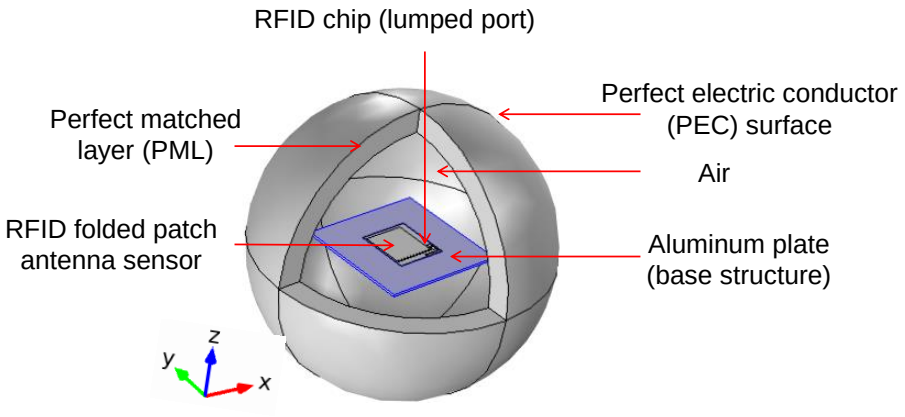

Fig. 3.16. Updated multi-physics simulation model of the folded patch antenna sensor with larger aluminum plate

Strain distributions on the antenna top copper cladding in x (width) and y (length) directions are shown in Fig. 3.17, when the strain applied to the aluminum plate is 2,000με in x-direction. The strain distribution ε_x on the top cladding is also to 2,000με as shown in Fig. 3.17(a). On the other hand, the strain ε_y around the center of the top cladding is less than 50 με, which is much smaller than ε_x.

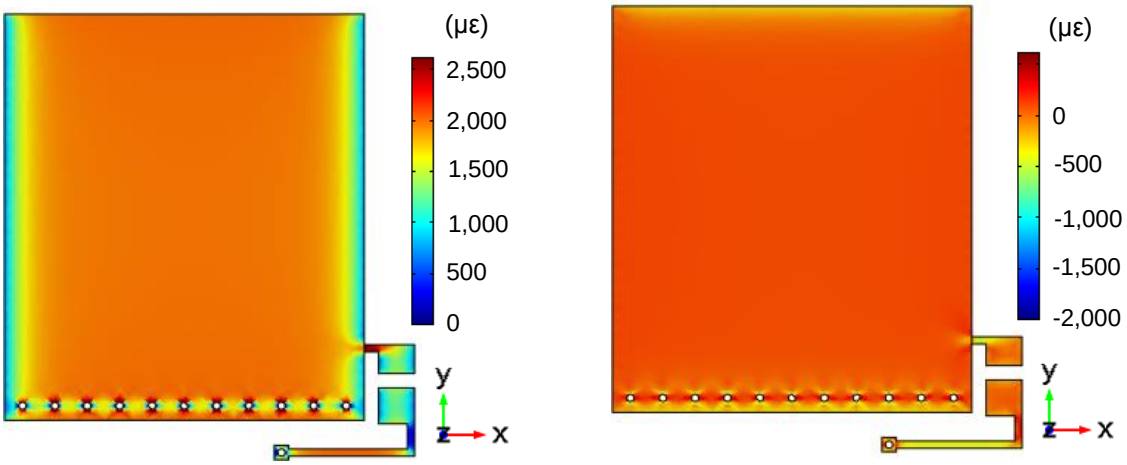

(a) Strain distribution in antenna width direction (ε_x)

(b) Strain distribution in antenna length direction (ε_y)

Fig. 3.17. Strain distributions in x and y directions

The corresponding S_{11} results are shown in Fig. 3.18(a). Although the applied strain in x direction is changed from 0με to 2,000με, the resonance frequency shift is very small compared with the frequency shift in Fig. 3.14(a), when the strain is applied in the senor length direction (y-direction). The corresponding normalized frequency change is plotted in Fig. 3.18(b). The normalized transverse sensitivity is 0.0066 ppm/με, which is only 0.73% of the longitudinal sensitivity in Fig. 3.14(c). The small normalized strain sensitivity in the transverse direction indicates that the width dimension variation has little effect on the resonance frequency shift of the folded patch antenna.

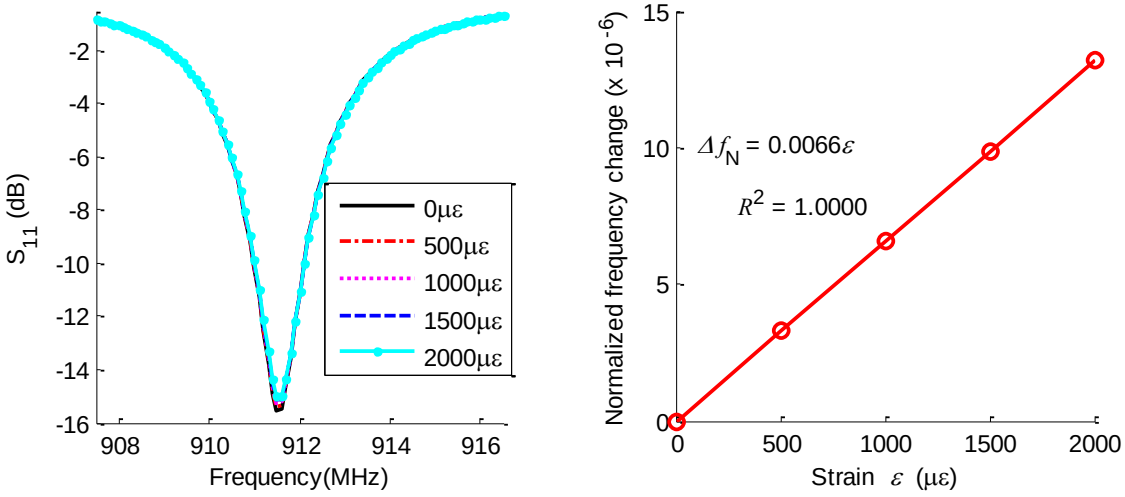

(a) Simulated S_{11} plots at different strain levels

(b) Normalized resonance frequency change Δf_N versus strain ε

Fig. 3.18. Simulation results of the folded patch antenna under transverse strain

3.3.2 Slotted Patch Antenna Sensor

This section describes the multi-physics modeling and simulation of a slotted patch antenna designed to reduce the sensor footprint by detouring the surface current path [72]. Although the folded patch antenna sensor shows good performance for wireless strain sensing, the sensor size is still relatively large. For further size reduction,

a slotted patch configuration is investigated. Fig. 3.19 shows an example slotted patch antenna design, whose dimension is reduced to 44 mm × 48 mm × 0.79 mm. An RFID chip is located in the top middle of the sensor for RFID signal modulation. Vias are also adopted to connect top copper cladding with bottom copper ground plane. The slots in the copper cladding generate a detoured surface current path. For the slotted patch antenna sensor, the initial resonance frequency can be estimated as:

$$f_{R0}^{\text{Slotted}} = \frac{c}{8(L+L')\sqrt{\beta_{r0}}} \tag{3.9}$$

and the shifted resonance frequency under strain is:

$$f^{\text{Slotted}} = \frac{c}{8(1+\varepsilon)(L+L')\sqrt{\beta_{r0}}} = \frac{f_0^{\text{Slotted}}}{1+\varepsilon} \approx f_0^{\text{Slotted}}(1-\varepsilon) \tag{3.10}$$

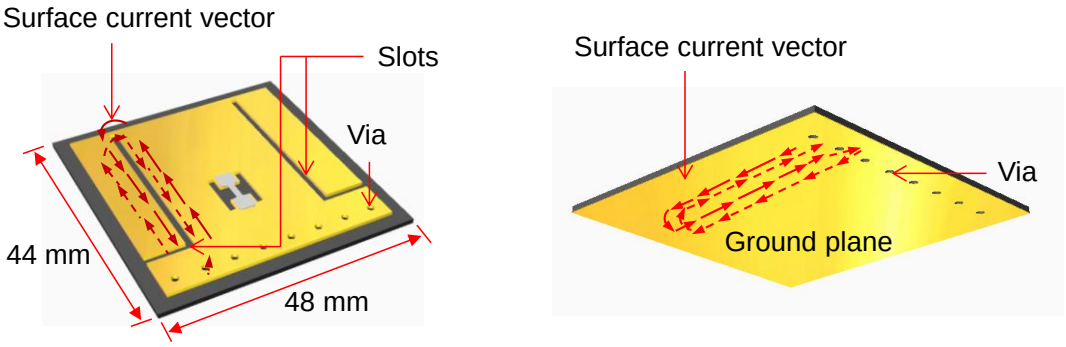

(a) Top skewed view (b) Bottom skewed view

Fig. 3.19. Illustration of the surface current flows in the slotted patch antenna (dotted lines represent current on the opposite surface of the view).

Fig. 3.20 shows the COMSOL simulation model of the passive slotted patch antenna sensor. All boundary conditions are similar as described in the Section 3.3.1. Prescribed displacements are applied at two ends of the aluminum plate, so that five different strain levels (from 0 to 2,000 με at an increment step of 500 με) are generated in the aluminum plate. The simulated frequency range is 909~915 MHz with a frequency step of 0.1 MHz. The resonance frequency is finally determined by picking the lowest peak of the S_{11} plot. Table 3.3 lists the number of each type of element, and the number

of DOFs in COMSOL model. The average computation time for one frequency point is about 498 seconds. The total computation time is also related with total frequencies points and strain steps. The total computation time for five strain steps and 61 frequency points is 151,911 seconds. The required memory for the computation in the frequency domain solver is around 2.5 GB, which is still acceptable.

Table 3.3. Number of elements and degrees of freedom in the slotted patch antenna sensor model

Number of Elements		Number of DOFs	
Tetrahedron	39,665	Mechanics	53,124
Prism	3,220		
Triangle	5,768	Electromagnetics	477,429
Quadrilateral	790		

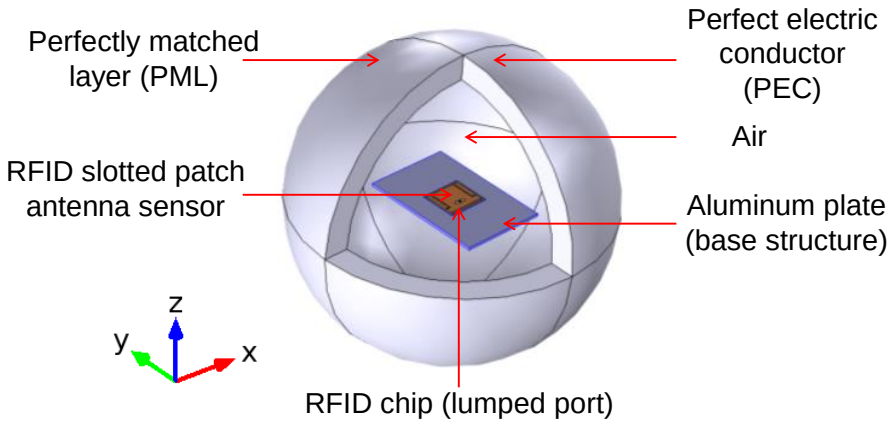

Fig. 3.20. Multi-physics simulation model of slotted patch antenna sensor using COMSOL

Fig. 3.21(a) presents simulated strain distribution in the longitudinal (y-direction) direction on the aluminum plate and the antenna sensor, when the applied strain in the plate is 2,000 με. Approximately uniform strain distribution is achieved around the center of the aluminum plate. On the other hand, the strain distribution on top copper cladding has large variations that are highly dependent on the slotted pattern. Fig. 3.21(b) shows the surface current density distribution in y-direction on the top copper cladding. The

figure clearly shows the surface current density detouring along the slots and the vias, which as intended enables sensor size reduction. Fig. 3.22(a) and Fig. 3.22(b) plot the normalized (magnitude) electric fields when the sensor is at zero strain, for two different interrogation frequencies (912.2 MHz and 910.8 MHz), respectively. Fig. 3.22 reveals that at zero strain, a 912.2 MHz interrogation signal results in stronger antenna sensor radiation than a 910.8 MHz interrogation signal (with the same power level). Fig. 3.23 shows simulated normalized electric fields at the same two interrogation frequencies, when the antenna is at 2,000 με strain. Opposite to Fig. 3.22, Fig. 3.23(a) shows weaker electric field than Fig. 3.23(b). In other words, at 2,000 με, a 910.8 MHz interrogation signal results in stronger antenna sensor radiation than a 912.2 MHz interrogation signal (with the same power level).

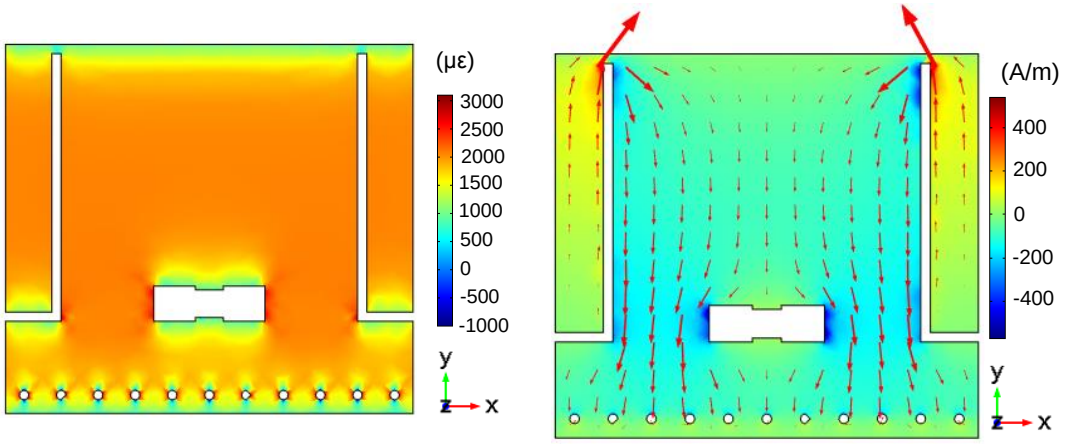

(a) Strain distribution in y-direction

(b) Surface current density in y-direction

Fig. 3.21. Field distributions from mechanics-electromagnetics coupled simulation

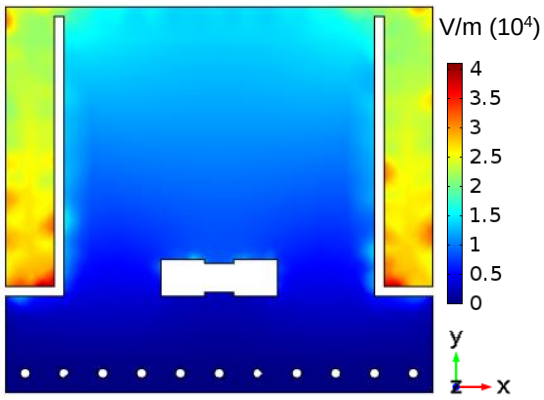

(a) Normalized electric field at 912.2 MHz (f_{R0} at 0 με)

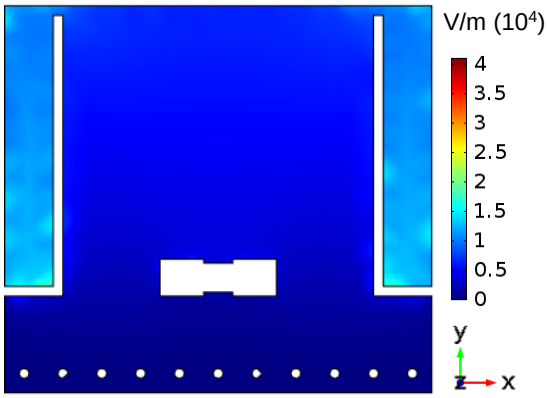

(b) Normalized electric field at 910.8 MHz

Fig. 3.22. Normalized electric field at two different operating frequencies of the slotted patch antenna sensor (0 με)

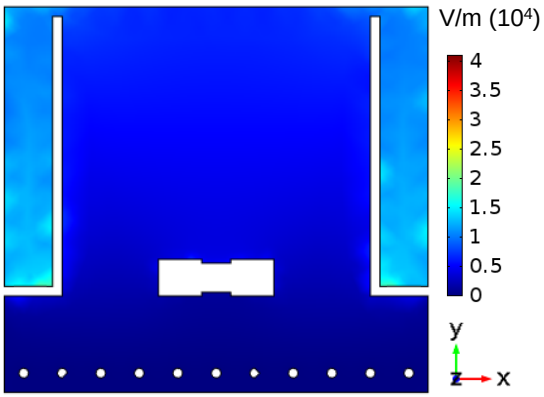

(a) Normalized electric field at 912.2 MHz

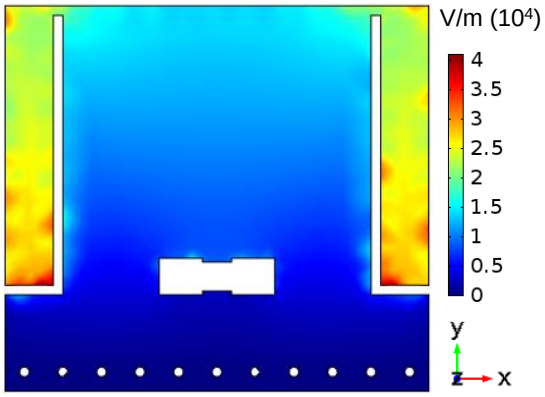

(b) Normalized electric field at 910.8 MHz (f_R at 2,000 με)

Fig. 3.23. Normalized electric field at two different operating frequencies of the slotted patch antenna sensor (2,000 με)

Fig. 3.24(a) shows simulated S_{11} plots at different strain levels. As expected, the resonance frequency of the antenna sensor reduces as the strain increases. The resonance frequency at each strain level is extracted and plotted in Fig. 3.24(b). Linear regression is applied to the data points and the regression results are shown in the figure. The strain sensitivity is –719 Hz/με, which means 1 με generated on the aluminum specimen

introduces 719 Hz resonance frequency decrement. The normalized resonance frequency is plotted against strain in Fig. 3.24(c). The normalized strain sensitivity is –0.784 ppm (part per million)/με, which means 1 με generated on the aluminum specimen causes the resonance frequency to decrease by 0.784 ppm. The coefficient of determination (R^2) is also calculated to show the linearity. A value of 0.9999 indicates very good linearity.

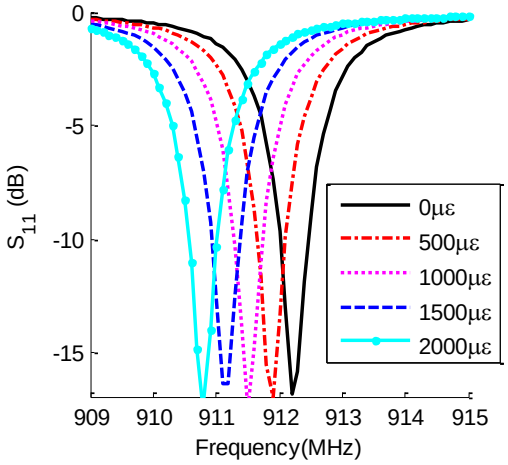

(a) S_{11} parameter

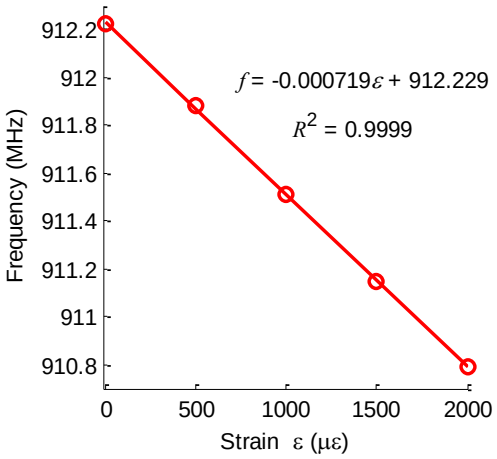

(b) Resonance frequency change versus strain ε

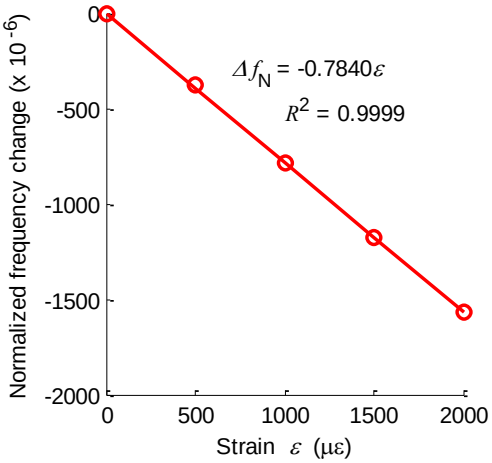

(c) Normalized resonance frequency change Δf_N versus strain ε (f_{R0} = 912.2 MHz)

Fig. 3.24. Strain simulation results of the passive slotted antenna sensor from COMSOL

Fig. 3.25 shows the design drawing and photo of a fabricated RFID slotted patch antenna sensor. The footprint of the slotted patch antenna is about half of the previously designed folded patch antenna (as described in Section 3.3.1).

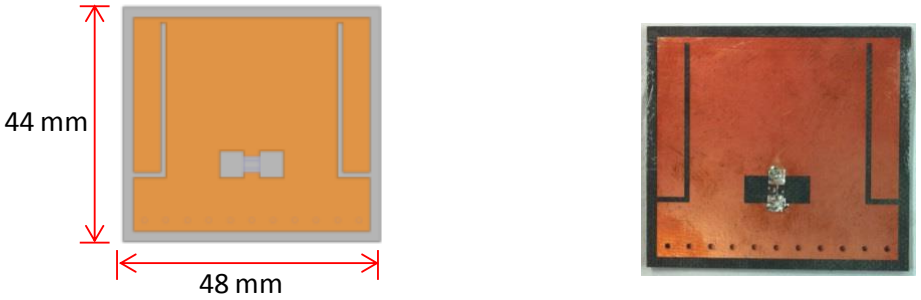

(a) Design drawing (b) Photo of fabricated sensor

Fig. 3.25. Slotted patch antenna sensor with passive RFID chip

In order to increase the interrogation distance of the antenna sensor, an active RFID chip is used to replace the passive RFID chip in a slotted patch antenna sensor. The adopted active RFID chip is SL3S1013 model from NXP Semiconductors. When a small power source (such as a solar cell) is available, the active RFID chip can be powered by solar cell and provide longer interrogation distance. Meanwhile, when power source is not available, the chip can still operate as a passive one. The slotted antenna pattern is tuned to match the impedance of the active RFID chip. Table 3.4 summarizes the parameters of the passive and active RFID chips. As shown in the table, the minimum operating power of the active RFID chip is -17.5 dBm when no external power source is connected, which is higher than the passive RFID chip. Since the smaller operating power indicates larger interrogation distance, the active slotted patch antenna sensor is expected to have larger interrogation distance even without external power source. When external power source such as solar cell is connected to the active sensor, the minimum operating power is further reduced to -27 dBm, which means more increment in interrogation distance.

Table 3.4. Parameter summaries of adopted passive and active RFID chips

Chip type	Model #	Impedance	Minimum operating power	Supply voltage	Supply current
Passive	NXP SL3ICS1002	13.3 – 122 j	-15 dBm	N/A	N/A
Active	NXP SL3S1013	8 – 288 j	-27 dBm (with power supply) -17.5 dBm (without power supply)	1.8 V	14 μA

Fig. 3.26 (a) shows simulated S_{11} plots of the active slotted patch antenna sensor at different strain levels. As expected, the resonance frequency of the antenna sensor reduces as strain increases. The resonance frequency at each strain level is extracted; the normalized resonance frequency is plotted against strain in Fig. 3.26 (b). The normalized strain sensitivity is –0.7672 ppm (part per million)/με, which means 1 με generated on the aluminum specimen causes the resonance frequency decreases by 0.7672 ppm. The coefficient of determination (R^2) is calculated to be 0.9996, indicating a good linearity.

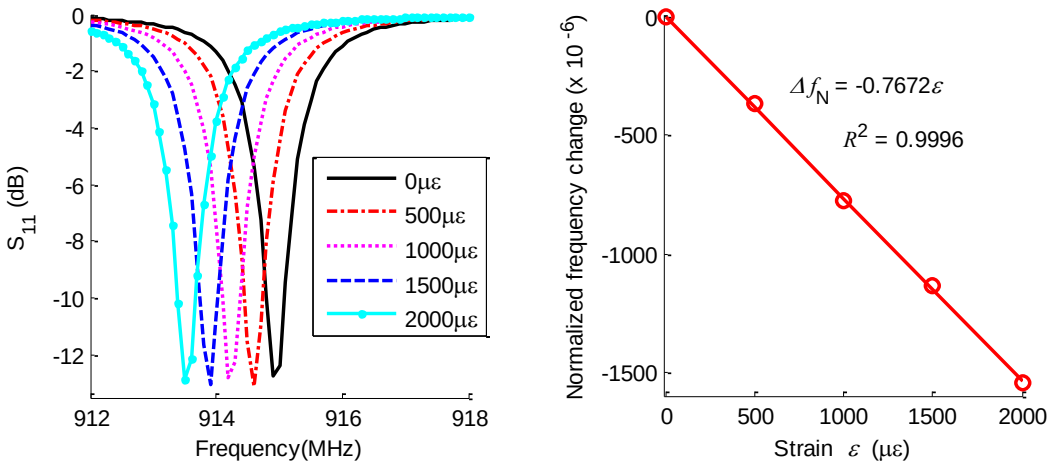

(a) S_{11} parameter (b) Resonance frequency versus strain

Fig. 3.26. Strain simulation results of the active slotted antenna sensor from COMSOL

Fig. 3.27 shows design drawing and photo of the active slotted patch antenna sensor. The footprint of the slotted patch antenna is the same as the passive slotted patch antenna sensor in Fig. 3.25.

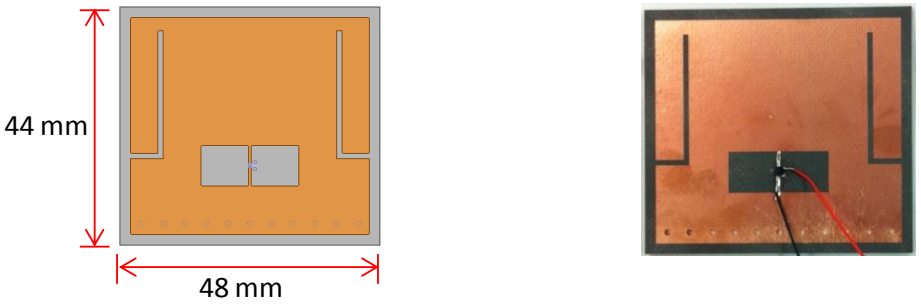

(a) Design drawing (b) Photo of fabricated sensor

Fig. 3.27. Slotted patch antenna sensor with active RFID chip

3.3.3 Frequency Doubling Antenna Sensor

As indicated by Eq. (2.8) and (2.10), if operating frequency of the antenna sensor is increased, not only strain sensitivity can be improved but also sensor size can be reduced. However, commercial passive RFID chips and readers are not available at GHz frequency range desired for high-resolution strain sensing. Alternative approaches need to be exploited in order to operate at higher frequencies. A novel wireless antenna sensor design is investigated in this research, which adopts a frequency doubling scheme to enable sensor operation at a high frequency [82]. The basic concept is to let the sensor double the frequency of reader interrogation signal (f) and backscatter signal at the doubled frequency ($2f$). Because environmental reflections to reader interrogation signal are concentrated at f, the reader only receives signal backscattered from the sensor at $2f$.

Section 3.3.3.1 presents the first frequency doubling sensor (prototype A) with a 2.9 GHz (f) and a 5.8 GHz ($2f$) patch antenna for receiving and transmitting, respectively. Section 3.3.3.2 describes the sensor prototype B, where the 5.8 GHz antenna is replaced

by a 5.8 GHz wideband antenna to remove any possible multiple peaks in the received power plot. Section 3.3.3.3 presents a modified design with the 5.8 GHz patch antenna rotated by 90 ° (prototype C), which intends to remove the coupling effect through the orthogonal polarization. Section 3.3.3.4 describes another modified design (prototype D) with the wideband antenna also rotated by 90 °to remove the coupling effect.

3.3.3.1 Prototype A with 5.8 GHz transmitting patch antenna

Fig. 3.28 shows design drawing and photo of the prototype A frequency doubling sensor. In this prototype, a 2.9 GHz patch functions as the receiving antenna and a 5.8 GHz patch functions as the transmitting antenna. Similar as the RFID antenna sensor simulation, the bonding between the bottom copper cladding of the frequency doubling antenna sensor and the aluminum plate is assumed to be ideal. Meanwhile, bonding between the top/bottom copper cladding and the substrate material is also assumed to be ideal.

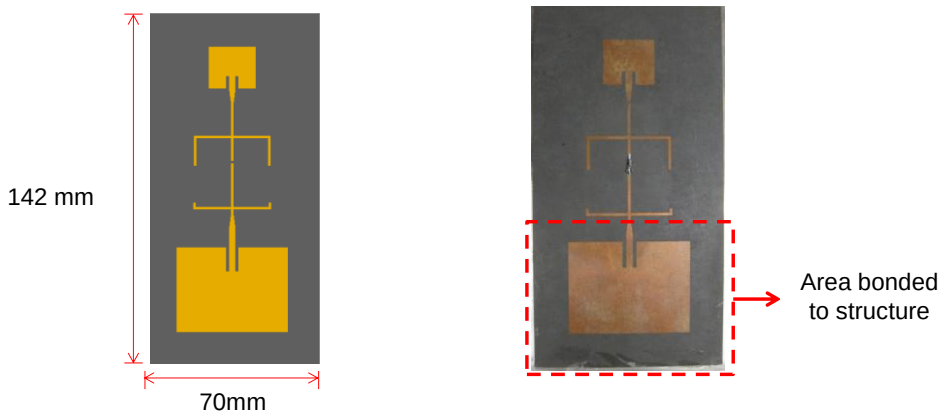

(a) Design drawing (b) Photo of fabricated sensor

Fig. 3.28. Frequency doubling sensor prototype A.

The 2.9 GHz patch antenna is first simulated in COMSOL. Fig. 3.29 shows the mechanics-electromagnetics coupled simulation model. The 2.9 GHz patch antenna, together with an aluminum plate is placed in the center of air sphere. Outside of the air

sphere is the PML, which used to truncate the simulation domain. To explore the strain sensing capability of the sensor, prescribed displacements are applied to the two ends of the aluminum plate. The 2.9 GHz antenna, which is bonded on top of the aluminum plate, deforms together the aluminum plate under applied displacements. All other parts of the sensor in Fig. 2.7, including the matching network and the 5.8 GHz transmitting antenna, are strain free. The prescribed displacements are adjusted so that about 500με is generated in the center of the aluminum plate at two adjacent steps. Fig. 3.30 shows S_{11} plot of 2.9 GHz patch antenna. The resonance frequency of the antenna at zero strain level is around 2.901 GHz. As the applied strain increases, the antenna resonance frequency decreases gradually as expected. Since the reflection coefficient S_{11} indicate the matching between antenna impedance and the port impedance, S_{11} can be converted to the antenna impedance according to the following equation [10]:

$$Z_a = Z_p \frac{1+S_{11}}{1-S_{11}} \tag{3.11}$$

where Z_p is the port impedance (i.e. 50 Ω in the 2.9 GHz parch antenna simulation); Z_a is the antenna impedance. The computed antenna impedances based on S_{11} results (in Fig. 3.30) are then used as input port (port 1 in Fig. 3.31) impedance of the matching network simulation.

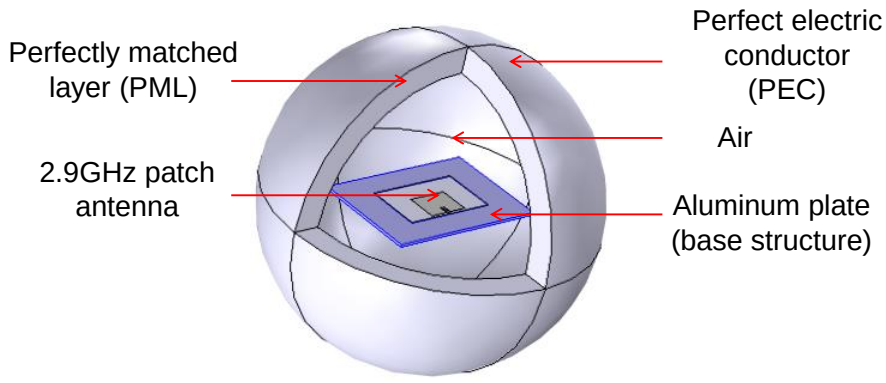

Fig. 3.29. Multi-physics simulation model of 2.9 GHz patch antenna using COMSOL

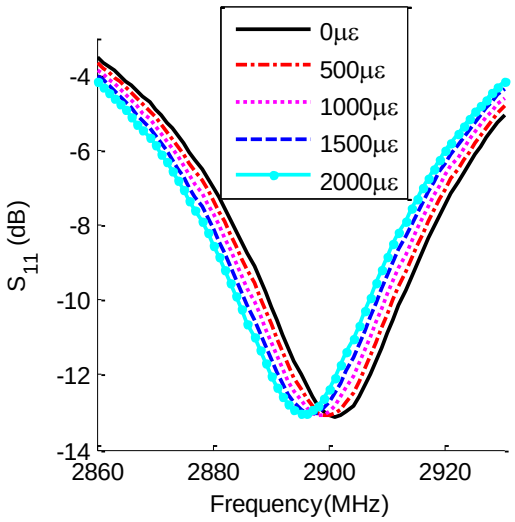

Fig. 3.30. Simulated S_{11} of the 2.9 GHz patch antenna

The matching network design integrating the diode, Skyworks SMS7621-079LF model, is then performed in the software package ADS (Advanced Design System). The matching network simulated in ADS is shown in Fig. 3.31. The dimension of the matching network is 56 mm × 30.5 mm. Because diode is a nonlinear circuit device, power loss of the diode-integrated matching network is dependent on input power level. To characterize backscattering behavior of the doubling sensor, sensor response for a neighborhood frequency range needs to be analyzed. To this end, power loss due to diode-integrated matching network is investigated by a harmonic balance simulation in ADS. The input power to the matching network at Port 1 is set to –10dBm. Furthermore, the input impedance at Port 1 is set as the 2.9 GHz antenna impedance calculated according to Eq. (3.11). In this case, the frequency response of the 2.9 GHz patch antenna is coupled with the matching network simulation. After the harmonic balance simulation, the output power at doubled frequency 2*f* from the simulated matching network at Port 2 is recorded. The results are plotted in Fig. 3.32. At zero strain level, the resonance frequency of the 2.9 GHz patch antenna and matching network combined, is around

2.898 GHz, which is about 3 MHz smaller than the 2.9 GHz patch antenna simulation. The shift of resonance frequency at zero strain level between two simulations indicates that it is necessary to perform the combined simulation in order to improve the accuracy. Furthermore, the resonance frequencies of the 2.9 GHz patch antenna and matching network combined simulation decreases as the increased strain experienced by the 2.9 GHz patch antenna. The output power at Port 2 of the matching network is then converted to the port voltage according to the following equation:

$$V_{\text{out}} = \sqrt{P_{\text{out}} Z_{\text{p}}} \tag{3.12}$$

where P_{out} is output power from Port 2; Z_{p} is the impedance of Port 2 (i.e. 50 Ω); V_{out} is the output voltage at Port 2. The calculated voltage from Eq. (3.12) is then used as input voltage at the port of 5.8 GHz patch antenna simulation.

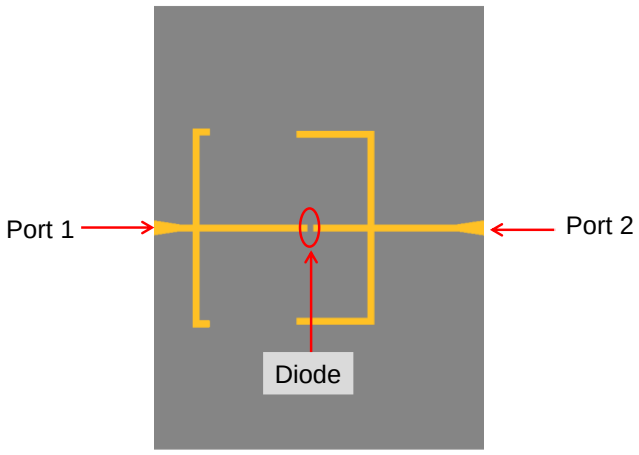

Fig. 3.31. Matching network model simulated in ADS

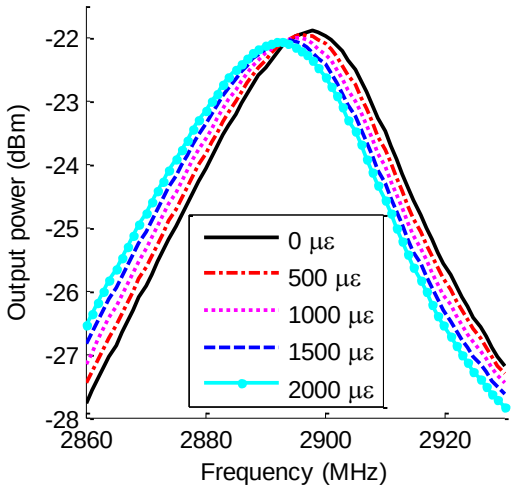

Fig. 3.32. Output power of diode-integrated matching network (input power at frequency *f*, output power at 2*f* as marked on the x-axis)

Fig. 3.33 shows the COMSOL simulation model of the 5.8 GHz patch antenna. It is similar as the 2.9 GHz patch antenna simulation, except that the input port voltage is based on the previous simulation combining 2.9 GHz patch antenna and matching network, instead of constant voltage in the 2.9 GHz patch antenna simulation.

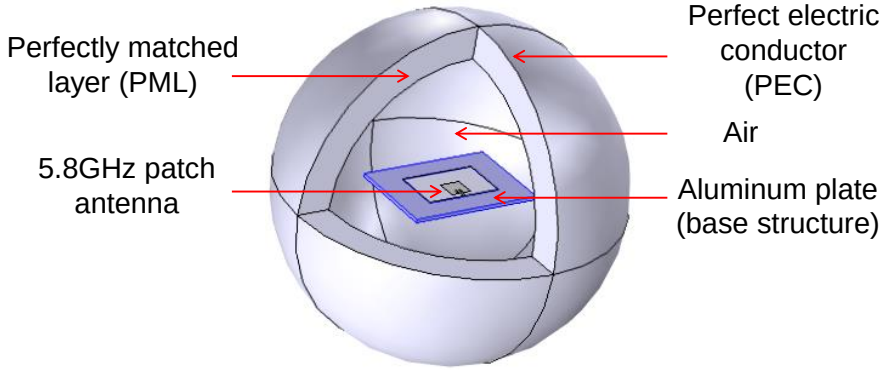

Fig. 3.33. Multi-physics simulation model of 5.8 GHz patch antenna using COMSOL

The relationship between output electric power and frequency at each strain level is again plotted in Fig. 3.34(a). Resonance frequency of the entire sensor is shown to decrease as strain increases. The resonance frequency at each strain level is extracted

from Fig. 3.34 (a), and plotted against strain in Fig. 3.34 (b). The figure shows simulated strain sensitivity at –5.471 kHz/με, which is more than five times higher than the RFID-based antenna sensor in Section 3.3.1 and 3.3.2.

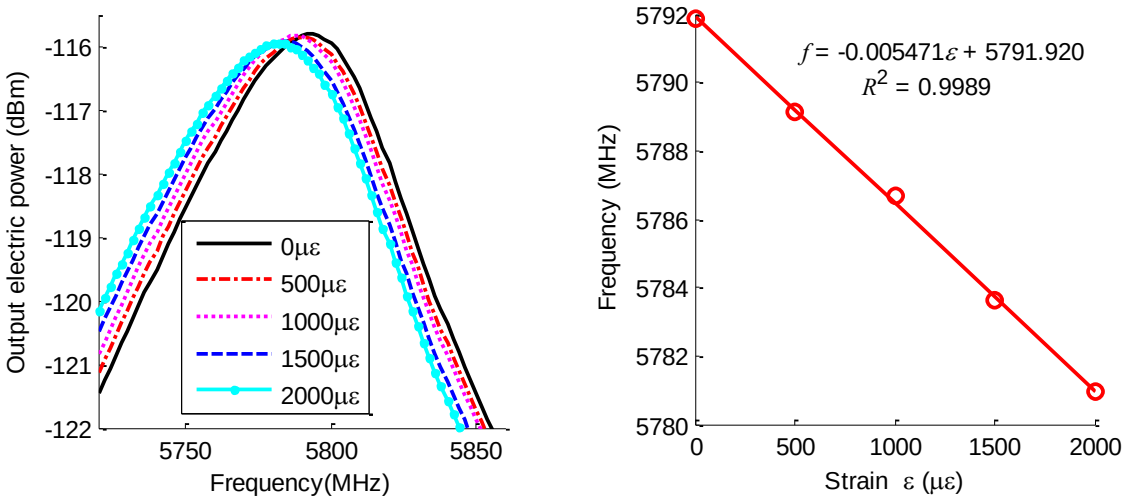

(a) Output electric power for multiple strain levels

(b) Resonance frequency versus strain

Fig. 3.34. Strain sensing simulation results for the frequency doubling antenna sensor

3.3.3.2 Prototype B with 5.8 GHz transmitting wideband antenna

Fig. 3.35 shows design drawing and photo of the frequency doubling sensor prototype B. In prototype B, the 5.8 GHz patch antenna of previous prototype A is replaced with a 5.8GHz wideband patch antenna. The 5.8 GHz wideband patch antenna is designed to remove any possible multiple peaks in the received power plot. In prototype A design, both 2.9 GHz and 5.8 GHz patch antennas are narrow band. If both antennas are well matched, i.e. 2.9 GHz patch has a resonance frequency at f_{R0} while 5.8 GHz patch has a resonance at $2f_{R0}$, then the overall response only has one peak. Due to limited design accuracy and fabrication error, the two resonance frequency of antennas may not

be exactly doubled. Without doubled resonance frequency, the overall frequency doubling sensor response can be wideband or even multiple peaks exist. In order to deal with the possible multiple peaks problem, the 5.8 GHz patch antenna is designed to be wideband. In this case, the sharpness of sensor overall response is only determined by 2.9 GHz patch antenna. The wideband patch antenna consists of a two-layer design, while 2.9 GHz and the matching network are single layer designs. An inductor of 33 nH from Panasonic Electronic Components (PCD1864CT) is also added in parallel to the diode, so that more electromagnetic energy passes through the diode.

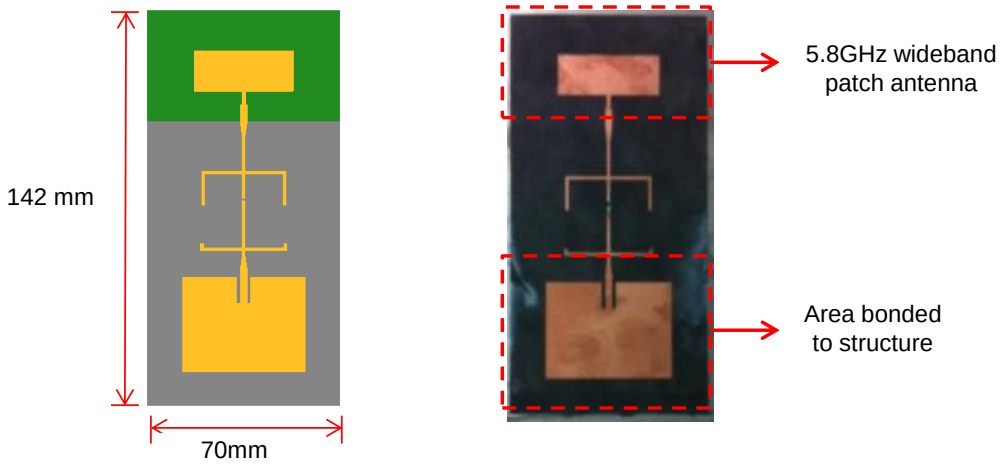

(a) Design drawing (b) Photo of fabricated sensor

Fig. 3.35. Frequency doubling sensor prototype B

3.3.3.3 Prototype C with 5.8GHz transmitting patch antenna rotated by 90 °

Fig. 3.36 shows design drawing and photo of the prototype C of the frequency doubling sensor. In the prototype C, the 5.8 GHz patch antenna of the previous prototype A is rotated by 90 °. In this case, the polarizations of the two patch antennas in the sensor are perpendicular to each other, which can reduce the coupling effect. In addition, a 33 nH inductor from Panasonic Electronic Components (PCD1864CT) is connected in parallel with the diode to improve its power transmission efficiency.

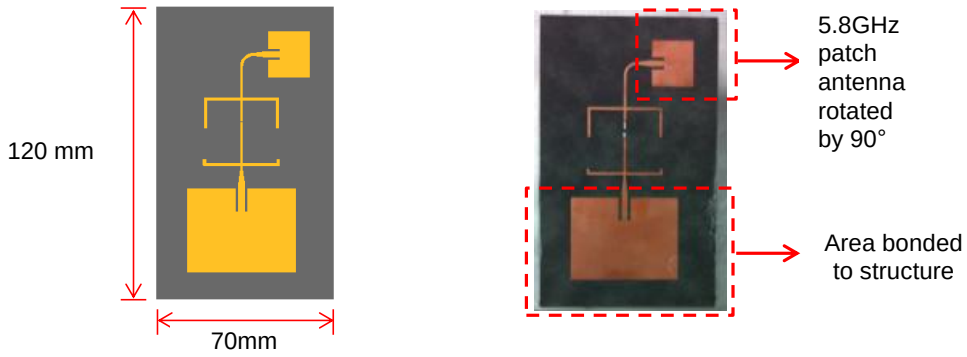

(a) Design drawing (b) Photo of fabricated sensor

Fig. 3.36. Frequency doubling sensor prototype C.

3.3.3.4 Prototype D with 5.8GHz transmitting wideband antenna rotated by 90 °

Fig. 3.37 shows design drawing and photo of the prototype D of the frequency doubling sensor. In the prototype D, the 5.8 GHz wideband patch antenna in the prototype B is rotated by 90 °. In this case, the polarizations of the two antennas in the sensor are perpendicular to each other, which can reduce the coupling effect. The 5.8 GHz wideband patch antenna is designed to remove any possible multiple peaks in the received power plot. The 5.8GHz wideband patch antenna is a two-layer design, while 2.9 GHz and the matching network are single layer design. An inductor of 33 nH is also added in parallel to the diode.

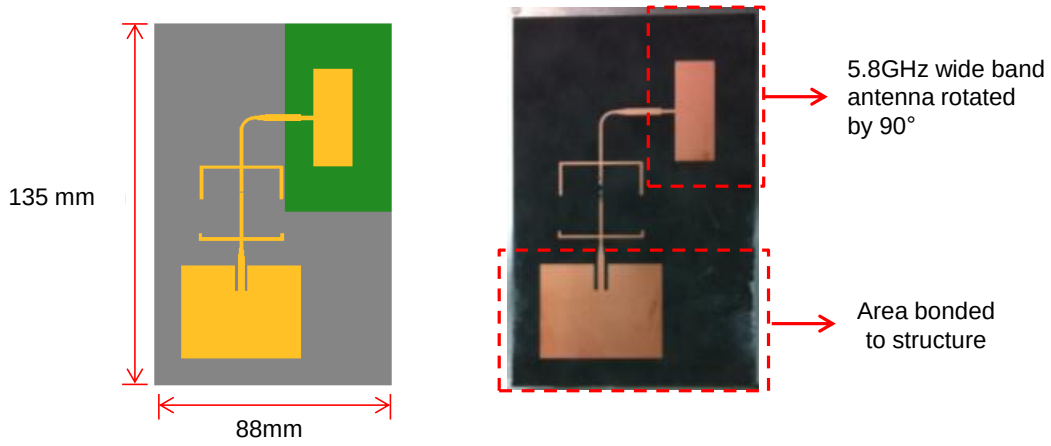

(a) Design drawing (b) Photo of fabricated sensor

Fig. 3.37. Frequency doubling sensor prototype D.

3.4 Summary

This chapter first presents a multi-physics coupled simulation framework for antenna sensor modeling. The accuracy and necessity of mechanics-electromagnetics coupled simulation is verified by results comparing between mechanics simulation and simple scaling. The mechanics-electromagnetics coupled simulation framework is used for RFID antenna sensor simulation. The folded patch antenna sensor and slotted patch antenna sensor are used as mechanics-electromagnetics coupled simulation examples. The coupled simulation of the folded patch antenna sensor demonstrates that the resonance frequency of the sensor decreases gradually as applied strain increases. An approximately linear relationship is observed between the resonance frequency and strain. The simulated strain sensitivity is –802 Hz/με for the folded patch antenna sensor, while the normalized strain sensitivity is –0.8928. The average simulation time for each frequency point is about 500 seconds.

The mechanics-electromagnetics coupled simulation is also performed in the slotted patch antenna sensor design. During the coupled simulation, the strain distribution

on the top copper cladding is first evaluated. The surface current density plots show that the current detours along the slots and vias, which fulfill the sensor size reduction by current detouring while maintaining the sensor resonance frequency around 900 MHz. The simulated normalized strain sensitivity is –0.784 for the passive slotted patch antenna sensor, which is slightly lower than the folded patch antenna sensor. The average simulation time for each frequency point is about 500 seconds. The active slotted patch antenna sensor is similarly simulated in COMSOL. The overall dimension of the active patch antenna sensor is the same as the passive slotted patch antenna sensor, but the interrogation distance of the active slotted patch antenna sensor is expected to be larger due to integration of the active RFID chip. The simulated normalized strain sensitivity of the active slotted patch antenna sensor is –0.7672, which is close to the results of passive slotted patch antenna sensor.

The multi-physics simulation of 2.9 GHz$\rightarrow$5.8 GHz frequency doubling antenna sensor is performed by combining functionalities in COMSOL and ADS. The sensor-side 2.9 GHz receiving patch antenna is first simulated in COMSOL with mechanics-electromagnetics coupled simulation. The strain-induced antenna port impedance variations are then extracted and used as input port impedance of the matching network simulation in ADS. The harmonic balance simulation is thus performed in the ADS and the output power at the second harmonic of the input frequency is evaluated. The related voltages from the output port of the matching network are then used as the input port voltage of the sensor-side 5.8 GHz transmitting patch antenna simulation in COMSOL. The overall mechanics-AC/DC-electromagnetics coupled simulation shows an approximately relationship between resonance frequency shifts of the sensor and applied strain on the 2.9 GHz patch antenna. The simulated strain sensitivity of the frequency doubling sensor is about five times higher than the RFID antenna sensor, including folded patch antenna and passive/active slotted patch antennas. Since the frequency doubling sensor is designed to prove the concept, the dimension of the frequency doubling sensor

is relatively large comparing with RFID antenna sensor. The dimension of the frequency doubling sensor can be further reduced by introducing extra vias like folded patch antenna sensor in Section 3.3.1 or slots like slotted patch antenna sensor in Section 3.3.2. For further performance improvement, three more frequency doubling antenna sensors are designed and the sensor layouts are also presented.

Although the coupled simulation provides improved simulation accuracy in the frequency domain solver compared with simple scaling results, the simulation efficiency is limited. During the frequency domain simulation, it is necessary to simulate many frequency points in a relatively large frequency span in order to determine the sensor resonance frequency point. The overall simulation time is roughly proportional to the number of strain steps and number of simulated frequency points. To alleviate the long computation time problem, the determination of sensor resonance frequency can be formulated as an eigenvalue problem. Instead of simulating the sensor in a large frequency span, the resonance frequency of the antenna sensor can be determined by solving the eigenvalue problem of the antenna sensor. Since we are only interested in one antenna resonance frequency, it is promising to improve simulation efficiency by solving eigenvalue problem. The antenna sensor design is formulated as an eigenvalue problem in the next chapter. To further improve the simulation efficiency while maintaining simulation accuracy from the coupled simulation, several eigenvalue perturbation techniques will also be discussed in the next chapter. Instead of solving the eigenvalue problem at every simulated strain step, the eigenvalue perturbation methods are adopted to update the sensor resonance frequency based on the results from an adjacent strain step.

The performance of the fabricated RFID antenna sensors, as well as the frequency doubling antenna sensors, is validated by extensive experiments. The performance indexes include strain sensing resolution, range, interrogation distance, emulated crack

detection, fatigue crack detection, *etc*. Relevant experimental results are summarized and presented in CHAPTER 5.

CHAPTER 4 EIGENVALUE PERTURBATION FOR EFFICIENT STRAIN SENSING SIMULATION

As described in previous chapter, the electromagnetic simulation of antenna sensors is typically conducted in frequency domain. The resonance frequency of an antenna is determined by sweeping through a large frequency range and identifying the minimum point from the reflection coefficient (S_{11}) plots. At the beginning of a sensor design, the frequency domain solver is necessary for checking the antenna radiation performance. However, it is time consuming and inefficient when frequency domain simulation is needed for many strain levels. This chapter proposes to simulate strain sensitivity of an antenna through a perturbed eigenvalue problem. Resonance frequency is extracted from the eigenvalue formulation of a finite element model of the antenna. Resonance frequencies at different strain steps are identified by soling perturbed eigenvalue problems of the deformed finite element models.

Section 4.1 first presents the finite element formulation for the eigenvalue problem. Several eigenvalue perturbation methods are then introduced in Section 4.2 and applied to the eigenvalue problem formulated in Section 4.1. Instead of solving a brand new eigenvalue problem at each strain step from scratch, the eigenvalues at next strain step is calculated based upon eigensolutions from previous strain step. The computed eigenvalues can be easily transformed to resonance frequency of antenna sensors through their inherent relationship. Section 4.2 explores two eigenvalue perturbation techniques, the first-order eigenvalue perturbation method and the inverse Rayleigh quotient iteration method followed by discussions of the perturbation flowchart, which elaborates the procedure of determining eigenvalues at current strain step based upon eigensolutions from previous strain steps by eigenvalue perturbation methods. Section 4.3 shows the eigenvalue perturbation results of a 2D dipole antenna and a slotted patch antenna sensor. The results are summarized and discussed in Section 4.4.

4.1 Finite Element Formulation of the Eigenvalue Problem

This section proposes finite element formulation of the eigenvalue problem for antenna sensor designs. Section 4.1.1 introduces finite element formulation. Section 4.1.2 provides frequency domain solution of the antenna sensor simulation, while Section 4.1.3 provides eigenfrequency solution for the same problem. Section 4.1.4 shows a comparison between frequency domain and eigenfrequency domain solution of the folded patch antenna sensor presented in Section 3.3.1.

4.1.1 Finite Element Formulation

For simulating the antenna sensor, Fig. 4.1 illustrates the domain involving an antenna sensor, an air sphere, and perfectly matched layer (PML). An antenna sensor usually includes a metallic surface and a dielectric substrate, which is used to separate the metallic surface from monitored structural surface. The metallic surface is usually modeled as perfect electric conductor (PEC). The boundary of the metallic surface is denoted as S_{PEC}, whose direction is $\hat{n}$. The volume of the dielectric substrate is denoted as V_d and the substrate relative permittivity and permeability are μ_r and β_r, respectively. Besides the PEC boundary, the simulation model may also include impedance sheet due to material losses. The surface of the impedance sheet is denoted as S_K. The whole antenna sensor is placed inside an air sphere, whose permittivity and permeability are μ_0 and β_0, respectively. Since a resonant antenna model is an open structure that has no definite physical boundaries, it is necessary to set termination boundaries so that the simulation domain is finite. The combination of PML and perfect electric conductor (PEC) is adopted in the 3D electromagnetic simulation. PML is a very effective absorbing medium, which is reflectionless for all incident angles, frequencies, and polarization [83]. There are various interpretations of the PML, its extension, and

generalization [84-91]. In this research, the PML medium is interpreted as coordinate stretching [84, 92], which is also adopted in the COMSOL formulation [37].

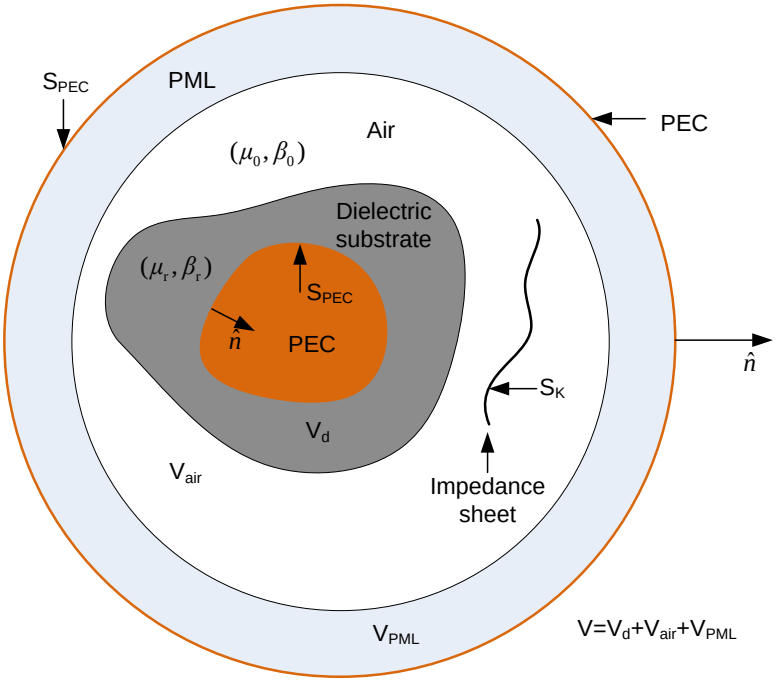

Fig. 4.1. Inhomogeneous structure enclosed by mesh termination boundaries (PML and PEC)

The Maxwell's equations in an inhomogeneous material have the general vector form [29, 93]:

$$\begin{aligned} \nabla_s \times \mathbf{E} &= -\mathrm{j}\tilde{\omega}\mu\mathbf{E} \\ \nabla_s \times \mathbf{H} &= \mathrm{j}\tilde{\omega}\beta\mathbf{H} + \mathbf{J} \\ \nabla_s \cdot (\beta\mathbf{E}) &= 0 \\ \nabla_s \cdot (\mu\mathbf{H}) &= 0 \end{aligned} \tag{4.1}$$

where $\mathbf{E} = E_x\hat{x} + E_y\hat{y} + E_z\hat{z}$ is the electric field; $\mathbf{H} = H_x\hat{x} + H_y\hat{y} + H_z\hat{z}$ is the magnetic field; $\mathbf{J}$ is the current vector; μ and β are the permeability and permittivity of the material, respectively; $\tilde{\omega}$ is the angular frequency; ∇_s is defined as [29]:

$$\nabla_s = \hat{x}\frac{1}{s_x}\frac{\partial}{\partial x} + \hat{y}\frac{1}{s_y}\frac{\partial}{\partial y} + \hat{z}\frac{1}{s_z}\frac{\partial}{\partial z} \tag{4.2}$$

According to Eq. (4.2), ∇_s is generally a standard curl (∇) operator in Cartesian coordinates whose *x*, *y*, and *z* are stretched by a factor of s_x, s_y, and s_z. The three stretching factors equal to one within the air and substrate domain. In this case, ∇_s is the same as standard ∇ operator and has no stretching behavior. The factors s_x, s_y, and s_z are complex number when the considered position is located inside the PML medium.

According to Ritz method, a functional for the total electric field can be expressed through a volume integral after considering boundary conditions of the simulation model [30, 94, 95]:

$$\begin{aligned} F = \int_V \left[\frac{1}{\mu}(\nabla_s \times \mathbf{E}) \cdot (\nabla_s \times \mathbf{E}) + \left(j\tilde{\omega} \right)^2 \beta \mathbf{E} \cdot \mathbf{E} \right] dv + \mathrm{j}\tilde{\omega}\mu_0 \int_{S_\mathrm{K}} \frac{1}{R_\mathrm{K}} \left[(\hat{n} \times \mathbf{E}) \cdot (\hat{n} \times \mathbf{E}) \right] dS \\ + \int_{S_0} \left[\mathbf{E} \cdot (\hat{n} \times \nabla_s \times \mathbf{E}) \right] dS + \int_V \mathbf{E} \cdot \mathbf{f}^i dv \end{aligned} \tag{4.3}$$

where μ_0 (=$4\pi\times10^{-7}$ N/A^2) is the air permeability. Due to the existence of PML and complex coordinate stretching factors, the angular frequency $\tilde{\omega}$ (=ω+jα) is a complex numbers as well. Here α is the exponential decay rate due to PML. R_K is the surface impedance on the impedance sheet S_K. S_0 denotes the surfaces within volume *V* for which the tangential component of electric field **E** and/or magnetic field **H** is discontinuous. $\mathbf{f}^i$ denotes the sources in the model. In finite element method, the whole solution domain is discretized into a finite number of elements. Each element occupies a separate volume V^e (e = 1, 2, …, $\mathrm{N_T}$), where $\mathrm{N_T}$ is the total number of elements. For each element, different 3D element types can be assigned, such as four-node tetrahedral element, eight-node hexahedral element, *etc*. The electric field can then be denoted in a vector form in terms of the polynomial basis functions $\mathbf{N}_i^e$ over a general *m*-edge finite element [29]:

$$\mathbf{E}^e = \sum_{i=1}^{m} E_i^e \mathbf{N}_i^e \tag{4.4}$$

where $\mathbf{N}_i^e$ is the *i*-th edge based vector basis function of element *e*; *m* is the total edge number of one element; E_i^e is the tangential electric field along the *i*-th edge of element *e*. Substituting Eq.(4.4) into Eq.(4.3), integrating over the volume of one element, and deriving according to variational principle, the following equation can be obtained [30]:

$$(\mathrm{j}\tilde{\omega})^2 \sum_{e=1}^{\mathrm{N_T}} \left[T^e\right]\left\{E^e\right\} + (\mathrm{j}\tilde{\omega}) \sum_{e=1}^{\mathrm{N_T}} \left[R^e\right]\left\{E^e\right\} + \sum_{e=1}^{\mathrm{N_T}} \left[C^e\right]\left\{E^e\right\} = \sum_{e=1}^{\mathrm{N_T}} \left\{\mathrm{f}^e\right\} \tag{4.5}$$

where $\left[C^e\right]$, $\left[R^e\right]$, and $\left[T^e\right]$ are elementary inductance, damping, and capacitance matrix, respectively; f^e is the source term due to incident voltage or current excitation at the port. The elements of the matrix $\left[C^e\right]$, $\left[R^e\right]$, and $\left[T^e\right]$ are given by

$$\begin{aligned} C_{ij}^e &= \int_{V^e} \frac{1}{\mu} \left(\nabla_s \times \mathbf{N}_i^e\right) \cdot \left(\nabla_s \times \mathbf{N}_j^e\right) dv \\ R_{ij}^e &= \mu_0 \left[\int_{S_0^e} \mathbf{N}_i^e \cdot \left(\hat{n} \times \mathbf{H}\right) dS - \int_{S_\mathrm{K}^e} \frac{1}{R_\mathrm{K}} \left(\hat{n} \times \mathbf{N}_i^e\right) \cdot \left(\hat{n} \times \mathbf{N}_i^e\right) dS \right] \\ T_{ij}^e &= \int_{V^e} \beta \mathbf{N}_i^e \cdot \mathbf{N}_j^e dv \end{aligned} \tag{4.6}$$

where S^e is the boundary of element *e*; S_K^e is the surface of element *e* on the impedance sheet.

4.1.2 Frequency Domain Solution

If incident wave is introduced to the simulation domain by voltage or current excitation at the feeding port as shown in Eq. (4.5), the problem becomes wave propagation and scattering. The source term $\{\mathrm{f}^e\}$ in Eq. (4.5) is nonzero and the excitation frequency $\tilde{\omega}$ are given. The electric field can be calculated based on the known $\left[C^e\right]$, $\left[R^e\right]$, and $\left[T^e\right]$, and excitation voltage/current. Based on the electric field

solution $\{E\}$ (or **E** in vector form), the magnetic field distribution can be found from Maxwell's equation:

$$\mathbf{H} = \frac{1}{-\mathrm{j}\tilde{\omega}\mu_0} \nabla \times \mathbf{E} \tag{4.7}$$

Based on the computed electric and magnetic field distributions, the antenna voltage and current calculated at the port are given by [96]:

$$V_{\mathrm{a}} = \int_1^2 \vec{E} \cdot d\vec{l} \tag{4.8a}$$

$$I_{\mathrm{a}} = \int_C \vec{H} \cdot d\vec{l} \tag{4.8b}$$

where 1 and 2 are two feeding points of the antenna; *C* is the cross-sectional contour of the antenna feeds. The antenna impedance can be simply found as:

$$Z_{\mathrm{a}} = \frac{V_{\mathrm{a}}}{I_{\mathrm{a}}} \tag{4.9}$$

Once the antenna impedance is known according to the field distributions, the reflection coefficient between the port and the antenna (S_{11}) is calculated as [96]:

$$S_{11} = \frac{Z_{\mathrm{a}} - Z_{\mathrm{p}}}{Z_{\mathrm{a}} + Z_{\mathrm{p}}} \tag{4.10}$$

where Z_{p} is the impedance of the feeding port, which equals to the IC chip impedance in the antenna sensor simulation and standard port impedance of 50 Ω set in the frequency doubling sensor simulation. Eq. (4.10) is basically another form of Eq. (3.11), which gives same physical meaning.

4.1.3 Eigenfrequency Solution

If no excitation is considered, then the source term $\{\mathrm{f}^e\}$ in Eq. (4.5) is ignored. The equation can be rewritten as [29]:

$$(\mathrm{j}\tilde{\omega})^2 \sum_{e=1}^{\mathrm{N_T}} \left[T^e\right]\left\{E^e\right\} + (\mathrm{j}\tilde{\omega}) \sum_{e=1}^{\mathrm{N_T}} \left[R^e\right]\left\{E^e\right\} + \sum_{e=1}^{\mathrm{N_T}} \left[C^e\right]\left\{E^e\right\} = \{0\} \tag{4.11}$$

The above equation can be further simplified as:

$$\lambda^2 [\mathrm{T}]\{\mathrm{E}\} + \lambda [\mathrm{R}]\{\mathrm{E}\} + [\mathrm{C}]\{\mathrm{E}\} = \{0\} \tag{4.12}$$

where $\lambda = \mathrm{j}\tilde{\omega}$; [C] is named as inductance matrix; [T] is named as capacitance matrix, while [R] is the damping matrix. The final formulation in Eq. (4.12) ends up with a quadratic eigenvalue problem [94, 97]. Using N to denote the total number of degrees of freedom in Eq. (4.12), [C] and [R] are N × N complex symmetric matrices, while [T] is an N × N symmetric matrix,. Since the entry T_{ij}^e in Eq. (4.6) includes material permittivity β, which is a small number on the order of 10^{-12}, the magnitudes of T_{ij}^e as well as entries in global matrix [T] are small. The entry R_{ij}^e in Eq. (4.6) is also small due to small magnitude of μ_0. With small-magnitude entries in [R] and [T], the matrices are usually ill-conditioned. To improve the condition number of the two matrices, scaling can be performed. To this end, Eq. (4.12) is reformulated as:

$$\tilde{\lambda}^2 \left[\mathrm{T}^s\right]\{\mathrm{E}\} + \tilde{\lambda} \left[\mathrm{R}^s\right]\{\mathrm{E}\} + [\mathrm{C}]\{\mathrm{E}\} = 0 \tag{4.13}$$

where

$$\left[\mathrm{R}^s\right] = \sqrt{s}[\mathrm{R}]; \qquad \left[\mathrm{T}^s\right] = s[\mathrm{T}]; \qquad \tilde{\lambda} = \lambda/\sqrt{s} \tag{4.14}$$

Here s is the scaling factor on the order of 10^{18}. Eq. (4.13) also shows that the eigenvalue problem is a quadratic eigenvalue problem with complex matrices. Instead of directly solving the quadratic eigenvalue problem as in Eq. (4.12), state-space formulation equivalently converts Eq. (4.13) into a generalized eigenvalue problem:

$$[\mathrm{A}]\{\Phi\} = \tilde{\lambda}[\mathrm{B}]\{\Phi\} \tag{4.15}$$

where

$$[\mathrm{A}] = \begin{bmatrix} -[\mathrm{C}] & [0] \\ [0] & [\mathrm{I}] \end{bmatrix}, \quad [\mathrm{B}] = \begin{bmatrix} [\mathrm{R}^s] & [\mathrm{T}^s] \\ [\mathrm{I}] & [0] \end{bmatrix}, \qquad \{\Phi\} = \begin{Bmatrix} \{\mathrm{E}\} \\ \tilde{\lambda}\{\mathrm{E}\} \end{Bmatrix} \tag{4.16}$$

[I] is an N×N identity matrix and [0] is an N×N zero matrix. The identity matrix [I] can also be replaced by any other nonsingular matrix. For example, if matrix $[\mathrm{T}^s]$ is nonsingular and replaces the identity matrices in Eq. (4.16), then both [A] and [B] can be formulated to be symmetric:

$$[\mathrm{A}] = \begin{bmatrix} -[\mathrm{C}] & [0] \\ [0] & [\mathrm{T}^s] \end{bmatrix}, \quad [\mathrm{B}] = \begin{bmatrix} [\mathrm{R}^s] & [\mathrm{T}^s] \\ [\mathrm{T}^s] & [0] \end{bmatrix}, \qquad \{\Phi\} = \begin{Bmatrix} \{\mathrm{E}\} \\ \tilde{\lambda}\{\mathrm{E}\} \end{Bmatrix} \tag{4.17}$$

The choice of the nonsingular matrix in [A] and [B] is determined by the properties of matrix [C], [R], and [T].

The eigenvalue $\tilde{\lambda}$ is closely related with resonance frequency of the antenna sensor f_{R} according to the following equation:

$$\tilde{\lambda} = \frac{\mathrm{j}\tilde{\omega}}{\sqrt{s}} = \frac{\mathrm{j}\omega - \alpha}{\sqrt{s}} = \frac{\mathrm{j}2\pi f_{\mathrm{R}} - \alpha}{\sqrt{s}} \tag{4.18}$$

As described in Section 2.1, the resonance frequency f_{R} is a key parameter [10] determining the strain effects of the antenna sensor. Associated with every eigenvalue $\tilde{\lambda}$ is eigenvector $\{\mathrm{E}\}$, representing for the electric field distribution of the antenna sensor simulation at each eigenmode. The plot of $\{\mathrm{E}\}$ field is an intuitive way to check the correctness of the antenna mode. Furthermore, the quality factor (Q) of the antenna sensor can be defined as [29]:

$$Q = \left| \frac{\omega}{2\alpha} \right| \tag{4.19}$$

Since the solution domain includes not only the antenna sensor structure, but also air sphere and PML, the calculated eigenmodes can be antenna mode and spurious mode,

which is due to the existence of PEC and PML boundary conditions [30]. If the calculated eigenmode is an antenna mode, a large Q is expected. Otherwise, Q is smaller due to large decay rate α caused by the boundary conditions. Therefore, Q is another indicator to distinguish antenna mode and spurious mode.

4.1.4 Comparison between Frequency Domain and Eigenfrequency Solutions

To validate the relationship between frequency domain results S_{11} and eigenfrequency results, the eigenfrequency solver in COMSOL is adopted to simulate the folded patch antenna sensor. The mechanical simulation of the antenna sensor structure is performed following the coupled simulation procedures described in Section 3.1. The deformed meshes are then transformed to the eigenfrequency domain solver for eigenfrequency calculation. The eigenfrequency solver is set to search eigenfrequencies close to 900 MHz, instead of solving all eigenfrequencies of the antenna sensor. After the computation, the related eigenfrequencies are plotted against applied strain in Fig. 4.2. The calculated resonance frequency of the folded patch antenna sensor from eigenfrequency solver is 911.58 MHz, which is 911.7 MHz from the frequency domain solver. The normalized strain sensitivity is –0.9012 ppm/με, which means 1 με strain experienced by the folded patch antenna introduces 0.9012 ppm decrease in resonance frequency. The normalized strain sensitivity is close to the simulation results from frequency domain solver in Section 3.3.1. The closely matched results between frequency domain solver and eigenfrequency solver validate the feasibility to compute sensor resonance frequency f_R according to eigenvalue problem formulation presented in Eq. (4.15). With same simulation model, the average computation time for one eigenfrequency is about 316 seconds. The total computation time is roughly proportional to number of strain steps and number of eigenfrequencies calculated. In this study with five strain steps and one eigenfrequency calculated, the total computing time is 4,827

seconds, which give much better simulation efficiency compared with the frequency domain solver. As presented in Section 3.3.1, the frequency domain solver consumes 455,216 seconds. However, the computation in the eigenfrequency solver requires about 12 GB memory, which means more hardware resources are required for eigenfrequency solver.

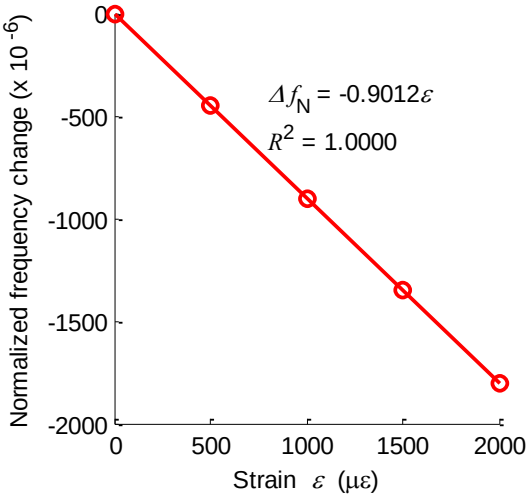

Fig. 4.2. Normalized resonance frequency change Δf_N versus strain ε of folded patch antenna sensor simulated from eigenfrequency solver (f_{R0} = 911.58 MHz)

4.2 Eigenvalue Perturbation Approaches for Strain Sensing Simulation

In a mechanics-electromagnetics coupled simulation, the matrices are updated at each strain level, which entails large amount of meshing and computation efforts. Furthermore, matrices [C], [R], and [T] usually have large dimensions, which greatly increase difficulty in eigenvalue computation. In order to further improve simulation efficiency, it is proposed to investigate eigenvalue perturbation approaches for efficiently solving Eq. (4.12) at gradually varying strain levels. Specifically, the proposed concept is to use the eigenvalues and eigenvectors in a previous strain level as the initial solution of current strain level. In other words, instead of starting from scratch, eigenvalue computation for next strain step can use results of the previous as an initial starting point,

by viewing strain effect as perturbations to the system matrices. This section first describes two eigenvalue perturbation approaches, namely the first-order eigenvalue perturbation method and the inverse Rayleigh quotient iteration method. The flowchart describing the whole perturbation process for determining resonance frequency of antenna sensors at all strain levels is then provided.

4.2.1 Review to Eigenvalue Perturbation Techniques

Eigenvalue computation is a rather active field due to its broad application to many engineering problems [43, 98]. As shown in Eq. (4.15), the multi-physics simulation problem in this research requires solving a generalized eigenvalue problem that involves three system matrices. Iteration methods, such as successive over-relaxation (SOR) method [99] and the conjugate gradient method [100], can be applied to search the eigenvalues. For large sparse and symmetric matrices [A] and [B], Lanczos method can transform the problem into the eigenvalue problem of a tri-diagonal matrix, for which efficient algorithms exist [43, 101]. A well-known method for large sparse non-symmetric eigenvalue problems is the implicitly restarted Arnoldi method [102], which has been implemented in the ARPACK software [103]. The ARPACK solver can be further integrated with other linear solver packages for solving sparse matrix systems, such as MUMPS (multifrontal parallel distributed symmetric and unsymmetric solver) [104-106], SPOOLES (sparse object oriented linear equations solver) [107], PARDISO [108-110], UMFPACK (unsymmetric multifrontal sparse LU factorization package) [111], *etc*. An extensive comparison between these solvers can be found in [112-114].

In the strain sensing simulation, since changes of system matrices [A] and [B] between neighboring strain levels are expected to be small, eigenvalue perturbation is a potentially effective approaching for solving the problem [115]. Instead of solving the entire eigenvalue problem from scratch, the eigenvalues and eigenvectors for current

strain level can be updated according to results from previous strain level. The approach can save computation time and effort by utilizing previous results. Among eigenvalue perturbation techniques, first order perturbation theory has been adopted for different regular matrix pairs [115], which provides enough accuracy in most engineering applications when perturbation is small. The first-order eigenvalue perturbation method has been applied for structural damage detection [116, 117] and structural dynamic modification [118]. Other techniques based upon first-order eigenvalue perturbation (FOP) method are also proposed and detailed comparisons can be found in [42, 119, 120]. When perturbation is large, Rayleigh quotient iteration (RQI) [121, 122] or homotopy method [44] can be implemented to further improve the calculation accuracy, while avoiding calculation of higher order perturbation items. In this research, both first-order eigenvalue perturbation method and inverse Rayleigh quotient iteration method will be investigated.

4.2.2 First-order Eigenvalue Perturbation (FOP) Method

Denote coefficient matrices at previous strain level ε_j as $[A_j]$ and $[B_j]$, and $[A_{j+1}]$ and $[B_{j+1}]$ as coefficient matrices at current strain ε_{j+1}. These matrices can be non-symmetric and complex, according to the formulations in Eq. (4.16). Relationship between coefficient matrices at two strain levels can be described as:

$$[A_{j+1}] = [A_j] + [\Delta A_j] \tag{4.20a}$$

$$[B_{j+1}] = [B_j] + [\Delta B_j] \tag{4.20b}$$

where $[\Delta A_j]$ and $[\Delta B_j]$ are (small) difference matrices between two adjacent strain steps ε_j and ε_{j+1}. The eigenvalue problems of the original and perturbed systems are:

$$[A_j][\Phi_j] = [B_j][\Phi_j][\Lambda_j] \tag{4.21a}$$

$$[A_j]^T[\Psi_j] = [B_j]^T[\Psi_j][\Lambda_j] \tag{4.21b}$$

$$[A_{j+1}][\Phi_{j+1}] = [B_{j+1}][\Phi_{j+1}][\Lambda_{j+1}] \tag{4.21c}$$

$$[A_{j+1}]^T[\Psi_{j+1}] = [B_{j+1}]^T[\Psi_{j+1}][\Lambda_{j+1}] \tag{4.21d}$$

where columns of $[\Phi_j]$ and $[\Psi_j]$ are right and left eigenvectors of the system matrices at previous strain level, and $[\Lambda_j]$ is a diagonal matrix whose diagonal entries are the eigenvalues. $[\Phi_{j+1}]$, $[\Psi_{j+1}]$, and $[\Lambda_{j+1}]$ contain right, left eigenvectors, and eigenvalues of the perturbed system. Due to orthogonality of eigenvectors, only M (<<N) modes are used in the perturbation process. The value of M will be determined in the specific examples. The dimensions of $[\Phi_j]$, $[\Psi_j]$, $[\Phi_{j+1}]$, and $[\Psi_{j+1}]$ are $2N \times M$, while dimensions of $[\Lambda_j]$ and $[\Lambda_{j+1}]$ are $M \times M$.

According to the first-order eigenvalue perturbation theory, a perturbed eigenvalue and eigenvector pair at strain ε_{j+1} can be formulated based on previous results [123]:

$$[\Lambda_{j+1}] = [\Lambda_j] + diag([P]) \tag{4.22a}$$

$$[\Phi_{j+1}] = [\Phi_j]([I] + [U]) \tag{4.22b}$$

$$[\Psi_{j+1}] = [\Psi_j]([I] + [V]) \tag{4.22c}$$

where [I] is an $M \times M$ identity matrix; *diag* denotes extraction of diagonal terms of matrix [P]; $[U]$ and $[V]$, which have dimensions of $M \times M$, are the first-order perturbation terms for right and left eigenvectors $[\Phi_j]$ and $[\Psi_j]$; the (*m*, *n*) entry of matrices $[U]$ and $[V]$ is calculated as:

$$U_{mn} = \frac{1}{\lambda_j^n - \lambda_j^m} P_{mn} \tag{4.23a}$$

$$V_{mn} = \frac{1}{\lambda_j^n - \lambda_j^m} R_{mn} \tag{4.23b}$$

$$[\mathrm{P}] = [\Psi_j]^{\mathrm{T}} \left(-[\Delta \mathrm{A}_j][\Phi_j] + [\Delta \mathrm{B}_j][\Phi_j][\Lambda_j] \right) \tag{4.23c}$$

$$[\mathrm{R}] = [\Phi_j]^{\mathrm{T}} \left(-[\Delta \mathrm{A}_j]^T[\Psi_j] + [\Delta \mathrm{B}_j]^T[\Psi_j][\Lambda_j] \right) \tag{4.23d}$$

where [P] and [R] both have dimensions of M×M. Without any further electromagnetic field computation, the eigenfrequency f_{R} and electric field distribution $\{\mathrm{E}^i_{j+1}\}$ (i.e. first half of eigenvector $\{\Phi^i_{j+1}\}$) at strain level ε_{j+1} can be easily updated according to Eq. (4.18), (4.22), and (4.23).

On the other hand, if symmetric [A] and [B] formulations in Eq. (4.17) are adopted, the FOP method in Eq. (4.22), and (4.23) can be simplified. The left eigenvectors $[\Psi]$ equal to right eigenvectors $[\Phi]$, so only matrices $[\mathrm{U}]$ in Eq. (4.23a) and [P] in Eq. (4.23c) need to be updated at each strain step.

If the perturbation is small, the FOP method can usually give accurate results. However, the FOP may give inaccurate results when the perturbation is relatively large. Under large perturbation step, the RQI can be an option.

4.2.3 Inverse Rayleigh Quotient Iteration (RQI) Method

The basic inverse RQI is shown in Fig. 4.3 [124, 125]:

for k = 1, 2, …

solve $[\mathrm{A}]\left\{x^{(\mathrm{k})}\right\} = [\mathrm{B}]\{q^{(\mathrm{k}-1)}\}$ for $\left\{x^{(\mathrm{k})}\right\}$;

$$\{q^{(\mathrm{k})}\} = \frac{\left\{x^{(\mathrm{k})}\right\}}{\left\|\left\{x^{(\mathrm{k})}\right\}\right\|};$$

$$\lambda^{(\mathrm{k})} = \frac{\{q^{(\mathrm{k})}\}^{\mathrm{H}}[\mathrm{A}]\{q^{(\mathrm{k})}\}}{\{q^{(\mathrm{k})}\}^{\mathrm{H}}[\mathrm{B}]\{q^{(\mathrm{k})}\}};$$

end

Fig. 4.3. Basic inverse RQI routine

where k is iteration number. The iteration gives smallest eigenvalue of the generalized eigenvalue problem in Eq. (4.15). To find the interested eigenfrequency for an antenna resonance mode, it is necessary to modify the shifted version of inverse RQI. As described in Eq. (4.16) and (4.17), there are symmetric and non-symmetric formulations of [A] and [B]. If both matrices are symmetric as in (4.17), the inverse RQI can be formulated accordingly. Denote $\tilde{\lambda}_j$ and $\tilde{\lambda}_{j+1}$ as the shifted eigenvalues at strain ε_j and ε_{j+1}; $\{\Phi_j\}$ and $\{\Phi_{j+1}\}$ as the right eigenvectors at strain ε_j and ε_{j+1}; $[\mathrm{A}_{j+1}]$ as the matrix [A] at strain ε_{j+1}; $[\mathrm{B}_{j+1}]$ as the matrix [B] at strain ε_{j+1}. The inverse RQI with shifted eigenvalue routine is shown in Fig. 4.4 [121]:

$\mu = \tilde{\lambda}_j; \qquad \{q\} = \{\Phi_j\};$

do {

$\quad$ solve $\left([\mathrm{A}_{j+1}] - \tilde{\lambda}_j [\mathrm{B}_{j+1}]\right)\{x\} = [\mathrm{B}_{j+1}]\{q\}$ for $\{x\}$;

$$\{q\} = \frac{\{x\}}{\|\{x\}\|};$$

$$\mu = \frac{\{q\}^{\mathrm{H}}[\mathrm{A}_{j+1}]\{q\}}{\{q\}^{\mathrm{H}}[\mathrm{B}_{j+1}]\{q\}};$$

$$\text{error} = \frac{\left\|[\mathrm{A}_{j+1}]\{q\} - \mu[\mathrm{B}_{j+1}]\{q\}\right\|}{\left\|[\mathrm{A}_{j+1}]\right\| + \left\|\mu[\mathrm{B}_{j+1}]\right\|};$$

while (error > tolerance)

$\tilde{\lambda}_{j+1} = \mu;$

$\{\Phi_{j+1}\} = \{q\}.$

Fig. 4.4. Inverse RQI routine for symmetric [A] and [B] formulations

On the other hand, if non-symmetric formulations of [A] and [B] in Eq. (4.17) are adopted, the inverse RQI routine can be modified accordingly. Under this circumstance, both left and right eigenvectors need to be computed for iteration. Denote $\{\Psi_j\}$ and

$\{\Psi_{j+1}\}$ as the right eigenvectors at strain ε_j and ε_{j+1}. The Rayleigh quotient iteration for non-symmetric generalized eigenvalue problem is formulated as below [122, 126]:

$\mu = \tilde{\lambda}_j; \qquad \{q\} = \{\Phi_j\}; \qquad \{p\} = \{\Psi_j\};$

do {

solve $\left([\mathrm{A}_{j+1}] - \mu[\mathrm{B}_{j+1}]\right)\{x\} = [\mathrm{B}_{j+1}]\{q\}$ for $\{x\}$;

solve $\left([\mathrm{A}_{j+1}] - \mu[\mathrm{B}_{j+1}]\right)^{\mathrm{H}}\{y\} = [\mathrm{B}_{j+1}]^{\mathrm{H}}\{p\}$ for $\{y\}$;

$$\{q\} = \frac{\{x\}}{\|\{x\}\|};$$

$$\{p\} = \frac{\{y\}}{\|\{y\}\|};$$

$$\mu = \frac{\{p\}^{\mathrm{H}}[\mathrm{A}_{j+1}]\{q\}}{\{p\}^{\mathrm{H}}[\mathrm{B}_{j+1}]\{q\}};$$

$$\text{error} = \frac{\|[\mathrm{A}_{j+1}]\{q\} - \mu[\mathrm{B}_{j+1}]\{q\}\|}{\|[\mathrm{A}_{j+1}]\| + \|\mu[\mathrm{B}_{j+1}]\|};$$

while (error > tolerance)

$\tilde{\lambda}_{j+1} = \mu;$

$\{\Phi_{j+1}\} = \{q\};$

$\{\Psi_{j+1}\} = \{p\}.$

Fig. 4.5. Inverse RQI routine for non-symmetric [A] and [B] formulations

While the inverse RQI method can be more robust, it requires solving linear equations and more iteration steps, and thus more computation time compared with FOP method. Both methods will be studied for simulating antenna sensor behavior under strain. Their perturbation efficiency and accuracy will be compared.

4.2.4 COMSOL-MATLAB Flowchart for Eigenvalue Perturbation

The antenna sensor models can be easily built in COMSOL through user friendly GUI interface, but it is not convenient to implement customized eigenvalue or linear solvers into COMSOL GUI interface. Instead, COMSOL Livelink for MATLAB allows to be opened in MATLAB, so that the customized solvers can be applied to COMSOL-generalized matrices in electromagnetic domain.

Fig. 4.6 shows the COMSOL-MATLAB communication process using eigenvalue perturbation techniques for updating sensor resonance frequencies at multiple strain levels. The simulation model is first built in COMSOL GUI interface with proper mechanical and electromagnetic boundary conditions. Matrices $[C_0]$, $[R_0]$, and $[T_0]$ in Eq. (4.12) are formulated in COMSOL and transferred to MATLAB. These matrices are then used to construct $[A_0]$ and $[B_0]$ according to Eq. (4.16) or (4.17). The eigenvalue λ_0 and eigenvector $\{\Phi_0\}$ are calculated through eigenvalue solver at zero strain level ε_0.

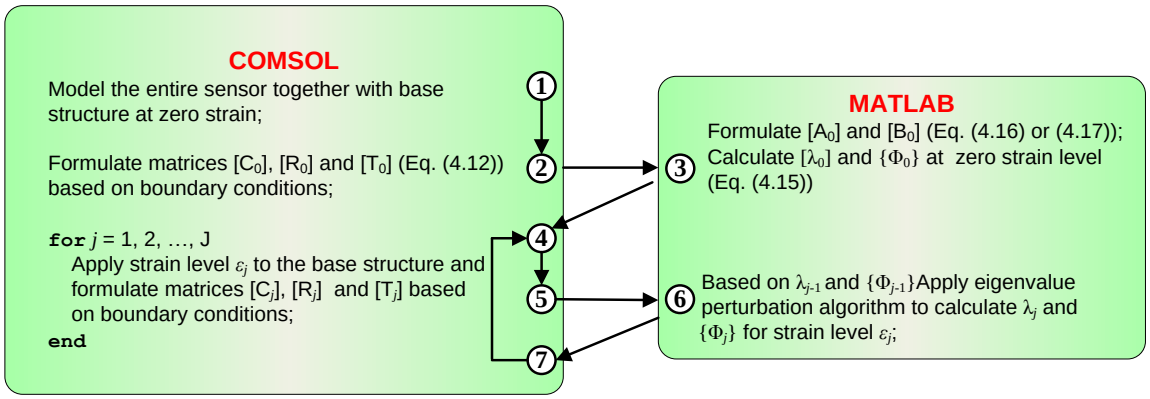

Fig. 4.6. COMSOL-MATLAB communication

After the simulation at zero strain level, the antenna structure subjects to loading that generates matrices for next strain level ε_j. The corresponding system matrices $[A_j]$ and $[B_j]$ again constructed. Eigenvalue perturbation methods can then be applied to calculate the eigenvalue λ_j and eigenvector $\{\Phi_j\}$ at strain ε_j in MATLAB. The updated

eigenvalues λ_j and eigenvectors $\{\Phi_j\}$ are taken as the basis for next perturbation at strain ε_{j+1}. The updating process continues for all required strain levels. In the end, the relationship between resonance frequency and applied strain is plotted in MATLAB.

4.3 Validation Examples

To validate the accuracy and efficiency of the proposed eigenvalue perturbation techniques, two examples are investigated. Section 4.3.1 presents a 2D dipole antenna example. Both first-order eigenvalue perturbation and inverse Rayleigh quotient iteration methods are studied and compared in terms of perturbation accuracy and efficiency. Section 4.3.2 presents perturbation results of a 3D model of the slotted patch RFID antenna sensor (Section 3.3.2).

4.3.1 2D Dipole Antenna

In this example, Section 4.3.1.1 first describes the 2D dipole antenna model. Section 4.3.1.2 presents simulation results from frequency domain and eigenfrequency solvers in COMSOL. Section 4.3.1.3 shows the perturbation result comparison between four solution methods, including two `eigs` solution methods with different starting vectors, FOP, and RQI.

4.3.1.1 Model description

A smaller 2D axi-symmetric dipole example is first analyzed to validate the eigenvalue perturbation algorithms. Fig. 4.7 shows the 0.15 m-long dipole antenna model and boundary setup built in COMSOL. The width of the dipole antenna is 0.0025 m. The material used for dipole antenna is copper, while the surrounding environment is air. The total triangular element, which models both air and copper dipole antenna, is 12,125. The degrees of freedom (DOFs) in the mechanical and electromagnetic simulations are 12,396

and 24,520, respectively. On the boundary of the symmetric axis, the magnetic field is zero, which means it can be treated as homogeneous Dirichlet boundary condition. Since the dipole antenna model is an open structure, which has no specific physical boundary, to limit the simulation domain to be finite, an absorbing boundary condition (ABC) is adopted at the outside surface of the bounding circle. The dipole antenna surface is perfect electric conductor (PEC), which means the tangential electric field is zero. At the dipole antenna feed port, since the input voltage or current is known, the feed line edge is also a homogeneous Dirichlet boundary.

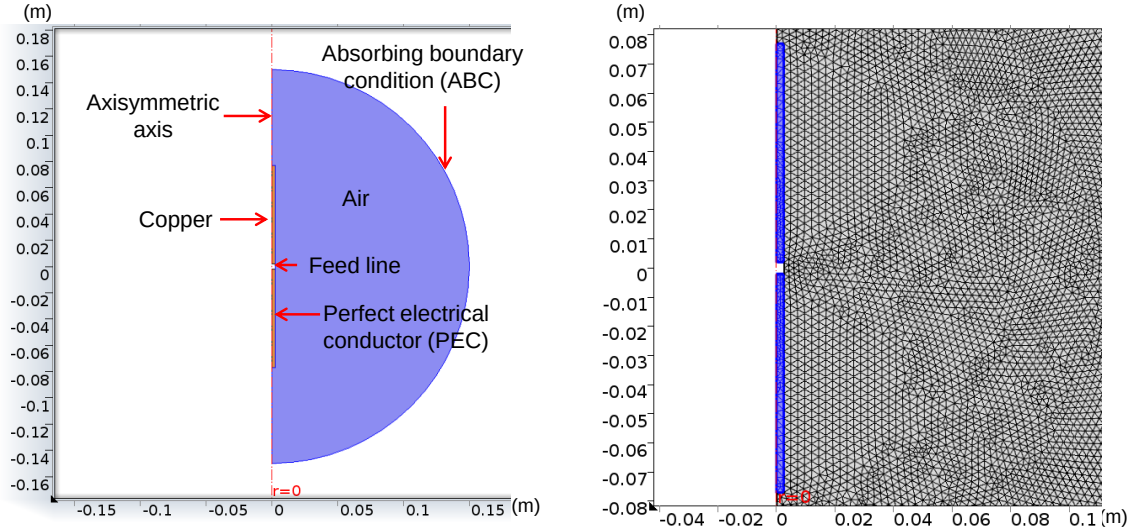

(a) Simulation model (b) Meshing

Fig. 4.7. 2D dipole antenna model and boundary condition setup

4.3.1.2 Result comparison between frequency domain and eigenfrequency domain solver

The dipole antenna model is analyzed in frequency domain and eigenfrequency domain separately to show the result consistency. The simulation is conducted on a desktop with Intel® Core™2 Duo processor and 8 GB RAM memory. The half-wavelength dipole antenna model in Fig. 4.7 has a length of 0.15 m (wavelength l_{λ}=0.3

m), which has a resonance frequency of 1 GHz in ideal case. The eigenfrequency solver is set to search two eigenfrequencies around 900 MHz. Fig. 4.8 and Fig. 4.9 present the electric and magnetic field distributions of the dipole antenna at its first eigenfrequency 830.325 MHz and second eigenfrequency 1.708 GHz, respectively. The field distribution patterns in both figures match with theoretical results, which verify the model [127]. The total simulation time for the eigenvalue solver is about 9 seconds when two eigenfrequencies are calculated.

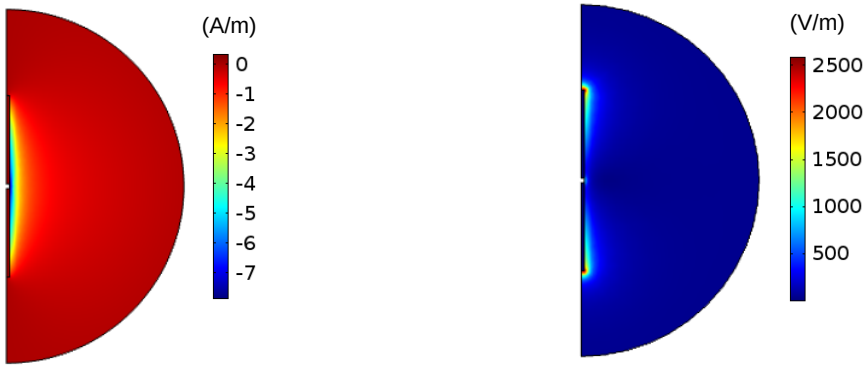

(a) H_ϕ plot (b) Normalized E plot

Fig. 4.8. Electric and magnetic field distribution at first antenna mode 830.325 MHz

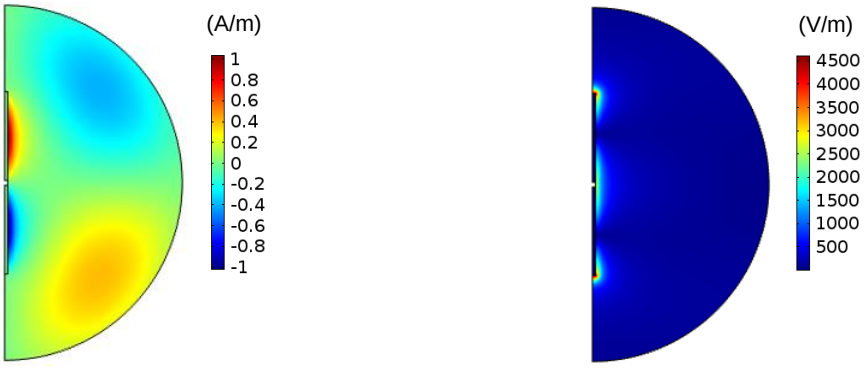

(a) H_ϕ plot (b) Normalized E plot

Fig. 4.9. Electric and magnetic field distribution at second antenna mode 1.708 GHz

The dipole antenna model is also simulated in the frequency domain when constant current is applied to the port. The simulated frequency ranges from 600 MHz to 2 GHz with a frequency step of 1 MHz. Fig. 4.10 shows S_{11} results from the frequency domain solver. There is one peak around 890 MHz, which is close to the first eigenfrequency shown in Fig. 4.8. The total simulation time for the 1,401 frequency points is about 1,433 seconds. In order to locate resonance frequency from the S_{11} plot, it is necessary to simulate a large frequency range to determine the minimum point of the curve. Therefore, for strain sensitivity simulation, the frequency domain approach usually requires longer simulation time compared with the eigenfrequency solver.

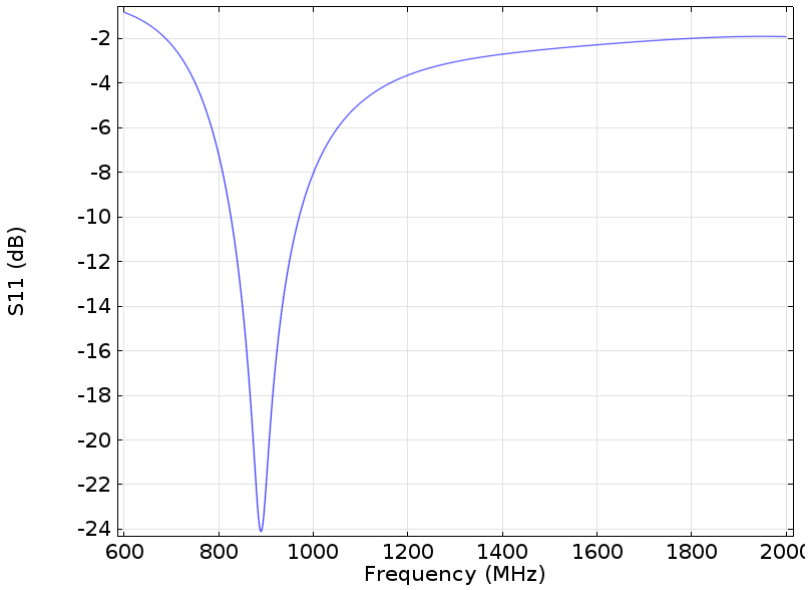

Fig. 4.10. S_{11} results of the dipole antenna from the frequency domain solver

4.3.1.3 Perturbation results

After the dipole antenna modeling in the eigenfrequency solver and frequency domain solver, the mechanical deformation is applied to the antenna in order to check the frequency response of the antenna with strain effect. In the mechanical simulation, only

the dipole antenna is involved, while the air sphere is excluded. Uniformly distributed prescribed displacements are applied at two ends of the dipole antenna, while the other ends close to the center feed line are fixed. The displacement is adjusted so that required strain levels are generated in the copper dipole antenna. After the mechanical simulation at each strain level, the deformed meshing is directly used for electromagnetic simulation to determine the resonance frequency of the dipole antenna under strain. Multiple strain steps are simulated and the eigenfrequency solver is used to calculate the antenna resonance frequency at each strain level.

First, 21 strain levels are simulated, ranging 0~2,000 με with a strain step of 100 με. The eigenvalues at each strain level are first calculated by `eigs` function in MATLAB, which adopts ARPACK Fortran library [128]. To check the effect of different starting vectors to the computation error and time, a randomly generated vector and an eigenvector from previous strain level are adopted as the starting vector for comparison. To improve the computation time, the symmetric [A] and [B] formulations in Eq. (4.17) are adopted. The eigenvalue perturbation methods, first-order eigenvalue perturbation (FOP) method and inverse Rayleigh quotient iteration (RQI) method, are applied to compare with two `eigs` solvers used in MATLAB. The error tolerance for RQI is set to 10^{-10}. The computed resonance frequency results from the four solvers are compared and summarized in Fig. 4.11. The legend "eigs-rand" denotes the results from `eigs` solver with randomly generated vector as starting vector. The legend "eigs-prev" indicates results from `eigs` solver with previous eigenvector as starting vector. The legend "FOP" and "RQI" refer to first-order eigenvalue perturbation method and inverse Rayleigh quotient iteration method, respectively. In this example, the resonance frequencies from `eigs`, FOP, and RQI show good match (Fig. 4.11(a)) at all strain steps.

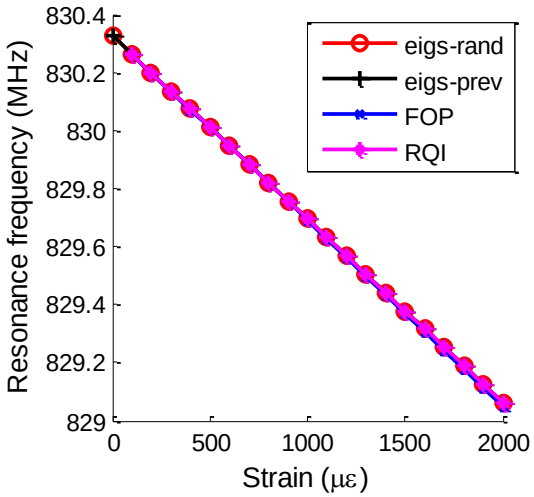

(a) Resonance frequency comparison

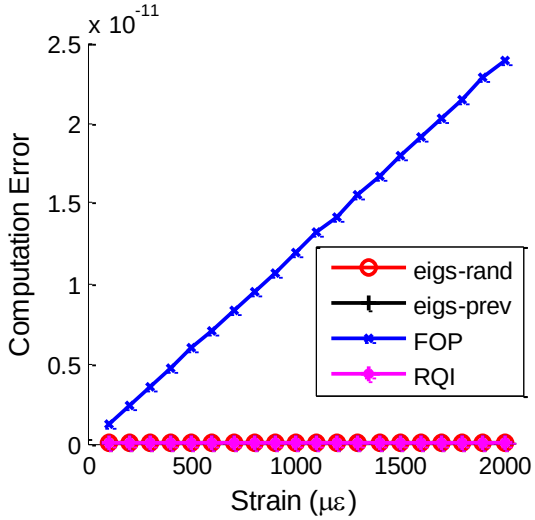

(b) Errors

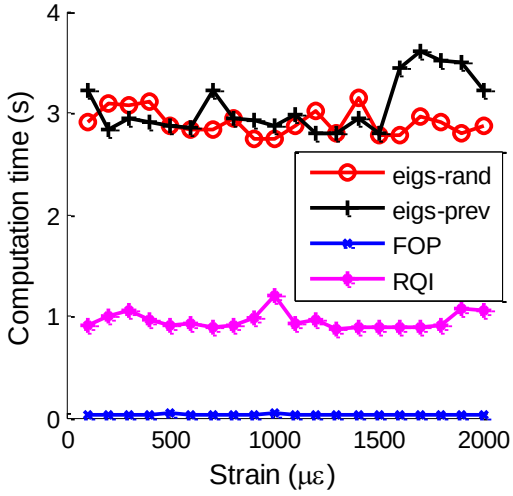

(c) Computing time

Fig. 4.11. Eigenfrequency result comparison between `eigs` solver, FOP, and RQI solvers (100 με)

To further quantify the solution accuracy, following error index is defined:

$$\text{error} = \frac{\left\| \mathrm{A}_j\{\Phi_j\} - \tilde{\lambda}_{j+1}\mathrm{B}_j\{\Phi_j\} \right\|}{\left\| \mathrm{A}_j \right\| + \left\| \tilde{\lambda}_j \mathrm{B}_j \right\|} \tag{4.24}$$

where $\tilde{\lambda}_j$ and $\{\Phi_j\}$ are the computed eigenvalue and right eigenvector at *j*-th strain step. As shown in Fig. 4.11(b), the perturbation error from RQI is in the order of 10^{-16}, while the errors from the `eigs` solver with random vector and previous eigenvector as starting vector are about 10^{-22} and 10^{-23}, respectively. The computation error comparison indicates that `eigs` solver with previous eigenvector as starting vector has best accuracy. Fig. 4.11(b) also shows that the FOP computation error increases as perturbed strain step increases. Nevertheless, the error at final perturbation strain step 2,000 με is on the order of 10^{-11}, which is still acceptable for this example.

The computation time comparison is summarized in Fig. 4.11(c). The computation time of FOP is around 0.05 second, which is about 60 times lower than the two `eigs` solvers in this example. The computation time of RQI is also about 3 times lower than the `eigs` solver. In this example, the two `eigs` solvers with different starting vectors have similar computation efficiencies.

To check the strain step size effect to the accuracies of the eigenvalue solvers, a 1,000 με step is later used instead of previous 100 με step. The resonance frequency comparisons are shown in Fig. 4.12. Fig. 4.12(a) shows while the perturbed resonance frequencies from RQI are still close to `eigs` results, much larger resonance frequency difference is observed between FOP and other three solvers. Fig. 4.12(b) shows again that the FOP approach has largest solution error. At the last strain step 20,000 με, the computation error from FOP is about 3×10^{-10}, while the error from RQI is around 2×10^{-14} and the error from two `eigs` solver with random starting vector and previous eigenvector as starting vector is about 10^{-22} and 10^{-23}, respectively. The results in Fig. 4.11 and Fig. 4.12 indicate that with same total number of perturbation steps, smaller perturbation size can improve the perturbation accuracy for the two perturbation methods (FOP and RQI). On the other hand, the perturbation step size does not affect the computation time of all four solvers, which is demonstrated in Fig. 4.12(c).

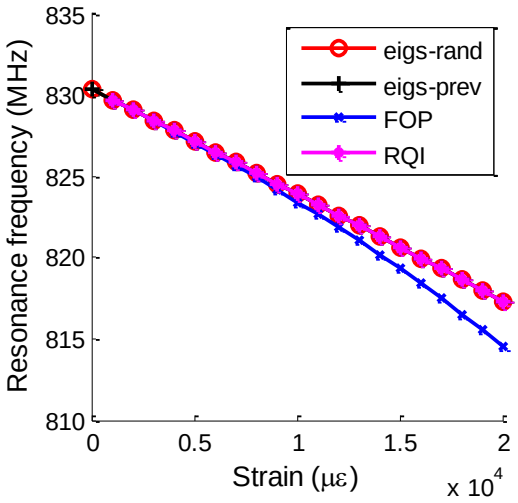

(a) Resonance frequency comparison

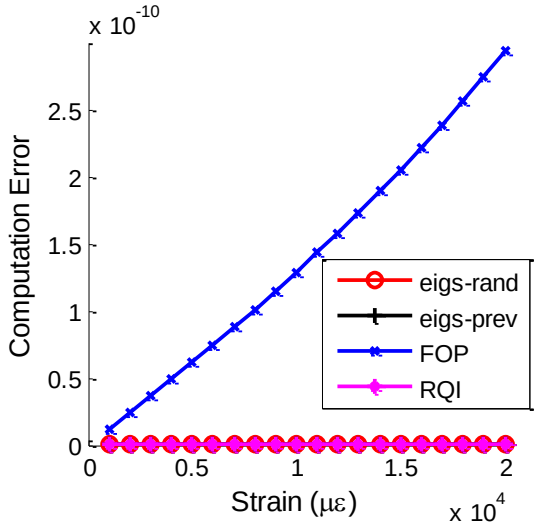

(b) Errors

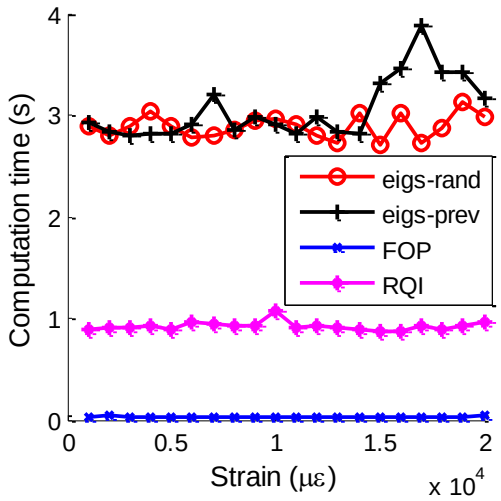

(c) Computation time

Fig. 4.12. Eigenfrequency results comparison between `eigs` solvers, FOP, and RQI solver (1,000 με)

4.3.2 Slotted Patch Antenna Sensor

In this 3D slotted patch antenna sensor example, Section 4.3.2.1 presents results from eigenfrequency solver of COMSOL and comparison with results from frequency

domain solver presented in Section 3.3.2. Section 4.3.2.2 shows the perturbation results from four solution methods.

4.3.2.1 Results from eigenfrequency domain solver in COMSOL

As a more complicated example, the passive slotted patch antenna sensor presented in Section 3.3.2 is studied. The sensor is first simulated in the COMSOL eigenfrequency solver to determine the resonance frequency change under strain. To have an faster comparison with perturbation techniques, the simulation model is tuned to use coarse meshing. While all other settings are kept the same as in Section 3.3.2, the number of DOFs in displacement field is tuned from 53,127 to 9,588, and number of DOFs in electric field is tuned from 477,429 to 65,527. The eigenfrequency solver is set to search several eigenfrequencies close to 900 MHz, the expected resonance frequency of the antenna.

The eigenfrequency result is plotted against strain in Fig. 4.13. The initial eigenfrequency of the sensor at zero strain is 909.5 MHz, which is almost the same as the results calculated from COMSOL frequency domain solver (in Section 3.3.2). The normalized strain sensitivity is –0.7573 ppm/με, which means that 1 με strain experienced by the sensor introduces 0.7573 ppm decrease in resonance frequency. The normalized strain sensitivity is also very close to the simulation result from frequency domain solver. The coefficient of determination of one indicates a good linearity between normalized frequency change and simulated strain. The closely matched results between frequency domain solver and eigenfrequency solver validate the feasibility to compute strain sensitivity using the more efficient eigenvalue approach (Eq. (4.15)). With simulation model, the average computation time for one eigenfrequency is about 110 seconds using COMSOL eigenfrequency solver. In this study with five strain steps and one eigenfrequency calculated, the total computing time is about 1,021 seconds, which is

much more computationally efficient compared with the frequency domain approach in Section 3.3.2.

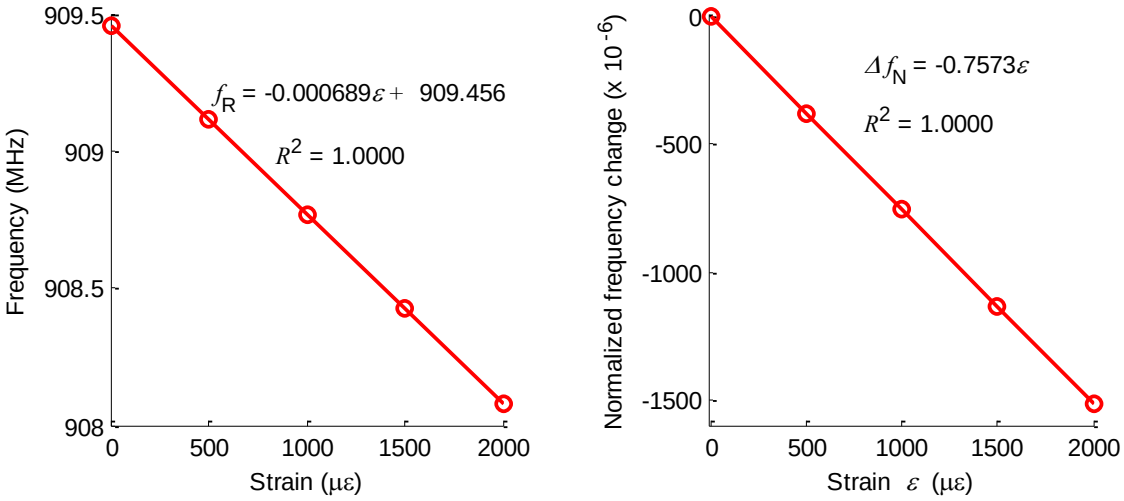

(a) Resonance frequency change versus strain ε

(b) Normalized resonance frequency change Δf_N versus strain ε

Fig. 4.13. Simulation results of slotted patch antenna sensor from eigenfrequency solver

4.3.2.2 Perturbation results

To further improve the simulation efficiency, the eigenvalue perturbation methods are applied using the COMSOL-MATLAB interface (Fig. 4.6). The simulated strain step is 100 με. In this example, symmetric formulations of [A] and [B] in Eq. (4.17) are adopted. Like previous 2D dipole example, the eigenvalues at each strain level are first calculated by `eigs` function in MATLAB with two different types of starting vectors, i.e. a randomly generated vector and the eigenvector from previous strain step. Then the two perturbation method, first-order eigenvalue perturbation (FOP) and inverse Rayleigh quotient iteration (RQI), are adopted to solve the eigenfrequencies at all strain steps.

The resonance frequency comparisons between the four solution methods are shown in Fig. 4.14. Fig. 4.14(a) shows as the perturbation step increases, the resonance

frequency difference between FOP and all other three methods increases gradually. Fig. 4.14(b) shows the computation error increases significantly with strain steps for FOP, which confirms that FOP has large accumulated error. The RQI computation error is much smaller than the FOP. The computation error from RQI at 2,000 με is about 2×10^{-14}. The two `eigs` methods errors are in the order of 10^{-20}, which is much smaller than FOP or RQI. Nevertheless, Fig. 4.14(a) demonstrates that the RQI method provides adequate accuracy for identifying strain sensitivity.

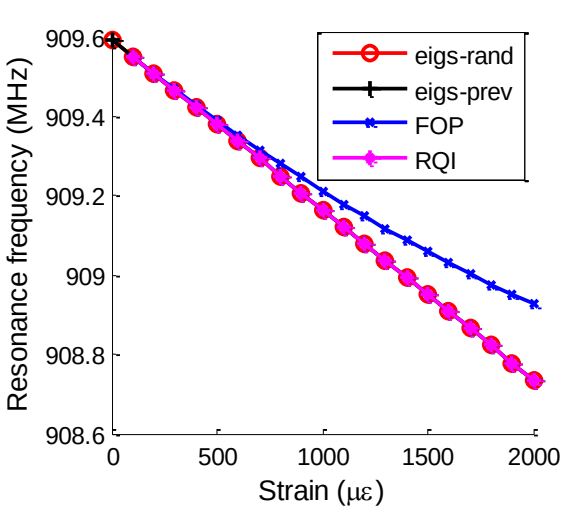

(a) Resonance frequency comparison

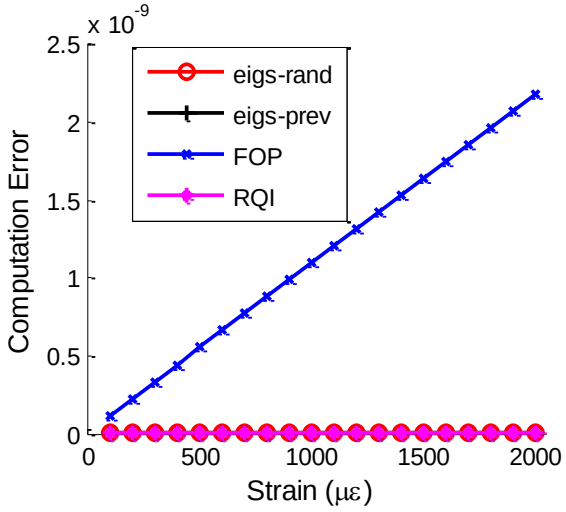

(b) Errors

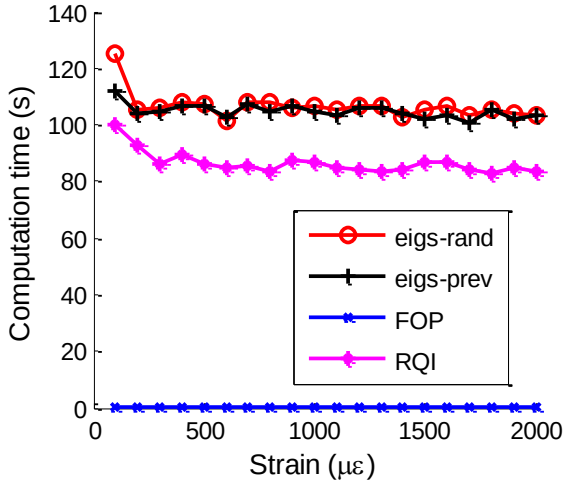

(c) Computation time

Fig. 4.14. Eigenfrequency results comparison between `eigs` solvers, FOP, and RQI solvers (100 με)

Fig. 4.12(c) shows the computation time comparison. The average computation time for the `eigs` solver is around 105 seconds, the RQI computation time is about 86 seconds, and FOP only takes about 0.3 second for each perturbation step. Since it takes more than 110 seconds per step for COMSOL eigenfrequency solver, all four solution methods being studied (`eigs` with a random starting vector, `eigs` with previous eigenvector as starting vector, FOP, and RQI) are faster than the COMSOL solver. Overall, it can be concluded that among methods that provide acceptable accuracy, the RQI method consumes the least time, and thus, is the most efficient in this example.

4.4 Summary

This chapter first presents electromagnetic finite element formulation of antenna sensors using both frequency domain solver and eigenfrequency solver. A folded patch antenna sensor simulation is performed using both solvers in COMSOL, and the calculated resonance frequency results are compared. The comparison shows that both solvers give similar strain sensitivity results. While the frequency domain solver requires smaller memory, it suffers longer computation time. On the other hand, the eigenfrequency solver provides faster computation speed, while the required hardware memory is larger.

To further reduce the computing time for solving the eigenvalue problem, especially when multiple strain steps are involved, two eigenvalue perturbation methods are studied. Instead of solving the entire eigenvalue problem from scratch, the eigenvalues and eigenvectors for current strain level can be updated according to results from previous strain level. The first-order eigenvalue perturbation method and the inverse Rayleigh quotient iteration method are introduced and applied to a 2D dipole antenna and the 3D slotted patch antenna sensor as illustration examples. The perturbation accuracy and efficiency are compared with MATLAB `eigs` command.

The 2D dipole antenna example shows that both FOP and RQI give acceptable computation accuracy when perturbation strain step is 100 με. The two `eigs` approaches, with different starting vectors, give best accuracy, but consume relatively more time. Two perturbation step sizes are studied in this example. The cumulative FOP computation error increases more significantly when perturbation strain step is 1,000 με. On the other hand, RQI still provides consistent computation accuracy.

The more complicated 3D slotted patch antenna sensor is then studied to validate the proposed perturbation techniques. The strain perturbation step is set to 100 με in this example. The FOP approach again shows significant cumulative computation error. Overall, it can be concluded that among methods that provide acceptable accuracy, the RQI method consumes the least time, and thus, is the most efficient in this example. With more efficient numerical solutions to strain sensitivity, efficiency of the antenna sensor design proves can be greatly improved.

CHAPTER 5 ANTENNA SENSOR DESIGNS AND EXPERIMENTAL RESULTS

After the proper sensor designs presented in previous several chapters, extensive experiments are conducted to evaluate sensor performances. The experiments validate key sensing parameters including strain sensing resolution, range, interrogation distance, consistency, sensor array, temperature stability. The sensors are also tested for emulated crack sensing and fatigue crack sensing. Section 5.1 presents experimental results of folded patch antenna sensor. Section 5.2 shows the results of a passive slotted patch antenna sensor. The results of an active slotted patch antenna sensor are presented in Section 5.3. To reduce sensor fabrication cost, a printed silver-nanoparticle antenna sensor is designed based on the folded patch antenna pattern. Section 5.4 presents strain sensing results of the silver-nanoparticle antenna sensor. Antenna sensors in the first four sections are RFID antenna sensors that operate at 900 MHz frequency range. Finally, the sensing results of four frequency doubling (2.9 GHz $\rightarrow$ 5.8 GHz) antenna sensors are presented in Section 5.5.

5.1 Folded Patch Antenna Sensor

The design drawing and photo of the folded patch antenna sensor is shown in Fig. 5.1. It includes three components: top copper cladding of the antenna pattern, bottom ground copper cladding, and substrate, which used to separate top copper cladding from bottom ground plane. An RFID chip is also integrated in the top copper antenna pattern for signal modulation. The sensor dimension is 61 mm $\times$ 69 mm $\times$ 0.79 mm.

The simulation results of the folded patch antenna sensor are presented in Section 3.3.1. This section presents experimental testing results of the folded patch antenna sensor. Section 5.1.1 shows the strain sensing resolution results. Section 5.1.2 presents the test on strain measurement range, i.e. the largest strain that can be measured by the

sensor. Measurement consistency at different interrogation distances is presented in Section 5.1.3. Section 5.1.4 presents the distributed strain sensing results through a sensor array. Section 5.1.5 explores temperature effect to strain sensing results. The emulated crack and fatigue crack sensing results are presented in Section 5.1.6 and 5.1.7, respectively. Finally, the substrate thickness effect to the sensor performance is evaluated in Section 5.1.8.

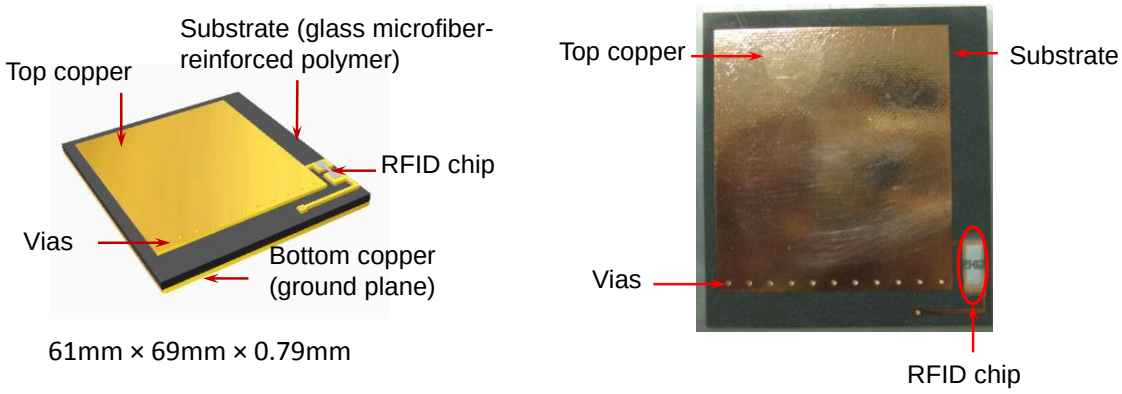

(a) Design drawing (b) Photo of the sensor

Fig. 5.1. Design drawing and photo of the folded patch antenna sensor

5.1.1 Strain Sensing Resolution Test

In order to investigate the strain sensing resolution of the prototype antenna sensor, tensile tests are conducted with small strain increment per loading step [56, 129]. Fig. 5.2(a) shows the center area of the tensile testing specimen, with the antenna sensor and seven (reference) metal foil strain gages measuring axial strain on the aluminum specimen. The antenna sensor is simply bonded to the specimen by superglue. Fig. 5.2(b) shows the tensile testing setup with a 22-kip SATEC machine. A Tagformance Lite reader from Voyantic Ltd. is adopted for interrogation power threshold measurement. The interrogation power threshold is the interrogation power transmitted by the reader

that is just enough to activate the RFID chip for signal modulation. When the interrogation frequency f by the reader equals the resonance frequency of the antenna sensor, the best impedance matching is achieved between the sensor-side antenna and the IC chip. In this scenario, the least amount of power needs to be transmitted by the reader for activating the IC chip. This means the interrogation power threshold plot $P(f)$ (measured by the reader) reaches minimum value at the resonance frequency.

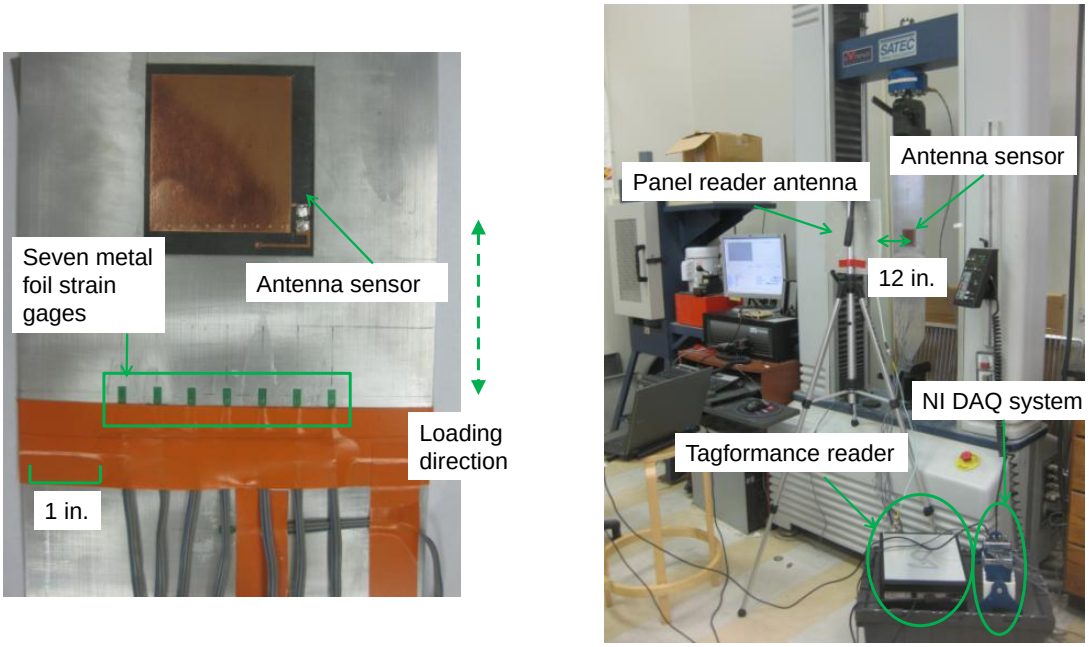

(a) Photo of the sensor instrumentation for wireless sensing experiments

(b) Photo of the experimental setup

Fig. 5.2. Experimental setup for the tensile tests

As shown in Fig. 5.2(b), the panel reader antenna is mounted on a tripod facing the antenna sensor. The distance between the reader antenna and the antenna sensor is set as 12 in. A National Instruments strain gage module (NI 9235), with a CompactDAQ Chassis (NI cDAQ-9172), is used for collecting data from metal foil strain gages.

The axial force applied by the tensile test machine is configured so that approximately a 20 με strain increment is achieved at each loading step. The test starts

with zero strain, and ends at around 200 με. The interrogation power threshold in dBm (dB-milliwatt) scale is measured by the Tagformance reader at each loading step. To reduce the environmental noise effect, five measurements are taken at each strain level and the average interrogation power, $P(f)$, is calculated. Although a total of ten strain levels are tested, for clarity Fig. 5.3(a) plots the average interrogation power threshold at only 11 με, 101 με, and 193 με. The strain levels in Fig. 5.3 are the average value among the seven metal foil strain gages. The interrogation power threshold reaches its minimum value at resonance frequency of the antenna sensor. Fig. 5.3(a) also shows a clear resonance frequency decrease during strain increase. Since the valley area of the interrogation power threshold plot is relatively flat, a 4th order polynomial curve fitting is performed to the valley area of each plot. The fitted 4th order polynomial is used for identifying the resonance frequency that corresponds to the minimum power.

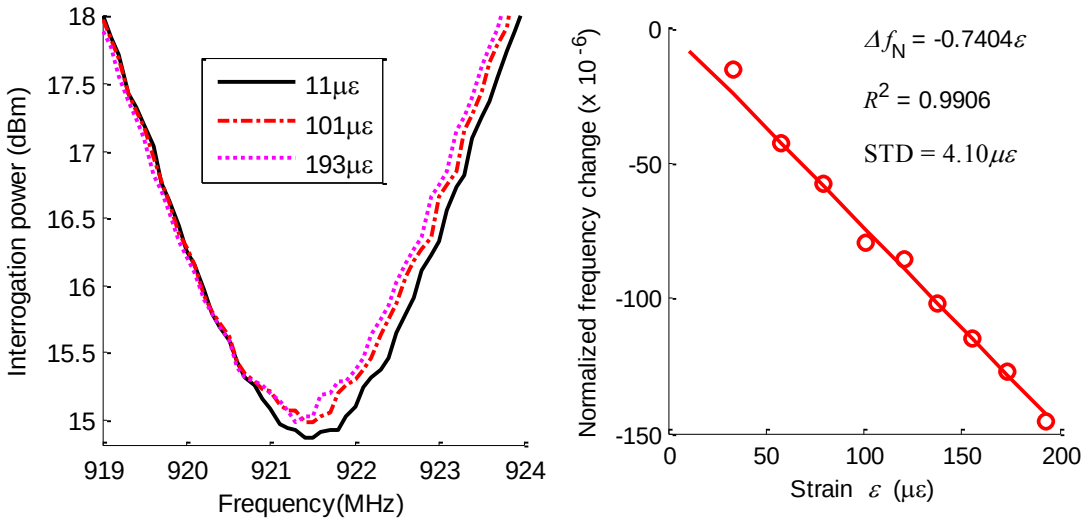

(a) Average interrogation power threshold

(b) Normalized resonance frequency change Δf_N versus strain ε (f_{R0}=921.472 MHz)

Fig. 5.3. Results for strain sensing resolution at 12 in. interrogation distance

Quality factor of the antenna affects the accuracy in wirelessly identified antenna resonance frequency. A larger quality factor corresponds to a longer wireless interrogation range, and an increased sharpness of the resonance peak in the interrogation power curve. Eq. (5.1) shows a general definition of the antenna quality factor:

$$Q_{\mathrm{T}} = \frac{f_{\mathrm{R}}}{\Delta f_{3\mathrm{dB}}} \tag{5.1}$$

where Q_{T} is the total quality factor of the antenna sensor. The sharpness of the resonance peak in the interrogation power curve is measured by the 3dB bandwidth around the resonance frequency, $\Delta f_{3\mathrm{dB}}$. According to Eq. (5.1), the quality factor of the antenna is calculated as 185.3, which indicates a relatively sharp peak in the interrogation power threshold curve.

According to Eq. (2.13), the normalized frequency change at each strain level is calculated. Fig. 5.3(b) confirms an approximately linear relationship between the normalized frequency change and strain. Slope of the curve indicates the normalized strain sensitivity, i.e. $\Delta f_{\mathrm{N}} = -0.7404$ ppm/με. This means that 1 με strain increase causes the resonance frequency of the antenna sensor to reduce by 0.7404 ppm. Compared with simulation results in Fig. 3.18(b), the experimental Δf_{N} is slightly lower. This is primarily due to strain transfer effect, i.e. only about 90% of the strain on aluminum surface is transferred to top copper layer of the sensor through the 0.79 mm thick substrate material Rogers 5880. The coefficient of determination, R^2, is 0.9906, which indicates acceptable linearity between strain and normalized resonance frequency change. In order to further check the measurement accuracy, the standard deviation of the measurement error is calculated as:

$$STD = \sqrt{\frac{1}{N-1}\sum_{i=1}^{N}\left(\Delta\varepsilon_i\right)^2} \tag{5.2}$$

where $\Delta\varepsilon_i$ is the difference between measured strain and strain estimated using the linear relationship at the i^{th} strain level; N is the total number of strain levels. Data shown in Fig. 5.3(b) has a standard deviation of 4.1 με. Although the standard deviation may not be sufficient when high accuracy strain measurement is needed, the results can be acceptable for many applications, particularly when only qualitative evaluation of stress concentration is needed.

5.1.2 Strain Sensing Range Test

Besides strain sensing resolution, maximum strain measurement range is another important performance to be quantified [56, 129]. Similar tensile testing is conducted with a 55-kip MTS-810 machine. To investigate antenna sensor performance at different strain levels, two loading stages are adopted. From 0 to 1,000 με, each loading step is configured to increase the strain level by about 100 με. From 1,000 με to 10,000 με, each loading step generates a strain increment of about 1,000 με. In total, twenty-six strain levels are tested. Other experimental setups and data processing remain the same as before.

Fig. 5.4(a) shows the average interrogation power threshold plot measured at different strain levels. For clarity, only five example strain levels are shown in the figure. Decrease in resonance frequency is observed when strain increases. From power threshold plots, resonance frequency is determined for each strain level. The normalized resonance frequency change Δf_N is plotted for all twenty-six strain levels in Fig. 5.4(b). Linear regression is performed separately to three segments of the plot. For segment ① with data points from 0 to 1,000 με, the normalized strain sensitivity is –0.7542 ppm/με, and the coefficient of determination is 0.9974. For segment ② with data points from 1,000 to 4,500 με, the normalized strain sensitivity is –0.7784 ppm/με, which is very close to the result in segment ①. The slight difference can be explained by Eq.(2.10),

which shows that the approximate linearity between resonance frequency and strain becomes weaker as strain becomes larger. For segment ③, the normalized strain sensitivity is reduced to –0.382 ppm/με. This is obviously caused by the yielding of both the aluminum specimen and the copper antenna, as well as the dielectric property change of the Rogers 5880 substrate. Determination coefficient for the third segment is smaller than the first two segments, because material property becomes more non-linear. The results demonstrate that the folded patch antenna sensor is capable of sensing strain as high as 10,000με, which is high enough for the structural member monitoring.

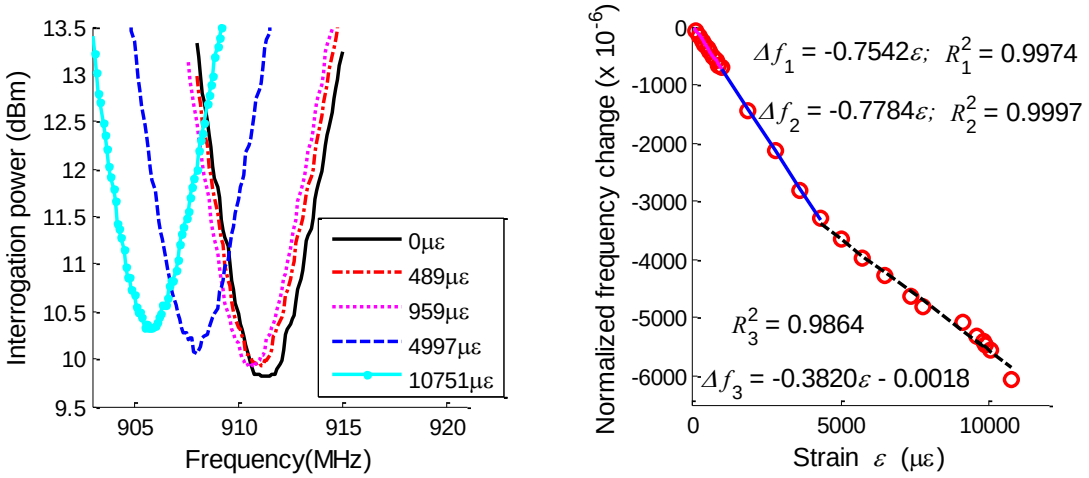

(a) Average interrogation power threshold

(b) Normalized frequency change Δf_N versus strain ε (f_{R0} = 911.407 MHz)

Fig. 5.4. Results for strain sensing range at 12 in. interrogation distance

5.1.3 Strain Sensing Consistency at Different Interrogation Distances

Wireless interrogation distance, which refers to the distance between reader antenna and the antenna sensor, is an important factor in field application. Section 5.1.3.1 describes the experiments to discover the longest achievable interrogation distance of the folded patch antenna sensor, when a panel antenna is used with the RFID

reader. Section 5.1.3.2 describes the tests when a high-gain Yagi reader antenna is used with the reader.

5.1.3.1 Interrogation distance test with a panel antenna

In order to investigate the largest interrogation distance that the prototype wireless system can provide, the antenna sensor under zero strain was tested with various interrogation distances first using a 8.5 dBi panel reader antenna (model number: S8658WPC from Cushcraft Corporation) [59]. For comparison, the sensor is tested in and outside an anechoic chamber, for which the experimental setups are shown in Fig. 5.5(a) and (b), respectively.

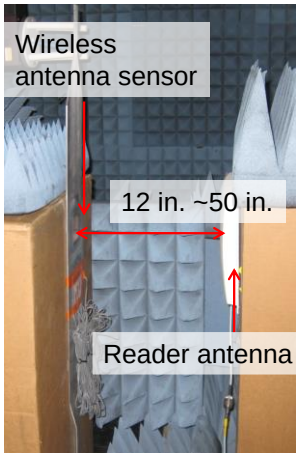

(a) Photo of the interrogation distance test in an anechoic chamber

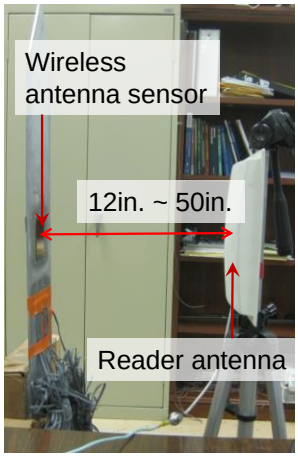

(b) Photo of the interrogation distance test outside the chamber

Fig. 5.5. Experimental setup for the interrogation distance analysis

Fig. 5.6(a) shows the average interrogation power threshold $P(f)$ plots at different distances measured in the anechoic chamber, and Fig. 5.6(b) shows the plots outside the chamber. For both scenarios, the distance varies from 12 in to 50 in.

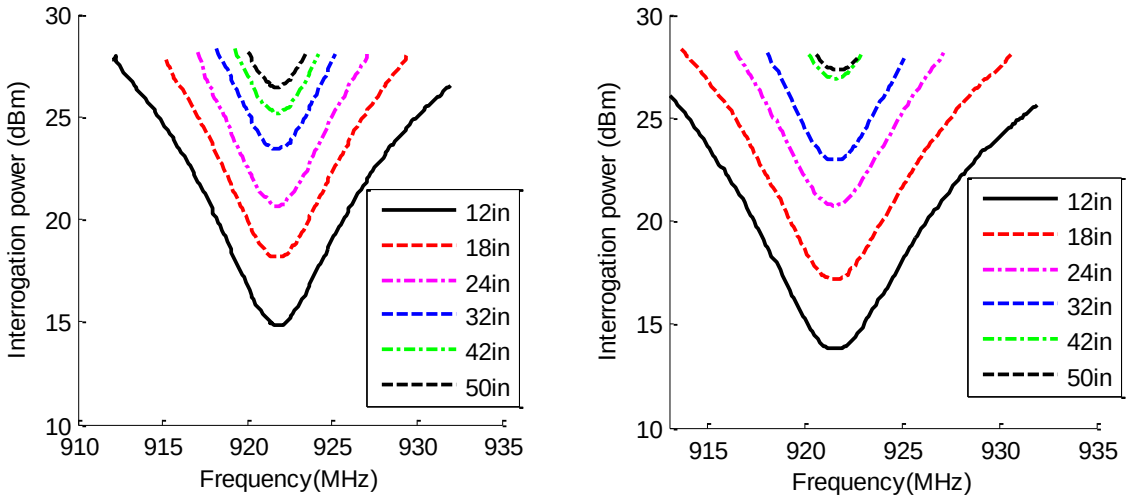

(a) Inside the anechoic chamber (b) Outside the anechoic chamber

Fig. 5.6. Average interrogation power threshold plots (at zero strain level) for different interrogation distances

The resonance frequencies at different distances are extracted and plotted in Fig. 5.7. The variation in the chamber is about 0.08 MHz, as shown in Fig. 5.7(a). For testing outside the chamber, as shown in Fig. 5.7(b), resonance frequency variation is of similar magnitude, except for the case at 50 in. The larger difference outside the chamber can be due to more multipath propagation of the electromagnetic wave, as well as more environmental noise. It should be noted that regardless of the resonance frequency variation at different interrogation distances, wireless strain sensing is feasible as long as the relationship between the strain and the resonance frequency remains approximately linear at a fixed interrogation distance. Nevertheless, future research will continue exploring advanced design, interrogation, or analysis techniques for more constant resonance frequencies at different interrogation distances.

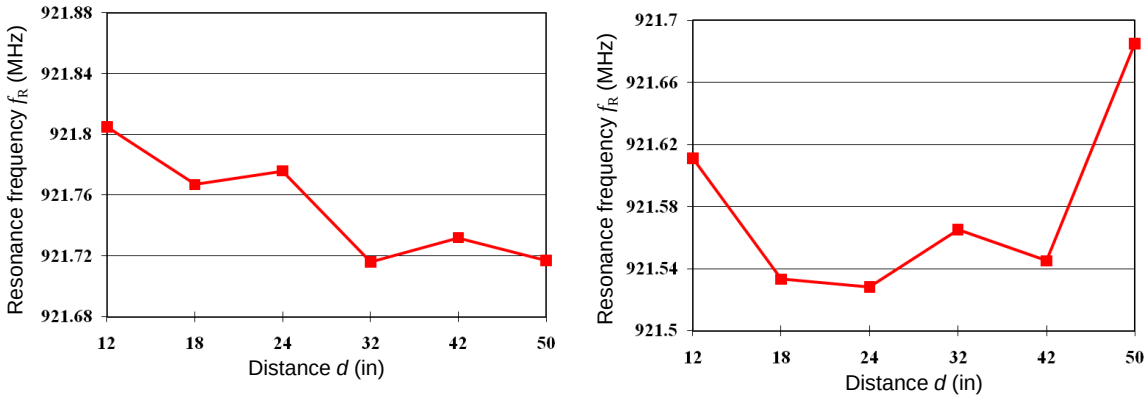

(a) Inside the anechoic chamber (b) Outside the anechoic chamber

Fig. 5.7. Resonance frequency f_R (at zero strain level) extracted from the transmitted power threshold plots

5.1.3.2 Wireless strain sensing with a high-gain Yagi antenna at 60 in. and 84 in. interrogation distance

To further investigate the strain sensing consistency at different interrogation distances, the reader antenna is changed to an 18 dBi high-gain Yagi antenna (APX-ANT-0918 from Technology Hardware & Resources) [56]. The experimental setup is shown in Fig. 5.8. With a high-gain reader antenna, less interrogation power is required in order to activate the RFID chip, which means the interrogation distance can be improved using the same interrogation power. Two different interrogation distances, 60 in. and 84 in., are tested for comparison. The tensile load is configured so that approximately 50 με increment is achieved at each loading step. All other experimental setups and data analysis remain the same as before.

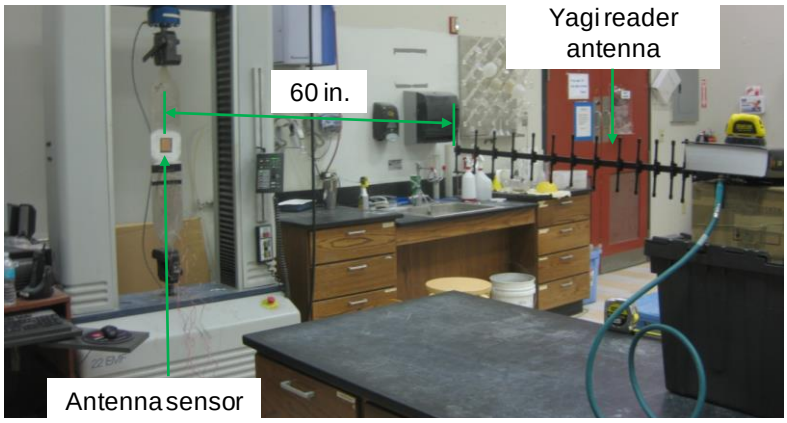

Fig. 5.8. Experimental setup for a tensile test with 60 in. interrogation distance

The interrogation power threshold plot for 60 in. interrogation distance is shown in Fig. 5.9. Seven strain levels are tested in total. For clarity, interrogation power threshold plots for only four strain levels are illustrated in Fig. 5.9(a). Fig. 5.9(b) shows the normalized strain sensitivity is –0.7346 ppm/με when the interrogation distance is 60 in. The corresponding coefficient of determination is 0.9948, which indicates reasonable linearity.

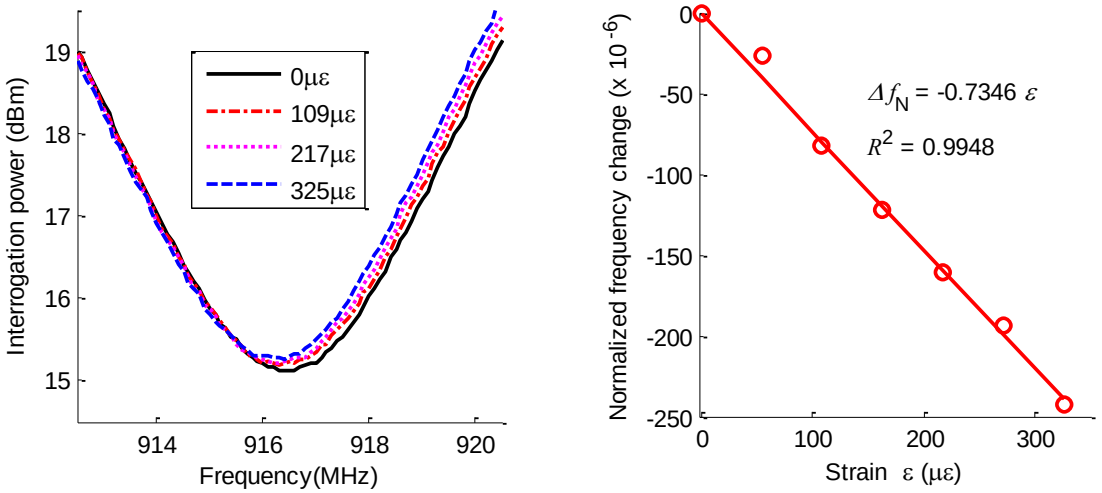

(a) Average interrogation power threshold

(b) Normalized resonance frequency change Δf_N versus strain ε (f_{R0}=916.455 MHz)

Fig. 5.9. Tensile testing results at 60 in. interrogation distance

The interrogation power threshold plot for 84 in. interrogation distance is shown in Fig. 5.10. Seven strain levels are tested in total. For clarity, interrogation power threshold plots for only four strain levels are illustrated in Fig. 5.10(a). Fig. 5.10(b) shows normalized strain sensitivity is –0.7907 ppm/με for 84 in. interrogation distance. The corresponding coefficient of determination is 0.9915, which indicates acceptable linearity. Nevertheless, future work is needed to further improve strain sensitivity consistency at different interrogation distances.

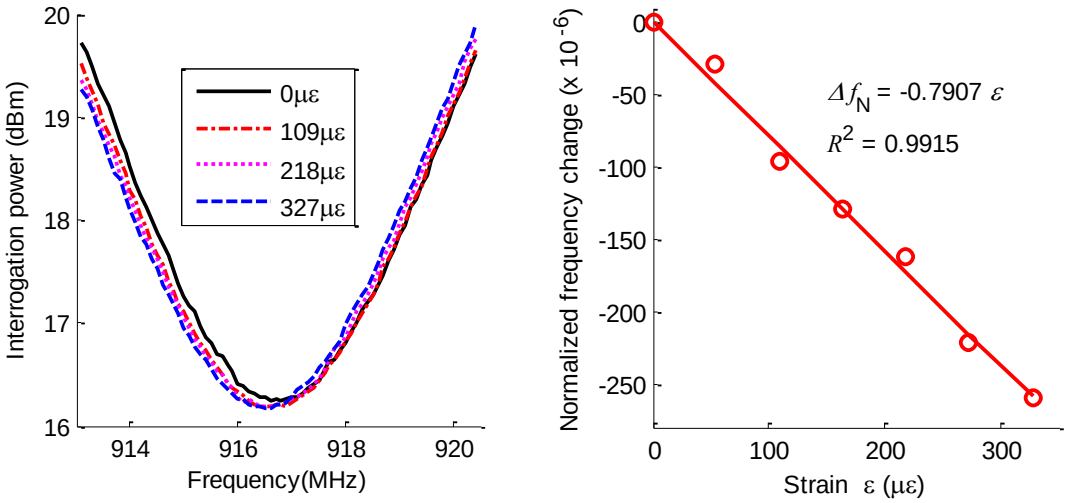

(a) Average interrogation power threshold

(b) Normalized resonance frequency change Δf_N versus strain ε (f_{R0}=916.738 MHz)

Fig. 5.10. Tensile testing results at 84 in. interrogation distance

5.1.4 Sensor Array Test

Besides harvesting electromagnetic power from the interrogation signal emitted by the reader, the RFID chip allows operation of multiple sensors in close proximity through its identification mechanism. The RFID chip integrated in the prototype sensor contains a 240-bit electronic product code (EPC) memory, which is utilized for

identification among multiple sensors. The performance of a three-sensor array is investigated [56, 130]. Fig. 5.11(a) shows the center area of the aluminum specimen, where three antenna sensors and four metal foil strain gages are installed. Fig. 5.11(b) shows the experimental setup for tensile testing. A panel antenna is placed 12 in. away from the specimen, facing the Antenna Sensor 2. Testing load is configured so that approximately 50με increment is achieved at each loading step. A LabVIEW program is implemented for the reader to activate one sensor at a time, using a unique identification code written to the EPC memory of every RFID chip, following Class-1 Generation-2 UHF RFID protocol. At one instant, only one selected sensor actively responds and communicates with the reader.

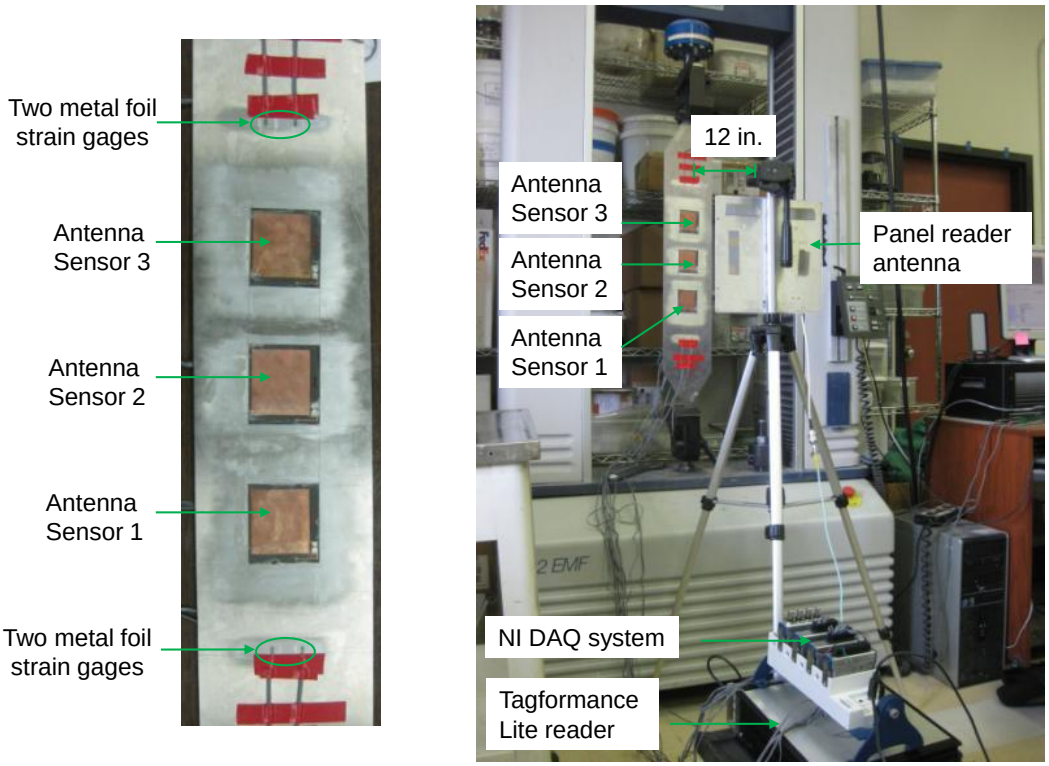

(a) Antenna sensor array on an aluminum specimen

(b) Experimental setup

Fig. 5.11. Experimental setup for the tensile test with an antenna sensor array

5.1.4.1 Three-sensor array

The average interrogation power thresholds of three sensors are plotted in Fig. 5.12(a), Fig. 5.13(a), and Fig. 5.14(a). For clarity, only four strain levels are shown in each interrogation power threshold plots. Resonance frequency shift is observed for all three sensors when strain increases. Normalized resonance frequency change is plotted against strain in Fig. 5.12(b), Fig. 5.13(b), and Fig. 5.14(b). The three normalized strain sensitivities are –0.7277 ppm/με, –0.7198 ppm/με, and –0.7264 ppm/με. The similarity among three sensitivities indicates that the antenna sensors can operate in close proximity with little electromagnetic interference. The normalized strain sensitivities in sensor array testing are also close to the sensitivity values from previous single sensor tests.

Although the results are overall promising, certain interference among neighboring sensors still exists. This is clearly demonstrated by the more zigzag interrogation power threshold plots as compared with the plots for single sensor testing. Even though only the selected RFID sensor responds to the reader with modulated signals, other RFID antennas still passively reflect un-modulated electromagnetic reflection to the reader. Because all three RFID antennas have close resonance frequencies, the electromagnetic reflection causes inevitable interference. Future study is needed to reduce the interference, for example, by designing antenna sensors with somewhat different initial resonance frequencies at zero strain level. Nevertheless, current sensor performance can be adequate for a qualitative measurement of stress concentration when small inaccuracies are acceptable.

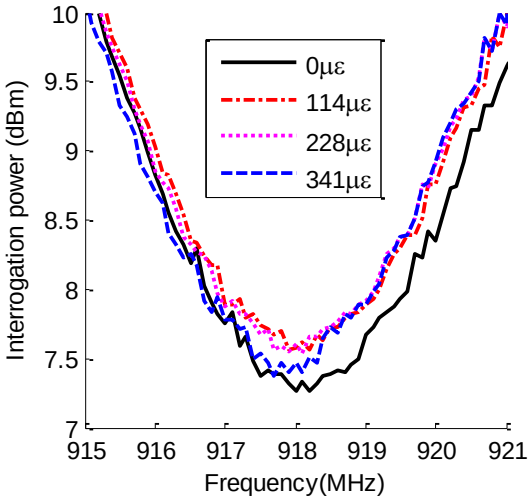

(a) Average interrogation power threshold

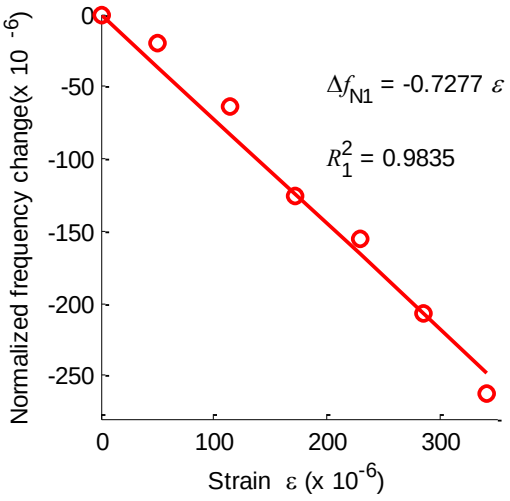

(b) Normalized resonance frequency change Δf_N versus strain ε (f_{R0}=918.127 MHz)

Fig. 5.12. Tensile testing results for Antenna Sensor 1

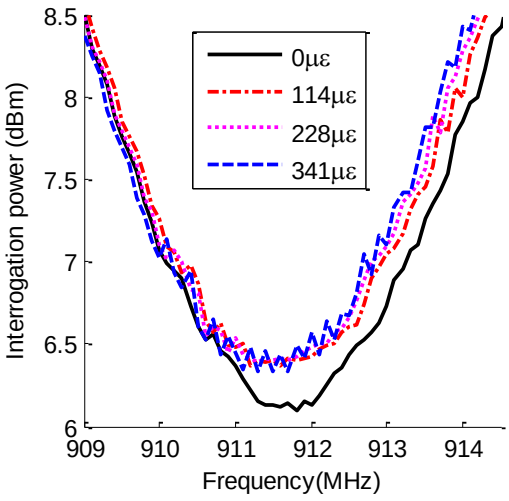

(a) Average interrogation power threshold

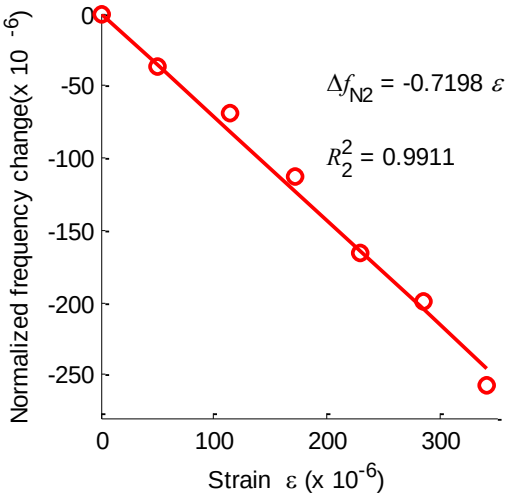

(b) Normalized resonance frequency change Δf_N versus strain ε (f_{R0}=911.611 MHz)

Fig. 5.13. Tensile testing results for Antenna Sensor 2

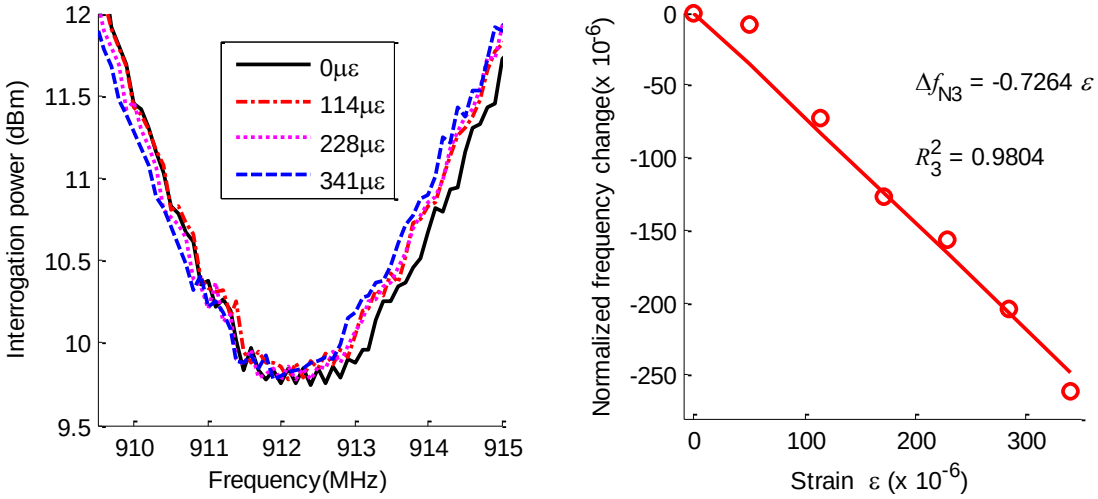

(a) Average interrogation power threshold

(b) Normalized resonance frequency change Δf_N versus strain ε (f_{R0}=912.326 MHz)

Fig. 5.14. Tensile testing results for Antenna Sensor 3

5.1.4.2 Six-sensor array

A six-sensor array is assembled to further validate the array performance. Six pieces of the RFID antenna sensors are mounted on an aluminum specimen. The interrogation distance between the reader and the antenna sensor array is set to 24 in. The test is conducted using a 55-kip MTS tensile testing machine. Fig. 5.15(a) shows the center area of the specimen, with the antenna sensor-array and ten metal foil strain gages (FLA-2-23-3LT, Texas Measurements, Inc.) measuring the axial strain. Fig. 5.15(b) shows the specimen installed on the testing machine. The reader antenna is mounted on a tripod and faces the wireless antenna sensor at a distance of 24 in.

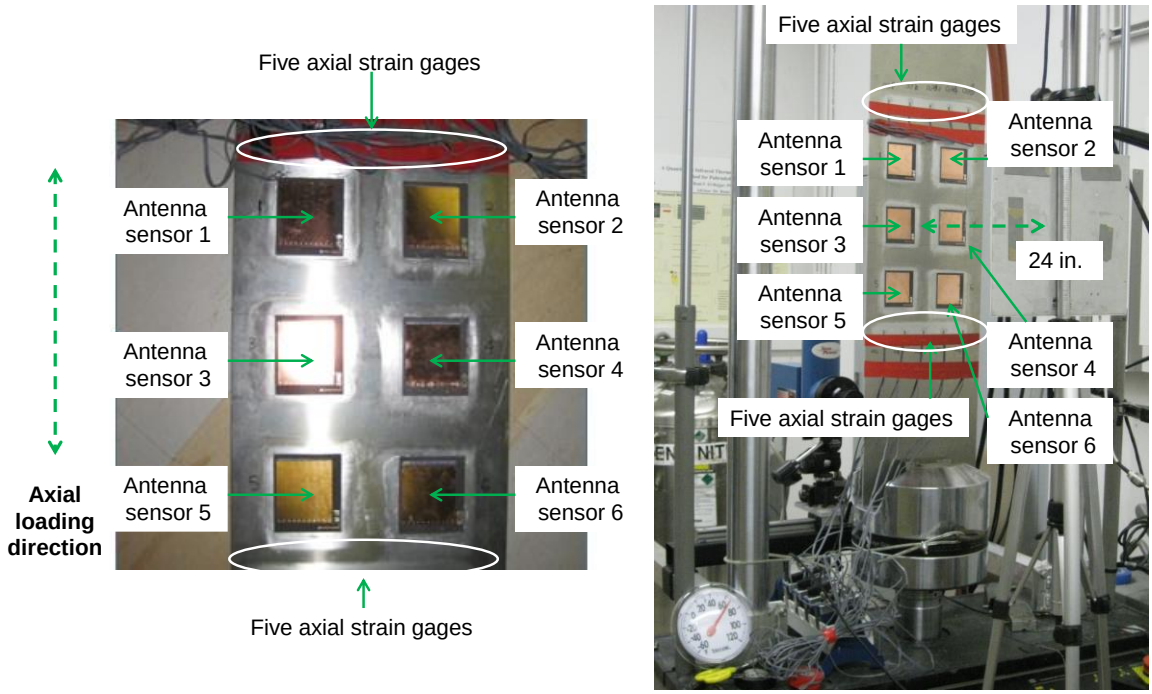

(a) Sensor instrumentation on the aluminum specimen

(b) Wireless strain sensing experiments

Fig. 5.15. Experimental setup for six-sensor array test

The interrogation power measurement is conducted similar as before. The interrogation power is plotted against interrogation frequency in Fig. 5.16 for data at four selected strain levels. The strain levels, as shown in the legend of Fig. 5.16, are calculated as the average among the ten axial strain gages. Although each curve is not very smooth, resonance frequency shift can be observed in the plots.

The resonance frequencies are then extracted at each strain level, and plotted against strain in Fig. 5.17 for all six sensors. The normalized strain sensitivity of six sensors ranges from –0.5342 ppm/με to –0.7322 ppm/με. The difference in the normalized strain sensitivity of six sensors is relatively large compared with the three-sensor array test results. The larger discrepancy is likely due to larger interference when more sensors are present in a small area. The interference can be reduced by increasing

the distance between adjacent sensors, and increase the difference in the initial zero-strain resonance frequency of the sensors.

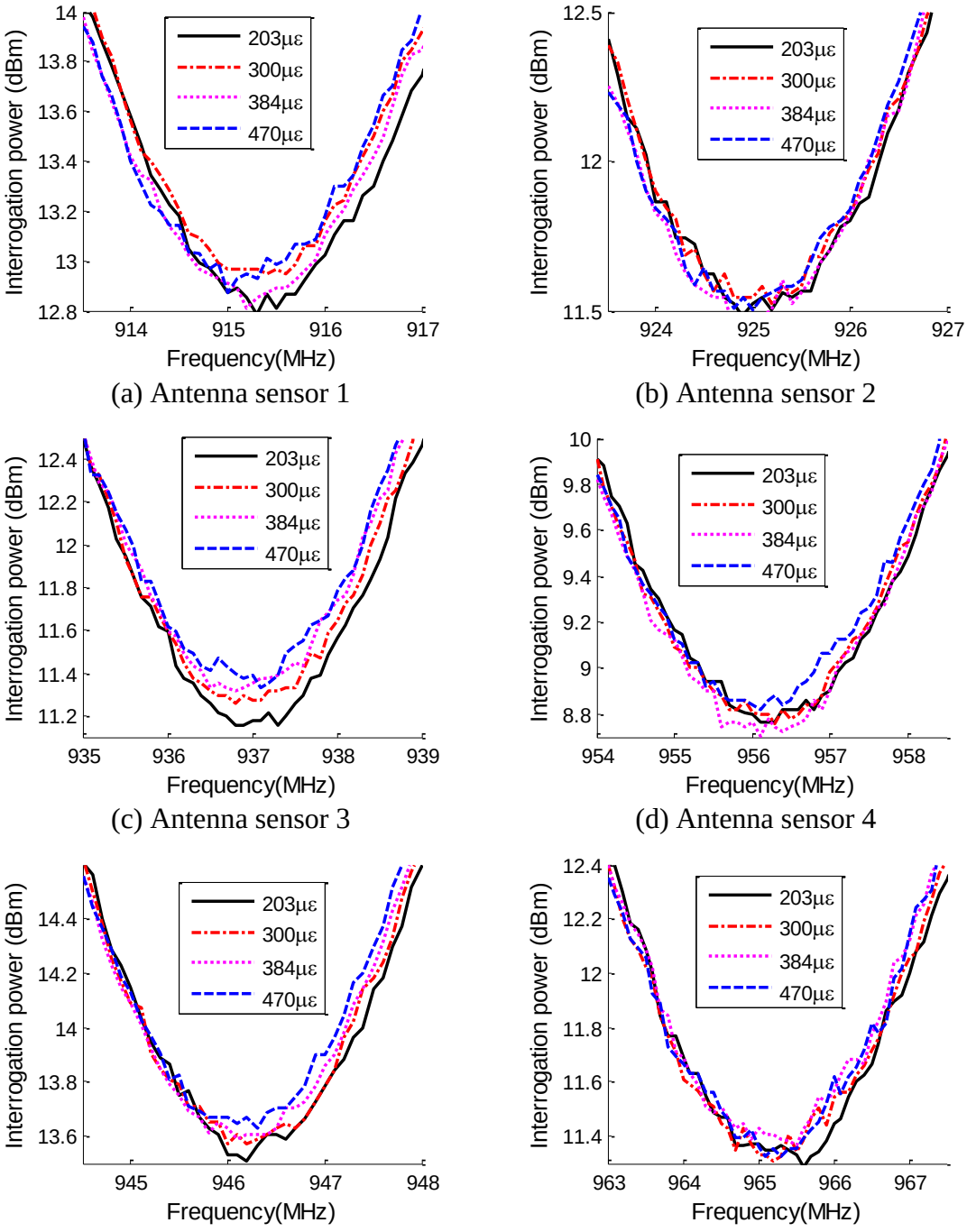

(a) Antenna sensor 1 (b) Antenna sensor 2

(c) Antenna sensor 3 (d) Antenna sensor 4

(e) Antenna sensor 5 (f) Antenna sensor 6

Fig. 5.16. Interrogation power plots for six-sensor array

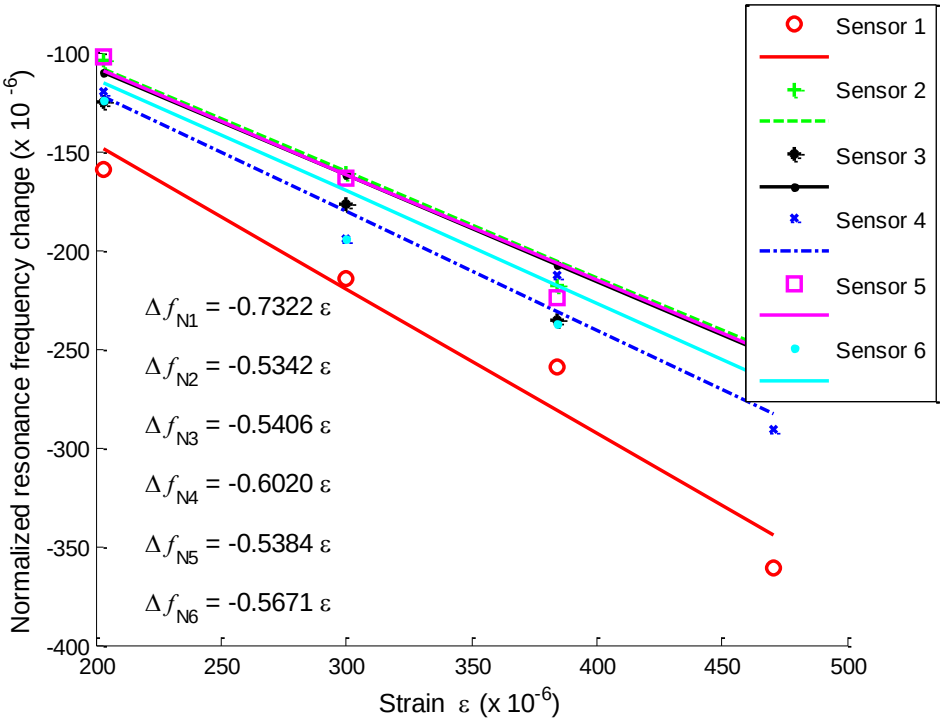

Fig. 5.17. Normalized frequency change versus strain for six-sensor array

5.1.5 Temperature Stability Test

Different from laboratory test with constant room temperatures, thermal effect is critical to the strain sensing on an in-situ structure. This section investigates thermal effects on antenna sensor performance [131]. Numerical simulations are first performed to study sensor deformation due to temperature increase, when the antenna sensor is bonded to an unconstrained aluminum specimen (Section 5.1.5.1). The temperature stability test is then conducted in the thermal chamber to verify the sensor performance, which is presented in Section 5.1.5.2.

5.1.5.1 Antenna sensor simulation under temperature change

Table 5.1 shows key material properties used in the simulation. Materials involved in the sensor include Rogers 5880 substrate and copper claddings. The three materials listed in Table 5.1 have different thermal expansion coefficients. In particular,

the substrate material Rogers 5880 is inhomogeneous, with different thermal coefficients along three dimensions. In order to evaluate complicated strain distributions due to temperature fluctuation, a thermal-mechanical coupled simulation is conducted using ANSYS software.

Table 5.1. Key material properties for thermal effect simulation

		Rogers 5880	**Copper cladding**	**Aluminum 6061**
Coefficient of thermal expansion (ppm/℉)	x	17	9	13
	y	27		
	z	132		
Dimension (mm^3)		61 × 69 × 0.79	50 × 56.5 × 0.018	711 × 152 × 3.175
Young's modulus (GPa)		1.07	1,100	69
Poisson's ratio		0.4	0.35	0.33

Most of the dimension and material properties in Table 5.1 reflect the actual scenario to be tested in a temperature chamber. The main difference is that aluminum specimen length is slightly reduced in simulation to save computing effort, though the difference should have little influence on thermal deformation of antenna sensor due to temperature. For simplicity, the bonding between the substrate and aluminum specimen is assumed to be ideal, i.e. top surface of aluminum specimen and bottom surface of the substrate share same finite element nodes between them. Small features such as the matching lines, vias, and bottom copper cladding are regarded to have minimal effect on mechanical analysis, and thus, not considered in this simulation. Exploiting the symmetry of the problem, only one quarter of the structure (dimensions listed in Table 5.1) is built in ANSYS. Fig. 5.18 illustrates the ANSYS meshing of the quarter model. A quarter of the antenna sensor is located in Area 1 (lower-left of the figure). Under the antenna sensor, a quarter of the aluminum specimen occupies all areas in the figure. Symmetric boundary condition is assigned to the left and lower sides of the model. Free boundary

condition is assigned to the upper and right side, to allow unconstrained stress-free thermal deformation.

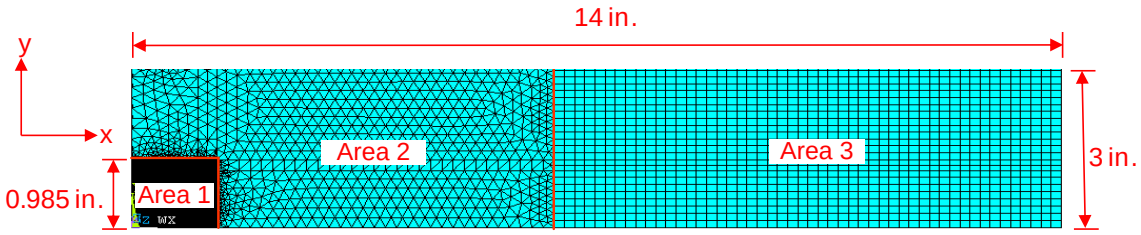

Fig. 5.18. Meshing of the quarter ANSYS model for mechanical simulation (Area 1: a quarter of the antenna sensor; Areas 1, 2, and 3 combined: a quarter of the aluminum specimen).

The copper cladding, sensor substrate, and aluminum specimen in Area 1 are modeled as ANSYS SOLID45 elements at high resolution. The aluminum specimen in Area 3 is modeled as SOLID45 elements at relative low resolution, to reduce computing effort. Since SOLID95 type is a 20-node element suitable for transiting between areas with different meshing resolutions, it is used to model elements in Area 2 that is between Areas 1 and 3. Along thickness direction of the sensor, one layer of elements is assigned for the copper claddings, and five layers of elements are assigned for the substrate. For the aluminum specimen, Area 1 has four layers along the thickness direction, Area 3 has two layers, and Area 2 is automatically meshed when transiting from two to four layers.

A uniform temperature increase of 90 ℉ is applied to the ANSYS model. Fig. 5.19 shows x-direction strain on the top surface of aluminum specimen. Fairly uniform strain distribution is observed at the right end of the specimen.

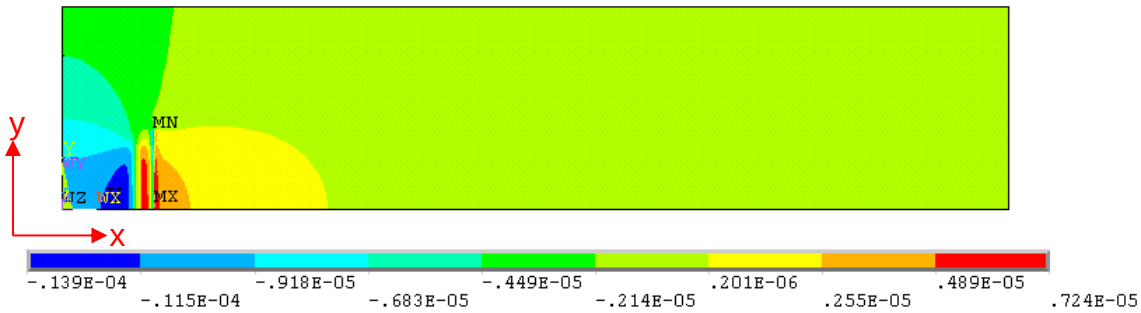

Fig. 5.19. X-direction strain on aluminum specimen

Fig. 5.20 shows strain distribution on the top surface of copper cladding. Strain on the copper is also uniformly distributed, except for the right edge. Average strain level on the copper cladding is approximately 1,100με.

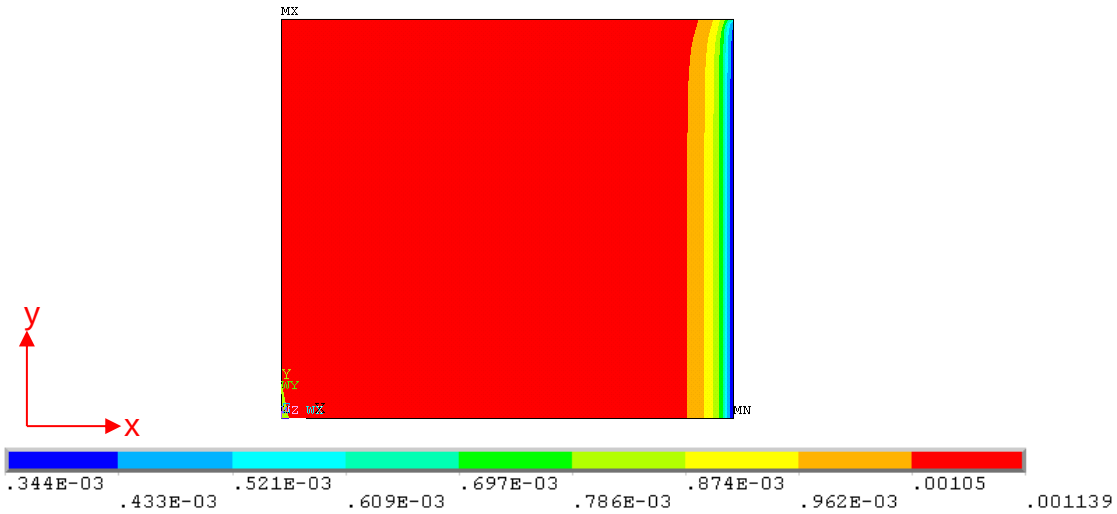

Fig. 5.20. X-direction strain on top copper cladding

The overall strain sensitivity on antenna surface in X-direction due to temperature change, α, is calculated as:

$$\alpha = \frac{1{,}100\mu\varepsilon}{90°\mathrm{F}} = 12.2\mu\varepsilon / °\mathrm{F} \tag{5.3}$$

Since the measured resonance frequency change due to strain is $S_\varepsilon \cong -750$ Hz/με, resonance frequency change of the sensor due to temperature change, S_T , can be estimated as:

$$S_T = S_\varepsilon' \cdot \alpha = -750 \times 12.2 = -9.15 \text{kHz} / ^\circ\text{F} \tag{5.4}$$

5.1.5.2 Temperature chamber test

Temperature chamber test is conducted to study the antenna resonance frequency change caused by temperature fluctuation. Fig. 5.21 shows the test setup. An antenna sensor together with aluminum specimen is placed in the chamber. The Tagformance reader is used for wireless interrogation. Reader antenna is placed 12 in. away from the sensor. Because all walls, ceiling, and floor of the temperature chamber are furnished with metal surfaces, large amount of electromagnetic wave reflection to reader interrogation signal is expected. To reduce the effect of reflection on wireless interrogation, four pieces of radiation-absorbent foams are places around the test specimen and reader antenna. To keep track of temperature fluctuations in the chamber, five thermometers are placed around the foams, as shown in Fig. 5.21(a).

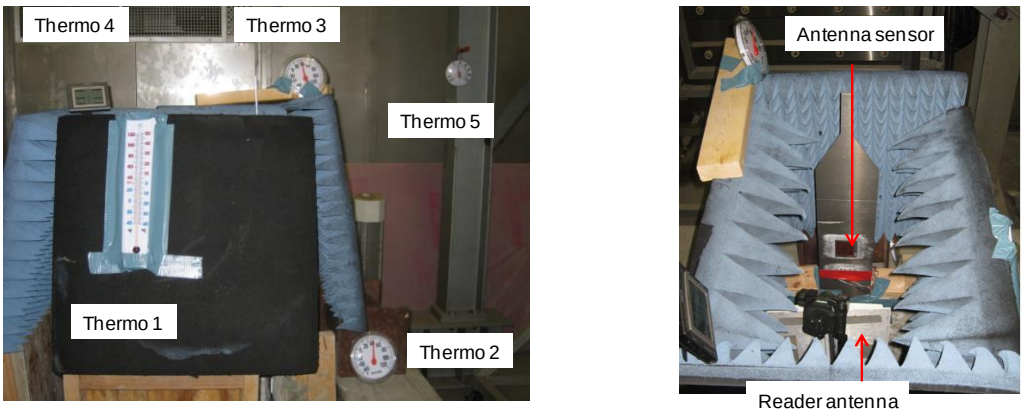

(a) Front view (test specimen is enclosed by radiation-absorbent foams)

(b) Top view

Fig. 5.21. Experimental setup for temperature chamber test

Fig. 5.22 shows the temperature steps of the test. The chamber temperature is first increased to 122 ℉ within 30 minutes, and held at 122 ℉ for 1 hour to achieve uniformity and stability. During the test, the chamber temperature is reduced by 9 ℉ after every 30 minutes, to the final level at 32 ℉. Interrogation power threshold measurement is conducted at each temperature level, before another 9 ℉ temperature reduction to next level.

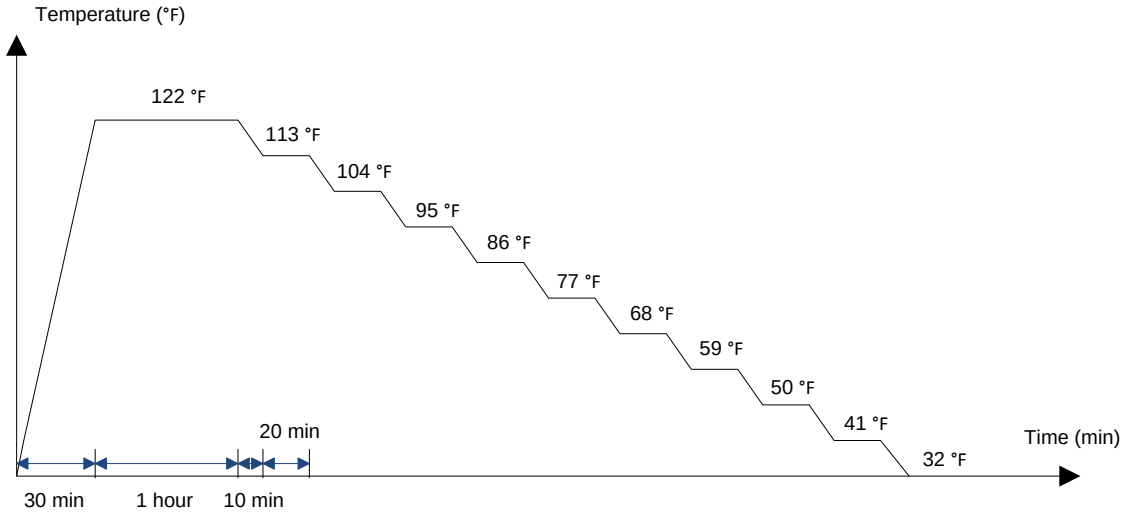

Fig. 5.22. Target temperature levels during temperature chamber test

To reduce environmental noise, five frequency sweeps are performed in the measurement. The average interrogation power threshold at different temperature levels are plotted in Fig. 5.23(a). For clarity, only four temperature levels are shown. The temperature numbers listed in the legend of Fig. 5.23(a) are the average reading among five thermometers around the specimen. Compared with target temperature levels shown in Fig. 5.22, actual measured temperatures are slightly lower. The discrepancy is because control thermostat is located close to an inlet opening on the wall, where temperature is higher than the center of the chamber. Resonance frequency of the antenna sensor decreases as the chamber temperature reduces. Since the valley area of each curve is not

smooth, a fourth order fitting is applied to curves shown in Fig. 5.23(a). Resonance frequency at each temperature level is thus determined by peak picking of each fitted curve, and shown in Fig. 5.23(b). A total of about 5 MHz resonance frequency decrease is observed when the chamber temperature reduces from 110 ℉ down to 32 ℉. As estimated in Eq. (5.4), the resonance frequency change of the sensor due to thermal expansions is only –9.15 kHz/ ℉. If thermal expansion were the only cause for resonance frequency change, the resonance should have increased by 0.714 MHz when temperature reduces from 110 ℉ down to 32 ℉. Because a much larger 5 MHz decrease is observed instead during the experiment, it is concluded that thermal deformation is not the main reason for resonance frequency change when temperature fluctuates.

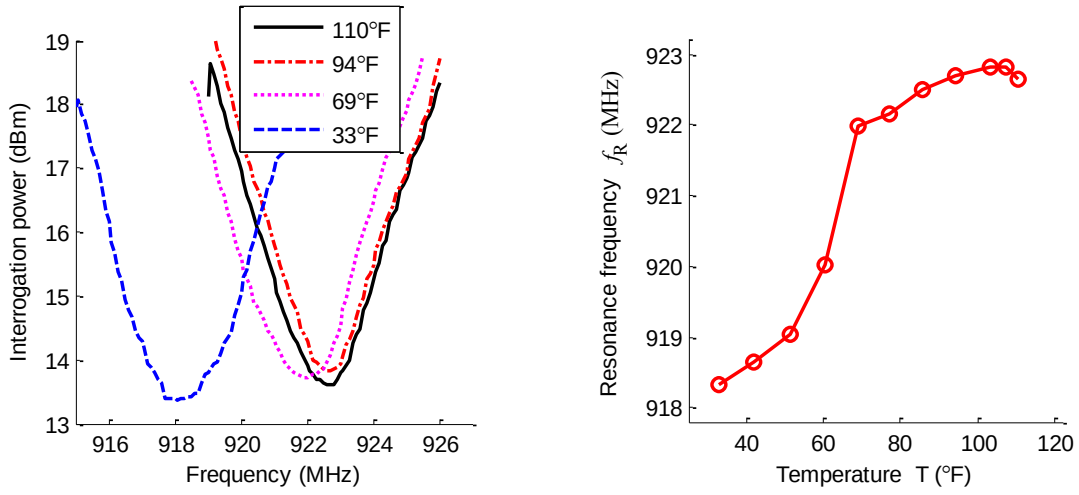

(a) Average interrogation power (in dBm)

(b) Resonance frequency change during temperature fluctuation

Fig. 5.23. Temperature chamber test results (antenna sensor with Rogers 5880 substrate)

After further diagnosis, it is identified that most of the resonance frequency change is caused by substrate dielectric constant change due to temperature fluctuation. Fig. 5.24(a) shows Rogers 5880 dielectric constant change due to temperature fluctuation. According to Eq.(2.6), decrease in the dielectric constant causes increase in resonance

frequency. Combining data in Fig. 5.24(a) and thermal expansion effect, the resonance frequency at different temperatures can be calculated. Define the zero-strain resonance frequency f_{R0} (see Eq.(2.11)) at room temperature 73 ℉ as reference state of the sensor. The resonance frequency at another temperature T is calculated as:

$$\begin{aligned} f_R^T &= f_R \sqrt{\frac{\beta_r}{\beta_r^T}} \\ &= (f_{R0} + \Delta f_R) \sqrt{\frac{\beta_r}{\beta_r^T}} \\ &\approx f_{R0} \sqrt{\frac{\beta_r}{\beta_r^T}} + S_T \cdot \Delta T \sqrt{\frac{\beta_r}{\beta_r^T}} \end{aligned} \tag{5.5}$$

where β_r and β_r^T is the substrate dielectric constant at reference temperature 73 ℉ and another temperature T, respectively; ΔT is the temperature difference from 73 ℉ reference; Δf_R ($\approx S_T \cdot \Delta T$) is the resonance frequency change due to thermal expansion.

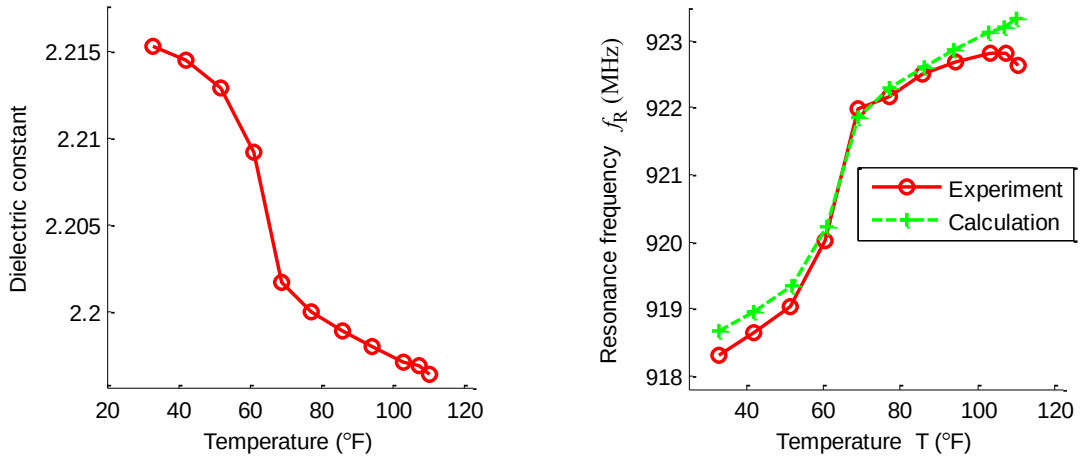

(a) Dielectric constant change during temperature fluctuation

(b) Resonance frequency change during temperature fluctuation

Fig. 5.24. Effect of dielectric constant change during temperature fluctuation (Rogers 5880 substrate)

Fig. 5.24(b) overlays the calculation results with experimental results, showing a closely match. It is therefore concluded that resonance frequency change during

temperature fluctuation is mainly caused by change in substrate dielectric constant. In order to have a stable strain measurement with large temperature variation, it is possible to explore different substrate material with stable dielectric constant under temperature. The results are presented in Section 5.1.8.

5.1.6 Emulated Crack Test

Emulated crack sensing performance of the prototype antenna sensor is described in this section [56, 132, 133]. To conveniently emulate crack propagation, a special crack testing device (Fig. 5.25(a)) is designed for the experiments. The crack testing device consists of three aluminum plates, i.e. a base plate (16 in. × 12 in. × 1 in.), a rotating top plate (8 in. × 4 in. × 0.5 in.), and a fixed bottom plate (8 in. × 4 in. × 0.5 in.). Due to their thickness, all three plates can be assumed to remain rigid during crack testing for the sensor. The fixed bottom plate is fastened to the base plate by four corner bolts. The rotating top plate is attached to the base plate by one bolt at the bottom right corner, which acts as the rotation axis. A fine-resolution displacement control screw (1mm threading) is installed at the top left corner of the rotating plate. By turning the screw, a rotation is imposed on the top plate and a crack/gap is opened between the top and bottom plates, as marked by the dashed line in Fig. 5.25(a). The crack opening size is measured by a digital dial gage (0.0001 in. resolution) mounted at the left side of the base plate. A spring-loaded probe from the gage pushes against an angle bracket that is fastened to the left edge of the rotating plate.

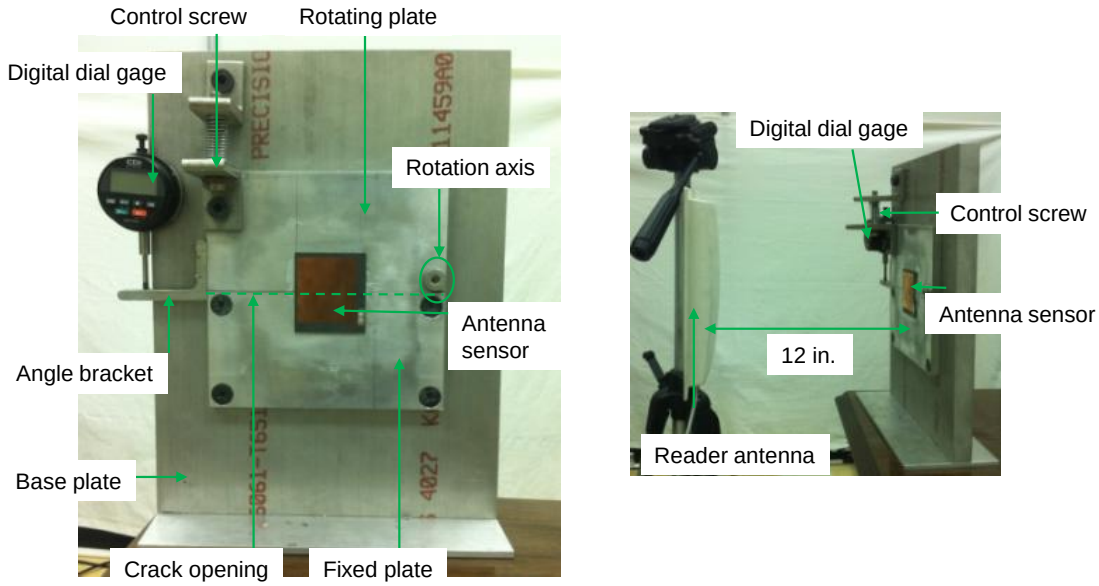

(a) Photo of the crack testing device (b) Experimental setup

Fig. 5.25. Experimental setup of emulated crack test

For crack sensing, the back side of a prototype antenna sensor is bonded on the rotating and fixed plates, above the gap and at the center of the crack opening line. The experimental setup for wireless interrogation is shown in Fig. 5.25(b). The panel reader antenna faces the center of the prototype sensor at a distance of 12 in. Through a coaxial cable, the reader antenna is connected with the Tagformance reader unit. At each crack opening size, the Tagformance reader sweeps through a frequency range to measure the interrogation power threshold, so that the resonance frequency of the antenna sensor can be determined. After the reader finishes interrogation at one crack opening size, the displacement control screw is turned to reach the next crack opening size.

Fig. 5.26 shows representative photos of the deformed/cracked antenna sensor at three different crack opening sizes. Crack size underneath the sensor is estimated from dial gage reading. Fig. 5.26(a) shows the sensor at 5-mil crack opening. No fracture occurs on the sensor, but slight deformation is observed on the top copper cladding. Fig. 5.26(b) shows when crack opening is 21-mil, which is the last strain level when the RFID

sensor responds. Small fractures have developed on the top copper and the substrate, but the sensor still functions properly. The loading step after 32-mil causes rapid breakage of the sensor, as shown in Fig. 5.26(c). At this point, the crack grows through the entire antenna width. No response from the antenna sensor can be received by the Tagformance reader.

(a) 5 mils (b) 21 mils (c) 32 mils

Fig. 5.26. Photos of deformed antenna sensor at different crack opening sizes

In total, fourteen crack opening sizes are wirelessly measured during the experiment. For clarity, Fig. 5.27(a) shows the interrogation power threshold plots for only five crack opening sizes. It is observed that the antenna resonance frequency reduces gradually when crack opening increases. The normalized resonance frequency change is plotted against crack opening size in Fig. 5.27(b). A linear regression is performed on the fourteen data points. The slope of −303 ppm/mil represents the emulated crack sensing sensitivity, which means 1 mil crack underneath the sensor causes the resonance frequency to reduce by 303 ppm.

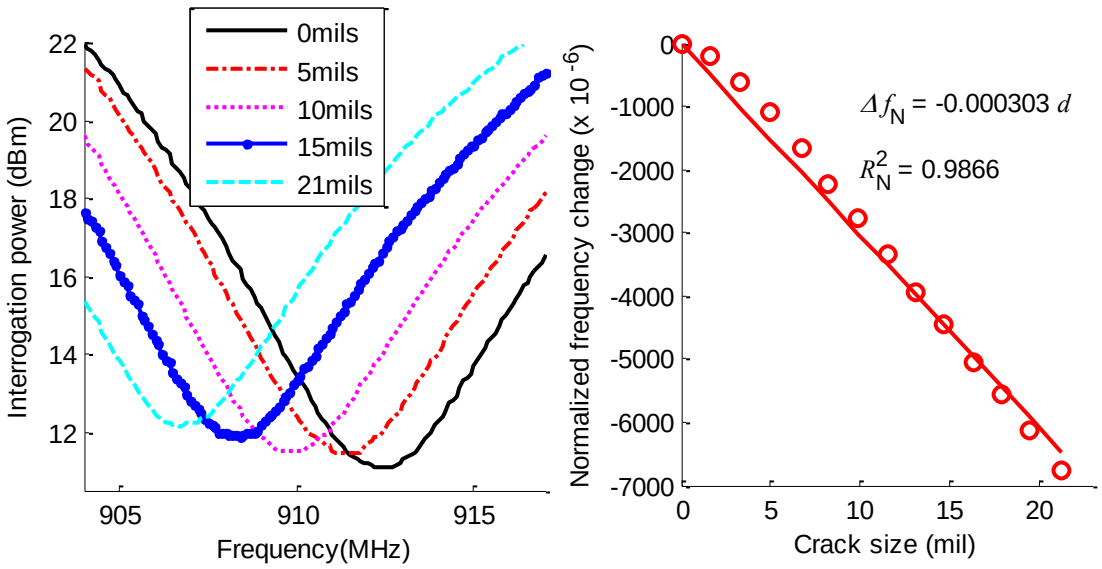

(a) Average interrogation power threshold $P(f)$

(b) Normalized frequency change Δf_N versus crack opening d (f_{R0} = 912.822 MHz)

Fig. 5.27. Experimental results for emulated crack test

Because the aluminum plates in Fig. 5.25 remain fairly rigid during the testing, crack opening in the testing is much simplified as compared to an actual fatigue crack that occurs on a structure in the field. However, it should be noted that as shown in Fig. 5.26, the sensor still experiences a complicated deformation process. At the beginning of the experiment, crack opening generated by the rotating plate causes stress concentration along the center line of the antenna ground plane, i.e. bottom copper layer. The strain/deformation also propagates through the substrate and into the top copper layer. When the crack opening increases to a certain point, fracture in the bottom copper starts, and gradually propagates to fracture in the substrate and top copper near the end of the testing. Although accurate measurement of bottom copper fracture is difficult to obtain, it is likely that most of the observed resonance frequency shift is caused by antenna strain/deformation, instead of by antenna fracture.

5.1.7 Fatigue Crack Test

To characterize sensor performance measuring fatigue crack, a compact-tension (CT) specimen is designed and fabricated according to ASTM standard E647-11 [56]. Fig. 5.28(a) shows the design drawing of the fatigue test specimen, and Fig. 5.28(b) shows a photo of the fatigue specimen made of Aluminum 6061-T651.

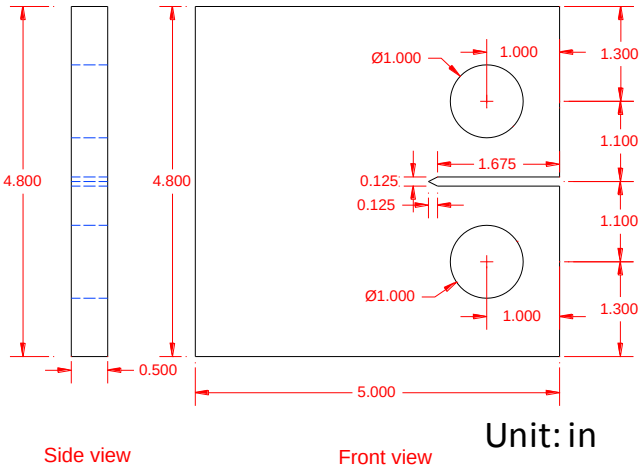

(a) Design drawing of fatigue specimen

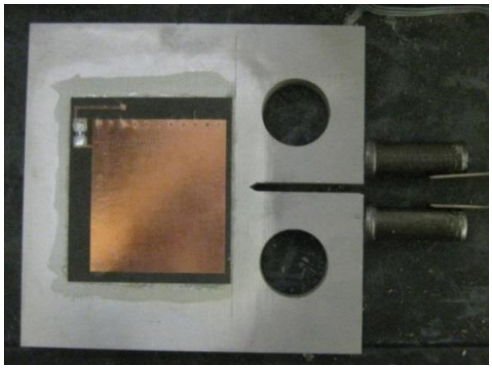

(b) Fatigue specimen together with prototype antenna sensor

Fig. 5.28. Design drawing and photo of a fatigue test specimen

A prototype sensor is installed at the center area of the 5 in. × 4.8 in. × 0.5 in. specimen. Experimental setup for the fatigue test is shown in Fig. 5.29. An extensometer is installed at the notch side of the specimen to measure crack opening width. Besides crack width measurement, crack length on the back of the CT specimen is measured. To identify crack tip location, dye penetrant is sprayed on the back surface for measuring crack length with a caliper. After a pre-crack is generated, the specimen is subject to 5 Hz cyclic loading. A loading ratio $L_R = P_{max}/P_{min} = 0.5$ is adopted. The loading level is determined by crack growth rate. In this test, the minimum and maximum load are 2 kips and 4 kips, respectively, to provide a crack growth rate that results in a reasonable

experiment duration. After every 10,000 cycles of loading, the specimen is held at 3 kips static load for wireless interrogation. Resonance frequency of the antenna sensor is interrogated by the Tagformance reader, with a panel reader antenna placed at 12 in. away from the sensor.

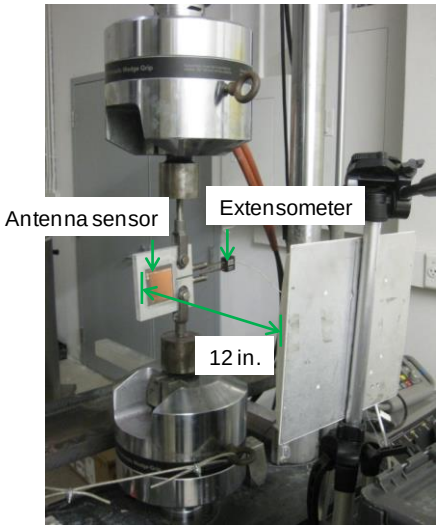

Fig. 5.29 Experiment setup for fatigue test

The specimen is broken apart after 110,000 cycles, which takes about 6 hours in total. Fig. 5.30(a) and Fig. 5.30(b) show photos of the front and back view of the specimen after 90,000 cycles. As shown in Fig. 5.30(b), the crack length after 90,000 cycles is 0.958 in. Fig. 5.30(c) and Fig. 5.30(d) show the front and back view of the failed specimen.

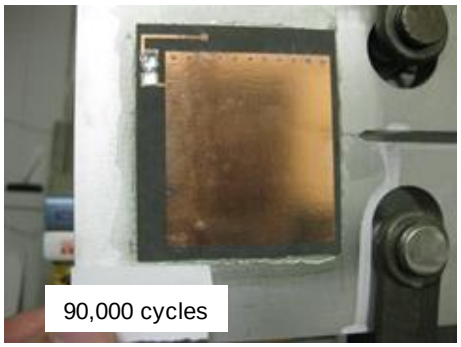

(a) Front view

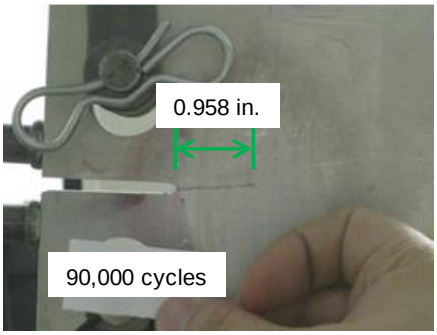

(b) Back view

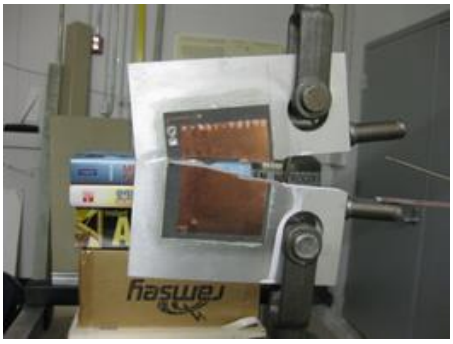

(c) Front view of the failed specimen

(d) Back view of the failed specimen

Fig. 5.30. Photos of fatigue specimen during test

Fig. 5.31(a) shows average interrogation power threshold at different crack lengths. Although measurements are obtained for ten different lengths, for clarity, plots for only four crack lengths are shown in Fig. 5.31(a). About 2MHz resonance frequency decrement is observed when the crack length increases to 0.958 in. Normalized resonance frequency changes at all crack lengths are shown in Fig. 5.31(b). Resonance frequency of the antenna sensor keeps decreasing when crack length increases. At the final stage when wireless measurement can still be obtained, crack length grows to 1.311 in. The final obtained resonance frequency drops down to 867.6MHz (i.e. 5.37% decrease in normalized resonance frequency). To make the trend in other points distinguishable, Fig. 5.31(b) does not show this final data point. Compared with the emulated crack testing result shown in Fig. 5.27(b), much less linearity is observed in fatigue testing data. This

is because more complicated deformation occurs in the sensor during fatigue testing, where stress concentration is highly localized around the crack tip. More quantitative studies, possibly through multi-physics simulation, can be performed in the future to investigate the phenomenon in detail.

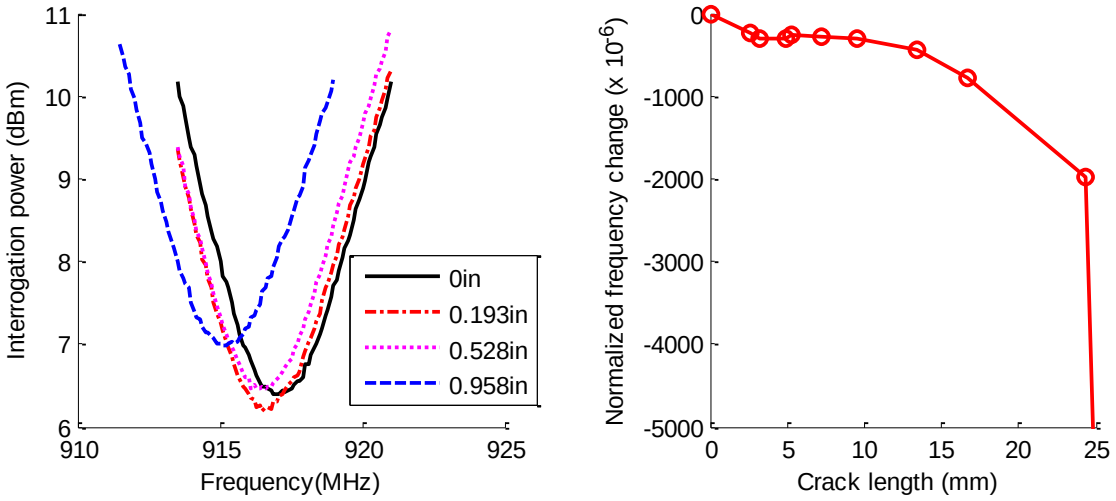

(a) Average interrogation power threshold

(b) Normalized frequency change Δf_N versus crack size d (f_{R0} = 917.101 MHz)

Fig. 5.31. Experimental results for fatigue test

5.1.8 Folded Patch Antenna Sensor Using Substrate Rogers 6202

To improve sensor reliability during temperature fluctuation, a new substrate material has been investigated [131]. The material has more stable dielectric constant under temperature fluctuation. This section describes the effort to re-design and test an antenna sensor with the new substrate material. The newly identified substrate material is Rogers 6202, a ceramic-filled PTFE composite. Table 5.2 lists key properties of substrate material Rogers 6202, as compared with Rogers 5880. The coefficients of thermal expansion of Rogers 6202 are reduced by half in x and y direction, and reduced by 87%

in z direction. With less thermal deformation under temperature fluctuation, more stable resonance frequency is also expected when temperature fluctuates.

Table 5.2. Key property comparison between Rogers 5880 and Rogers 6202

		Rogers 5880	**Rogers 6202**
Material type		Glass microfiber reinforced PTFE composite	Ceramic filled PTFE composite
Coefficient of thermal expansion (ppm/ ℉)	x	17	8
	y	27	8
	z	132	17
Dielectric constant (β_{r0}) at 73 ℉		2.2	2.94

More importantly, dielectric constant of Rogers 6202 at different temperatures is plotted in Fig. 5.32. Much smaller dielectric constant change is observed, as compared with Rogers 5880 shown in Fig. 5.24(a). With smaller dielectric constant change and less thermal deformation under temperature fluctuation, more stable resonance frequency is expected when temperature fluctuates.

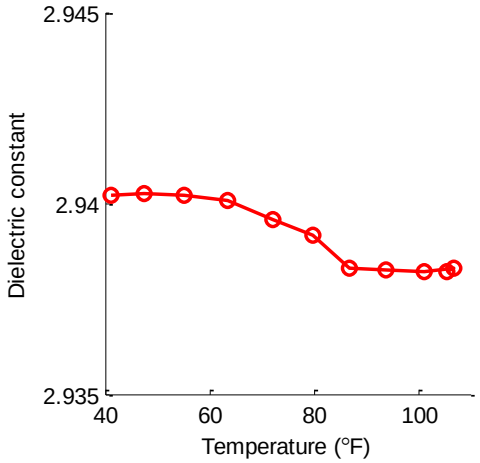

Fig. 5.32. Dielectric constant change of Rogers 6202 due to temperature fluctuation (provided by manufacturer)

The new sensor design with Rogers 6202 substrate is shown in Fig. 5.33. Since the dielectric constant magnitude of Roger 6202 is larger than Roger 5880, total copper size of the sensor decreases from 2.15 in. × 1.97 in. to 1.91 in. × 1.73 in. Matching lines are re-tuned to match the impedance of the RFID chip.

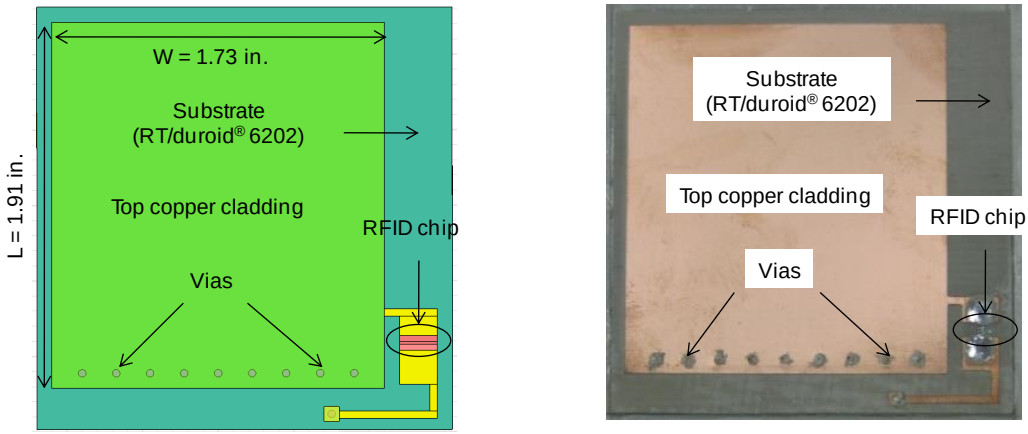

(a) Design drawing (b) Photo of manufactured sensor

Fig. 5.33. Antenna sensor with Rogers 6202 substrate material

5.1.8.1 Temperature stability test

After the antenna sensor with Rogers 6202 substrate is fabricated, temperature chamber test is conducted [131]. The test is similar to previous test for Rogers 5880 substrate, as described in Section 5.1.5. The antenna sensor with Rogers 6202 substrate together with aluminum specimen is placed in the chamber. The Tagformance reader antenna is placed 12 in. away from the sensor. Four pieces of foams are places around the test specimen and reader antenna. To keep track of temperature fluctuations in the chamber, five thermometers are placed around the foams. The experimental results are shown in Fig. 5.34. Average interrogation power threshold at different temperatures is plotted in Fig. 5.34(a). For clarity, only four temperature levels are shown. The extracted resonance frequencies at different temperatures are plotted in Fig. 5.34(b). Overall, the

resonance frequency change is only about 0.2 MHz when temperature changes from 41 ℉ to 105 ℉. Compared with previous sensor design with Rogers 5880 substrate, it is obvious that Rogers 6202 provides much better temperature stability in resonance frequency.

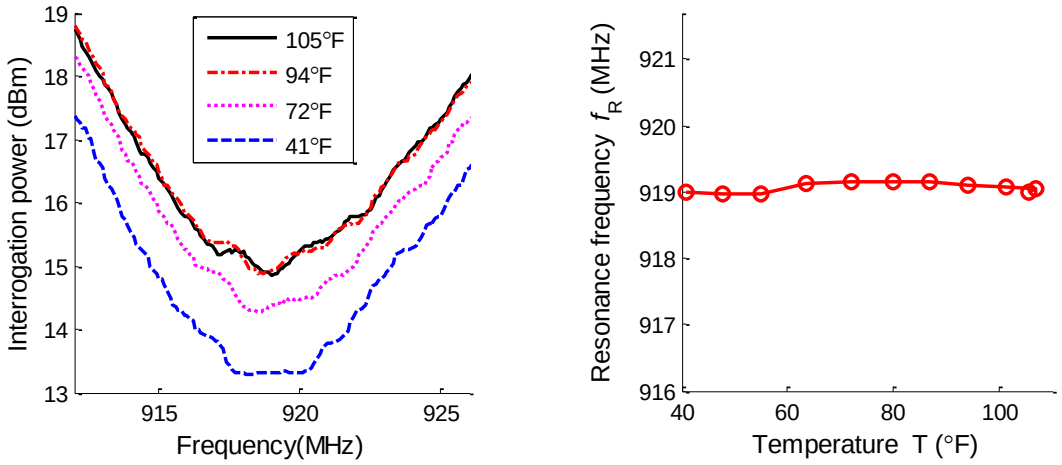

(a) Average interrogation power threshold (b) Resonance frequency change during temperature fluctuation

Fig. 5.34. Temperature chamber test results (antenna sensor with Rogers 6202 substrate)

5.1.8.2 Strain sensing test

Wireless strain sensing test for the Rogers 6202-based antenna sensor is conducted using a 55-kip MTS testing machine. Fig. 5.35(a) shows the center area of the specimen, with an antenna sensor and five metal foil strain gages (FLA-2-23-3LT, Texas Measurements, Inc) measuring the axial strain. Fig. 5.35(b) shows the specimen installed on the testing machine. The reader antenna faces the antenna sensor at a distance of 12 in.

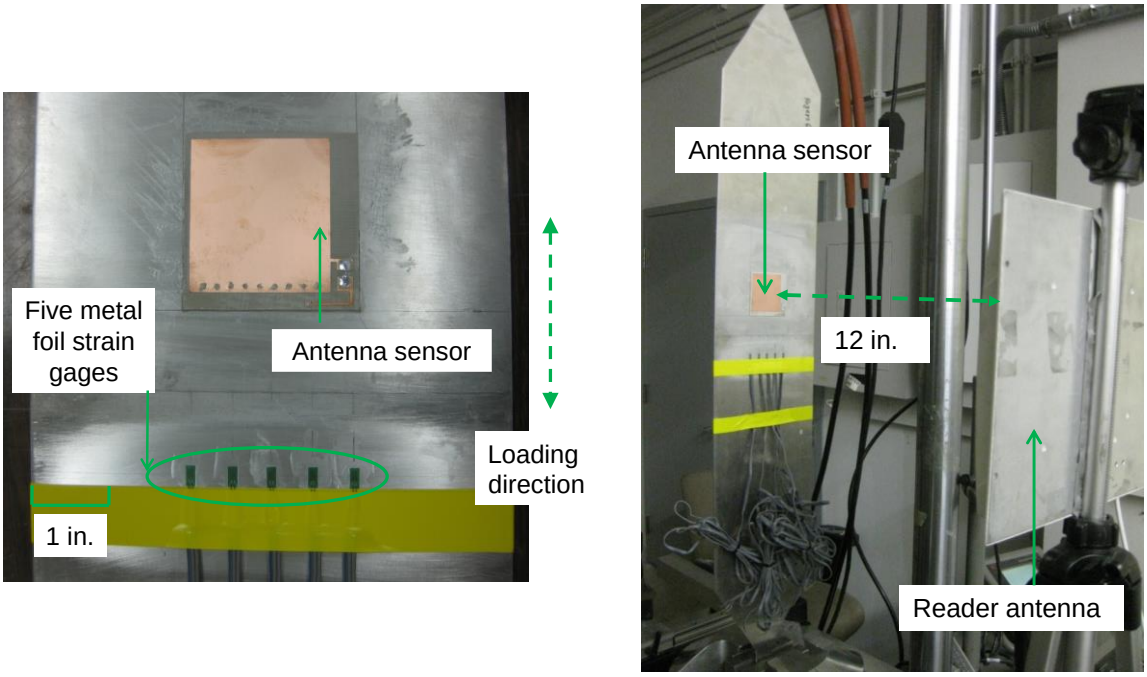

(a) Sensor instrumentation on an aluminum specimen

(b) Wireless strain sensing experiment

Fig. 5.35. Experimental setup for the tensile testing

The tensile load applied by the testing machine is configured so that approximately 50με increment is achieved at each loading step. The data analysis procedure is the same as used for the folded patch antenna sensor using Rogers 5880 substrate. Fig. 5.36(a) shows the interrogation power threshold plot for different strain levels. For clarity, only four strain levels are shown. The strain levels are calculated as the average among the five axial strain gages. Fig. 5.36(b) shows how the normalized resonance frequency of the antenna sensor changes with strain. The slope value of –0.6872 ppm/με is the normalized strain sensitivity of the antenna sensor, which means that 1 με increment on the specimen causes 0.6872 ppm decrease in the resonance frequency of the wireless strain sensor. Fig. 5.36(b) also shows the coefficient of determination $R^2 = 0.965$ from the linear regression.

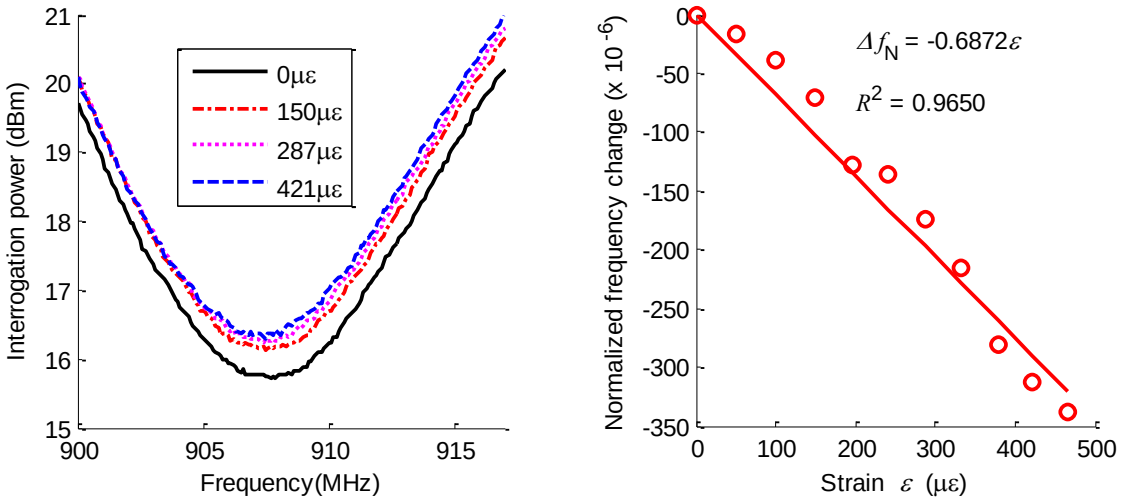

(a) Average interrogation power threshold (b) Resonance frequency f_R versus strain ε

Fig. 5.36. Tensile test results for the antenna sensor with Rogers 6202 substrate

5.1.9 Summary

Extensive experiments are conducted to verify the performance of the folded patch antenna sensor. The results demonstrate that the antenna sensor is capable of sensing strain as small as 20με and as high as 10,000 με. The strain sensing results are also consistent with different interrogation distance. The strain sensing tests are conducted at 60 in. and 84 in. distances, which show reliable measurement results. The sensor is also capable of measuring strain distribution in a small area, which is demonstrated by three and six sensor-array tests. The signal differentiation between adjacent antenna sensors is achieved by the anti-collision mechanism of the adopted RFID chip. The sensor is also validated for its crack sensing performance by emulated crack and fatigue crack tests. The results show that the antenna sensor can sense the milli-meter crack propagation, which is sufficient for the crack monitoring in the early stage.

To validate the sensor performance of the antenna sensor under temperature, the antenna sensor is tested in the temperature chamber. The resonance frequency shifts

according to temperature is measured. The results show that the folded patch antenna sensor is sensitive to the temperature change and is directly related with the substrate dielectric constant change due to temperature fluctuation. In order to calibrate the temperature change in the field monitoring, another dummy antenna sensor experiencing no strain effect is required to be installed in the monitoring area. An alternative about the temperature effect calibration is to design an antenna sensor on a substrate with stable dielectric constant under temperature. To this end, another folded patch antenna sensor is designed on the Rogers 6202 substrate. The temperature chamber test shows that the antenna sensor with Rogers 6202 substrate has consistent resonance frequency under temperature fluctuation. Further strain sensing results demonstrate that the antenna sensor is also have similar strain sensitivity as the folded patch antenna sensor on Rogers 5880 substrate.

5.2 Passive Slotted Patch Antenna Sensor

The design drawing and photo of the passive slotted patch antenna sensor is shown in Fig. 5.37. The total dimension of the sensor is 44 mm × 48 mm. The sensor size is reduced by detouring surface current along slots on the top copper cladding.

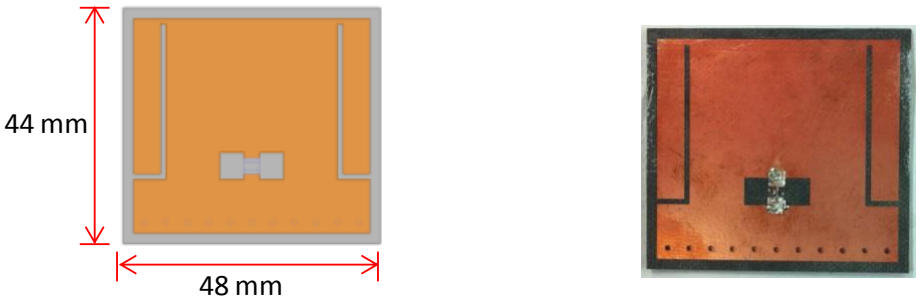

(a) Design drawing (b) Photo of fabricated sensor

Fig. 5.37. Slotted patch antenna sensor with passive RFID chip

The simulation results of passive slotted patch antenna sensor are presented in Section 3.3.2. The simulated strain sensitivity of the passive slotted patch antenna sensor is similar as the folded patch antenna sensor in Section 5.1. To evaluate sensor performance, extensive experiments are conducted to evaluate sensor performance. Section 5.2.1 presents test results of strain sensing resolution under tension, followed by results under compression in Section 5.2.2. Section 5.2.3 presents the results of strain sensing range test. Section 5.2.4 presents the strain sensing consistency evaluation at different interrogation distances. The fatigue crack sensing results are presented in Section 5.2.5 for single crack measurement. Section 5.2.6 presents test results for double cracks measurement.

5.2.1 Strain Sensing Resolution under Tension

This section describes the tensile strain sensing resolution of the passive slotted patch antenna sensor. The experimental setup is shown in Fig. 5.38. During this experiment, the reader antenna is an 18 dBi high-gain Yagi antenna. The interrogation distance is 36 in. The tensile load is configured so that approximately 20 με increment is achieved at each loading step. All other experimental setups and data analysis remain the same as before.

The interrogation power threshold plot is shown in Fig. 5.39. Eleven strain levels are tested. For clarity, interrogation power threshold plots for only four strain levels are illustrated in Fig. 5.39(a). Fig. 5.39(b) shows the normalized strain sensitivity is –0.6811 ppm/με when the interrogation distance is 36 in. The corresponding coefficient of determination is 0.9857, which indicates acceptable linearity.

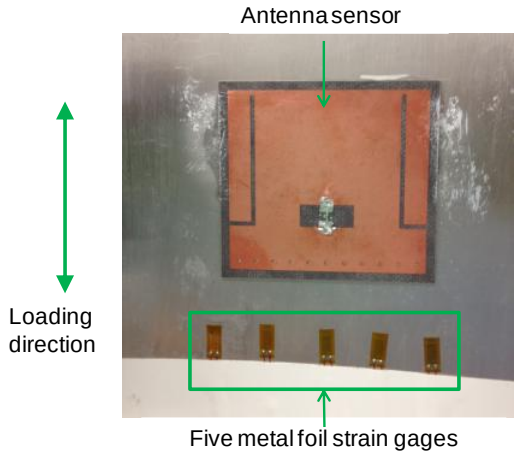

(a) Sensor instrumentation on an aluminum specimen

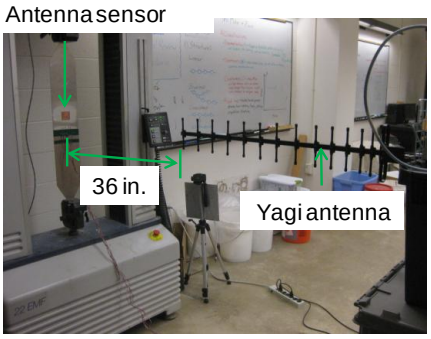

(b) Wireless strain sensing experiment

Fig. 5.38. Experimental setup for a tensile test with 36 in. interrogation distance

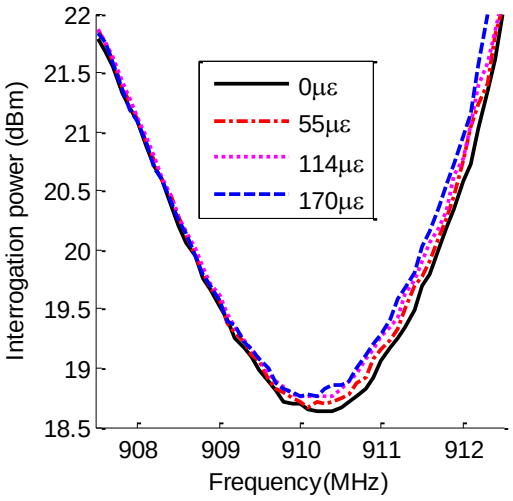

(a) Average interrogation power threshold

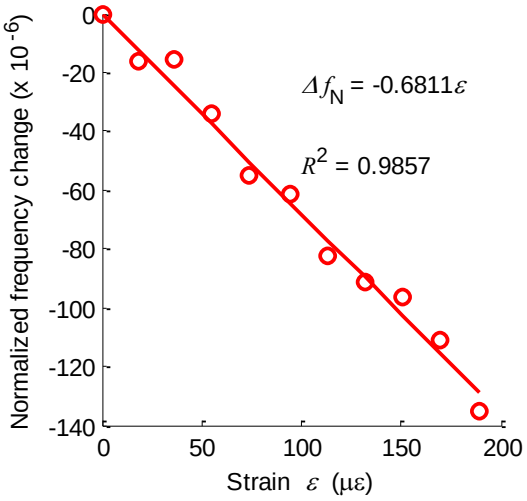

(b) Normalized resonance frequency change Δf_N versus strain ε (f_{R0} = 910.239 MHz)

Fig. 5.39. Tensile testing results at 36 in. interrogation distance

5.2.2 Strain Sensing Resolution under Compression

This section describes the compression strain sensing test of the passive slotted patch antenna sensor. The experimental setup is shown in Fig. 5.40(a), with a tapered

aluminum specimen designed to generate constant compressive strain on the surface. The compression setup includes one strong base plate with a pair of bearings in the middle of the front side. The specimen fits between the base plate and the bearings. To generate compression strain on the specimen, two bolts through the upper and lower ends of the base plate are screwed towards the specimen that is constrained by bearings in the middle. The mechanism essentially provides a 3-point bending in the side view of Fig. 5.40(b). The passive slotted patch antenna sensor is installed in the middle of the specimen, together with five metal foil strain gages for comparison. The reader antenna is an 18 dBi high-gain Yagi antenna. The interrogation distance is 20 in. The two blots are turned so that approximately -20 με increment is achieved at each loading step. All other experimental setups and data analysis remain the same as before.

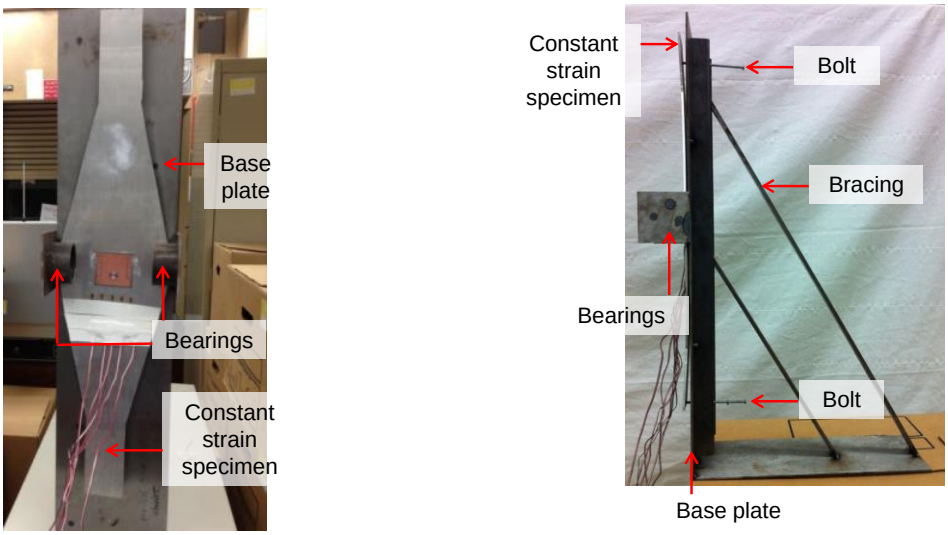

(a) Front view of the compression setup (b) Side view of the compression setup

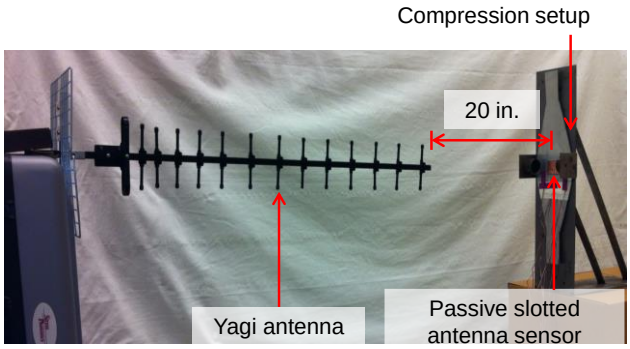

(c) Experimental setup

Fig. 5.40. Compression testing at 20 in. interrogation distance

Eleven strain levels are tested. For clarity, interrogation power threshold plots of only four strain levels are illustrated in Fig. 5.41(a). Fig. 5.41(b) shows the normalized strain sensitivity is –0.6658 ppm/με when the interrogation distance is 20 in. The corresponding coefficient of determination is 0.9826, which indicates acceptable linearity.

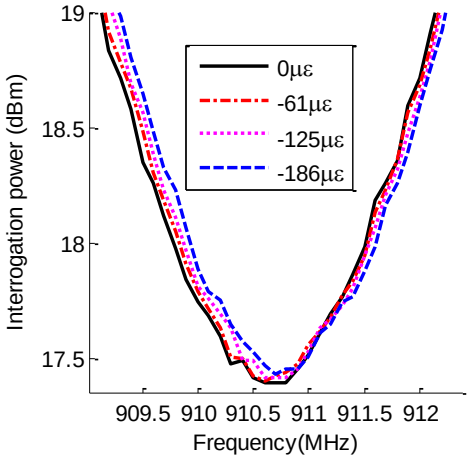

(a) Average interrogation power threshold

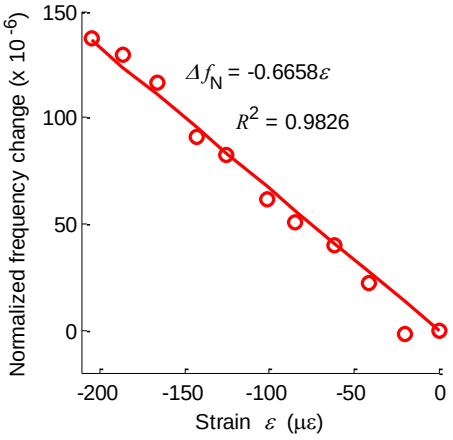

(b) Normalized resonance frequency change Δf_N versus strain ε (f_{R0} = 910.64 MHz)

Fig. 5.41. Compressive testing results at 20 in. interrogation distance

5.2.3 Large-strain Test

A large strain test is also conducted on the compression setup. The experimental setup is similar as in Section 5.2.2. The aluminum specimen is bended at three points so that approximately −100 με increment is achieved at each compression loading step. The loading increases till about −1,000 με is reached. All other experimental setups and data analysis remain the same as before. The interrogation power threshold plot is shown in Fig. 5.42. Eleven strain levels are tested in total. For clarity, interrogation power threshold plots for only four strain levels are illustrated in Fig. 5.42(a). Fig. 5.42(b) shows the normalized strain sensitivity is −0.8338 ppm/με. The corresponding coefficient of determination is 0.9906, which indicates acceptable linearity.

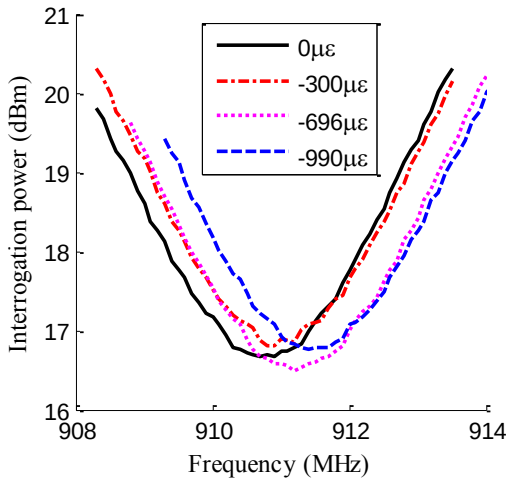

(a) Average interrogation power threshold

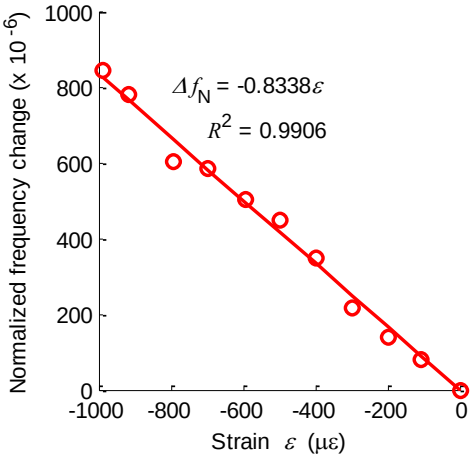

(b) Normalized resonance frequency change Δf_N versus strain ε (f_{R0} = 910.853 MHz)

Fig. 5.42. Compressive testing results at 20 in. interrogation distance

5.2.4 Sensing Consistency at Different Interrogation Distances

This section describes the strain sensing consistency of the passive slotted patch antenna sensor at different interrogation distances. The reader antenna used in the testing is an 18 dBi high-gain Yagi antenna. Section 5.2.4.1 first describes the limit of the sensor interrogation distance. Two different interrogation distances, 36 in. and 60 in., are tested for strain sensing. The results are described in Sections 5.2.4.2 and 5.2.4.3.

5.2.4.1 Interrogation distance test

Fig. 5.43(a) shows the center area of an aluminum testing specimen, with the wireless antenna sensor installed. Fig. 5.43(b) shows the experimental setup for the interrogation distance test. The Yagi reader antenna faces the wireless strain sensor, and the distance between the sensor and the reader antenna is gradually increased from 12 in. up to 90 in. The reader antenna is connected with Tagformance reader. The interrogation power threshold is recorded by the reader at different interrogation distances.

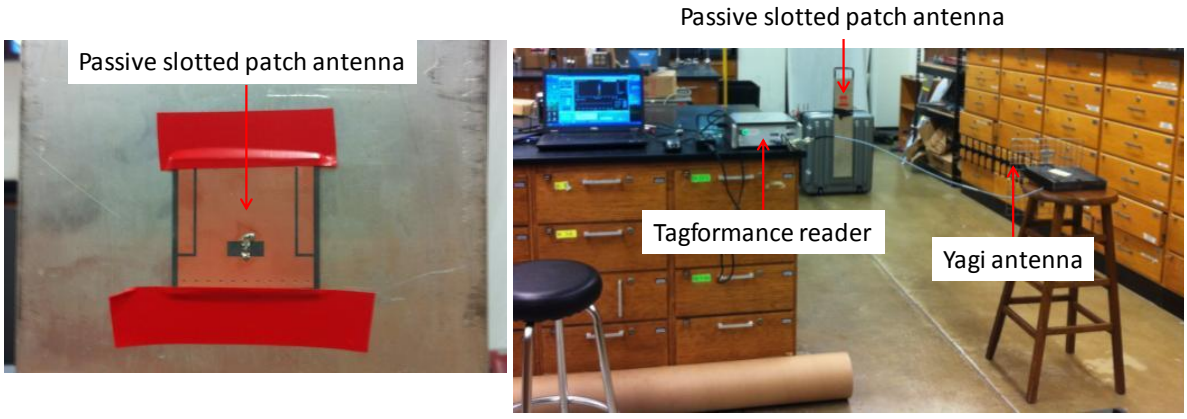

(a) Photo of the sensor installation (b) Photo of the experimental setup

Fig. 5.43. Experimental setup for the interrogation distance test.

The interrogation power from the Tagformance reader at different interrogation distances are plotted in Fig. 5.44. When the interrogation distance is 12 in., the

interrogation power threshold around the resonance frequency is less than 12 dBm, meaning a low interrogation power is needed to activate the passive sensor. When the interrogation distance is increased up to 90 in., the reader is still capable of measuring 3dB bandwidth (needed for reliably extracting resonance frequency) of the interrogation power curve. The power level around the resonance frequency increases to about 23 dBm, i.e. larger interrogation power is needed at a longer distance.

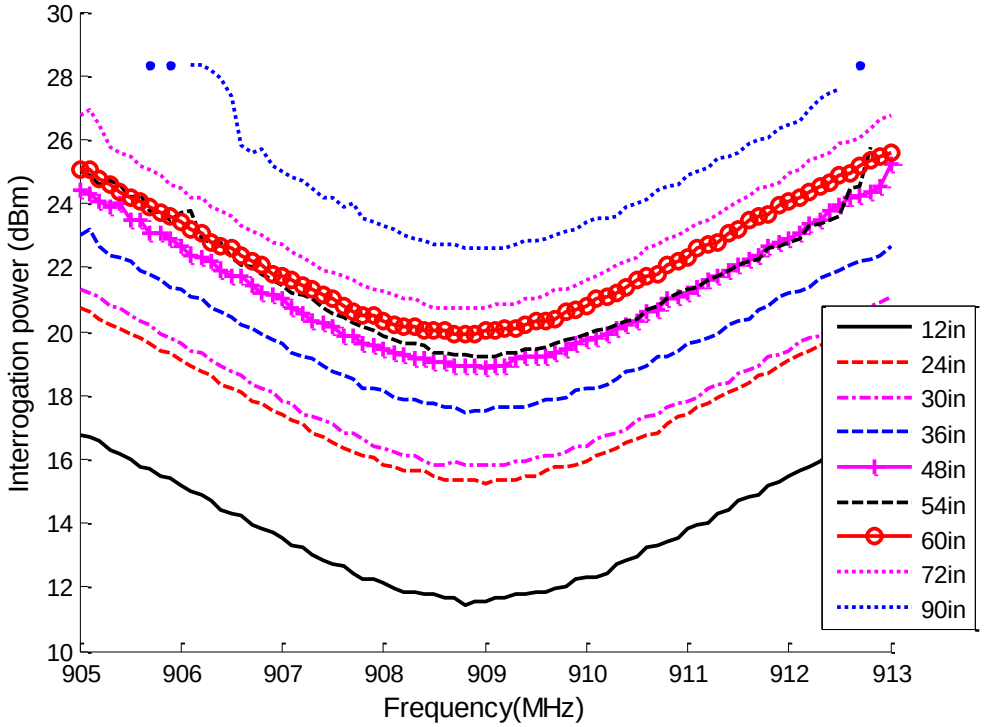

Fig. 5.44. Interrogation power at different interrogation distances

5.2.4.2 Wireless strain sensing at 36 in. interrogation distance

Wireless strain sensing is first conducted at a relatively long interrogation distance of 36 in. The tensile load is configured so that approximately 50 με increment is achieved at each loading step. All other experimental setups and data analysis remain the same as before. For clarity, interrogation power threshold plots for only four strain levels

are illustrated in Fig. 5.45(a). Fig. 5.45(b) shows the normalized strain sensitivity is –0.6626 ppm/με. The corresponding coefficient of determination is 0.9731.

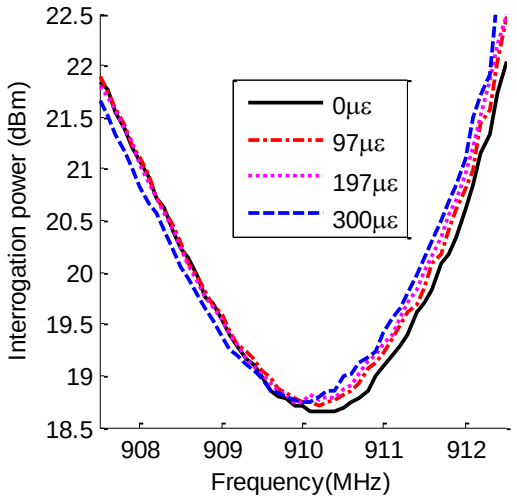

(a) Average interrogation power threshold

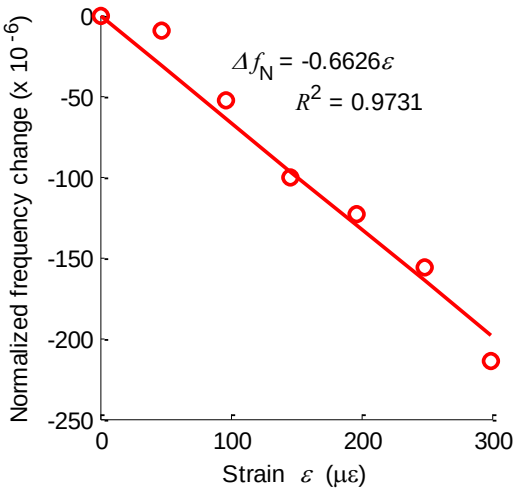

(b) Normalized resonance frequency change Δf_N versus strain ε (f_{R0} = 910.238 MHz)

Fig. 5.45. Tensile testing results at 36 in. interrogation distance

5.2.4.3 Wireless strain sensing at 60 in. interrogation distance

The interrogation distance is later increased to 60 in. for wireless strain sensing test. The tensile load is configured so that approximately 50 με increment is achieved at each loading step. All other experimental setups and data analysis remain the same as before. For clarity, interrogation power threshold plots for only four strain levels are illustrated in Fig. 5.46(a). Fig. 5.46(b) shows the normalized strain sensitivity is –0.6086 ppm/με. The corresponding coefficient of determination is 0.9734, which indicates acceptable linearity at 60 in. interrogation distance.

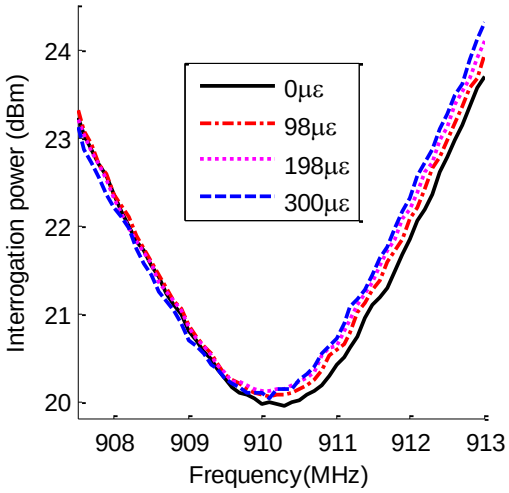

(a) Average interrogation power threshold

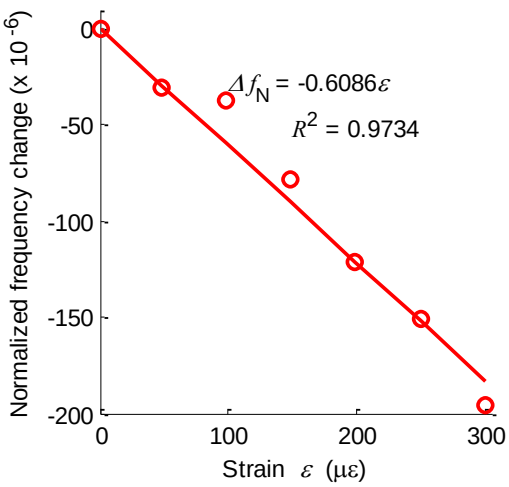

(b) Normalized resonance frequency change Δf_N versus strain ε (f_{R0} = 910.182 MHz)

Fig. 5.46. Tensile testing results at 60 in. interrogation distance

5.2.5 Single Crack Fatigue Test (Steel Specimen)

Fatigue crack test with a steel specimen has been conducted with the slotted patch antenna sensor. Fig. 5.47 shows the specimen configuration and experimental setup. A passive slotted patch antenna sensor is installed to measure crack propagation. To measure crack opening of the specimen during cyclic loading, a magnetostrictive position sensor from MTS Sensors (CS-194-AV) is installed next to the notch. The reader antenna adopted in this experiment is a 900 MHz Yagi antenna placed 36 in. away from the center of the steel specimen, as shown in Fig. 5.47(b).

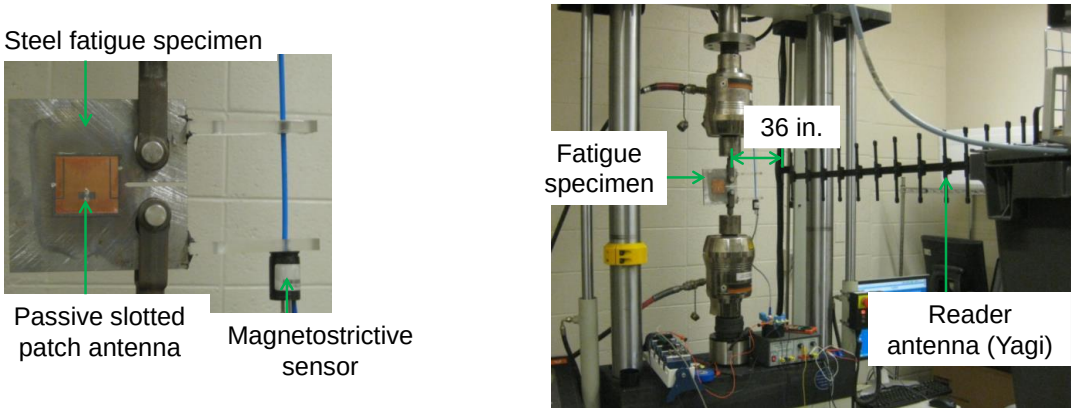

(a) Fatigue specimen (b) Experimental setup

Fig. 5.47 Experimental setup for the fatigue crack test of passive slotted-patch antenna sensor

Table 5.3 summarizes cyclic loading procedures and measurement results. The sinusoidal cyclic loading frequency is set as 5 Hz during the entire test. A small pre-crack of 0.082 in. is first generated using a larger loading range, oscillating at 1.2 ~ 4.8 kips for 15,000 cycles. After pre-crack, the tensile load oscillates in a smaller range for each of the following nine cyclic loading stages, every stage consisting of 10,000 cycles (Table 5.3). At the end of every stage, the Instron machine is paused with a static load at 3 kips for taking measurements. Interrogation power threshold of the RFID antenna sensors is first wirelessly measured using the Tagformance Lite reader unit. After applying dye penetrant on the back side of the specimen, the crack length is measured by a caliper. Crack width refers to crack opening at the initial tip of the specimen, which is converted from magnetostrictive sensor data according to the specimen dimension. After all measurements are read, the next cyclic loading stage starts.

The fatigue test continues until no signal can be received from the antenna sensor, which occurred after loading stage #9. In this fatigue test, the RFID sensor stopped responding to reader before the steel specimen breaks apart into two pieces. Therefore, the test finished without breaking the specimen. Fig. 5.48 shows representative photos of

the specimen after different loading stages. Fig. 5.48(a) through (i) show the back view of the specimen immediately after loading stage #1 through #9.

Table 5.3. Cyclic loading procedures and crack measurements during steel fatigue test

Loading stage #	Range (kips)	# of cycles	Crack length (in)	Crack width (in)
1	1.2~4.8	15,000	0.082	0
2	1.5~4.5	10,000	0.198	0.0009
3	1.5~4.5	10,000	0.243	0.0010
4	1.7~4.3	10,000	0.395	0.0011
5	1.9~4.1	10,000	0.504	0.0012
6	1.9~4.1	10,000	0.538	0.0012
7	1.9~4.1	10,000	0.596	0.0013
8	1.9~4.1	10,000	0.688	0.0014
9	1.2~4.8	10,000	0.785	0.0016

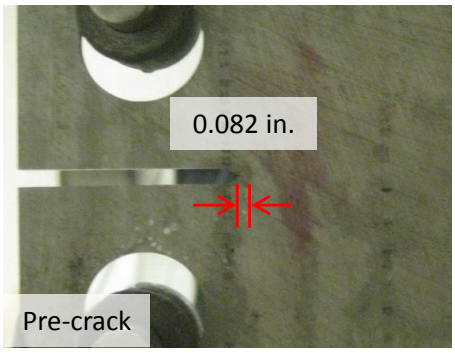

(a) Loading stage #1

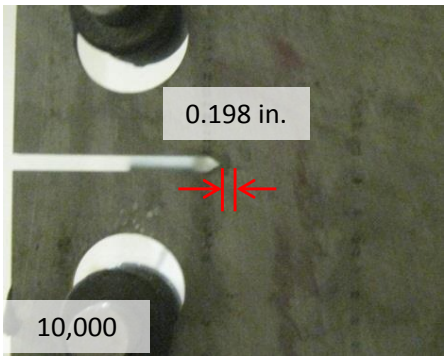

(b) Loading stage #2

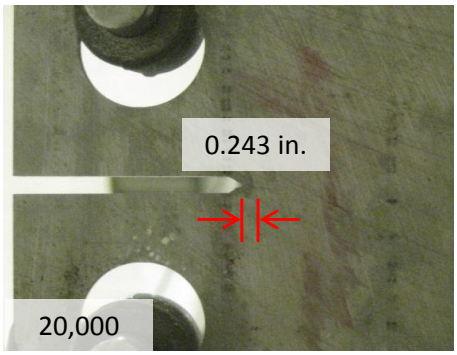

(c) Loading stage #3

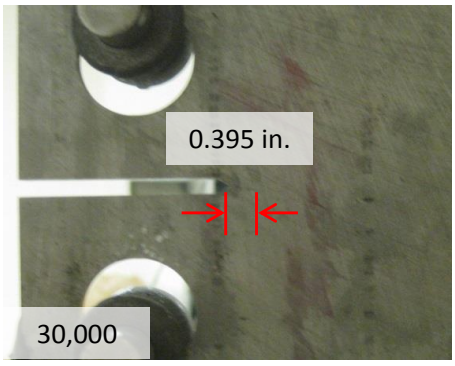

(d) Loading stage #4

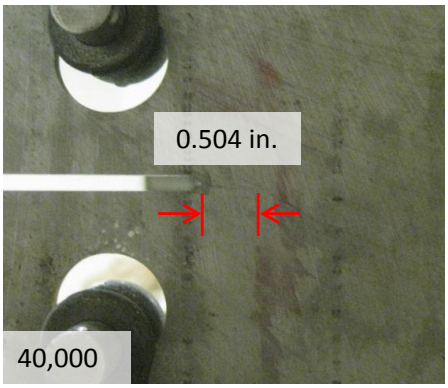

(e) Loading stage #5

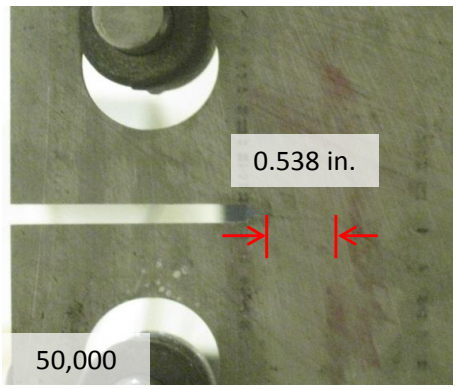

(f) Loading stage #6

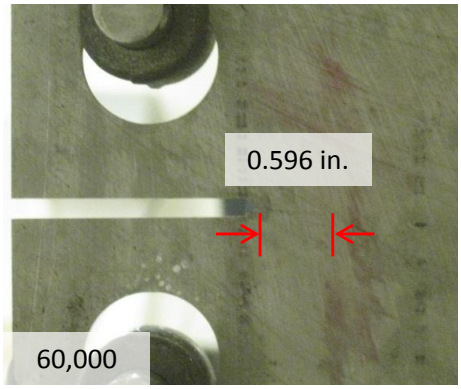

(g) Loading stage #7

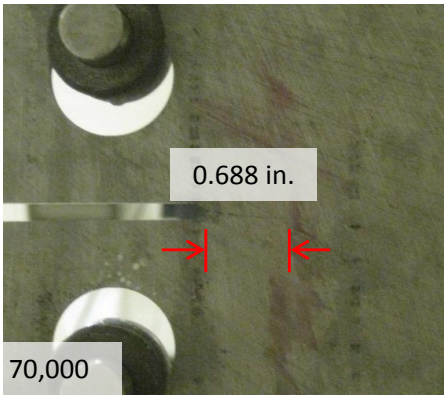

(h) Loading stage #8

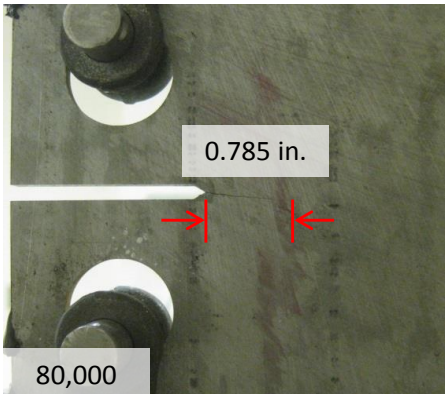

(i) Loading stage # 9

Fig. 5.48. Steel specimen photos at different crack lengths

Fig. 5.49(a) plots the average interrogation power thresholds of the antenna sensor at four example crack lengths. The resonance frequencies at all crack lengths are

extracted, and plotted in Fig. 5.49(b) against the length. Overall, about 3.5 MHz resonance frequency decrease is observed, when the crack length increases to 0.688 in. In practice, such a large frequency decrease is easy to measure by a wireless reader.

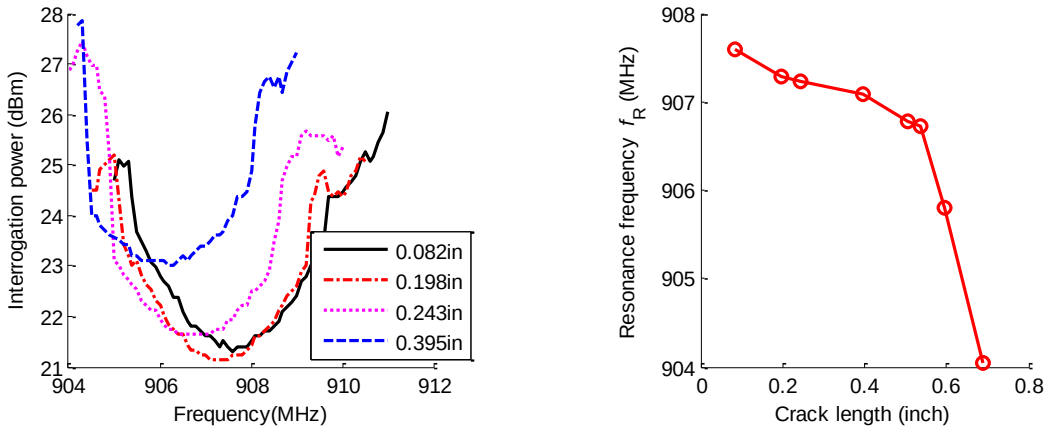

(a) Average interrogation power threshold (b) Resonance frequency versus crack length

Fig. 5.49. Fatigue test results of the passive slotted-patch antenna sensor

5.2.6 Double Crack Fatigue Test (Aluminum Specimen)

Fatigue crack test with an aluminum double-crack specimen has also been conducted to investigate sensing performance of the slotted patch antenna sensor. Fig. 5.50 shows the specimen configuration and experimental setup for fatigue crack test. Antenna sensors #1 and #2 are installed along the crack propagation paths of upper and lower notches, respectively. To measure crack opening of the specimen during cyclic loading, one magnetostrictive position sensor from MTS Sensors (CS-194-AV) is installed for each notch. Magnetostrictive sensor #1 measures upper crack opening, and magnetostrictive sensor #2 measures lower crack opening. The reader antenna adopted in this experiment is a 900MHz Yagi antenna placed 16 in. away from the center of the double-crack specimen, as shown in Fig. 5.50(b).

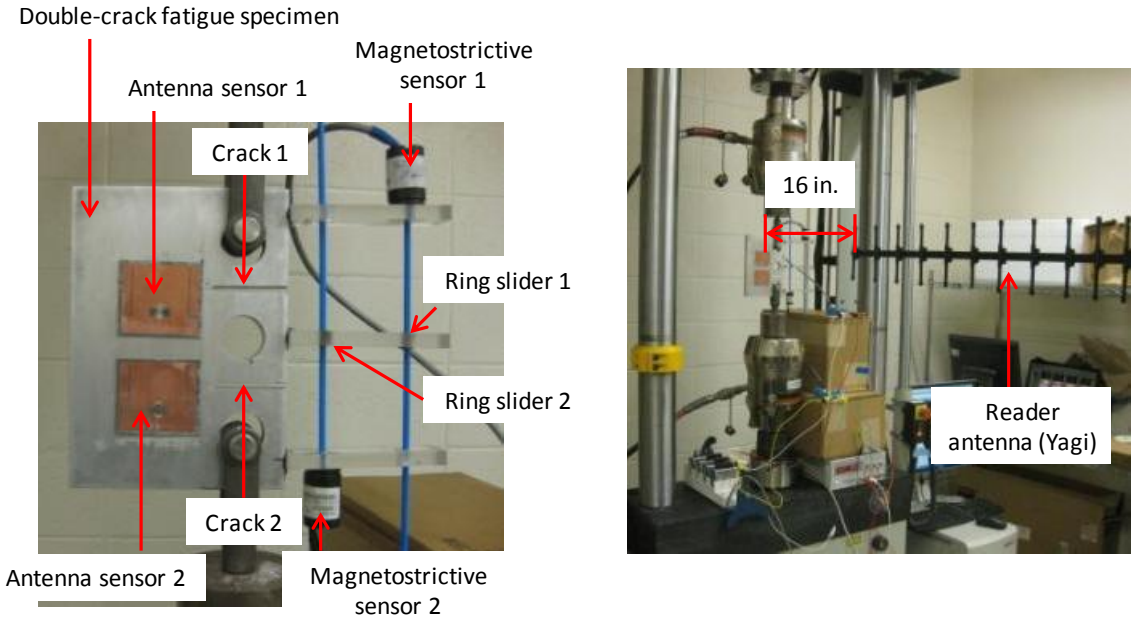

(a) Fatigue specimen (b) Experimental setup

Fig. 5.50 Experimental setup for the fatigue test of passive slotted-patch antenna sensor

Table 5.4 summarizes cyclic loading procedures and measurement results. The sinusoidal cyclic loading frequency is set as 5 Hz during the entire test. A small pre-crack of 0.071 in. is first generated using a higher load level, oscillating at 2.25 ~ 4.5 kips for 15,000 cycles. After pre-crack, the tensile load oscillates at 2 ~ 4 kips for each of the following nine cyclic loading stages, every stage consisting of 10,000 cycles. The measurement process remains the same as in Section 5.1.7 and is not repeated herein.

The fatigue test continues until the specimen broke and antenna sensor #1 debonds from the specimen, which occurs after loading stage #10. Fig. 5.51 shows representative photos of the specimen at different loading stages. Fig. 5.51(a) through (i) show the back view of the specimen after loading stages #1 through #9, with crack lengths marked on each photo. Fig. 5.51(j) shows the front view of the specimen after the final stage #10, when the sensor is debonded from the specimen.

Table 5.4. Cyclic loading procedures and crack measurements during double-crack fatigue testing

Loading stage #	Loading range (kips)	Number of cycles	Lower crack length (in)	Lower crack width (in)	Upper crack length (in)	Upper crack width (in)
1	2.25~4.5	15,000	0.11	0.00032	0.08	0.00023
2	2~4	10,000	0.14	0.00176	0.11	0.00138
3	2~4	10,000	0.237	0.00231	0.15	0.00146
4	2~4	10,000	0.262	0.00233	0.2	0.00178
5	2~4	10,000	0.362	0.00272	0.29	0.00218
6	2~4	10,000	0.375	0.00304	0.355	0.00288
7	2~4	10,000	0.455	0.00346	0.525	0.00399
8	2~4	10,000	0.579	0.00371	0.658	0.00422
9	2~4	10,000	0.787	0.00611	1.027	0.00797
10	2~4	6,395	Antenna sensor 1 debonded from the specimen			

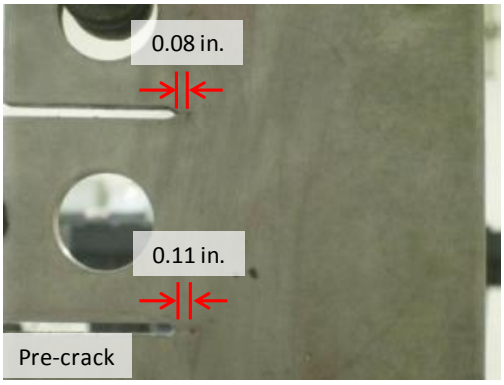

(a) Loading stage #1

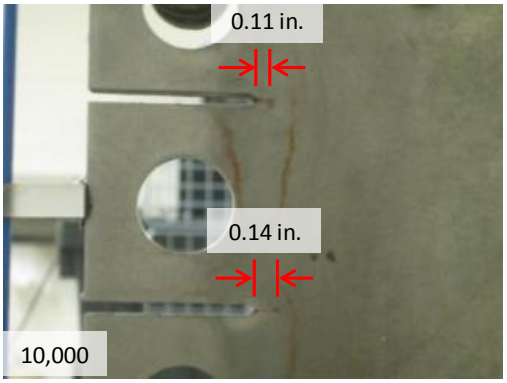

(b) Loading stage #2

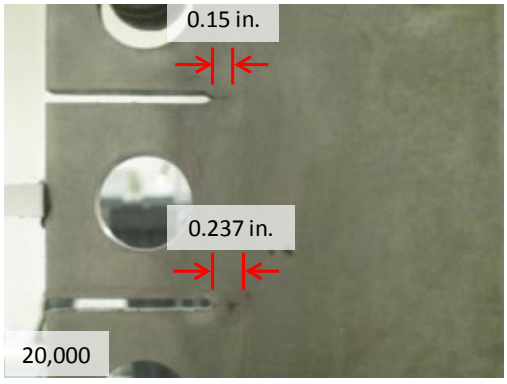

(c) Loading stage #3

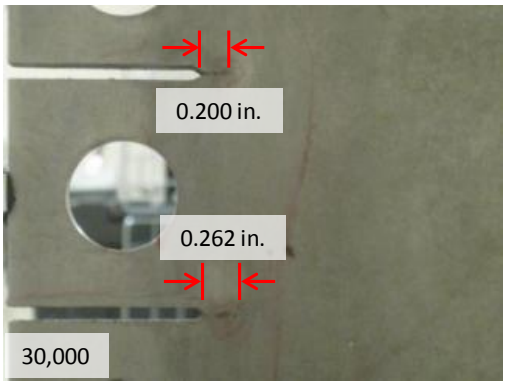

(d) Loading stage #4

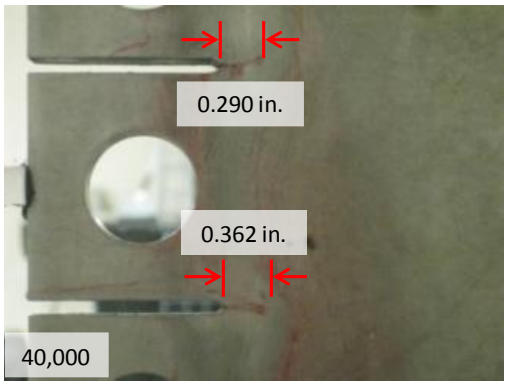

(e) Loading stage #5

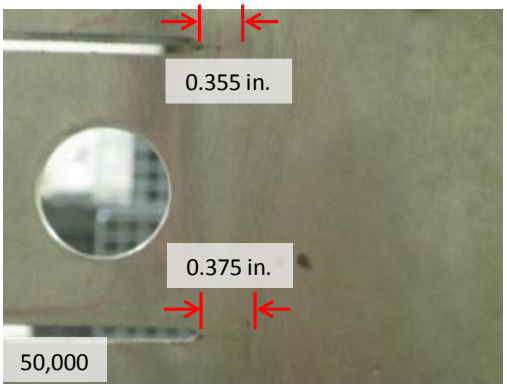

(f) Loading stage #6

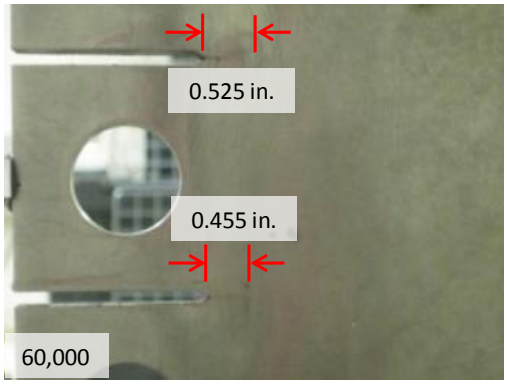

(g) Loading stage #7

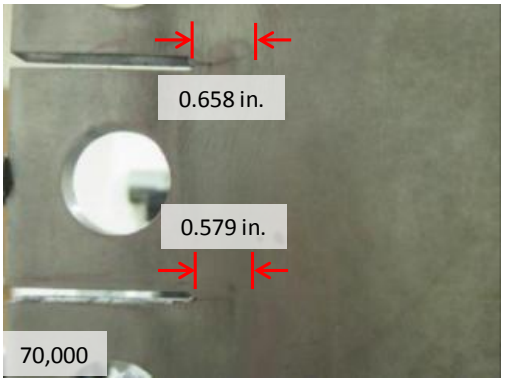

(h) Loading stage #8

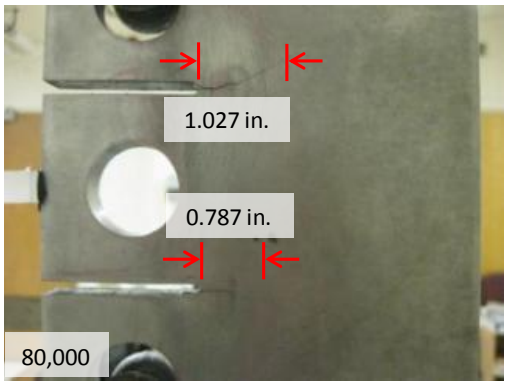

(i) Loading stage #9

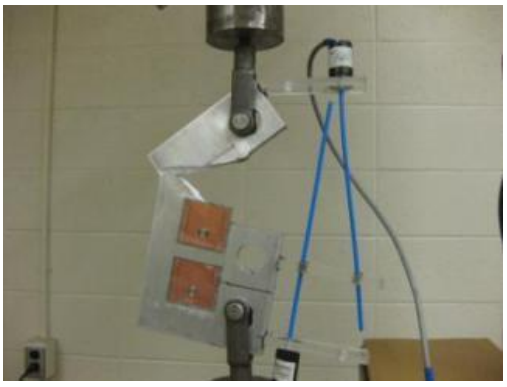

(j) Sensor #1 debonded

Fig. 5.51. Photos of double-crack specimen at different crack lengths

Fig. 5.52(a) and (b) plot the average interrogation power thresholds at different crack lengths of two antenna sensors. The resonance frequencies at all crack lengths and

widths are extracted, and plotted in Fig. 5.52(c) and (d). Overall, about 1.5 MHz resonance frequency decrease is observed from the antenna sensor #1, when the upper crack length increases to 1.027 in. Such large frequency decrease is relatively easy to measure in practice. However, much smaller resonance frequency is observed at antenna sensor #2, mainly due to the relatively smaller growth of the lower crack. The curves in Fig. 5.52(c) and (d) also show resonance frequency increments when the crack length/width are small. The results mean that at the beginning of the test, the antenna sensors experience mainly compression rather than tension. The phenomenon only occurred in double-crack test, and didn't occur in any of the single-crack tests. This could be explained by initial in-plane bending of the specimen when the testing machine is paused with a static load at 3 kips for taking wireless measurements. Nevertheless, after cracks grow near the antenna sensors, the sensors start experiencing more tension. Overall, the antenna sensors have shown clear capability of detecting stress concentration (either tension or compression).

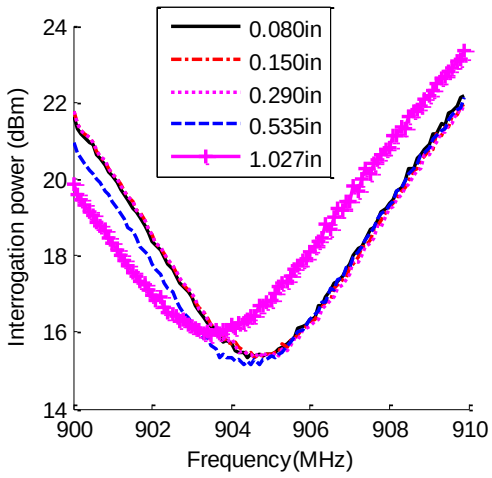

(a) Average interrogation power from Antenna sensor #1

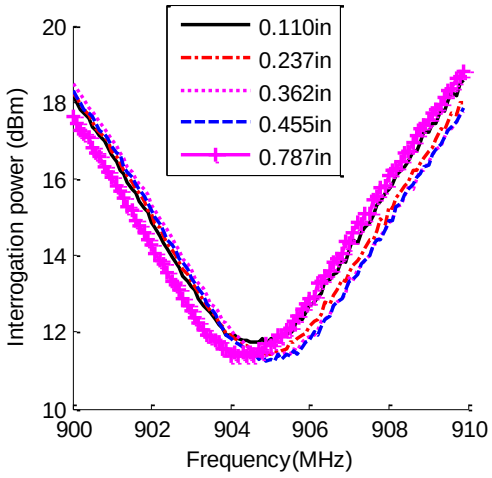

(b) Average interrogation power from Antenna sensor #2

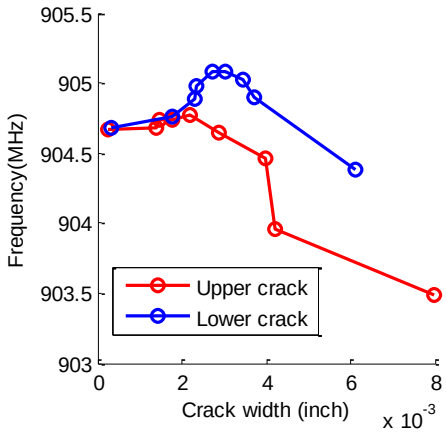

(c) Resonance frequency versus crack width

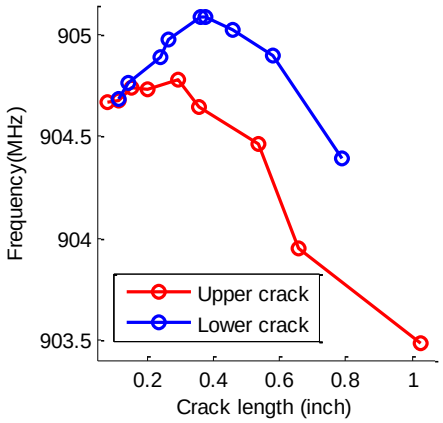

(d) Resonance frequency versus crack length

Fig. 5.52. Fatigue test results of the passive slotted-patch antenna sensors

5.2.7 Summary

Compared with the folded patch antenna sensor in Section 5.1, the passive slotted patch antenna sensor is designed to reduce sensor footprint, while maintaining sensor's operating frequency around 900 MHz. The size reduction is achieved by introducing slots on the top copper cladding to detour the surface current. The sensor size is reduced to 44 mm × 48 mm, whose area is only half of the folded patch antenna sensor. Extensive experiments are performed to verify the sensor performance. The test results show that the passive slotted patch antenna sensor is capable of sensing small strain as 20 με. The sensor can monitor not only tensile strain, but also compressive strain with same sensing mechanism. The strain sensing test results demonstrate that the sensor has consistent measurement performance at different interrogation distances. The interrogation distance test also shows that the sensor can be measured when the reader is even 90 in. away from the sensor. The single fatigue crack test indicates that the sensor can track the millimeter crack propagation generated on a steel specimen. Further double crack fatigue test shows

that the sensor can measure the crack propagation on an aluminum specimen, as well as multiple cracks monitoring in a small area.

Although the sensor can be interrogated in a distance of 90 in., it is still relatively limited for field testing in a real application. To further improve the interrogation distance, an active slotted patch antenna sensor is designed by integrating an active RFID chip. The results are presented in the following section.

5.3 Active Slotted Patch Antenna Sensor

The design drawing and photo of the active slotted patch antenna sensor is shown in Fig. 5.53. The sensor has the same outer dimension as the passive slotted patch antenna sensor (44 mm × 48 mm). The active RFID chip is integrated to boost the interrogation distance of the sensor. The simulation results have been presented in Section 3.3.2. The simulated strain sensitivity of the active slotted patch antenna sensor is similar as the passive slotted patch antenna sensor.

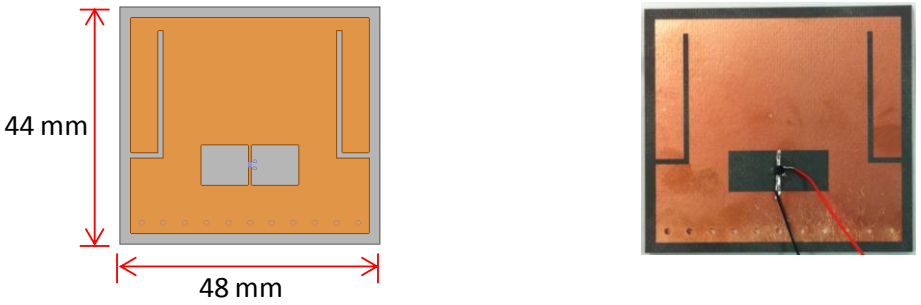

(a) Design drawing (b) Photo of fabricated sensor

Fig. 5.53. Slotted patch antenna sensor with active RFID chip

After the evaluation for passive slotted patch antenna sensor, the performance of the active slotted patch antenna sensor is similarly validated by various experiments. This section summarizes the test results of the active slotted patch antenna sensor. Section

5.3.1 presents the test results of strain sensing resolution under tension. Section 5.3.2 describes the strain sensing range results under compression. The strain sensing consistency results are similarly presented in Section 5.3.3.

5.3.1 Strain Sensing Resolution under Tension

This section describes the tensile strain sensing results of the active slotted patch antenna sensor powered by a solar cell. The experimental setup is shown in Fig. 5.54. During this experiment, the reader antenna is an 18 dBi high-gain Yagi antenna. The interrogation distance is 96 in. A solar cell is used with the active RFID sensor. Instead of sunshine, weaker in-door light is used for convenience with tensile testing. The tensile load is configured so that approximately 20 με increment is achieved at each loading step. All other experimental setups and data analysis remain the same as before.

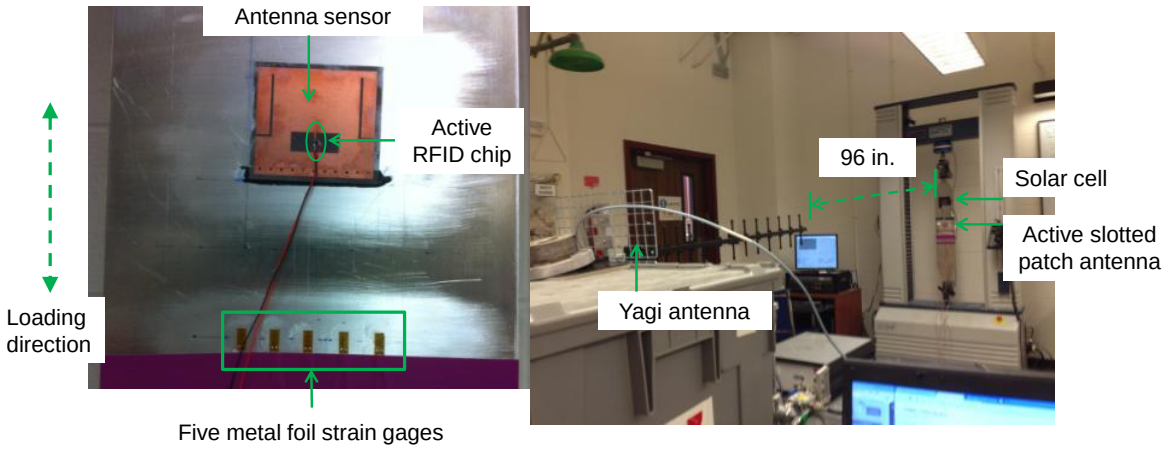

(a) Sensor instrumentation on an aluminum specimen

(b) Wireless strain sensing experiment

Fig. 5.54. Experimental setup for a tensile test with 96 in. interrogation distance

The interrogation power threshold plot is shown in Fig. 5.55. Eleven strain levels are tested in total. For clarity, interrogation power threshold plots for only four strain

levels are illustrated in Fig. 5.55(a). Fig. 5.55(b) shows the normalized strain sensitivity is –0.7054 ppm/με. The corresponding coefficient of determination is 0.9301, which needs additional improvement.

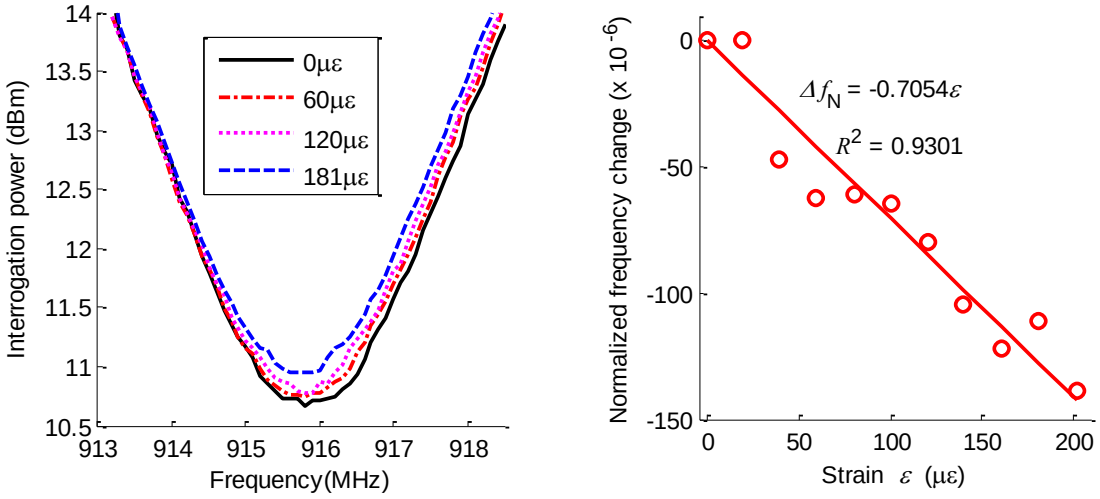

(a) Average interrogation power threshold

(b) Normalized resonance frequency change Δf_N versus strain ε (f_{R0}=915.827 MHz)

Fig. 5.55. Tensile testing results at 96 in. interrogation distance

5.3.2 Large Compressive Strain Test

A large compression strain measurement is later conducted on the active slotted patch antenna sensor. The experimental setup is similar as in Fig. 5.40. During this experiment, the reader antenna is an 18 dBi high-gain Yagi antenna. The interrogation distance is 54 in. The power source used in this scenario is the solar cell with indoor light. The aluminum specimen is bended at three points so that approximately -100 με increment is achieved at each loading step. All other experimental setups and data analysis remain the same as before. The interrogation power threshold plot is shown in Fig. 5.56. There are eleven strain levels in total. For clarity, interrogation power threshold plots for only four strain levels are illustrated in Fig. 5.56(a). Fig. 5.56(b) shows the

normalized strain sensitivity is −0.817 ppm/με. The corresponding coefficient of determination is 0.9919, which indicates acceptable linearity.

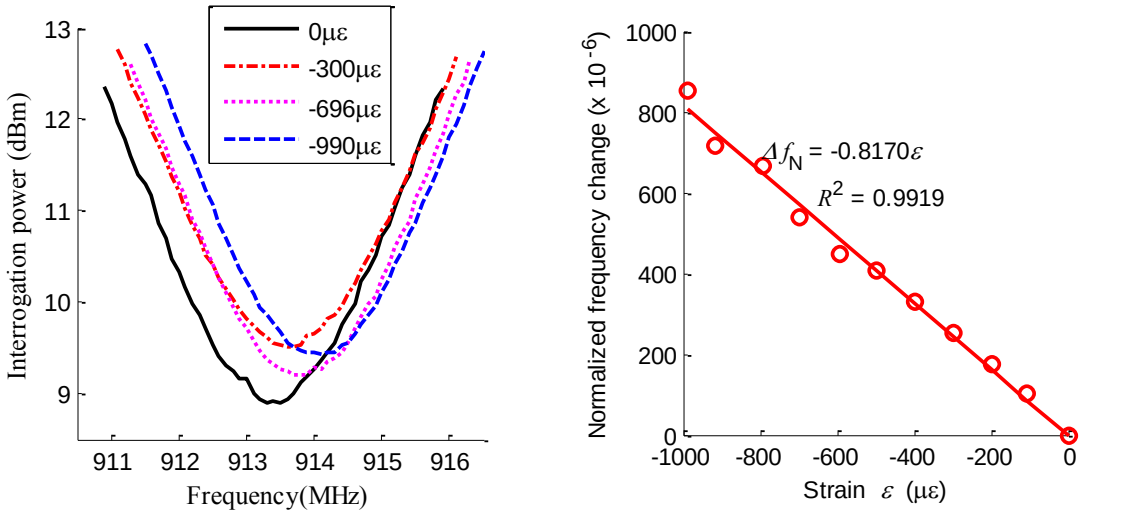

(a) Average interrogation power threshold

(b) Normalized resonance frequency change Δf_N versus strain ε (f_{R0}=913.492 MHz)

Fig. 5.56. Tensile testing results at 54 in. interrogation distance

5.3.3 Strain Sensing Consistency at Different Interrogation Distances

This section describes the strain sensing consistency of the active slotted patch antenna sensor at different interrogation distances. The reader antenna adopted in the experiments is an 18 dBi high-gain Yagi antenna. The interrogation distance test is first conducted to investigate the limit of the sensor interrogation distance. Strain sensing is then performed at a long interrogation distance of 96 in.

5.3.3.1 Interrogation distance test

Fig. 5.57(a) shows the center area of the aluminum testing specimen with the active slotted patch antenna sensor, which is connected with a solar cell (AM-8701 from

SANYO Semiconductor Co., Ltd.). Fig. 5.57(b) shows the experimental setup for the interrogation distance test. The Yagi reader antenna faces the antenna sensor. The distance between the sensor and the reader antenna is gradually increased from 12 in. up to 180 in.

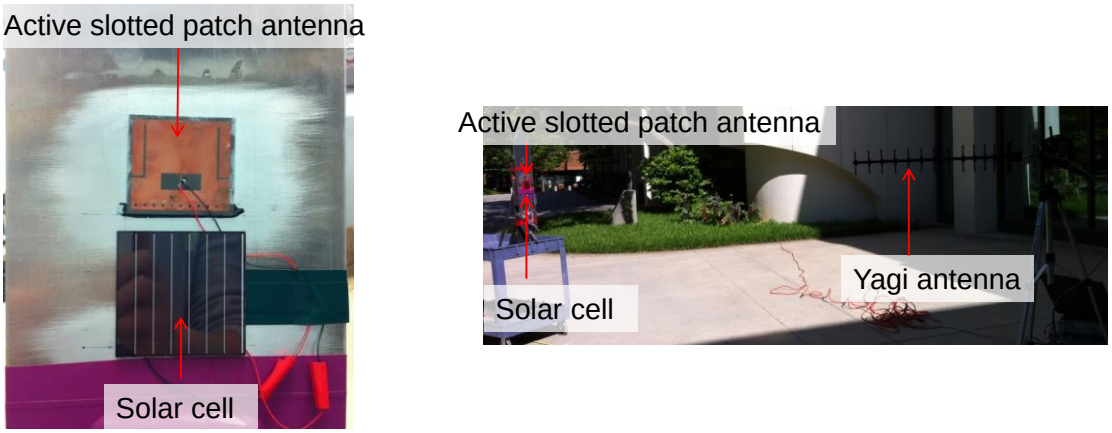

(a) Photo of the sensor installation (b) Photo of the experimental setup

Fig. 5.57. Experimental setup for the interrogation distance test.

The interrogation power from the Tagformance reader at different interrogation distances are plotted in Fig. 5.58. When the interrogation distance is 36 in., the interrogation power threshold around the resonance frequency is less than 9 dBm (i.e. very little power is needed). When the interrogation distance is increased to 156 in., the reader is still capable of measuring 3dB bandwidth of the interrogation power threshold curve; the required interrogation power level around the resonance frequency increases to 21 dBm.

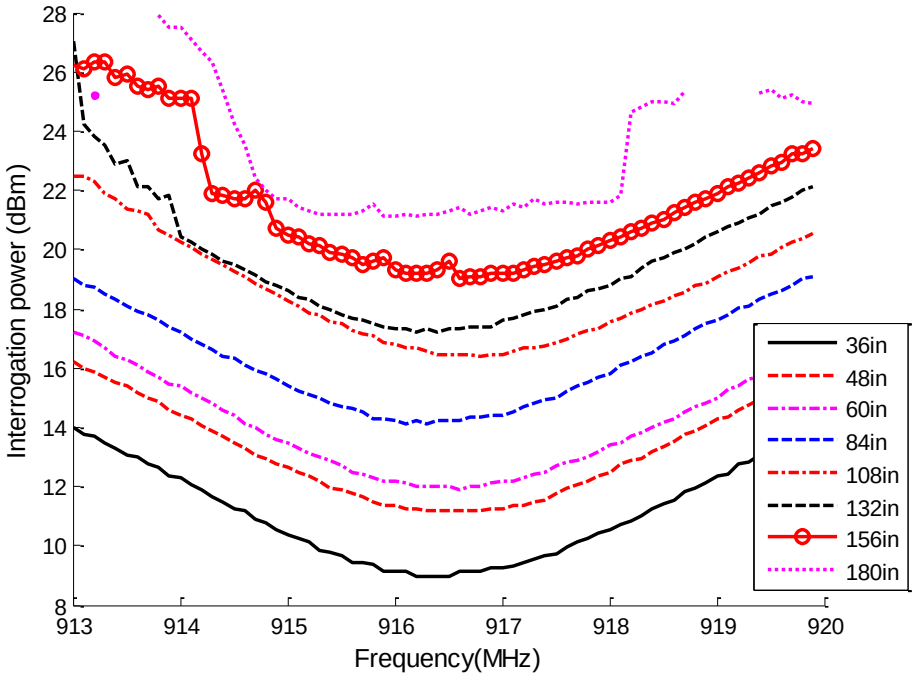

Fig. 5.58. Interrogation power at different interrogation distances

5.3.3.2 Wireless strain sensing at 96 in. interrogation distance

Strain sensing is performed with the active RFID sensor when the interrogation distance increases to 96 in. The tensile load is configured so that approximately 50 με increment is achieved at each loading step. All other experimental setups and data analysis remain the same as before. The interrogation power threshold plot is shown in Fig. 5.59. For clarity, interrogation power threshold plots for only four strain levels are illustrated in Fig. 5.59(a). Fig. 5.59(b) shows the normalized strain sensitivity is –0.7499 ppm/με. The corresponding coefficient of determination is 0.9898, which indicates acceptable linearity at this long interrogation distance of 96 in.

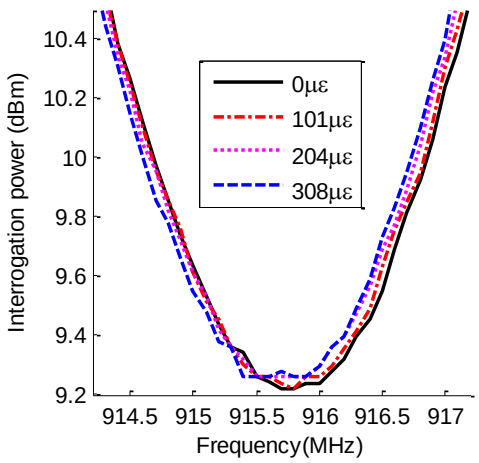

(a) Average interrogation power threshold

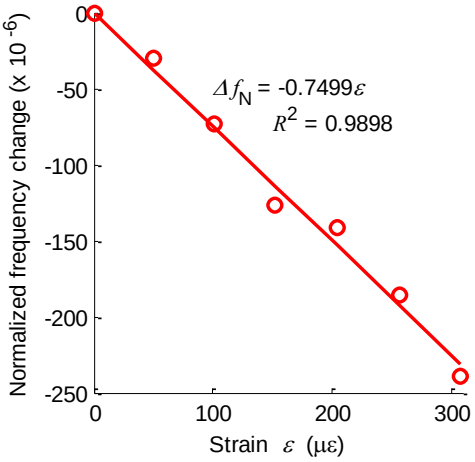

(b) Normalized resonance frequency change Δf_N versus strain ε (f_{R0}=915.791 MHz)

Fig. 5.59. Tensile testing results at 96 in. interrogation distance

5.3.4 Summary

The active slotted patch antenna sensor shows significant improvement in the interrogation distance by integrating an active RFID chip. The external power can be simply supplied by a solar cell with a dimension similar as the sensor. In this case, the solar cell can be stacked on top of the sensor, which can maintain the dimension of the overall sensor-solar cell system same as the sensor. The experimental results show that the active slotted patch antenna sensor is capable of sensing small strain as 20 με with reasonable accuracy. The sensor can also monitor the compressive strain with same sensing mechanism. The interrogation distance test results indicate that the sensor can be detected when the distance between the sensor and reader antenna is up to 156 in. The larger interrogation distance enables easier field installation and testing.

The folded patch antenna sensor presented in Section 5.1 and slotted patch antenna sensor in 5.2 and 5.3 are fabricated by PCB manufacturers, which are relatively expensive. In order to reduce the mass production cost, it is necessary to find an

alternative fabrication process. To this end, a silver nanoparticle printed sensor is designed. Instead of using copper cladding, the antenna pattern is directly printed on top of substrate by inkjet-printing techniques. The silver ink printed antenna sensor design and test results are presented in the following section.

5.4 Silver-nanoparticle Antenna Sensors

The antenna sensors presented in Section 3.3 are fabricated by milling machines or wet etching techniques. While providing accurate and reliable fabrication quality, these two methods entail expensive production cost [134]. In order to further reduce sensor cost at large quantity production, inkjet printing of silver nanoparticle is investigated for fabricating folded patch antennas. Inkjet-printing technique has been widely adopted for printing RFID temperature sensor, gas sensor, antennas, and other RF electronics [135, 136]. Different inks can be used in printing, such as silver nanoparticles [137] and carbon nanotubes (CNTs) [138]. Using this technology, a thin silver layer is inkjet-printed to replace copper for electric current conduction on the antenna sensor [139]. Section 3.1 introduces the design of silver nanoparticle printed patch antenna sensor. Section 3.2 presents strain sensing resolution tests. Section 3.3 describes large strain test of the printed antenna sensor.

5.4.1 Inkjet Printing of Silver Nanoparticle Antenna Sensors

To replace copper conductor with inkjet-printed silver nanoparticle, an absorbent surface is needed for the ink to stay and solidify. Because the Rogers RT/duroid®5880 substrate (31-mil thickness) is hydrophobic, the substrate surface is not absorbent to silver nanoparticle ink and not suitable for directly printing upon. Therefore, prior to designing the printed antenna sensor, some printing trials are performed. Based upon the trials, Kapton HN thin film with 5-mil thickness is selected as the printing substrate to

provide a more absorbent surface to silver ink, so that the printed silver ink layer has acceptable conductivity. The film has a tensile modulus of 370 ksi at room temperature, and provides elongation up to 82% at room temperature. However, because the 5-mil Kapton film is much thinner than the 31-mil Rogers substrate, antenna performance deteriorates if the Kapton film is used to completely replace the Rogers substrate. The performance deterioration includes decrease in both antenna gain and interrogation distance. Furthermore, the Kapton film has a higher relative permittivity (β_r=3.5) compared with previous Rogers substrate (β_r=2.2). The higher relative permittivity can also result in larger signal loss. Therefore, the Kapton film is not used to completely replace the Rogers substrate, but rather as the thin film to print upon. To complete the entire antenna sensor with comparable performance as before, the Kapton film printed with silver ink is laid on top of Rogers substrate. Fig. 5.60 shows that from top to bottom, the four layers of the antenna sensor are the printed silver ink, the 5-mil Kapton HN thin film, the 31-mil Rogers RT/duroid®5880 substrate, and the copper ground plane. The manufacturer of the Rogers substrate provides ordering option that allows the substrate to be purchased with a copper layer attached on one side as the ground plane.

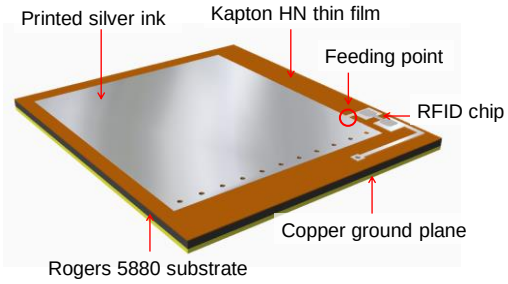

Fig. 5.60. Drawing of printed antenna sensor (perspective view)

Adding a 5-mil Kapton HN film onto the original copper antenna sensor changes electromagnetic behavior of the sensor. Based on the RFID folded patch antenna sensor, the antenna pattern needs to be redesigned for printing, so that the resonance frequency

remains at around 915 MHz. Therefore, length of the top conducting layer is reduced by 2mm, along with change of matching line and feeding point for impedance matching with the RFID chip. The dimension of the Rogers RT/duroid®5880 substrate remains 61mm × 69mm, same as previous copper antenna sensor (Fig. 5.61).

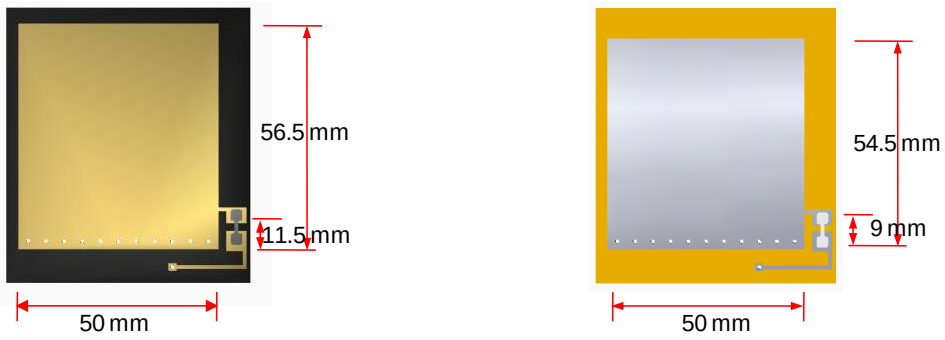

(a) RFID folded patch antenna sensor (using copper conductor)

(b) Printed RFID antenna sensor

Fig. 5.61. Design modification of the antenna sensor.

Early researchers have used a Dimatix Materials printer to inkjet-print silver nanoparticles on various substrate materials to form antennas and other RF electronics [134, 135]. The silver nanoparticle ink adopted in this research is Cabot Conductive Ink CCI-300. The Dimatix Materials printer (Fig. 5.62(a)) uses a cartridge (Fig. 5.62(b)) to hold the silver nano-particle ink, and is able to print drop sizes of 1pL (pico-Liter) or 10pL onto a smooth, hydrophobic surface. The Cabot Conductive Ink CCI-300, which contains surface modified ultra-fine silver nanoparticles, is engineered for high resolution, low resistivity, and conductive features on a variety of substrates (including Kapton HN thin film).

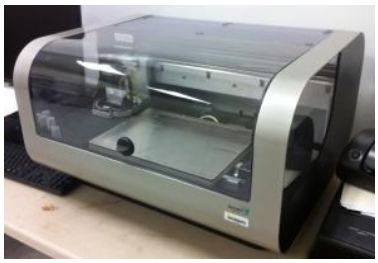

(a) Dimatix Materials printer: 673 mm(L) x 584 mm(W) x 419 mm(H)

(b) Cartridge: 90 mm(L) x 55 mm(W) x 15 mm(H)

Fig. 5.62. Equipment for inkjet printing silver nanoparticle sensors

To achieve high conductivity, the printed silver nanoparticle layer must be cured at 100~150^{o}C, depending on the substrate used. Since the CCI-300 silver nanoparticles have reduced melting and sintering temperatures compared to micro-sized particles, the printed layer can be cured at temperatures as low as 100^{o}C. The curing procedure is important because the ink needs to be set in high temperature for the particles to create a solid cohesive layer. After curing, the individual silver nanoparticles conglomerate into a solid conductive layer, which is required to provide adequate antenna performance [140]. Different printing and curing procedures have also been explored to optimize the antenna performance. In the end, it is decided to print 15 or 20 layers of silver nanoparticles in total on 5-mil Kapton HN thin film. The ink drop size is 1pL, in order to achieve smooth printed surface and a fine printing resolution. Since 15-layer or 20-layer ink is relatively thick for one-time curing, the printed antenna pattern is cured after every 5 layers of printing. With less newly printing layers every time, the curing quality has been improved. During each curing process, the printed ink is cured for 2 hours at 120 ^{o}C. The printed antenna pattern is shown in Fig. 5.63. The printed antenna pattern is bonded with the Rogers RT/duroid® 5880 substrate (thickness of 31 mils) by M-bond 610 glue from Vishay. Holes are punctured through the Kapton HN film at the vias locations of the Rogers substrate. Conductive epoxy from CircuitWorks (CW2460) is then applied inside vias to connect top silver ink printed antenna pattern with the bottom ground plane. In the

end, the RFID chip from NXP Semiconductors is soldered to complete the printed antenna sensor.

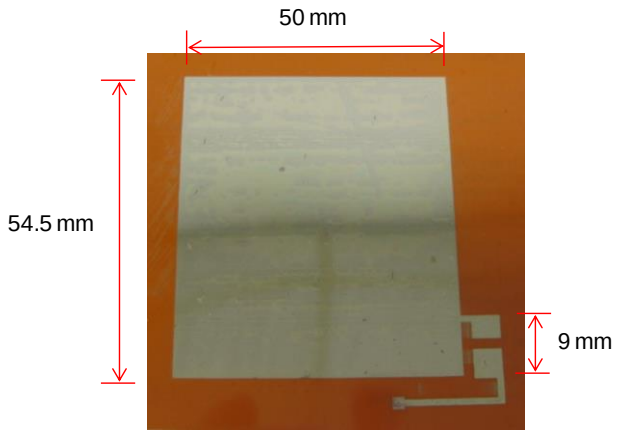

Fig. 5.63. Photo of the inkjet-printed antenna sensor pattern on Kapton HN material (3 in. × 3 in.)

5.4.2 Strain Sensing Resolution Test

Tensile tests are conducted to check the strain sensing resolutions of antenna sensors printed with 15 and 20 layers of silver nanoparticles. The experimental setup is similar as in Section 5.1.1. A panel antenna from Cushcraft Corporation (S8658WPC) serves as the reader antenna, which is placed 12 in. away from the center of the printed antenna sensor. The tensile load applied by the testing machine is configured so that approximately a 50με increment is obtained at each loading step. The interrogation power threshold of the printed antenna sensor is measured by Tagformance Lite reader at each loading step. The applied strain is increased up to around 300με in seven steps. Section 5.4.2.1 presents tensile test results of a sensor with 15 layers of printed silver ink. Section 5.4.2.2 presents results for a 20-layer printed sensor. Section 5.4.3 describes strain sensing range for a 30-layer printed sensor.

5.4.2.1 15-layer printed sensor

Fig. 5.64(a) shows the average interrogation power threshold at different strain levels. The resonance frequency is plotted against each strain level in Fig. 5.64(b). The normalized strain sensitivity is −1.0083 ppm/με and the coefficient of determination is 0.8519. Although the sensitivity is close to that of the folded patch antenna sensor, the linearity is low.

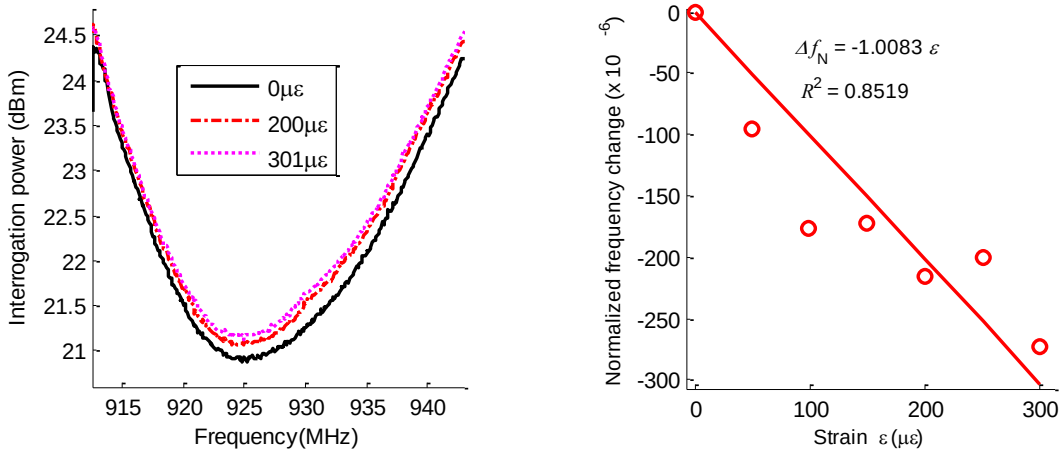

(a) Average interrogation power threshold

(b) Normalized resonance frequency change Δf_N versus strain ε (f_{R0}=925.410 MHz)

Fig. 5.64. Strain sensing results of 15-layer printed sensor

5.4.2.2 20-layer printed sensor

Since the linearity of the 15-layer printed sensor is relatively low, a 20-layer sensor is printed and tested for performance comparison. The average interrogation power threshold is plotted in Fig. 5.65(a). The interrogation power threshold around the resonance frequency is lower than that in Fig. 5.64(a), which means that the printed sensor with 20-layer silver ink requires less interrogation power to turn on the RFID chip. The reason is that the 20-layer silver ink is more conductive than the 15-layer ink. The

resonance frequency versus strain curve is plotted in Fig. 5.65(b). The normalized strain sensitivity is −1.0455 ppm/με, which is higher than the 15-layer sensor presented in Fig. 5.64. The corresponding coefficient of determination is 0.9175 which is also higher than the 15-layer sensor. The improved strain sensitivity and linearity indicate that the sensor performance is better with 20-layer fabrication. Nevertheless, the linearity of the 20-layer fabrication is still relatively low compared with previous copper antenna sensor.

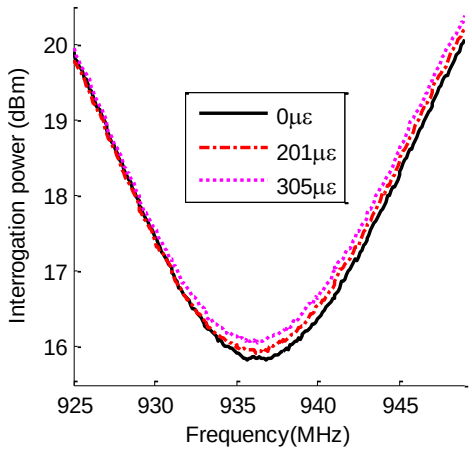

(a) Average interrogation power threshold

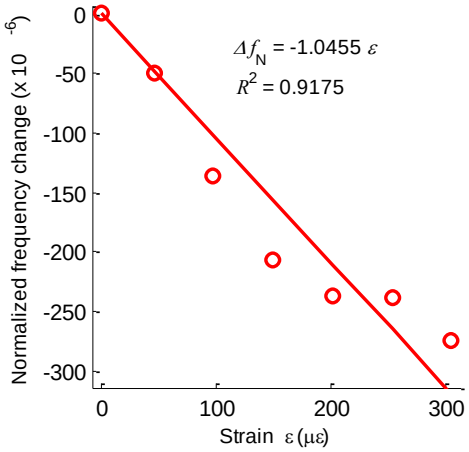

(b) Normalized resonance frequency change Δf_N versus strain ε (f_{R0}=936.436 MHz)

Fig. 5.65. Strain sensing results of 20-layer printed sensor

5.4.3 Large Strain Test (30-layer)

In this scenario, a 30-layer printed antenna sensor is tested up to 2,000 με with 500 με/step to check the strain sensing performance. Fig. 5.66(a) shows a 30-layer printed antenna sensor installed in the middle of an aluminum specimen, together with seven strain gages for reference. Fig. 5.66(b) shows experimental setup of the wireless strain sensing test. Other experimental setups and data processing remain the same as in Section 5.4.2.1.

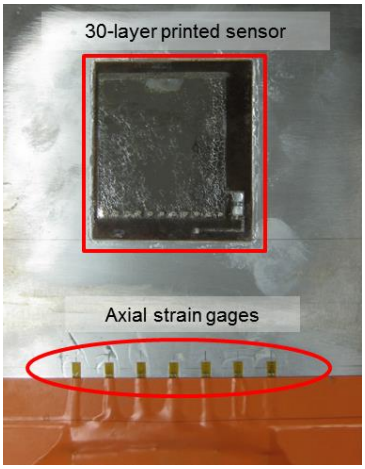

(a) Photo of the sensor instrumentation for wireless sensing experiments

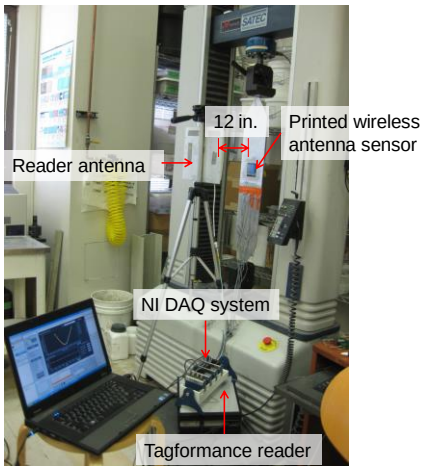

(b) Photo of the wireless strain sensing experiments relationship

Fig. 5.66 Experimental setup for the tensile tests of printed nanoparticles sensor

Fig. 5.67 (a) shows the average interrogation power threshold plot measured at different strain levels. For clarity, only four example strain levels are shown in the figure. The normalized resonance frequency change Δf_N over strain is plotted in Fig. 5.67 (b). The normalized strain sensitivity is –0.8547 ppm/με, which is close to previous copper antenna sensors. The corresponding coefficient of determination is 0.9953. The linearity of the 30-layer printed sensor is further improved compared with previous 15-layer and 20-layer printed sensor.

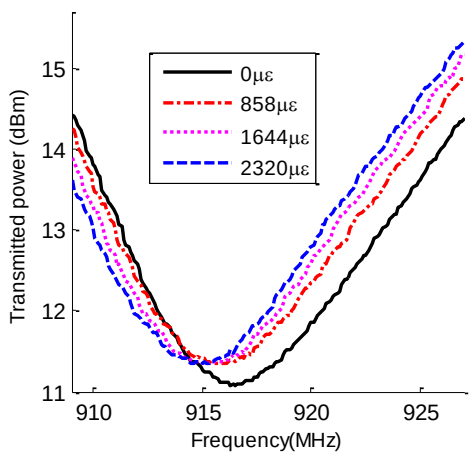

(a) Average interrogation power threshold

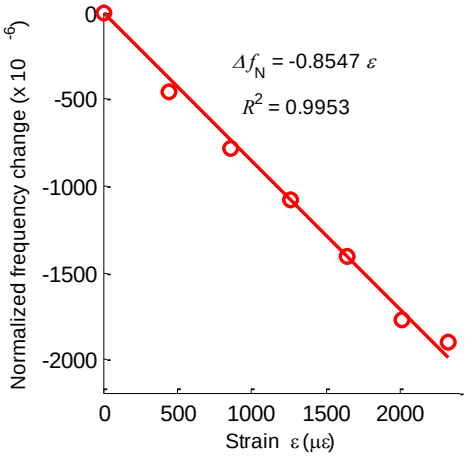

(b) Normalized resonance frequency change Δf_N versus strain ε (f_{R0}=916.544 MHz)

Fig. 5.67 Strain sensing results of 30-layer printed sensor

5.4.4 Summary

This section presents a passive RFID antenna sensor made through inkjet-printing of silver nanoparticle ink. In previous sections, although a copper antenna sensor shows good performance for strain and crack sensing, the sensor fabrication cost is relatively high. To lower fabrication cost, this section investigates inkjet printing technique for sensor fabrication. Silver nanoparticle ink is printed on a Kapton polyimide thin film to form the conducting layers of the antenna pattern. First, the copper antenna sensor is redesigned by integrating 5-mil Kapton HN thin film into the sensor. Strain sensing performance of the printed antenna sensor is then validated through numerical simulation. For experimental validation, two sensors are fabricated, one with 15-layer printing and the other with 20 layers. Both sensors are tested for strain sensing. The tensile test results show that the strain sensing linearity of the 20-layer sensor is higher than the 15-layer sensor, which indicates that the printed sensor performance can be improved by increasing the number of printed silver ink layers. Meanwhile, the strain sensitivity of the

printed antenna sensor is also similar as the previous copper patch antenna sensor. Future work is needed to improve the strain sensing linearity of the printed sensor. The footprint of the copper antenna sensor will be further reduced by implementing miniaturization techniques.

5.5 Frequency Doubling Antenna Sensor

This section presents test results for four different prototypes of the frequency doubling antenna sensor. Section 5.5.1 presents strain sensing results of Prototype A frequency doubling antenna sensor, which adopts 2.9 GHz patch antenna as sensor-side receiving antenna and 5.8 GHz patch antenna as sensor-side transmitting antenna. Section 5.5.2 presents test results of Prototype B, which replaces 5.8 GHz patch antenna with 5.8 GHz wideband antenna as the sensor-side transmitting antenna. The 5.8 GHz wideband antenna is intentionally designed to avoid multiple peaks of the overall receiving power curve. Section 5.5.3 describes the test results of Prototype B, which uses 90 ° rotated patch antenna as the 5.8 GHz sensor-side transmitting antenna to reduce possible coupling effect between receiving and transmitting antennas. Finally, the test results of Prototype D are presented in Section 5.5.4. Prototype D adopts 90 ° rotated 5.8 GHz wideband patch antenna as the transmitting antenna.

5.5.1 Frequency Doubling Antenna Sensor — Prototype A

The design drawing and photo of the frequency doubling sensor Prototype A are shown in Fig. 5.68. The prototype A frequency doubling antenna sensor includes a 2.9 GHz patch antenna, a diode-integrated matching network, and a 5.8 GHz patch antenna sensor. The total dimension of the prototype A sensor is 142 mm × 70 mm. During operation, the reader-side transmitting antenna emits an interrogation signal at frequency *f* first. The 2.9 GHz receiving antenna at the sensor-side receives the interrogation signal

and transmits the signal to the sensor side transmitting antenna through diode integrated matching network. The signal received at the sensor-side transmitting antenna has a frequency of 2*f*, which has been doubled by the diode. Then the signal with doubled frequency is transmitted back to the reader for interpretation. Since the return signal from the sensor has different frequency compared with interrogation signal from the reader, the reader can easily differentiate signal from frequency doubling antenna sensor to the unwanted environmental noise. To improve the energy transmission efficiency across the diode integrated matching network, a 33 nH is installed in parallel with the diode.

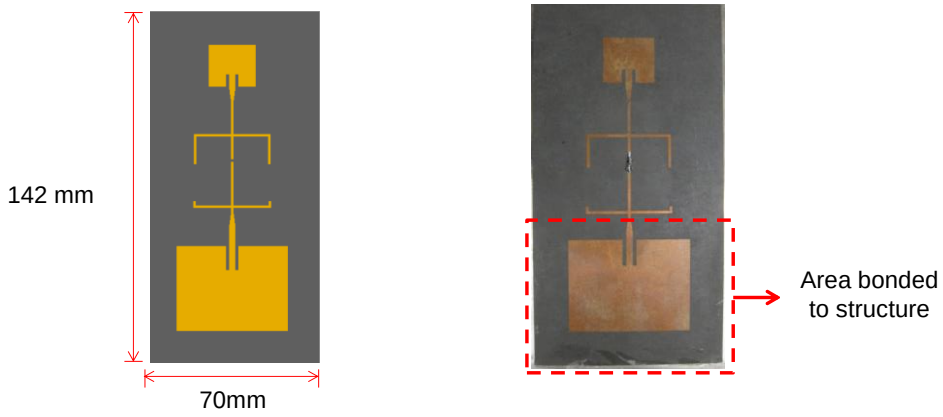

(a) Design drawing (b) Photo of fabricated sensor

Fig. 5.68. Frequency doubling sensor prototype A.

During the strain sensing test, only the 2.9 GHz transmitting antenna is bonded to the structural surface, while all other components are floating over the structural surface. To check the result consistency, the strain sensing performance with different combinations of reader antennas is investigated. Three different reader antennas: double ridge horn antenna, 2.9 GHz pyramidal horn antenna, and 5.8 GHz pyramidal horn antenna, are adopted for comparing sensing performance. The key parameters of these three reader antennas are summarized in the Table 5.5. As shown in this table, the double ridge horn antenna is a wideband antenna, while the antenna gain is also low. On the

other hand, the two pyramidal horn antennas, 2.9 GHz and 5.8 GHz antennas, are relatively narrowband and have much higher antenna gains. The vertical beamwidths of the two pyramidal horn antennas are also small, which may not be good for antenna alignment, although the lab experiments are acceptable.

Table 5.5. Key antenna parameters of the three reader antennas

	Double ridge horn antenna	Pyramidal horn antenna	
		2.9GHz	5.8 GHz
Part number	AH-118	PE9863/SF-20	PE9859/SF-20
Frequency range (GHz)	1-18	2.6-3.95	5.85-8.2
Gain (dBi)	7.2-10.4	20	20
Vertical beamwidth ( )	N/A	17.2	18.7
Horizontal beamwidth ( )	N/A	16.5	18.8

Section 5.5.1.1 shows the results with a double ridged horn antenna as the 2.9 GHz reader transmitting antenna, and a 5.8GHz pyramidal horn antenna as the 5.8 GHz reader receiving antenna. Section 5.5.1.2 presents the results with two pyramidal horn antennas as the reader-side transmitting and receiving antenna.

5.5.1.1 Strain sensing scenario #1 (double ridged horn antenna / 5.8 GHz pyramidal horn antenna)

In this experiment scenario, a double ridged horn antenna serves as 2.9 GHz transmitting antenna at the reader side, while a 5.8 GHz pyramidal horn antenna serves as the receiving antenna, as shown in Fig. 5.69. The interrogation distance between reader antennas and the sensor is set to 20 in. The tensile loading is increased to generate strain up to 300 με with 50 με per loading step. The received power at different frequencies are recorded and plotted in Fig. 5.70(a). The resonance frequencies at different strain levels is thus extracted and plotted in Fig. 5.70(b), showing a strain sensitivity of −5.774 kHz/με and a determination coefficient of 0.9844.

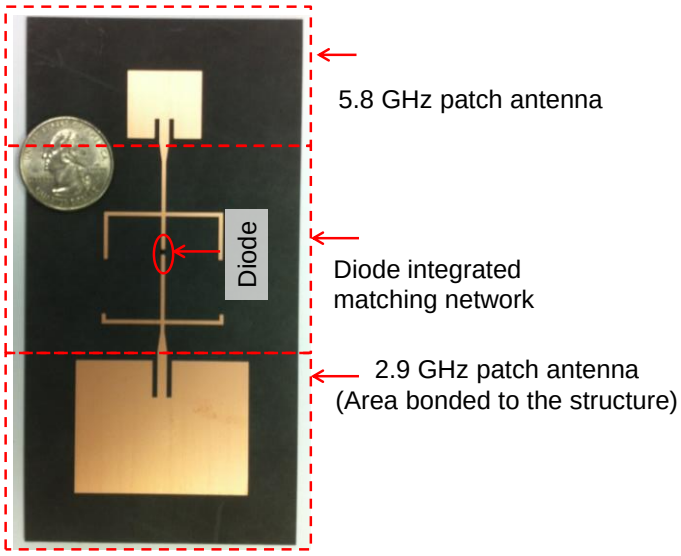

(a) Components of prototype A frequency doubling antenna

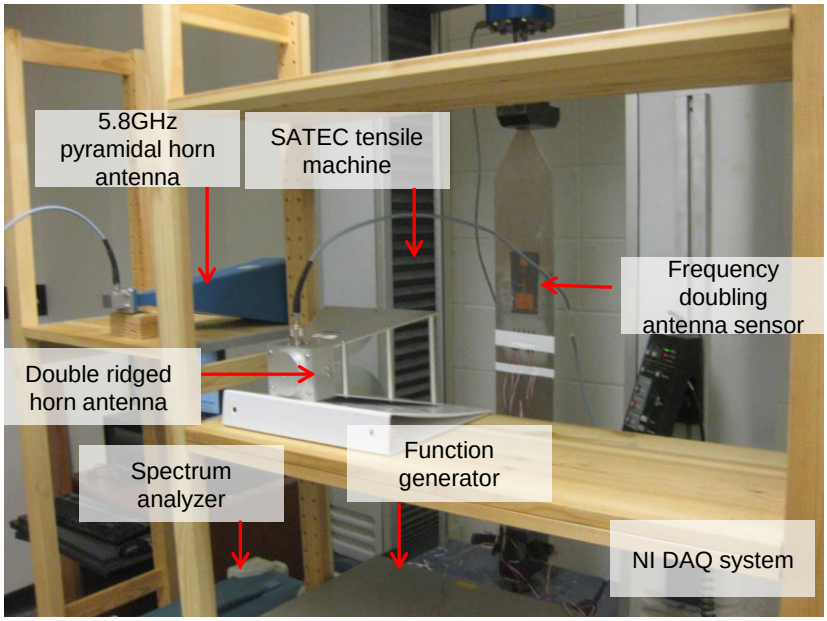

(b) Experimental setup

Fig. 5.69. Tensile test setup of the Prototype A frequency doubling sensor

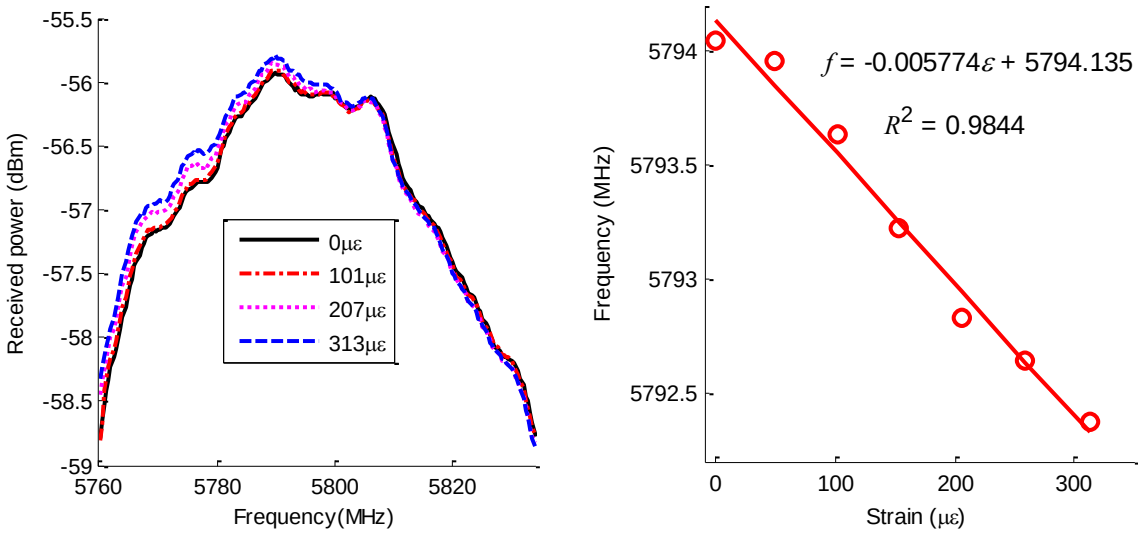

(a) Average received power plot at different strain levels

(b) Resonance frequency versus strain

Fig. 5.70. Experimental results of the frequency doubling sensor (prototype A); a double ridged horn and a 5.8 GHz pyramidal horn are used at reader side.

A similar test is performed to the sensor when the 33nH inductor is removed. The power transmission efficiency of the diode is therefore lower, and the interrogation distance is reduced to 12 in. The test results are plotted in Fig. 5.71. The strain sensitivity is –3.247 kHz/με and a determination coefficient is 0.9850.

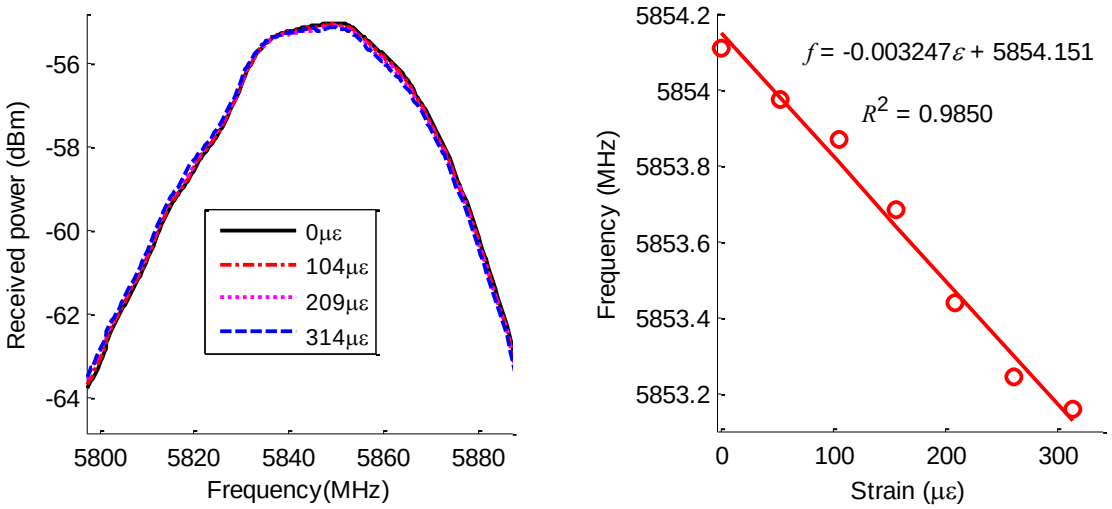

(a) Average received power plot at different strain levels

(b) Resonance frequency change with strain

Fig. 5.71. Experimental results of the frequency doubling sensor (prototype A) without inductor; a double ridged horn and a 5.8 GHz pyramidal horn are used at reader side.

5.5.1.2 Strain sensing scenario #2 (2.9 & 5.8 GHz pyramidal horn antenna)

In this scenario, two pyramidal horn antennas serve as 2.9 GHz transmitting and 5.8 GHz receiving antennas at the reader side. The interrogation distance between reader antennas and the sensor is set to 20 in. Fig. 5.72(a) shows the average received power plot. The resonance frequencies at all strain levels are then extracted and plotted in Fig. 5.72(b). The strain sensitivity and the determination coefficient are –5.252 kHz/με and 0.9611, respectively.

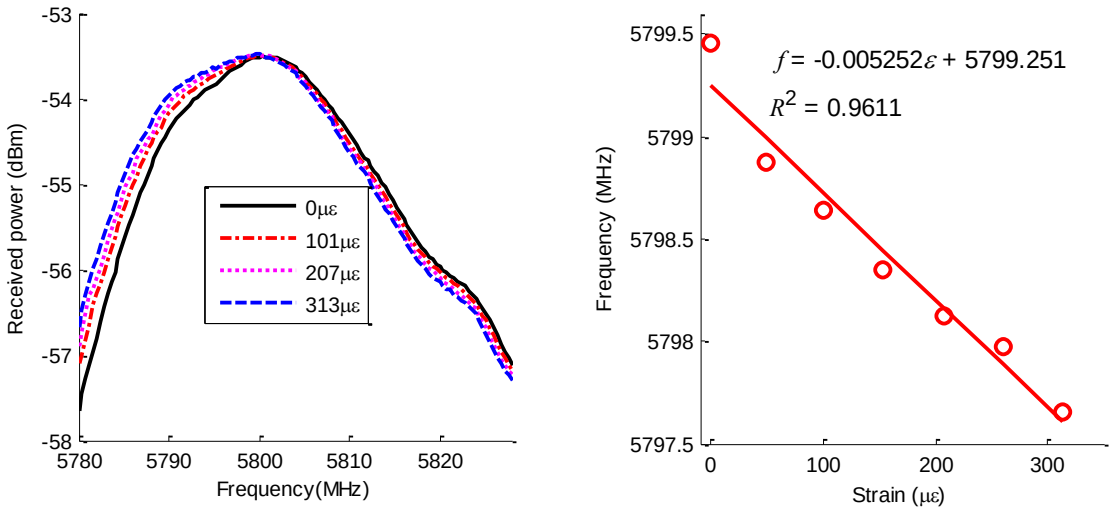

(a) Average received power plot at different strain levels

(b) Resonance frequency versus strain

Fig. 5.72. Experimental results of the frequency doubling sensor (prototype A); two pyramidal horns are used at reader side.

5.5.2 Prototype B with a 5.8GHz Wideband Antenna

The design drawing and photo of the Prototype B are shown in Fig. 5.73. Instead of using a 5.8 GHz patch antenna as the sensor-side transmitting antenna, a 5.8 GHz wideband patch antenna is adopted. In prototype A design, both 2.9GHz and 5.8 GHz patch antennas have their own resonance frequencies. When the resonance frequency of 2.9GHz patch antenna is changed due to strain effect, the sharpness of the overall frequency response could be weaken because of the existence of 5.8GHz resonance frequency peak. To reduce the effect from 5.8GHz patch antenna, a wideband patch antenna is designed as the 5.8GHz transmitting antenna. When the 5.8GHz antenna is wideband, the S_{11} plot is relatively flat, i.e. no peak exists in the frequency response. Since the matching network is also designed to work in a large frequency range, no peak exists in the frequency response. So the peak of the overall frequency response is only due to the peak of the 2.9 GHz patch antenna.

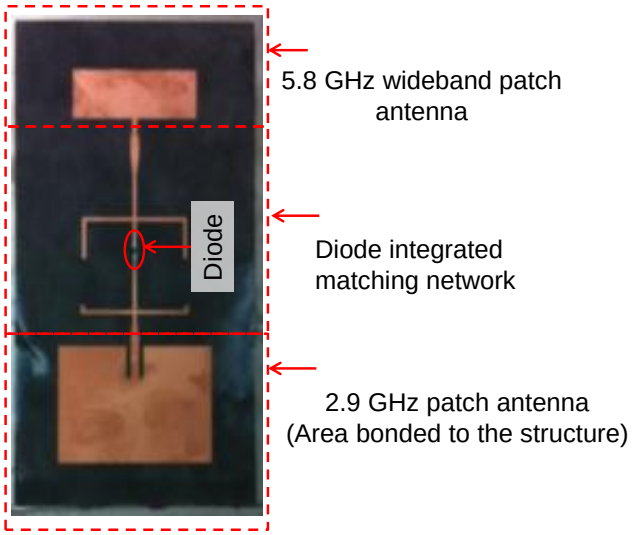

Fig. 5.73. Components of prototype B frequency doubling antenna sensor

During the strain sensing test, only 2.9 GHz transmitting antenna is bonded to the structural surface, while all other components are floating over the structural surface. To check the results consistency, the strain sensing performance with different combinations of reader antennas is investigated. Section 5.5.2.1 shows the results with a double ridged horn antenna as reader-side 2.9 GHz transmitting antenna, and a 5.8 GHz pyramidal horn antenna as the reader-side 5.8 GHz receiving antenna. Section 5.5.2.2 presents the results with two pyramidal horn antennas as the reader-side transmitting and receiving antenna.

5.5.2.1 Strain sensing scenario #1 (double ridged horn antenna / 5.8 GHz pyramidal horn antenna)

In this scenario, a double ridged horn antenna serves as 2.9 GHz transmitting antenna at the reader side, while a 5.8 GHz pyramidal horn antenna serves as the receiving antenna. The interrogation distance between reader antennas and the sensor is set to 20 in. The transmitted interrogation power is fixed at 15 dBm. Fig. 5.74 (a) shows the average received power plot. The resonance frequencies at all strain levels are then

extracted and plotted in Fig. 5.74 (b).The strain sensitivity and the determination coefficient are –3.775 kHz/με and 0.9193 respectively.

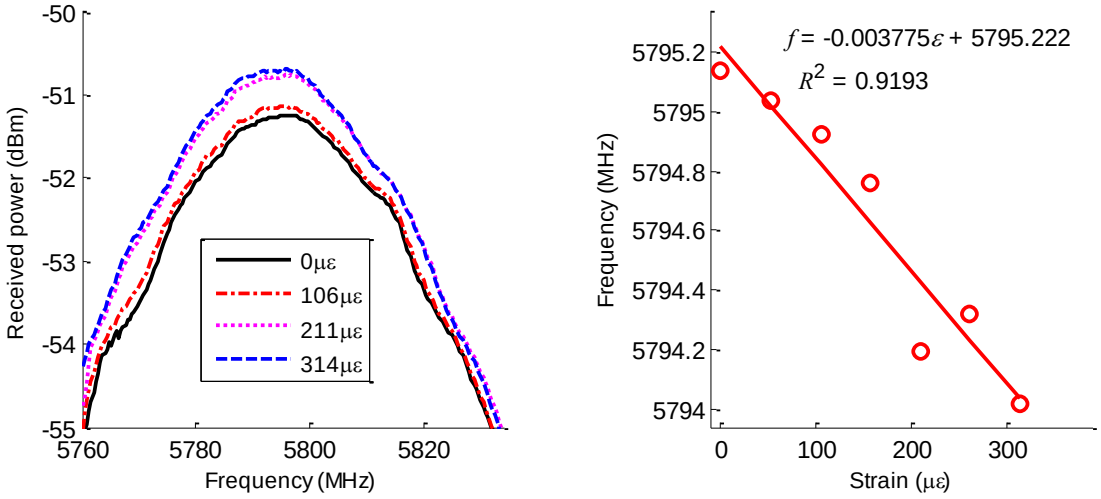

(a) Average received power plot at different strain levels

(b) Resonance frequency versus strain

Fig. 5.74. Experimental results of the frequency doubling sensor (prototype B); a double ridged horn and a 5.8GHz pyramidal horn are used at reader side.

5.5.2.2 Strain sensing scenario #2 (2.9 & 5.8 GHz pyramidal horn antenna)

In this scenario, a pyramidal horn antenna serves as the 2.9 GHz transmitting antenna at the reader side, and another pyramidal horn antenna serves as the 5.8 GHz receiving antenna. The interrogation distance between reader antennas and the sensor is set to 20 in. Fig. 5.75(a) shows the average received power plot. The resonance frequencies at all strain levels are then extracted and plotted in Fig. 5.75(b). The strain sensitivity and the determination coefficient are –2.549 kHz/με and 0.9811, respectively.

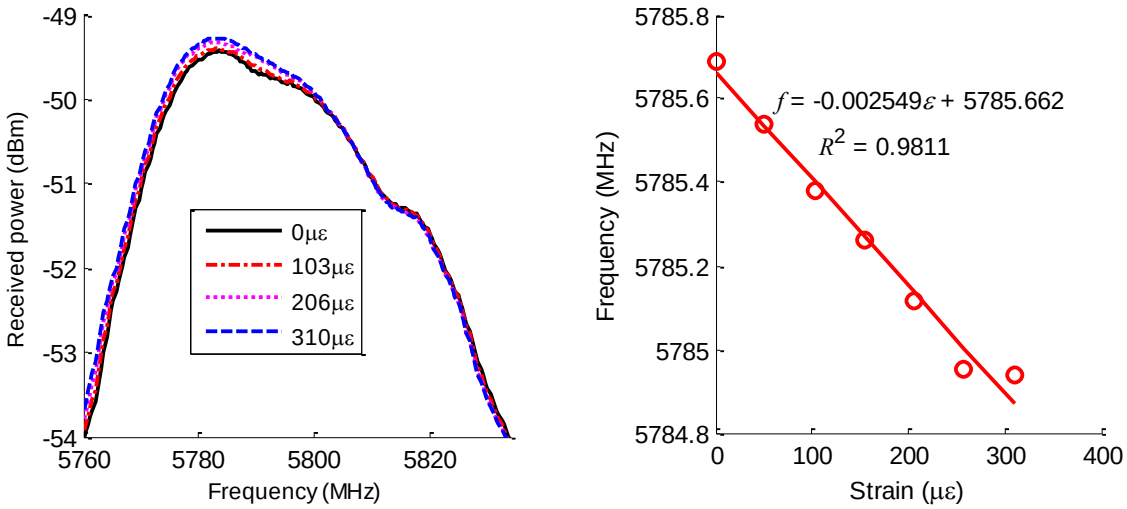

(a) Average received power plot at different strain levels

(b) Resonance frequency versus strain

Fig. 5.75. Experimental results of the frequency doubling sensor (prototype B); two pyramidal horns are used at reader side.

5.5.3 Prototype C with a 5.8 GHz Patch Antenna Rotated by 90 °

The design drawing and photo of the prototype C are shown in Fig. 5.76. The prototype C frequency doubling antenna sensor is composed of a 2.9 GHz patch antenna, diode integrated matching network, and a 5.8 GHz patch antenna rotated by 90 °. The difference between prototype A and C is that the 5.8 GH patch antenna is rotated by 90 °. The 90 ° rotation of 5.8 GHz patch antenna is intended to reduce the coupling effect between 2.9GHz and 5.8 GHz patch antenna.

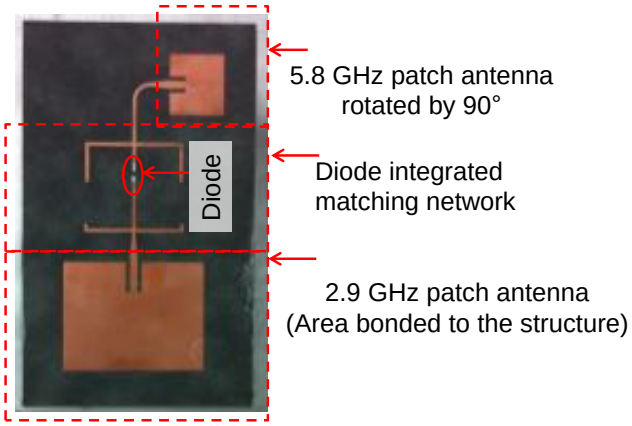

Fig. 5.76. Components of prototype C frequency doubling antenna sensor

During the strain sensing test, only 2.9 GHz transmitting antenna is bonded to the structural surface, while all other components of the sensor are floating over the structural surface. To check the results consistency, the strain sensing performance with different combinations of reader antennas is investigated. Section 5.5.3.1 shows the results with double ridged horn antenna as 2.9 GHz reader transmitting antenna and 5.8 GHz pyramidal horn antenna as the 5.8 GHz reader receiving antenna. Section 5.5.3.2 presents the results with two pyramidal horn antennas as the reader-side transmitting and receiving antenna.

5.5.3.1 Strain sensing scenario #1 (double ridged horn antenna / 5.8GHz pyramidal horn antenna)

In this scenario, a double ridged horn antenna serves as 2.9 GHz transmitting antenna at the reader side, while a 5.8 GHz pyramidal horn antenna serves as the receiving antenna. The interrogation distance between reader antennas and the sensor is set to 20 in. Fig. 5.77(a) shows the average received power plot. The resonance frequencies at all strain levels are then extracted and plotted in Fig. 5.77(b). The strain sensitivity and the determination coefficient are –3.932 kHz/με and 0.9964, respectively. To check the repeatability, one more test is conducted with the same setup. The

experimental results are shown in Fig. 5.78. The strain sensitivities and the determination coefficient are –3.137 kHz/με and 0.8492, respectively (Fig. 5.78).

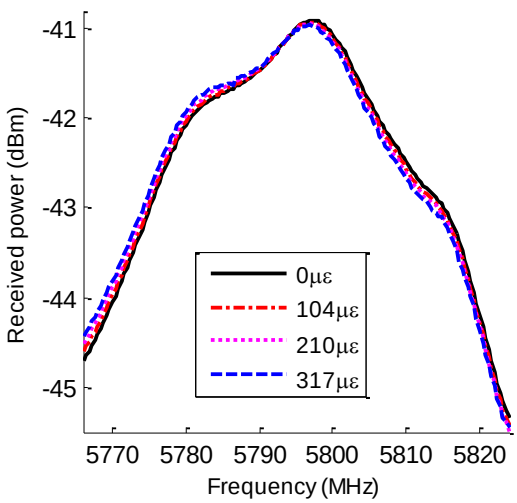

(a) Average received power plot at different strain levels

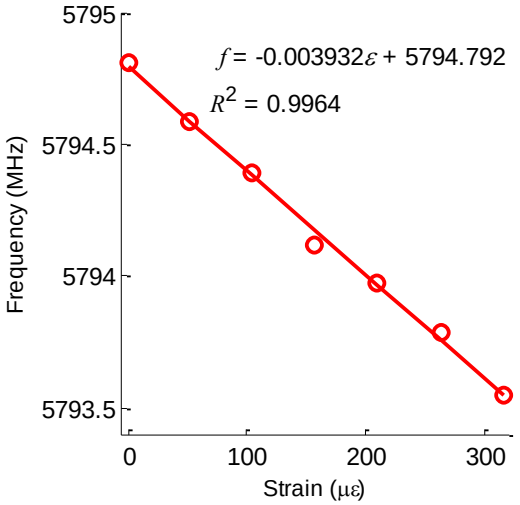

(b) Resonance frequency versus strain

Fig. 5.77. Experimental results of the frequency doubling sensor (prototype C); a double ridged horn and a 5.8 GHz pyramidal horn are used at reader side.

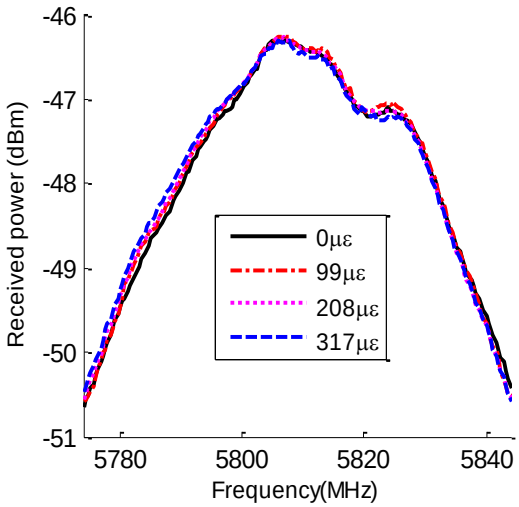

(a) Average received power plot at different strain levels

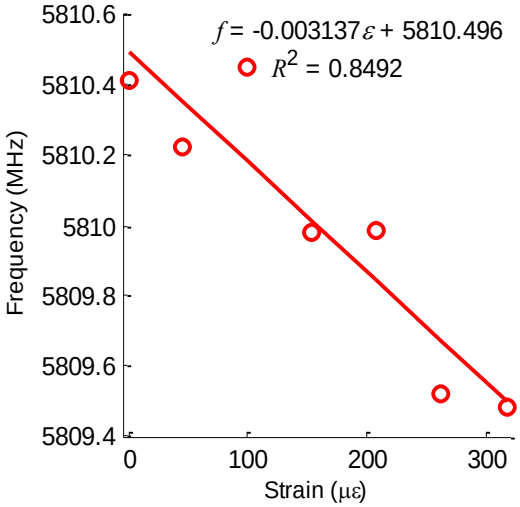

(b) Resonance frequency versus strain

Fig. 5.78. Experimental results of the frequency doubling sensor (prototype C); a double ridged horn and a 5.8 GHz pyramidal horn are used at reader side.

5.5.3.2 Strain sensing scenario #2 (2.9 & 5.8GHz pyramidal horn antenna)

In this scenario, a pyramidal horn antenna serves as the 2.9 GHz transmitting antenna at the reader side, and another pyramidal horn antenna serves as the 5.8 GHz receiving antenna. The interrogation distance between reader antennas and the sensor is set to 20 in. Fig. 5.79(a) shows the average received power plot. The resonance frequencies at all strain levels are then extracted and plotted in Fig. 5.79(b). The strain sensitivity and the determination coefficient are –3.471 kHz/με and 0.9134, respectively.

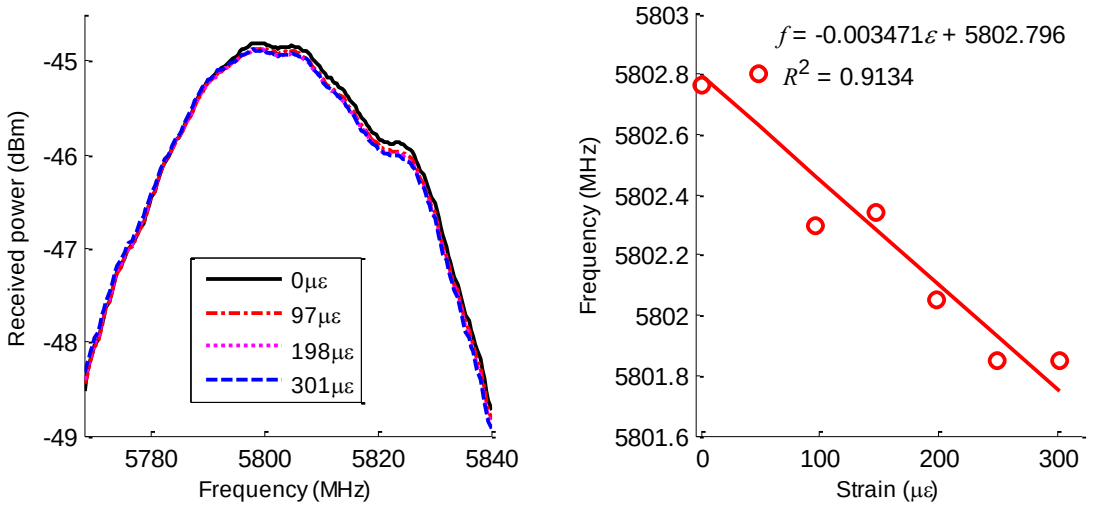

(a) Average received power plot at different strain levels

(b) Resonance frequency versus strain

Fig. 5.79. Experimental results of the frequency doubling sensor (prototype C); 2.9 GHz and 5.8 GHz pyramidal horns are used at reader side.

5.5.4 Prototype D with a 5.8GHz Wideband Patch Antenna Rotated by 90 °

The design drawing and photo of the Prototype D are shown in Fig. 3.37. The prototype D frequency doubling antenna sensor is composed of a 2.9 GHz patch antenna, diode integrated matching network, and a 5.8 GHz wideband patch antenna rotated by 90 °. The difference between prototype B and D is that the 5.8 GH wideband patch antenna is rotated by 90 °. The 90 ° rotation of 5.8 GHz wideband patch antenna is

intended to reduce the coupling effect between 2.9 GHz patch antenna and 5.8 GHz wideband patch antenna.

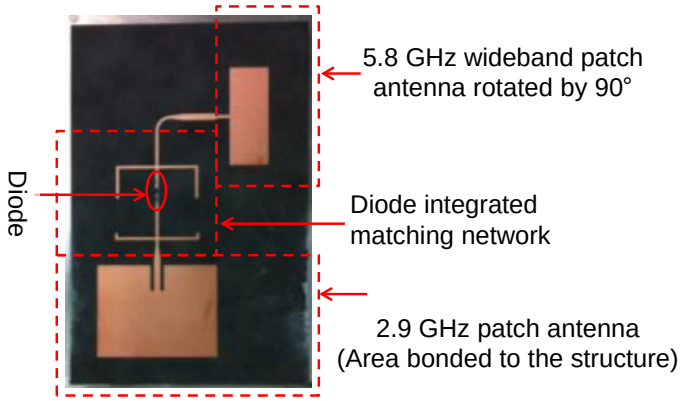

Fig. 5.80. Components of prototype D frequency doubling antenna sensor

During the strain sensing test, only 2.9 GHz transmitting antenna is bonded to the structural surface, while all other components of the sensor are floating over the structural surface. To check the performance consistency, strain sensing is investigated with different combinations of reader antennas. Section 5.5.4.1 shows the results with a double ridged horn antenna as the sensor-side 2.9 GHz transmitting antenna and a 5.8 GHz pyramidal horn antenna as the sensor-side 5.8 GHz reader receiving antenna. Section 5.5.4.2 presents the results with two pyramidal horn antennas as the reader-side transmitting and receiving antenna.

5.5.4.1 Strain sensing scenario #1 (double ridged horn antenna / 5.8 GHz pyramidal horn antenna)

In this scenario, a double ridged horn antenna serves as 2.9 GHz transmitting antenna at the reader side, while a 5.8 GHz pyramidal horn antenna serves as the receiving antenna. The interrogation distance between reader antennas and the sensor is set to 20 in. Fig. 5.81(a) shows the average received power plot. The resonance

frequencies at all strain levels are then extracted and plotted in Fig. 5.81(b). The strain sensitivity and the determination coefficient are –5.257 kHz/με and 0.9970, respectively.

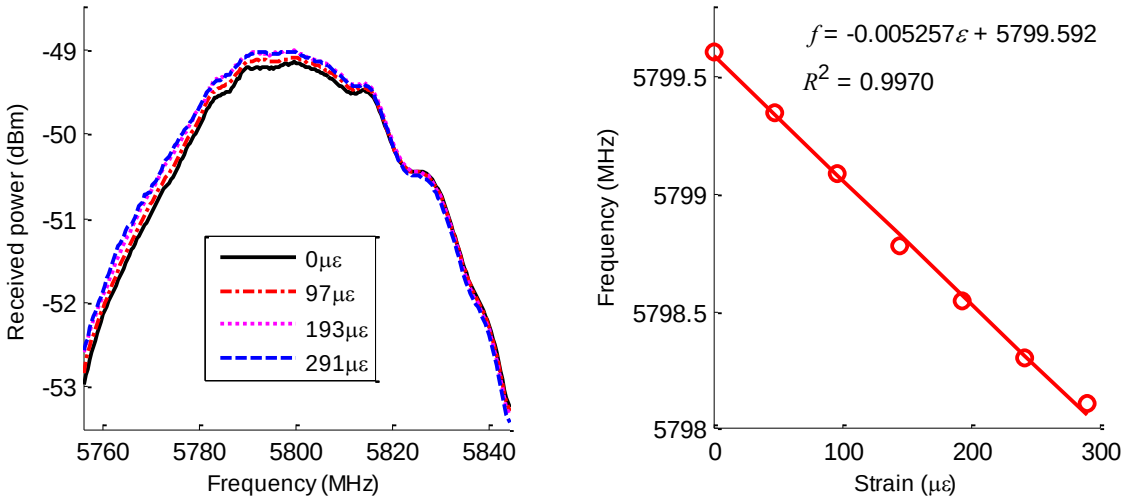

(a) Average received power plot at different strain levels

(b) Resonance frequency versus strain

Fig. 5.81. Experimental results of the frequency doubling sensor (prototype D); a double ridged horn and a 5.8 GHz pyramidal horn are used at reader side.

5.5.4.2 Strain sensing scenario #2 (2.9 & 5.8 GHz pyramidal horn antenna)

In this scenario, a pyramidal horn antenna serves as the 2.9 GHz transmitting antenna at the reader side, and another pyramidal horn antenna serves as the 5.8 GHz receiving antenna. The interrogation distance between reader antennas and the sensor is set to 20 in. Fig. 5.82(a) shows the average received power plot. The resonance frequencies at all strain levels are then extracted and plotted in Fig. 5.82(b). The strain sensitivity and the determination coefficient are –3.156 kHz/με and 0.9853, respectively.

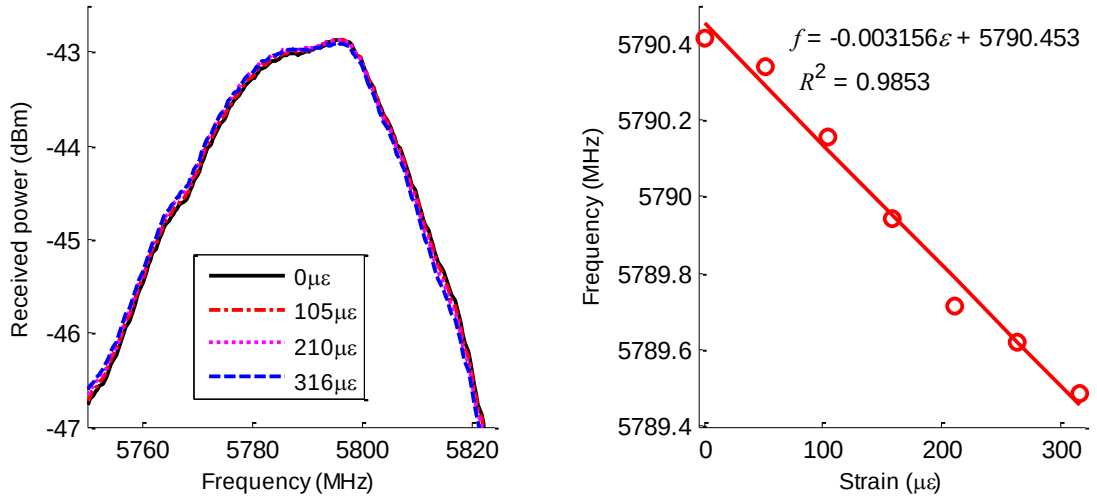

(a) Average received power plot at different strain levels

(b) Resonance frequency versus strain

Fig. 5.82. Experimental results of the frequency doubling sensor (prototype D); two pyramidal horns are used at the reader side

5.5.5 Summary

The section presented experimental results about multiple frequency doubling antenna sensors. A Schottky diode is integrated in the sensor design for generating output signal at doubled frequency of the input signal, which allows the wireless reader to easily distinguish backscattered sensor signal from unwanted environmental reflections. Two patch antennas, serving as 2.9 GHz receiving antenna and 5.8 GHz transmitting antenna, are first designed as key components of a frequency doubling sensor. To explore the most optimal design, frequency doubling antenna sensors with different 5.8 GHz antennas are developed. The strain sensing results show that the strain sensitivity of the frequency doubling antenna sensor is about 5 times higher than RFID antenna sensors presented in Sections 5.1~5.4. When the 5.8 GHz wideband antenna rotated by 90 ° is taken as the 5.8GHz sensor-side transmitting antenna, the received power is higher. At the same time, the linearity between resonance frequency and applied strain is greatly improved.

CHAPTER 6 SUMMARY

The research has invented and validated a series of wireless antenna sensors that are developed for convenient and low-cost monitoring of bridge structures. Building upon latest wireless and nano technologies, both RFID antenna sensors and frequency doubling sensors are designed for strain/crack monitoring. Both passive and active antenna sensors have been investigated. In the design process of antenna sensors, multi-physics coupled simulation is adopted to improve the simulation accuracy. Furthermore, eigenvalue perturbation methods are introduced to improve the simulation efficiency. The main contributions are summarized in Section 6.1. Section 6.2 presents future work of the research.

6.1 Contributions

The dissertation has made contributions in the following areas:

1. Based on extended experiences on antenna sensor designs, multi-physics coupled simulation framework is proposed to improve the simulation accuracy. The mechanics-electromagnetics coupled simulation is adopted for RFID antenna sensor design. Due to the nonlinear diode, the mechanics-AC/DC-electromagnetics coupled simulation is used for frequency doubling antenna sensor design. The simulation accuracy is improved compared with simple scaling process.

2. To further improve the simulation accuracy, an appropriate method to quantify the dielectric constant change under strain is proposed and validated by experiments. With updated dielectric constant at different strain levels, the coupled simulation gives more accurate simulation results and reduces the discrepancy between simulation and experimental results.

3. In order to improve the simulation efficiency, eigenvalue perturbation techniques are applied to the eigenvalue problems formulated in the electromagnetic domain. Instead of solving the electromagnetic eigenvalue problem at every strain step, the eigenvalue at a new strain step is directly updated according to eigenvalue results in the previous strain step. Two perturbation methods, first-order eigenvalue perturbation method and inverse Rayleigh quotient iteration, are studied and compared. Two antenna example, a 2D dipole antenna and the slotted patch antenna sensor, are used to validate the algorithm performance. The simulation efficiency can be greatly improved with reasonable simulation accuracy by the proposed perturbation techniques. The perturbation efficiency and accuracy are analyzed under different strain step sizes.

4. A passive RFID folded patch antenna sensor is first developed. Test results show that the sensor can measure strain as small as 20 με and as high as 10,000 με. Using a Yagi reader antenna, the antenna sensor can achieve consistent strain sensing results when the interrogation distance is increased up to 84 in. Furthermore, sensor arrays formed by multiple antenna sensors are demonstrated to be capable of measuring strain distribution in close proximity. Two scenarios of crack sensing performance are presented, including emulated crack sensing and fatigue crack sensing. The experimental results demonstrate that the antenna sensor is capable of measuring small cracks and tracking crack propagation.

5. To reduce the temperature effect on the antenna sensor, another antenna sensor is designed on a temperature insensitive substrate (Rogers 6202). The temperature chamber test shows that the folded patch antenna sensor with Rogers 6202 substrate has a stable frequency response under temperature. The further strain sensing results demonstrate that this antenna sensor also has similar strain sensitivity as the folded patch antenna sensor on Rogers 5880.

6. To reduce the antenna sensor footprint, two RFID slotted patch antenna sensors are designed. The area is only about a half of the folded patch antenna sensor. With an

active slotted patch antenna sensor that receives power from a small solar cell, the interrogation distance can be further increased to 156 in. The slotted patch antenna sensors are also capable of tension and compression strain sensing, emulated crack sensing, and fatigue crack sensing of both aluminum and steel specimens.

7. To further reduce sensor cost in large-quantity production, inkjet-printing techniques of silver nanoparticles have been investigated for fabricating folded patch antenna sensors. To validate strain sensing performance, the printed antenna sensor is mounted on an aluminum specimen for tensile testing. To achieve better uniformity in the printed silver, the printing is performed on a flexible and ink-absorbent 5-mil Kapton polyimide film. Bottom of the Kapton thin film is then bonded on a Rogers RT/duroid® 5880 substrate. The tensile test results show that the measured strain sensitivity of inkjet-printed sensors is very close to that of the copper antenna sensors made of traditional fabrication techniques.

8. Multiple frequency doubling antenna sensors are designed and fabricated to operate at higher GHz frequencies. A Schottky diode is integrated in the sensor design for generating output signal at doubled frequency of the input signal, which allows the wireless reader to easily distinguish backscattered sensor signal from unwanted environmental reflections. Because operation power of the diode is captured from wireless interrogation signal emitted by a reader, no other power source is needed by the sensor. Two patch antennas, serving as 2.9 GHz receiving antenna and 5.8 GHz transmitting antenna, are first designed as key components of a frequency doubling sensor. A Schottky diode simulation model is first verified by experimental measurements, and then used for designing a matching network between the two antennas. Consisting of the three components, the frequency doubling antenna sensor is fabricated and extensively tested for strain sensing. Furthermore, to explore the most optimal design, frequency doubling antenna sensors with different 5.8 GHz antennas are developed. When a wideband antenna sensor rotated by 90 ° is adopted as the 5.8GHz

sensor-side transmitting antenna, the received power is higher and the linearity between the resonance frequency and the applied strain is also improved.

6.2 Future Work

Building upon current work, future research can be expanded along following directions.

1. Although the inverse Rayleigh quotient iteration method shows promising perturbation accuracy and efficiency, it can be further improved by embedding the perturbation algorithm into COMSOL directly. Currently, the global matrices are extracted from COMSOL and the perturbation algorithms are conducted in the MATLAB environment. Instead of involving computation in two software environments, it is more efficient to perform the perturbation directly in COMSOL. The perturbation algorithms can be implemented as external functions and embedded directly in COMSOL to eliminate the communication between COMSOL and MATLAB to improve the computation efficiency.

2. Sensing consistency, particularly at longer interrogation distances, can be improved. For example, antenna sensors providing higher strain sensitivity and higher backscattered power can improve strain sensing consistency. For higher strain sensitivity, novel antenna patterns (instead of simple patches) need to be devised to provide larger resonance frequency shift under strain. For higher backscattered power, appropriate power amplification solutions can be investigated.

3. Currently, the antenna sensor can only measure the strain in one direction. In order to measure the strain in different directions, multiple sensors need to be installed in a small area. However, the sensor dimensions are still relatively large. In order to measure strain in different direction, it is necessary to design an antenna sensor that can sense strain in three directions, which then can be used to derive shear strain.

4. The interference between sensors in close proximity is another issue that requires more investigation. Sensor placement can be optimized in order to improve signal-to-noise ratios. Another way to reduce the interference is to differentiate initial resonance frequency f_{R0} of sensors in close proximity. This approach allows each sensor to change its resonance frequencies within a different range, and thus minimizes interference.

5. Although this research focuses upon application on steel structures, sensor performance can be investigated when the antenna sensor is installed on concrete. Since smaller reflection is expected from concrete surface compared with steel surface, better signal-to-noise ratio is expected and may have better strain or crack sensing results. Validation experiments can be designed and conducted to evaluate sensor performance on concrete structures.

6. Consistency of the frequency doubling sensor is another topic that needs further study. Although the frequency doubling sensor has relatively large strain sensitivity, the performance is susceptible to location and orientation of reader antennas.

7. Portability of the Tagformance reader makes it highly feasible to deploy the RFID sensors in the field. Nevertheless, prior to long-term field deployment, large amount of studies need to be devoted to reliability and robustness of the antenna sensors in outdoor conditions. Waterproof packaging needs to be designed, and the effect of packaging on strain/crack sensing performance should also be studied.

In summary, harnessing latest wireless and nano technologies, the research has developed a number of novel battery-free wireless antenna sensors that are demonstrated to be effective in strain and crack sensing. Without any requirement of cabling or battery power, the antenna sensors have the great potential of low-cost large-scale monitoring of engineering structures. Application of the sensors is not only for bridges, but also can easily extend to other civil, mechanical, and aerospace structures.

REFERENCES

[1] H. Sohn, C. R. Farrar, F. M. Hemez, D. D. Shunk, D. W. Stinemates, and B. R. Nadler, *A Review of Structural Health Monitoring Literature: 1996-2001*, Los Alamos National Laboratory, Los Alamos, NM Report No. LA-13976-MS, 2003.

[2] M. Çelebi, *Seismic Instrumentation of Buildings (with Emphasis on Federal Buildings)*, United States Geological Survey, Menlo Park, CA Report No. 0-7460-68170, 2002.

[3] E. G. Straser and A. S. Kiremidjian, *A Modular, Wireless Damage Monitoring System for Structures*, John A. Blume Earthquake Eng. Ctr., Stanford University, Stanford, CA Report No. 128, 1998.

[4] B. F. Spencer, Jr., M. E. Ruiz-Sandoval, and N. Kurata, "Smart sensing technology: opportunities and challenges," *Structural Control and Health Monitoring*, vol. 11, pp. 349-368, 2004.

[5] J. P. Lynch, K. H. Law, A. S. Kiremidjian, E. Carryer, C. R. Farrar, H. Sohn, *et al.*, "Design and performance validation of a wireless sensing unit for structural health monitoring applications," *Structural Engineering and Mechanics*, vol. 17, pp. 393-408, 2004.

[6] Y. Wang, J. P. Lynch, and K. H. Law, "A wireless structural health monitoring system with multithreaded sensing devices: design and validation," *Structure and Infrastructure Engineering*, vol. 3, pp. 103-120, 2007.

[7] J. P. Lynch and K. J. Loh, "A summary review of wireless sensors and sensor networks for structural health monitoring," *The Shock and Vibration Digest*, vol. 38, pp. 91-128, 2006.

[8] G. Park, T. Rosing, M. D. Todd, C. R. Farrar, and W. Hodgkiss, "Energy harvesting for structural health monitoring sensor networks," *Journal of Infrastructure Systems*, vol. 14, pp. 64-79, March 2008 2008.

[9] A. Deivasigamani, A. Daliri, C. H. Wang, and S. John, "A review of passive wireless sensors for structural health monitoring," *Modern Applied Science*, vol. 7, pp. 57-76, 2013.

[10] K. Finkenzeller, *RFID Handbook*, 2nd ed. New York: John Wiley & Sons, 2003.

[11] F. Gasco, P. Feraboli, J. Braun, J. Smith, P. Stickler, and L. DeOto, "Wireless strain measurement for structural testing and health monitoring of carbon fiber composite," *Composite Part A: Applied Science and Manufacturing*, vol. 42, pp. 1263-1274, 2011.

[12] J. C. Butler, A. J. Vigliotti, F. W. Verdi, and S. M. Walsh, "Wireless, passive, resonant-circuit, inductively coupled, inductive strain sensor," *Sensors and Actuators A: Physical*, vol. 102, pp. 61-66, 2002.

[13] K. J. Loh, J. P. Lynch, and N. A. Kotov, "Inductively coupled nanocomposite wireless strain and pH sensors," *Smart Structures and Systems*, vol. 4, pp. 531-548, 2008.

[14] Y. Jia, K. Sun, F. J. Agosto, and M. T. Quinones, "Design and characterization of a passive wireless strain sensor," *Measurement Science and Technology*, vol. 17, pp. 2869-2876, Nov 2006.

[15] R. Matsuzaki, M. Melnykowycz, and A. Todoroki, "Antenna/sensor multifunctional composites for the wireless detection of damage," *Composites Science and Technology*, vol. 69, pp. 2507-2513, 2009.

[16] A. Daliri, A. Galehdar, S. John, C. H. Wang, W. S. T. Towe, and K. Ghorbani, "Wireless strain measurement using circular microstrip patch antennas," *Sensors and Actuators A: Physical*, vol. 184, pp. 86-92, 2012.

[17] R. Melik, N. K. Pergoz, E. Unal, C. Puttlitz, and H. V. Demir, "Bio implantable passive on-chip RF-MEMS strain sensing resonators for orthopedic application," *Journal of Micromechanics and Microengineering*, vol. 18, p. 115017, 2008.

[18] S. Deshmukh and H. Huang, "Wireless interrogation of passive antenna sensors," *Measurement Science and Technology*, vol. 21, 2010.

[19] X. Xu and H. Huang, "Battery-less wireless interrogation of microstrip patch antenna for strain sensing," *Smart Materials and Structures*, vol. 21, p. 125007, 2012.

[20] D. J. Thomson, D. Card, and G. E. Bridges, "RF cavity passive wireless sensors with time-domain gating-based interrgoation for SHM of civil structures," *IEEE Sensors Journal,* vol. 9, pp. 1430-1438, 2009.

[21] C. Occhiuzzi, C. Paggi, and G. Marrocco, "Passive RFID strain-sensor based on meander-line antennas," *IEEE Transcations on Antennas and Propagation,* vol. 59, pp. 4836-4840, 2011.

[22] EPCglobal Inc., *EPC™ Radio-frequency Identity Protocols Class-1 Generation-2 UHF RFID Protocol for Communications at 860 MHz-960 MHz* EPCglobal Inc. Version 1.2.0, 2008.

[23] S. Berndie and C. Kai, "5.8-GHz cricularly polarized rectifying antenna for wireless microwave power transmission," *IEEE Transactions on Microwave Theory and Techniques,* vol. 50, pp. 1870-1876, 2002.

[24] C. Bruce G. and B. Gilles, "Harmonic radar transceiver design: miniature tags for insect tracking," *IEEE Transactions on Antennas and Propagation,* vol. 52, pp. 2825-2832, 2004.

[25] P. Suzette M., W. Thomas M., S. Steven, and R. Michael, "High efficiency diode doubler with conjugate-matched antennas," *Proceedings of the 37th European Microwave Conference*, Munich, 2007, pp. 250-253.

[26] K. S. Yee, "Numerical solution of initial boundary-value problems involving Maxwell's equations in isotropic media," *IEEE Transactions on Antennas and Propagation,* vol. AP-14, pp. 302-307, 1966.

[27] A. Taflove, "Review of the formulation and applications of the finite-difference time-domain method for numerical modeling of electromagnetic wave interactions with arbitrary structures," *Wave Motion,* vol. 10, pp. 547-582, 1988.

[28] N. A. Bushyager and M. M. Tentzeris, *MRTD (Multi Resolution Time Domain) Method in Electromagnetics*. USA: Morgan & claypool, 2005.

[29] J. M. Jin, *The Finite Element Method in Electromagnetics*, 2nd ed. New York: John Wiley & Sons, Inc., 2002.

[30] J. L. Volakis, A. Chatterjee, and L. C. Kempel, *Finite Element method for Electromagnetics: with Applications to Antenna, Microwave Circuits, and Scattering*. New York, NY: The Institute of Electrical and Electronics Engineers, Inc., 1998.

[31] M. Clemens and T. Weiland, "Discrete electromagnetism with the finite integration technique," *Progress in Electromagnetics Research,* vol. 32, pp. 65-87, 2001.

[32] M. M. Ney, "Method of moments as applied to electromagnetics problems," *IEEE Transcations on Microwave Theory and techniques,* vol. 33, pp. 972-980, 1985.

[33] A. A.T., "An introduction to the method of moments," *Computer Physics Communications,* vol. 68, pp. 1-18, 1974.

[34] W. J. R. Hoefer, "The transmission-line matrix method-theory and applications," *IEEE Transcations on Microwave Theory and techniques,* vol. 33, pp. 882-893, 1985.

[35] C. C., *The Transmission-Line Modeling Method (TLM)*. New York, NY: IEEE Press, 1995.

[36] R. Pregla, *Analysis of Electromagnetic Fields and Waves: The Method of Lines (RSP)*. Chichester, England: John Wiley & Sons, Ltd, 2008.

[37] COMSOL, *COMSOL multiphysics reference guide*, COMSOL, Inc., Burlington, MA, USA2012.

[38] ANSYS Inc., *ANSYS Coupled-field Analysis Guide*, ANSYS Inc., Canonsburg, PA, USA2005.

[39] CST, *CST microwave studio-workflow & solver overview*, CST-Computer Simulation Technology, Darmstadt, Germany2010.

[40] X. Yi, Y. Wang, M. M. Tentzeris, and R. T. Leon, "Multi-physics modeling and simulation of a slotted patch antenna for wireless strain sensing," *Proceedings of 9th International Workshop on Structural Health Monitoring (IWSHM)*, Standford, CA, USA, 2013.

[41] L. Yu, L. Cheng, L. H. Yam, and Y. J. Yan, "Application of eigenvalue perturbation theory for detecting small structural damage using dynamic responses," *Composite Structures,* vol. 78, pp. 402-409, 2007.

[42] S. H. Chen, X. W. Yang, and H. D. Lian, "Comparison of several eigenvalue reanalysis methods for modified structures," *Structural and Multidisciplinary Optimization,* vol. 20, pp. 253-259, 2000.

[43] B. N. Parlett, *The Symmetric Eigenvalue Problem*. Englewood Cliffs, NJ: Prentice-Hall, 1980.

[44] T. Zhang, K. H. Law, and G. H. Golub, "On the homotopy method for perturbed symmetric generalized eigenvalue problems," *SIAM Journal on Scientific Computing,* vol. 19, pp. 1625-1645, 1998.

[45] G. Sliva, A. Brezillon, J. M. Cadou, and L. Duigou, "Study of the eigenvalue sensitivity by homotopy and perturbation methods," *Journal of Computational and Applied Mathematics,* vol. 234, pp. 2297-2302, 2010.

[46] F. Massa, T. Tison, B. Lallemand, and O. Cazier, "Structural modal reanalysis methods using homotopy perturbation and projection techniques," *Computer Methods in Applied Mechanics and Engineering,* vol. 200, pp. 2971-2982, 2011.

[47] H. Chen, "Efficient methods for determining modal parameters of dynamic structures with large modifications," *Journal of Sound and Vibration,* vol. 298, pp. 462-470, 2006.

[48] X. Dai, L. He, and A. Zhou, "Adaptive finite element analysis based on perturbation arguments," *Proceedings of International Conference Applications of Mathematics*, prague, Czech Republic, 2012.

[49] J. C. Slater, *Microwave Electronics*. New York, NY: D. Van Nostrand, 1950.

[50] G. E. Dombrowski, "Matrix formulation of Slater's cavity perturbation theorem," *Journal of Applied Physics,* vol. 55, pp. 2648-2650, 1984.

[51] K. Brackebusch and U. van Pienen, "Eigenmode computation for cavities with perturbed geometry based on a series expansion of unperturbed eigenmodes,"

Proceedings of International Particle Accelerator Conference (IPAC), New Orlean, Louisiana, USA, 2012.

[52] S. G. Johnson, M. Ibanescu, S. M.A., O. Weisberg, and J. D. Joannopoulos, "Perturbation theory for Maxwell's equations with shifting material boundaries," *Physical Review. E,* vol. 65, p. 066611, 2002.

[53] C. Kottke, A. Farjadpour, and S. G. Johnson, "Perturbation theory for anisotropic dielectic interfaces, and application to sub-pixel smoothing of discretized numerical methods," *Physical Review E.*, vol. 77, p. 036611, 2008.

[54] I. A. a. P. Society, "IEEE Standard Definitions of Terms for Antennas," ed. New York, NY: The Institute of Electrical and Electronics Engineers, Inc., 1993.

[55] R. Bhattacharyya, C. Floerkemeier, and S. Sarma, "Towards tag antenna based sensing utilizing ordinary RFID tags," *Conference Name*|, Conference Location|, Year|.

[56] X. Yi, C. Cho, J. Cooper, Y. Wang, M. M. Tentzeris, and R. T. Leon, "Passive wireless antenna sensor for strain and crack sensing-electromagnetic modeling, simulation, and testing " *Smart Materials and Structures*, vol. 22, p. 085009, 2013.

[57] H. Huang, "Flexible wireless antenna sensor: a review," *IEEE Sensors Journal*, vol. 13, pp. 3865-3872, 2013.

[58] M. M. Andringa, D. P. Neikirk, N. P. Dickerson, and S. L. Wood, "Unpowered wireless corrosion sensor for steel reinforced concrete," *Proceedings of IEEE Sensors*, Irvine, CA, 2005.

[59] X. Yi, T. Wu, Y. Wang, R. T. Leon, M. M. Tentzeris, and G. Lantz, "Passive wireless smart-skin sensor using RFID-based folded patch antennas," *International Journal of Smart and Nano Materials*, vol. 2, pp. 22-38, Jan 2011.

[60] GAO RFID Inc., *2.45GHz Active Vibration Sensor RFID Tag*, GAO RFID Inc., Toronoto, Ontario, Canada2014.

[61] NephSystem Technologies, *NephSystem NSAT Series Active RFID Tags*, NephSystem Technologies, Delta BC, Canada2014.

[62] M. T. Faber, J. Chramiec, and M. E. Adamski, *Microwave and Millimeter-Wave Diode Frequency Multipliers*. Norwood, MA: Artech House, 1995.

[63] R. Want, "An introduction to RFID technology," *IEEE Pervasive Computing,* vol. 5, pp. 25-33, 2006.

[64] J. Landt, "The history of RFID," *IEEE Potentials,* vol. 24, pp. 8-11, 2005.

[65] R. Bansal, "Coming soon to a Wal-Mart near you," *IEEE Antennas and Propagation Magazine,* vol. 45, pp. 105-106, 2003.

[66] R. S. Sangwan, R. G. Qiu, and D. Jessen, "Using RFID tags for tracking patients, charts and medical equipment within an integrated health delivery network," *Proceedings of IEEE International Conference on Networking Sensing and Control*, Tucson, AZ, 2005, pp. 1070-1074.

[67] NXP Semiconductors, *SL3ICS1002_1202 product data sheet*, NXP Semiconductors, Eindhoven, Netherlands2009.

[68] C. A. Balanis, *Antenna Theory: Analysis and Design*, 2nd ed. New York: John Wiley and Sons Inc., 1997.

[69] K. Kurokawa, "Power waves and the scattering matrix," *Microwave Theory Technology, IEEE Transactions on,* vol. 13, pp. 194-202, 1965.

[70] C. A. Balanis, *Advanced Engineering Electromagnetics*. New York: Wiley & Sons, 1989.

[71] J. R. Riley and A. D. Simith, "Design considerations for an harmonic radar to investigate the flight of insects at low altitude," *Computers and Electronics in Agriculture,* vol. 35, pp. 151-169, 2002.

[72] X. Yi, C. Cho, B. Cook, Y. Wang, M. M. Tentzeris, and R. T. Leon, "Design and simulation of a slotted patch antenna sensor for wireless strain sensing," *Proceedings of SPIE, Nondestructive Characterization for Composite Materials, Aerospace Engineering, Civil Infrastructure, and Homeland Security*, San Diego, California, USA, 2013.

[73] S. A. Maas, *Nonlinear Microwave and RF Circuits*, 2nd ed. Norwood, MA: Artech House, 2003.

[74] A. S. o. T. Materials, "ASTM D3380-10 Standard test Method for Relative Permittivity (Dielectric Constant) and Dissipation Factor of Polymer-Based Microwave Circuit Substrates," ed. West Conshohocken, PA, USA: ASTM International, 2010.

[75] J. Q. Howell, "A quick accurate method to measure the dielectric constant of microwave integrated circuit substrates," *IEEE Transcations on Microwave Theory and techniques,* vol. 21, pp. 142-144, 1973.

[76] N. K. Das, S. M. Voda, and D. M. Pozar, "Two methods for the measurement of substrate dielectric constant," *IEEE Transcations on Microwave Theory and techniques,* vol. 35, pp. 636-642, 1987.

[77] I. o. P. Circuits, "Stripline Test for Complex Relative Permittivity of Circuit Board Materials to 14 GHz," ed. Northbrook, IL, USA: IPC, 1998.

[78] I. o. P. Circuits, "Stripline Test for Permittivity and Loass Tangent (Dielectric Constant and Dissipation Factor) at X-Band," ed. Northbrook, IL, USA: IPC, 1998.

[79] E. Li, Z. Nie, G. Guo, and Q. Zhang, "Broadband measurements of dielectric properties of low-loss materials at high temperatures uisng circular cavity method," *Progress in Electromagnetics Research,* vol. 92, pp. 103-120, 2009.

[80] N. Damaskos and B. J. Kelsall, "Measuring dielectric constants of low loss materials using a broadband cavity technique," *Microwave Journal,* vol. 38, p. 140, 1995.

[81] R. M. Pannell and B. W. Jervis, "Two simple methods for the measurement of the dielectric permittivity of low-loss microstrip substrates," *IEEE Transcations on Microwave Theory and techniques,* vol. 29, pp. 383-386, 1981.

[82] X. Yi, C. Cho, Y. Wang, B. Cook, J. Cooper, R. Vyas, *et al.*, "Passive frequency doubling antenna sensor for wireless strain sensing," *Proceedings of the ASME 2012 Conference on Smart Materials, Adapative Structures and Intelligent Systems,* Stone Mountain, GA, USA, 2012.

[83] J. L. Volakis, A. Chatterjee, and L. C. Kempel, *Finite Element Method for Electromagnetics: with Applications to Antennas, Microwave Circuits, and Scattering*. New York, NY: Instiute of Electrical and Electronics Engineers, Inc., 1998.

[84] W. C. Chew and W. H. Weedon, "A 3D perfectly matched medium from modified Maxwell's equations with stretched coordinates," *Microwave and Optical Technology Letters,* vol. 7, pp. 599-604, 1994.

[85] Z. S. Sacks, D. M. Kingsland, R. Lee, and J.-F. Lee, "A perfectly matched anisotropic absorber for use as absorbing boundary condition," *IEEE Transactions on Antennas and Propagation,* vol. 43, pp. 1460-1463, 1995.

[86] J.-P. Berenger, "Three-dimensional perfectly matched layer for the absorption of electromagnetic waves," *Journal of Computational Physics,* vol. 127, pp. 363-379, 1996.

[87] C. M. Rappaport, "Interpreting and improving the PML absorbing boundary condition using anisotropic lossy mapping of space," *IEEE Transcations on Magnetics,* vol. 32, pp. 968-974, 1996.

[88] J. Jin and W. C. Chew, "Combining PML and ABC for finite element analysis of scattering problems," *Microwave and Optical Technology Letters,* vol. 12, pp. 192-197, 1996.

[89] J.-Y. Wu, D. M. Kingsland, J.-F. Lee, and R. Lee, "A comparison of anisotrpic PML to Berenger's PML and its application to the finite-element method for EM scattering," *IEEE Transactions on Antennas and Propagation,* vol. 45, pp. 40-50, 1997.

[90] F. L. Teixeira and W. C. Chew, "Differential forms, metrics, and the reflectionless absorption of electromagnetic waves," *Journal of Electromagnetic Waves and Applications,* vol. 13, pp. 665-686, 1999.

[91] W. Shin and S. Fan, "Choice of the perfectly matched layer boundary condition for frequency-domain Maxwell's equations solvers," *Journal of Computational Physics,* vol. 231, pp. 3406-3431, 2012.

[92] F. L. Teixeira and W. C. Chew, "General closed-form PML constitutive tensors to match arbitrary bianisotropic and dispersive linear media," *IEEE Microwave and Guided Wave Letters,* vol. 8, pp. 223-225, 1998.

[93] W. C. Chew and W. H. Weedon, "A 3-D perfectly matched medium from modified Maxwell's equations with stretched coordinates," *Microwave and Optical Technology Letters,* vol. 7, pp. 599-604, 1994.

[94] H. Guo, B. Oswald, and P. Arbenz, "3-dimensional eigenmodal analysis of plasmonic nanostructures," *Optics Express,* vol. 20, pp. 5481-5500, 2012.

[95] A. Chatterjee, J. M. Jin, and J. L. volakis, "Edge-based finite elements and vector ABC's applied to 3-D scattering," *IEEE Transactions on Antennas and Propagation* vol. 41, pp. 221-226, 1993.

[96] D. M. Pozar, *Microwave Engineering*, 4th ed. New York, 2012.

[97] F. Tisseur and K. Meerbergen, "The quadratic eigenvalue problem," *SIAM Review,* vol. 43, pp. 235-286, 2001.

[98] J. H. Wilkinson, *The Algebric Eigenvalue Problem*. Oxford: Oxford University Press, 1965.

[99] A. Ruhe, "SOR methods for the eigenvalue problem with large sparse algorithm for eigenvalue analysis," *Mathematics of Computatoin,* vol. 28, pp. 695-710, 1974.

[100] G. M., "The computational efficiency of a new minimizatoin algorithm for eigenvalue analysi," *Journal of Sound and Vibration,* vol. 3, pp. 319-331, 1971.

[101] G. H. Golub and C. F. van Loan, *Matrix Computations*. Baltimore: Johns Hopkins University Press, 1983.

[102] D. C. Sorensen, "Implicit application of polynomial filters in a k-step Arnoldi method," *SIAM Journal of Matrix Analysis and Application,* vol. 13, pp. 357-385, 1992.

[103] R. B. Lehoucq, D. C. Sorensen, and Y. C., *ARPACK User's Guide: Solution of Large Scale Eigenvalue Problems with Implicitly Restarted Arnoldi Methods*, 1997.

[104] P. R. Amestoy, I. S. Duff, and J.-Y. L'Excellent, "Multifrontal parallel distributed symmetric and unsymmetric solvers," *Computer Methods in Applied Mechanics and Engineering*, vol. 184, pp. 501-520, 2000.

[105] P. R. Amestoy, I. S. Duff, J.-Y. L'Excellent, and J. Koster, "A fully asymchronous multifrontal solver using distributed dynamic scheduling," *SIAM Journal of Matrix Analysis and Application*, vol. 23, pp. 15-41, 2001.

[106] P. R. Amestoy, A. Guermouche, J.-Y. L'Excellent, and S. Pralet, "Hybrid scheduling for the parallel solution of linear systems," *Parallel Computing*, vol. 32, pp. 126-156, 2006.

[107] C. Ashcraft and R. G. Grimes, "SPOOLES: an object-oriented sparse matrix library," *Proceedings of the Ninth SIAM Conference on Parallel Processing for Scientific Computing*, San Antonio, Texas, USA, 1999.

[108] A. Kuzmin, M. Luisier, and O. Schenk, "Fast methods for computing selected elements of the Green's function in massively parallel nanoelectronic device simulations," *Euro-Par 2013 parallel Processing*, Aachen, Germany, 2013, pp. 533-544.

[109] O. Schenk, M. Bollhofer, and R. A. Romer, "On large scale diagonalization techniques for the anderson model of localization," *SIAM Journal of Scientific Computing*, vol. 28, pp. 963-983, 2006.

[110] O. Schenk, A. Wachter, and M. Hagemann, "Matching-based preprocessing algorithms to the solution of saddle-point problems in large-scale nonconvex interior-point optimization," *Computational Optimization and Applications*, vol. 36, pp. 321-341, 2007.

[111] T. A. Davis and I. S. Duff, "An unsymmetric-pattern multifrontal method for sparse LU factorization," *SIAM Journal of Matrix Analysis and Applications*, vol. 18, pp. 140-158, 1997.

[112] A. Gupta and Y. Muliadi, "An experimental comparison of some direct sparse solver packages," *Proceedings of the 15th International Parallel & Distributed Processing Symposium*, San Francisco, CA, 2001.

[113] P. R. Amestoy, I. S. Duff, J.-Y. L'Excellent, and X. S. Li, "Analysis and comparison of two general sparse solvers for distributed memory computers," *ACM Transactions on Mathematical Software,* vol. 27, pp. 388-421, 2001.

[114] M. P. Raju and S. K. Khaitan, "High performance computing of three-dimensional finite element codes on a 64-bit machine," *Journal of Applied Fluid Mechanics,* vol. 5, pp. 123-132, 2012.

[115] G. W. Stewart and J.-g. Sun, *Matrix Perturbation Theory*. Boston: Academic Press, Inc., 1990.

[116] L. Yu, L. Cheng, L. H. Yam, and Y. J. Yan, "Application of eigenvalue perturbation theory for detecting small structural damage using dynamic responses," *Composite Structures,* vol. 78, pp. 402-409, 2007.

[117] S. karl A., "Perturbation method of structural design relevant to holographic vibration analysis," *AIAA Journal,* vol. 13, pp. 457-459, 1975.

[118] J. A. Brandon, *Strategies for structure dynamic modification*. Taunton, England, UK: Research Studies Press, 1990.

[119] T. Y. Li and T. Sauer, "Homotopy method for generalized eigenvalue problems Ax=ΛBx," *Linear Algebra and its Applications,* vol. 91, pp. 65-74, 1987.

[120] M. T. Chu, "A note on the homotopy method for linear algebraic eigenvalue problems," *Linear Algebra and its Applications,* vol. 105, pp. 225-236, 1988.

[121] B. N. Parlett, "The rayleigh quotient iteration and some generalizations for nonnormal matrices," *Mathematics of Computatoin,* vol. 28, pp. 679-693, 1974.

[122] A. Amiraslani and L. P., "Rayleigh quotient algorithms for nonsymmetric matrix pencils," *Numerical Algorithms,* vol. 51, pp. 5-22, 2009.

[123] S. Chen, *Matrix Perturbation Theory in Structural Dynamic Design*. Beijing, China: Science Press, 2007.

[124] S. H. Crandall, "Iterative procedures related to relaxation methods for eigenvalue problems," *Proceedings of the Royal Society of London, Series A, Mathematical and Physical Sciences*, vol. 207, pp. 416-423, 1951.

[125] G. H. Golub and Q. Ye, "Inexact inverse iterations for the generalized eigenvalue problems," *BIT Numerical Mathematics*, vol. 40, pp. 671-684, 2000.

[126] A. Amiraslani, D. A. Aruliah, and R. M. Corless, "The rayleigh quotient iteration for generalized companion matrix pencils," *Preprint*, 2006.

[127] C. A. Balanis, *Antenna Theory: Analysis and Design*, 3rd ed. New York: John Wiley & Sons, 2005.

[128] T. G. Wright and L. N. Trefethen, "Large-scale computation of pseudospectra using ARPACK and eigs," *Journal of Scientific Computing*, vol. 23, pp. 591-605, 2001.

[129] X. Yi, T. Wu, G. Lantz, J. Cooper, C. Cho, Y. Wang, *et al.*, "Sensing resolution and measurement range of a passive wireless strain sensor," *Proceedings of the 8th International Workshop on Structural Health Monitoring*, Stanford, CA, USA, 2011.

[130] X. Yi, C.-H. Fang, J. Cooper, C. Cho, R. Vyas, Y. Wang, *et al.*, "Strain sensing through a passive wireless sensor array," *Proceeding of ASCE Structures Congress* Chicago, IL, USA, 2012.

[131] X. Yi, R. Vyas, C. Cho, C.-H. Fang, J. Cooper, Y. Wang, *et al.*, "Thermal effects on a passive wireless antenna sensor for strain and crack sensing," *Proceedings of SPIE, Sensors and Smart Structures Technologies for Civil, Mechanical and Aerospace Systems*, San Diego, CA, USA, 2012.

[132] X. Yi, J. Cooper, Y. Wang, M. M. Tentzeris, and R. T. Leon, "Wilress crack sensing using an RFID-based folded patch antenna," *Proceeding of the 6th International Conference on Bridge Maintenance, Safety and Management*, Lake Como, Italy, 2012.

[133] X. Yi, C. Cho, C.-H. Fang, Y. Wang, R. T. Leon, J. Cooper, *et al.*, "Wireless strain and crack sensing using a folded patch antenna," *Proceedings of 6th European Conference on Antenna and Propagation*, Prague, Czech Republic, 2012.

[134] R. Vyas, V. Lakafosis, H. Lee, G. Shaker, L. Yang, G. Orecchini, *et al.*, "Inkjet printed, self powered, wireless sensors for environmental, gas, and authentication-based sensing," *IEEE Sensors Journal*, vol. 11, pp. 3139-3152, 2011.

[135] G. Shaker, S. Safavi-Naeini, N. Sangary, and M. M. Tentzeris, "Inkjet printing of ultrawideband (UWB) antennas on paper-based substrates," *IEEE Antennas and Wireless Propagation Letters*, vol. 10, pp. 111-114, 2011.

[136] R. Vyas, V. Lakafosis, H. Lee, G. Shaker, L. Yang, G. Orecchini, *et al.*, "Inkjet printed, self powered, wireless sensors for environmental,gas, and authentication-based sensing," *IEEE Sensors Journal*, vol. 11, pp. 3139-3152, 2011.

[137] S. Merilampi, T. Bjorninen, U. Leena, P. Ruuskanen, and L. Sydanheimo, "Embedded wireless strain sensors based on printed RFID tag," *Sensor Review*, vol. 31, pp. 32-40, 2011.

[138] C. Occhiuzzi, A. Rida, G. Marrocco, and M. M. Tentzeris, "RFID passive gas sensor integrating carbon nanotubes," *IEEE Transcations on Microwave Theory and techniques*, vol. 59, pp. 2674-2684, 2011.

[139] C. Cho, X. Yi, Y. Wang, T. Le, M. M. Tentzeris, and R. T. Leon, "Inkjet-printed RFID antenna sensor for strain monitoring," *Proceedings of 11th International Conference on Structural Safety & Reliability*, New York, NY, USA, 2013.

[140] R. Vyas, V. Lakafosis, A. Rida, N. Chaisilwattana, S. Travis, J. Pan, *et al.*, "Paper-based RFID-enabled wireless platforms for sensing applications," *IEEE Transactions on Microwave Theory and Techniques*, vol. 57, pp. 1370-1382, May 2009.